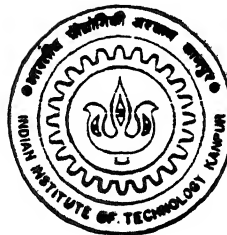


EXPERIMENTAL STUDY OF RAYLEIGH-BENARD CONVECTION USING INTERFEROMETRIC TOMOGRAPHY

94/10.561

by
DEBASISH MISHRA

TH
NET/1998/P
M687e



NUCLEAR ENGINEERING AND TECHNOLOGY PROGRAMME

Indian Institute of Technology, Kanpur

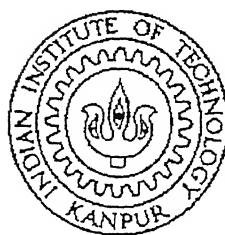
APRIL, 1998

EXPERIMENTAL STUDY OF RAYLEIGH-BENARD CONVECTION USING INTERFEROMETRIC TOMOGRAPHY

A Thesis Submitted
In Partial Fulfilment of the Requirements
for the Degree of
Doctor of Philosophy

by

Debasish Mishra



to the
NUCLEAR ENGINEERING AND TECHNOLOGY PROGRAMME
INDIAN INSTITUTE OF TECHNOLOGY, KANPUR
INDIA
April, 1998

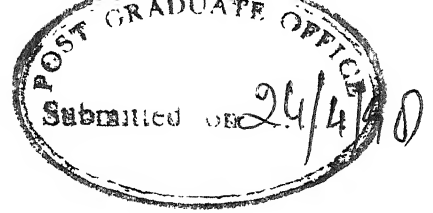
4 AUG 1999
CENTRAL LIBRARY
I. I. T., KANPUR

Acc. No. A 128770

DE/2226/1
1986/1



A128770



Certificate

It is certified that the work contained in the thesis entitled "EXPERIMENTAL STUDY OF RAYLEIGH-BENARD CONVECTION USING INTERFEROMETRIC TOMOGRAPHY" by Debasish Mishra, has been carried out under our supervision and that this work has not been submitted elsewhere for a degree.

A handwritten signature in dark ink, appearing to read "Prabhat Munshi".

Prabhat Munshi

A handwritten signature in dark ink, appearing to read "K. Murali".

K. Murali

Department of Mechanical Engineering and
Nuclear Engineering and Technology Programme
IIT Kanpur

Department of Mechanical Engineering
IIT Kanpur

April, 1998

Abstract

An experimental study of Rayleigh-Benard convection in an intermediate aspect ratio box that is square in plan is reported. An intermediate range of Rayleigh numbers has been considered in the study. The fluid employed is air. A Mach-Zehnder interferometer has been used to collect the line-of-sight projections of the temperature field in the form of interferometric fringes. Images have been recorded after a sufficient time has elapsed for the initial transients to have been eliminated. Interferograms have been collected from four to six view angles. These are used to obtain the three dimensional temperature field inside the cavity by using tomography. An algebraic reconstruction technique has been used for the inversion of the projection data. The convergence of the iterative inversion procedure was unambiguous and asymptotic. The reconstructed temperature field with a subset of the total data was found to be consistent with the remaining unused projections.

Results for three Rayleigh numbers, namely 13900, 34800 and 40200 have been reported. These were found to correspond to two distinct flow regimes. At these Rayleigh numbers, a well-defined steady state was not observed. At the lower Rayleigh number, the fringes away from the wall showed mild unsteadiness. At the higher Rayleigh number, the fringes were found to switch between two patterns. Results for the dominant mode also have been presented for this problem. At a Rayleigh number of 13900, three dimensional flow structures, whose influence is equivalent to longitudinal rolls have been observed. At Rayleigh numbers of 34800 and 40200, the flow was seen to be organised in the form of cubic cells. The associated flow pattern has been inferred to be a plume rising from the heated plate. The local Nusselt number variation seen to be consistent with the observed flow patterns for all the Rayleigh numbers studied.

Acknowledgements

I am sincerely thankful to my supervisors Professor K. Muralidhar and Professor Prabhat Munshi for rendering their valuable knowledge, excellent guidance and immeasurable help. They helped me at all stages of this work. Their interest and confidence in me was the reason for all the success I have achieved. They always promptly solved my problems with the first priority.

I am grateful to Professor Gautam Biswas, Professor Vinayak Eswaran for their valuable suggestions during my thesis and course work.

Special thanks to Mr Sambhunath Sharma for the excellent fabrication of my experimental setup and other accessories.

My parents were a constant source of encouragement for me throughout this work. They are perhaps the happiest people in this world at the successful completion of this work.

I am thankful to Anjali. She is a great friend. Her helping hand was always there for all sorts of problems.

Mr Apurva Prakash and Mr Sameer Agarwal helped me to solve graphics and other software related problem. I express my sincere thanks to them.

Mr Arun Kumar Saha and Mr Atul Srivastava gave a good company in the laboratory. I am thankful to them for their help and cooperation.

I take this opportunity to thank Dr Pradipta Panigrahi, Dr Subrata Sarkar, Mr Premananda Bera, Mr Gaurav Raghuvanshi, Mr Satyananda Sahoo, Mr Kamal Kant Mohapatra, Mr Rabi Narayan Panda Mr Dilip Chand and Mr Asim Chatterjee for various help on different occasions.

I was supported by the Dr K S Krishnan Fellowship of the Department of Atomic Energy Govt. of India. I am thankful to the organisation for the financial assistance.

Debasish Mishra

Contents

Certificate	iii
Abstract	v
Acknowledgements	vii
Contents	ix
List of Figures	xiii
List of Tables	xxiii
Nomenclature	xxvii
1 Introduction	1
1.1 Literature Review	6
1.1.1 Interferometric Tomography in Heat and Mass Transfer	6
1.1.2 Rayleigh-Benard Convection	8
1.1.3 Experimental Studies in Rayleigh-Benard Convection	10
1.1.4 Theoretical Aspects of Rayleigh-Benard Convection	17
1.1.5 Tomographic Algorithm	24
1.2 Objectives of the Present Work	24

2	Description of Experiments	27
2.1	Test Cell for Rayleigh-Benard Convection	28
2.2	Mach-Zehnder Interferometer	32
2.2.1	Laser Source	33
2.2.2	CCD Camera	34
2.2.3	Pneumatic Isolation Mount	35
2.2.4	Temperature Recorder	35
2.3	Alignment of the Interferometer	35
2.4	Recording Interferometric Projections	38
2.5	Uncertainty and Measurement Errors	41
3	Image Processing and Fringe Thinning	43
3.1	Image Processing	44
3.1.1	Filtering of Images	45
3.1.2	Image Enhancement	53
3.2	Fringe Thinning	58
3.2.1	Automatic Fringe Thinning Algorithm	60
3.2.2	Curve Fitting Approach	64
3.2.3	Paint-brush Drawing	66
4	Interferometry and Evaluation of Interferograms	69
4.1	Interferometry	69
4.2	Evaluation of Interferograms	77
4.3	Temperature Data over a Grid by Interpolation	79
5	Tomographic Reconstruction of the Temperature Field	83
5.1	ART	86
5.1.1	Simple ART	86

5.1.2	Gordon ART	
5.1.3	Gilbert ART	
5.1.4	Anderson ART	
5.2	MART	
5.3	AVMART	
5.4	Maximum Entropy	
5.5	Minimum Energy	
5.6	Testing of Tomographic Algorithms	
5.7	Performance Characteristics of Tomography Algorithms	
6	Results and Discussion	
6.1	Convection at $Ra=13900$	
6.1.1	Interferometric Projections	
6.1.2	Interferometric Tomography with 2 Projections	
6.1.3	Interferometric Tomography with 4 Projections	
6.1.4	Cross-checks on Reconstructed Temperature Field	
6.1.5	Local and Average Heat Transfer Rates	
6.2	Convection at $Ra=34800$ and 40200	
6.2.1	Cross-checks on Reconstructed Temperature Field	
6.2.2	Local and Average Heat Transfer Rates	
6.3	Convection at $Ra=51800$	
7	Conclusions and Scope for Future Work	1
7.1	Conclusions	1
7.2	Scope for Future Work	1
	References	10

A	Sensitivity of Reconstructed Field on Fringe Thinning Algorithm	173
B	Sensitivity of Tomographic Inversion to Initial Guess	181
B.1	Sensitivity Analysis for Initial Guess with a Two Dimensional Longitudinal Roll Pattern	181
B.2	Sensitivity Analysis for Initial Guess with a Three Dimensional Cubic Cell Pattern	194
C	Sensitivity to Noise in Projection Data	207
C.1	Sensitivity of Longitudinal Rolls	208
C.2	Sensitivity of Cubic Cells	218
D	Implementation of the Lagrange Multiplier Technique	229
D.1	Maximization of Entropy Through Lagrangian Multipliers	229
D.2	Minimization of Energy Through Lagrangian Multipliers	230

List of Figures

2.1	Schematic of the Apparatus for Rayleigh-Benard Convection.
2.2	Schematic of the Traversing Mechanism
2.3	Schematic Drawing of the Mach-Zehnder Interferometer
2.4	Infinite Fringe Setting of the Interferometer
2.5	Candle Flame in the Infinite Fringe Setting of the Interferometer
2.6	Wedge Fringe Setting of the Interferometer
2.7	Candle Flame in the Wedge Fringe Setting of the Interferometer
2.8	Definition of View Angle
3.1	Schematic of Butterfly Algorithm, for Implementation of FFT
3.2	An Original Interferogram
3.3	Two Dimensional Fourier Transform of the Intensity Function
3.4	Schematic of an One Dimensional Band Pass Filter
3.5	Original and Fourier Filtered Intensity Distribution
3.6	Filtered Interferogram
3.7	Contrast-improved Interferogram, (Histogram Equalization)
3.8	Median-filtered Interferogram
3.9	Intensity Distribution in Fourier-filtered and Median-filtered Interferogram
3.10	Template for High-boost Image Preparation
3.11	Contrast Improved Interferogram, (High Boost image)

3.12 Contrast Improved Interferogram, (High Boost image)	59
3.13 Two Major Directions for Tracing of Fringes	61
3.14 Four Possible Turning Options for Fringes	62
3.15 Eight Possible Directions for Movement	62
3.16 Thinned Images, Automatic Fringe Thinning Algorithm	64
3.17 Superimposed Thinned Images (Automatic Fringe Thinning Algorithm) with Original Images	65
3.18 Thinned Images, Curve Fitting Method for Fringe Thinning	65
3.19 Superimposed Thinned Images (Curve fitting method) with Original Images	66
3.20 Thinned Images, Paint-brush Drawing Method for Fringe Thinning	66
3.21 Superimposed Thinned Images (Paint-brush method) with Original Images	67
4.1 Calculation of Bending Angle of Light Ray due to Refraction effects	74
4.2 Bending of Light Ray in the Fluid Medium due to Refraction Effects . . .	75
4.3 Method of Computing Absolute Fringe Temperature from an Idealized Fringe Skeleton	78
4.4 Data Transfer to a 2 Dimensional Grid for the Idealized Fringe Pattern . .	80
4.5 Collection of Thinned Images, $Ra=13900$	80
4.6 Isotherms Obtained from Interpolated Temperature Data, $Ra=13900$. . .	81
4.7 Width-averaged Temperature Profile from the Interferograms, $Ra=13900$.	81
4.8 Width-averaged Temperature Profile from the Interferograms, $Ra=40200$.	81
5.1 Discretization of a Horizontal Plane of the Fluid Layer	85
5.2 Streamlines of the Roll Pattern, Generated for Validation of AVMART algorithms	100
5.3 Temperature Surface (Left) and Isotherms (Right) of the midplane of the Fluid Layer Corresponding to Two Dimensional Longitudinal Rolls	100
5.4 Temperature Surface (Left) and Isotherms (Right) of the midplane of the Fluid Layer Corresponding to Three Dimensional Cubic Cells	101

5.5	Numerically Generated Projection Data Corresponding to Rolls Formation in the Fluid Layer, Top left 0° , Top right 60° , Bottom left 90° and Bottom right 150°	
5.6	Numerically Generated Projection Data Corresponding to Cubic Cells Formation in the Fluid Layer, Top left 0° , Top right 60° , Bottom left 90° and Bottom right 150°	
6.1	(a) Original Interferograms at Neighbouring Locations of the Fluid Layer and (b) Collection of Interferograms, 0° Projection, $Ra=13900$	
6.2	(a) Original Interferograms at Neighbouring Locations of the Fluid Layer and (b) Collection of Interferograms, 30° Projection, $Ra=13900$	
6.3	(a) Original Interferograms at Neighbouring Locations of the Fluid Layer and (b) Collection of Interferograms, 60° Projection, $Ra=13900$	
6.4	(a) Original Interferograms at Neighbouring Locations of the Fluid Layer and (b) Collection of Interferograms, 90° Projection, $Ra=13900$	
6.5	(a) Original Interferograms at Neighbouring Locations of the Fluid Layer and (b) Collection of Interferograms, 120° Projection, $Ra=13900$	
6.6	(a) Original Interferograms at Neighbouring Locations of the Fluid Layer and (b) Collection of Interferograms, 150° Projection, $Ra=13900$	
6.7	Collection of Thinned Images, 0° Projection, $Ra=13900$	
6.8	Collection of Thinned Images, 30° Projection, $Ra=13900$	
6.9	Collection of Thinned Images, 60° Projection, $Ra=13900$	
6.10	Collection of Thinned Images, 90° Projection, $Ra=13900$	
6.11	Collection of Thinned Images, 120° Projection, $Ra=13900$	
6.12	Collection of Thinned Images, 150° Projection, $Ra=13900$	1
6.13	Reconstructed Temperature Surface at $y/h = 0.15$, $Ra=13900$, 2-view Tomography	1
6.14	Reconstructed Temperature Surface at $y/h = 0.5$, $Ra=13900$, 2-view Tomography	1
6.15	Reconstructed Temperature Surface at $y/h = 0.85$, $Ra=13900$, 2-view Tomography	1
6.16	Isotherms over a Horizontal Plane, $y/h = 0.15$, $Ra=13900$, 2-view Tomography	12

6.17 Isotherms over a Horizontal Plane, $y/h = 0.5$, $Ra=13900$, 2-view Tomography	124
6.18 Isotherms over a Horizontal Plane, $y/h = 0.85$, $Ra=13900$, 2-view Tomography	124
6.19 Reconstructed Temperature Surface at $y/h = 0.15$, $Ra=13900$, 4-view Tomography	125
6.20 Reconstructed Temperature Surface at $y/h = 0.5$, $Ra=13900$, 4-view Tomography	126
6.21 Reconstructed Temperature Surface at $y/h = 0.85$, $Ra=13900$, 4-view Tomography	127
6.22 Isotherms over a Horizontal Plane, $y/h = 0.15$, $Ra=13900$, 4-view Tomography	127
6.23 Isotherms over a Horizontal Plane, $y/h = 0.5$, $Ra=13900$, 4-view Tomography	128
6.24 Isotherms over a Horizontal Plane, $y/h = 0.85$, $Ra=13900$, 4-view Tomography	128
6.25 Numerically Generated Projection from the Reconstructed Temperature Field, 0° Projection, $Ra=13900$	129
6.26 Numerically Generated Projection from the Reconstructed Temperature Field, 60° Projection, $Ra=13900$	129
6.27 Numerically Generated Projection from the Reconstructed Temperature Field, 90° Projection, $Ra=13900$	130
6.28 Numerically Generated Projection from the Reconstructed Temperature Field, 150° Projection, $Ra=13900$	130
6.29 (a) Experimentally obtained Projection, (b) Numerically Generated Projection from the Reconstructed Temperature Field, 30° , $Ra=13900$	131
6.30 (a) Experimentally obtained Projection. (b) Numerically Generated Projection from the Reconstructed Temperature Field. 120° , $Ra=13900$	132
6.31 Experimentally obtained Line Integrals of the Nusselt Number for both the Plates, $Ra=13900$	135
6.32 Nusselt Number Surfaces for Top and Bottom Plates, $Ra=13900$	136
6.33 Comparison of Experimentally obtained Line Integrals of the Nusselt Number with Numerically Generated Line Integrals of the Nusselt Number for Projection Angles not used in Tomography, $Ra=13900$	137
6.34 Comparison of Experimentally obtained Line Integrals of the Nusselt Number with Numerically Generated Line Integrals of the Nusselt Number from the Reconstructed Temperature Field, $Ra=13900$	139

- 6.35 The Sequence of Fringe Patterns Formed during the Switching phenomenon
Cubic Cell Pattern (1st) Longitudinal Rolls Pattern (2nd) and back to Cu
bic Cell Pattern (3rd), $Ra=34800$
- 6.36 Interferograms of the Central Region of the Fluid Layer, 0° Projection (left)
and 90° Projection (right), $Ra=34800$
- 6.37 Thinned Images, Top left 0° , Top right 90° , Bottom left 30° and Bottom
right 60° , $Ra=34800$
- 6.38 Reconstructed Temperature Surfaces and Isotherms over Three Horizontal
Planes of the Fluid Layer, $y/h = 0.15$ (top), $y/h = 0.5$ (middle) and
 $y/h = 0.85$ (bottom), $Ra=34800$
- 6.39 Comparison of the Ray-averaged Nusselt Number for the Top and the Bot-
tom Plate
- 6.40 (a) Original Interferograms at Neighbouring Locations of the Fluid Layer
and (b) Collection of Interferograms, 0° Projection, $Ra=40200$
- 6.41 (a) Original Interferograms at Neighbouring Locations of the Fluid Layer
and (b) Collection of Interferograms, 90° Projection, $Ra=40200$
- 6.42 Original Interferogram at the Central Layer of Fluid Region, 30° Projection
(left) and 60° Projection (right), $Ra=40200$
- 6.43 Collection of Thinned Images, 0° Projection, $Ra=40200$
- 6.44 Collection of Thinned Images, 90° Projection, $Ra=40200$
- 6.45 Reconstructed Temperature Surface at $y/h = 0.15$, $Ra=40200$
- 6.46 Reconstructed Temperature Surface at $y/h = 0.5$, $Ra=40200$
- 6.47 Reconstructed Temperature Surface at $y/h = 0.85$, $Ra=40200$
- 6.48 Isotherms over a Horizontal Plane at $y/h = 0.15$ (left), $y/h = 0.5$ (middle)
and $y/h = 0.85$ (right), $Ra=40200$
- 6.49 Schematic of the Cubic Cells and the Rising Plume Inside the Cavity
- 6.50 Comparison of Experimentally obtained Thinned Images with Generated
Projections for Cross-check of Reconstructed Temperature Field, $Ra=40200$ 1
- 6.51 Experimentally obtained Line Integrals of the Nusselt Number for both the
Plates, $Ra=40200$ 1
- 6.52 Comparison of Experimentally obtained Line Integrals of the Nusselt Num-
ber with Numerically Generated Line Integrals of the Nusselt Number from
the Reconstructed Temperature Field, $Ra=40200$ 1

6.53	Comparison of Experimentally obtained Line Integrals of the Nusselt Number with Numerically Generated Line Integrals of the Nusselt Number from the Reconstructed Temperature Field, $Ra=40200$	159
6.54	Nusselt Number Surfaces for Top and Bottom Plates, $Ra=40200$	160
6.55	Sequence of Fringe Patterns in Unsteady Convection at $Ra=51800$	161
7.1	Summary of Flow Transitions in Rayleigh-Benard Convection	165
A.1	Width-averaged Temperature Profile of the Projection Temperature Field Inside a Roll	175
A.2	Reconstructed Temperature Surfaces Within the Cavity at the Central Horizontal Plane	176
A.3	Local Nusselt Number Variation over the Hot and Cold Plates; Comparison of the three Thinning Algorithms	179
B.1	Reconstructed Temperature Surface (Left) and Isotherms (Right) of the midplane of the Fluid Layer using AVMART1, Initial Guess (1), Two Dimensional Longitudinal Rolls.	182
B.2	Reconstructed Temperature Surface (Left) and Isotherms (Right) of the midplane of the Fluid Layer using AVMART2, Initial Guess (1), Two Dimensional Longitudinal Rolls.	183
B.3	Reconstructed Temperature Surface (Left) and Isotherms (Right) of the midplane of the Fluid Layer using AVMART3, Initial Guess (1), Two Dimensional Longitudinal Rolls.	183
B.4	Reconstructed Temperature Surface (Left) and Isotherms (Right) of the midplane of the Fluid Layer using AVMART1, Initial Guess (2), Two Dimensional Longitudinal Rolls.	185
B.5	Reconstructed Temperature Surface (Left) and Isotherms (Right) of the Mid plane of the Fluid Layer Using AVMART2, Initial Guess (Case 2), Two Dimensional Longitudinal Rolls.	185
B.6	Reconstructed Temperature Surface (Left) and Isotherms (Right) of the midplane of the Fluid Layer using AVMART3, Initial Guess (2), Two Dimensional Longitudinal Rolls.	186
B.7	Reconstructed Temperature Surface (Left) and Isotherms (Right) of the midplane of the Fluid Layer using AVMART1, Initial Guess (3), Two Dimensional Longitudinal Rolls	187

- B.8 Reconstructed Temperature Surface (Left) and Isotherms (Right) of the midplane of the Fluid Layer using AVMART2, Initial Guess (3), Two Dimensional Longitudinal Rolls
- B.9 Reconstructed Temperature Surface (Left) and Isotherms (Right) of the midplane of the Fluid Layer using AVMART3, Initial Guess (3), Two Dimensional Longitudinal Rolls
- B.10 Reconstructed Temperature Surface (Left) and Isotherms (Right) of the midplane of the Fluid Layer using AVMART1, Initial Guess (4), Two Dimensional Longitudinal Rolls
- B.11 Reconstructed Temperature Surface (Left) and Isotherms (Right) of the midplane of the Fluid Layer using AVMART2, Initial Guess (4), Two Dimensional Longitudinal Rolls
- B.12 Reconstructed Temperature Surface (Left) and Isotherms (Right) of the midplane of the Fluid Layer using AVMART3, Initial Guess (4), Two Dimensional Longitudinal Rolls
- B.13 Filtered Reconstructed Temperature Surface (Left) and Isotherms (Right) of the midplane of the Fluid Layer using AVMART1, Initial Guess (4), Two Dimensional Longitudinal Rolls
- B.14 Filtered Reconstructed Temperature Surface (Left) and Isotherms (Right) of the midplane of the Fluid Layer Using AVMART2, Initial Guess (4), Two Dimensional Longitudinal Rolls
- B.15 Filtered Reconstructed Temperature Surface (Left) and Isotherms (Right) of the midplane of the Fluid Layer Using AVMART3, Initial Guess (4), Two Dimensional Longitudinal Rolls
- B.16 Reconstructed Temperature Surface (Left) and Isotherms (Right) of the midplane of the Fluid Layer using AVMART1, Initial Guess (1), Cubic Cell Pattern
- B.17 Reconstructed Temperature Surface (Left) and Isotherms (Right) of the midplane of the Fluid Layer using AVMART2, Initial Guess (1), Cubic Cell Pattern
- B.18 Reconstructed Temperature Surface (Left) and Isotherms (Right) of the midplane of the Fluid Layer using AVMART3, Initial Guess (1), Cubic Cell Pattern
- B.19 Reconstructed Temperature Surface (Left) and Isotherms (Right) of the midplane of the Fluid Layer using AVMART1, Initial Guess (2), Cubic Cell Pattern
- B.20 Reconstructed Temperature Surface (Left) and Isotherms (Right) of the midplane of the Fluid Layer using AVMART2, Initial Guess (2), Cubic Cell Pattern

B.21 Reconstructed Temperature Surface (Left) and Isotherms (Right) of the midplane of the Fluid Layer using AVMART3, Initial Guess (2), Cubic Cell Pattern	198
B.22 Reconstructed Temperature Surface (Left) and Isotherms (Right) of the midplane of the Fluid Layer using AVMART1, Initial Guess (3), Cubic Cell Pattern	199
B.23 Reconstructed Temperature Surface (Left) and Isotherms (Right) of the midplane of the Fluid Layer using AVMART2, Initial Guess (3), Cubic Cell Pattern	200
B.24 Reconstructed Temperature Surface (Left) and Isotherms (Right) of the midplane of the Fluid Layer using AVMART3, Initial Guess (3), Cubic Cell Pattern	200
B.25 Reconstructed Temperature Surface (Left) and Isotherms (Right) of the midplane of the Fluid Layer using AVMART1, Initial Guess (4), Cubic Cell Pattern	201
B.26 Reconstructed Temperature Surface (Left) and Isotherms (Right) of the midplane of the Fluid Layer using AVMART2, Initial Guess (4), Cubic Cell Pattern	202
B.27 Reconstructed Temperature Surface (Left) and Isotherms (Right) of the midplane of the Fluid Layer using AVMART3, Initial Guess (4), Cubic Cell Pattern	202
B.28 Filtered Reconstructed Temperature Surface (Left) and Isotherms (Right) of the midplane of the Fluid Layer using AVMART1, Initial Guess (4), Cubic Cell Pattern	203
B.29 Filtered Reconstructed Temperature Surface (Left) and Isotherms (Right) of the midplane of the Fluid Layer using AVMART2, Initial Guess (4), Cubic Cell Pattern	204
B.30 Filtered Reconstructed Temperature Surface (Left) and Isotherms (Right) of the midplane of the Fluid Layer using AVMART3, Initial Guess (4), Cubic Cell Pattern	204
C.1 Noisy Projection Data corresponding to Longitudinal Roll Formation in the Fluid Layer, Top left 0° , Top right 60° , Bottom left 90° and Bottom right 150°	208
C.2 Noisy Projection Data corresponding to Cubic Cell Formation in the Fluid Layer, Top left 0° , Top right 60° , Bottom left 90° and Bottom right 150°	209
C.3 Reconstructed Temperature Surface (Left) and Isotherms (Right) of the midplane of the Fluid Layer using AVMART1, Noisy Projection Data, 2-view Reconstruction, Two Dimensional Longitudinal Rolls	210

- C.4 Reconstructed Temperature Surface (Left) and Isotherms (Right) of the midplane of the Fluid Layer using AVMART2, Noisy Projection Data, 2-view Reconstruction, Two Dimensional Longitudinal Rolls
- C.5 Reconstructed Temperature Surface (Left) and Isotherms (Right) of the midplane of the Fluid Layer using AVMART3, Noisy Projection Data, 2-view Reconstruction, Two Dimensional Longitudinal Rolls
- C.6 Fourier Filtered Reconstructed Temperature Surface (Left) and Isotherms (Right) of the midplane of the Fluid Layer Using AVMART1, Noisy Projection Data, 2-view Reconstruction, Two Dimensional Longitudinal Rolls
- C.7 Fourier Filtered Reconstructed Temperature Surface (Left) and Isotherms (Right) of the midplane of the Fluid Layer Using AVMART2, Noisy Projection Data, 2-view Reconstruction, Two Dimensional Longitudinal Rolls
- C.8 Fourier Filtered Reconstructed Temperature Surface (Left) and Isotherms (Right) of the midplane of the Fluid Layer Using AVMART3, Noisy Projection Data, 2-view Reconstruction, Two Dimensional Longitudinal Rolls
- C.9 Reconstructed Temperature Surface (Left) and Isotherms (Right) of the midplane of the Fluid Layer using AVMART1, Noisy Projection Data, 4-view Reconstruction, Two Dimensional Longitudinal Rolls
- C.10 Reconstructed Temperature Surface (Left) and Isotherms (Right) of the midplane of the Fluid Layer using AVMART2, Noisy Projection Data, 4-view Reconstruction, Two Dimensional Longitudinal Rolls
- C.11 Reconstructed Temperature Surface (Left) and Isotherms (Right) of the midplane of the Fluid Layer using AVMART3, Noisy Projection Data, 4-view Reconstruction, Two Dimensional Longitudinal Rolls
- C.12 Fourier-filtered Reconstructed Temperature Surface (Left) and Isotherms (Right) of the midplane of the Fluid Layer using AVMART1, Noisy Projection Data, 4-view Reconstruction, Two Dimensional Longitudinal Rolls .
- C.13 Fourier-filtered Reconstructed Temperature Surface (Left) and Isotherms (Right) of the midplane of the Fluid Layer using AVMART2, Noisy Projection Data, 4-view Reconstruction, Two Dimensional Longitudinal Rolls .
- C.14 Fourier-filtered Reconstructed Temperature Surface (Left) and Isotherms (Right) of the midplane of the Fluid Layer using AVMART3, Noisy Projection Data, 4-view Reconstruction, Two Dimensional Longitudinal Rolls .
- C.15 Reconstructed Temperature Surface (Left) and Isotherms (Right) of the midplane of the Fluid Layer using AVMART1, Noisy Projection Data, 2-view Reconstruction, Cubic Cell Pattern
- C.16 Reconstructed Temperature Surface (Left) and Isotherms (Right) of the midplane of the Fluid Layer using AVMART2, Noisy Projection Data, 2-view Reconstruction, Cubic Cell Pattern

C.17 Reconstructed Temperature Surface (Left) and Isotherms (Right) of the midplane of the Fluid Layer using AVMART3, Noisy Projection Data, 2-view Reconstruction, Cubic Cell Pattern	219
C.18 Fourier-filtered Reconstructed Temperature Surface (Left) and Isotherms (Right) of the midplane of the Fluid Layer using AVMART1, Noisy Projection Data, 2-view Reconstruction, Cubic Cell Pattern	220
C.19 Fourier-filtered Reconstructed Temperature Surface (Left) and Isotherms (Right) of the midplane of the Fluid Layer using AVMART2, Noisy Projection Data, 2-view Reconstruction, Cubic Cell Pattern	221
C.20 Fourier-filtered Reconstructed Temperature Surface (Left) and Isotherms (Right) of the midplane of the Fluid Layer using AVMART3, Noisy Projection Data, 2-view Reconstruction, Cubic Cell Pattern	222
C.21 Reconstructed Temperature Surface (Left) and Isotherms (Right) of the midplane of the Fluid Layer using AVMART1, Noisy Projection Data, 4-view Reconstruction, Cubic Cell Pattern	222
C.22 Reconstructed Temperature Surface (Left) and Isotherms (Right) of the midplane of the Fluid Layer using AVMART2, Noisy Projection Data, 4-view Reconstruction, Cubic Cell Pattern	223
C.23 Reconstructed Temperature Surface (Left) and Isotherms (Right) of the midplane of the Fluid Layer using AVMART3, Noisy Projection Data, 4-view Reconstruction, Cubic Cell Pattern	223
C.24 Fourier-filtered Reconstructed Temperature Surface (Left) and Isotherms (Right) of the midplane of the Fluid Layer using AVMART1, Noisy Projection Data, 4-view Reconstruction, Cubic Cell Pattern	224
C.25 Fourier-filtered Reconstructed Temperature Surface (Left) and Isotherms (Right) of the midplane of the Fluid Layer using AVMART2, Noisy Projection Data, 4-view Reconstruction, Cubic Cell Pattern	225
C.26 Fourier-filtered Reconstructed Temperature Surface (Left) and Isotherms (Right) of the midplane of the Fluid Layer using AVMART3, Noisy Projection Data, 4-view Reconstruction, Cubic Cell Pattern	226
C.27 Reconstructed Temperature Surface (Left) and Isotherms (Right) of the midplane of the Fluid Layer using MART3, Noisy Projection Data, 2-view Reconstruction, Two Dimensional Longitudinal Rolls	227

List of Tables

2.1	Specifications of the constant temperature bath (huber model: variostat	
2.2	Specifications of the Helium-Neon laser	
2.3	Specifications of the Temperature Recorder	
5.1	Reconstruction Errors from Different ART Algorithms: Comparison with AVMART2	
5.2	Fractional Distribution of the E_1 Error over the Fluid Domain.	
5.3	Reconstruction Errors from Different MART Algorithms: Comparison with AVMART2	
5.4	Fractional Distribution of the E_1 Error over the Fluid Domain.	
5.5	Reconstruction Errors from Different AVMART Algorithms: Comparison with AVMART2	
5.6	Fractional Distribution of the E_1 Error over the Fluid Domain.	
5.7	Summary of Performance of AVMART2	
6.1	Differences between 2-view and 4-view Tomography in the Reconstructed Temperature Field, Ra=13900	
6.2	Fractional Distribution of the E_1 Error over the Fluid Domain: Comparison between 2-view and 4-view Tomography, Ra=13900	
6.3	Comparison of Average Nusselt Number with Gebhart <i>et al.</i> , (1988), Ra = 13900.	
6.4	Comparison of the Average of the Ray-averaged Nusselt Number with Geb- hart <i>et al.</i> , 1988, Ra=34800.	1
6.5	Comparison of Average Nusselt Number with Gebhart <i>et al.</i> , (1988), Ra = 40200	1

A.1	Reconstruction Errors from the three Fringe Thinning Algorithms.	178
A.2	Fractional Distribution of the E_1 Error over a Horizontal Plane.	178
A.3	Comparison of Average Nusselt Number Based on the Width of a Single Roll	179
B.1	Comparison of the Three AVMART Algorithms: Initial Guess (1), Temperature Field in the Form of Longitudinal Rolls	184
B.2	Fractional Distribution of the E_1 Error over the Fluid Domain, Initial Guess (1), Temperature Field in the Form of Longitudinal Rolls	184
B.3	Comparison of the Three AVMART Algorithms: Initial Guess, (2), Temperature Field in the Form of Longitudinal Rolls	186
B.4	Fractional Distribution of the E_1 Error over the Fluid Domain, Initial Guess (2), Temperature Field in the Form of Longitudinal Rolls	187
B.5	Comparison of the Three AVMART Algorithms: Initial Guess (3), Temperature Field in the Form of Longitudinal Rolls	189
B.6	Fractional Distribution of the E_1 Error over the Fluid Domain, Initial Guess (3), Temperature Field in the Form of Longitudinal Rolls	189
B.7	Comparison of the Three AVMART Algorithms: Initial Guess (4), Temperature Field in the Form of Longitudinal Rolls	189
B.8	Fractional Distribution of the E_1 Error over the Fluid Domain, Initial Guess (4), Temperature Field in the Form of Longitudinal Rolls	191
B.9	Comparison of the Three AVMART Algorithms: Initial Guess (1), Temperature Field in the Form of Cubic Cells	194
B.10	Fractional Distribution of the E_1 Error over the Fluid Domain, Initial Guess (1), Temperature Field in the Form of Cubic Cells	196
B.11	Comparison of the Three AVMART Algorithms: Initial Guess (2), Temperature Field in the Form of Cubic Cells	198
B.12	Fractional Distribution of the E_1 Error over the Fluid Domain, Initial Guess (2), Temperature Field in the Form of Cubic Cells	199
B.13	Comparison of the Three AVMART Algorithms: Initial Guess (3), Temperature Field in the Form of Cubic Cells	201
B.14	Fractional Distribution of the E_1 Error over the Fluid Domain, Initial Guess (3), Temperature Field in the Form of Cubic Cells	201

B.15	Comparison of the Three AVMART Algorithms: Initial Guess (4), Temperature Field in the Form of Cubic Cells	
B.16	Fractional Distribution of the E_1 Error over the Fluid Domain, Initial Guess (4), Temperature Field in the Form of Cubic Cells	
C.1	Comparison of the Three AVMART Algorithms: Temperature Field in the Form of Longitudinal Rolls, with 5% Added Noise in Projection Data. 2-view Reconstruction	
C.2	Fractional Distribution of the E_1 Error over the Fluid Domain, Temperature Field in the Form of Longitudinal Rolls, with 5% Added Noise in Projection Data, 2-view Reconstruction	
C.3	Comparison of the Three AVMART Algorithms: Temperature Field in the Form of Longitudinal Rolls, with 5% Added Noise in Projection Data. 4-view Reconstruction	
C.4	Fractional Distribution of the E_1 Error over the Fluid Domain, Temperature Field in the Form of Longitudinal Rolls, with 5% Added Noise in Projection Data, 4-view Reconstruction	
C.5	Comparison of the Three AVMART Algorithms: Temperature Field in the Form of Cubic Cells, with 5% Added Noise in Projection Data. 2-view Reconstruction	
C.6	Fractional Distribution of the E_1 Error over the Fluid Domain, Temperature Field in the Form of Cubic Cells, with 5% Added Noise in Projection Data. 2-view Reconstruction	1
C.7	Comparison of the Three AVMART Algorithms: Temperature Field in the Form of Cubic Cells, with 5% Added Noise in Projection Data, 4-view Reconstruction	1
C.8	Fractional Distribution of the E_1 Error over the Fluid Domain, Temperature Field in the Form of Cubic Cells, with 5% Added Noise in Projection Data, 4-view Reconstruction	2
C.9	Comparison of the MART3 Algorithm with AVMART2 Algorithm: Temperature Field in the Form of Two Dimensional Longitudinal Rolls. with 5% Added Noise in Projection Data, 2-view Reconstruction	2
C.10	Fractional Distribution of the E_1 Error over the Fluid Domain: Comparison Between MART3 and AVMART2 Algorithms, Temperature Field in the Form of Two Dimensional Longitudinal Rolls, with 5% Added Noise in Projection Data, 2-view Reconstruction	2

Nomenclature

g	Accelaration due to gravity
h	Height of the cavity
j	Imaginary unit
L	Distance traversed by the laser beam through the test cell
M	Integer number (Chapter 3), number of rays (Chapter 5)
n	Refractive index of the fluid
N	Number of samples (Chapter 3), number of pixels (Chapter 5)
Nu	Nusselt number (line-of-sight and surface averaged)
Pr	Prandtl number of the fluid, (ν/α)
Ra	Rayleigh number
s	Coordinates along an axis inclined at an angle to the x axis.
T	Temperature
ΔT_e	Temperature difference between successive fringes
W	Total value of weight function along a ray
w	Weight function computed on a local grid
x, y, z	Cartesian co-ordinates
α	Thermal diffusivity of the fluid
β	Coefficient of volume expansion of the fluid
λ	Wavelength of the laser
μ	Relaxation factor
ν	Kinematic viscocity of the fluid
ϕ	Experimental projection data
$\bar{\phi}$	Numerically computed projection data
θ	Projection angle
ω	Wavenumber

Subscripts

avg	Average of the three dimensional temperature field along the light ray
cold	Cold wall
hot	Hot wall
i	Index of samples in the spatial domain (Chapter 3), ray number (Chapter 5)
rc	Ray number of all the rays passing through the j th pixel
j	Pixel number
ref	Ambient reference temperature

Superscripts

k	Iteration number
-----	------------------

Chapter 1

Introduction

Non-intrusive techniques are becoming increasingly popular in engineering measurements. These techniques generally employ radiation sources as probes. Radiation-based measurements share a common feature of generating data of a cross-sectional field of view. This is to be contrasted with mechanical probes which are concerned with measurements at a point in space and can accomplish this task only after the field to be studied has been physically perturbed. Hence the scanning of a cross-section of the physical region using radiation-based probes results in a large volume of information with practically no time delay.

The choice of the radiation source in a radiation-based measurement is problem specific and cannot be generalized to all classes of problems. The technique to be chosen for a problem has to be decided from both experimental and theoretical points-of-view. The radiation employed in any measurement is generally required to be monochromatic. Its wavelength depends on the application concerned. A variety of sources such as gamma rays, ultrasonics and lasers have been used in engineering. Material testing employs ultrasonic waves or X-rays to permit the transmission of radiation in the solid region. Oil exploration, on the other hand uses phenomena such as disturbances in the earth's magnetic field and scattering of mechanical vibrations that are directed towards the earth's interior. In optical systems specific to fluid mechanics applications, lasers in the visible range are employed. One can then collect the information on optical path length and frequency shifts of the scattered light from particles contained in the fluid. The selection of the detector system depends on the radiation employed and the measurement accuracy.

desired. The method of data reduction also shows considerable variability, depending among other factors on the quantity to be measured.

When the wavelength of radiation used is in the visible range, the measurement procedure classifies as an optical technique. The region being scanned appears then on a screen as an image that is visible to the naked eye. Optical techniques require the medium under study to be transparent. In thermal sciences as well as fluid mechanics, there has been a revival of optical techniques for temperature and velocity measurements in fluids, primarily for the following reasons:

- Commercially available lasers have a high degree of coherence (both spatial and temporal) and are cost-effective.
- Optical images can be recorded conveniently through computers and can be processed as a string of numbers through numerical algorithms.

The implications are that: (1) coherence generates stable image patterns which truly reflect fluid behaviour and (2) computer programs now simplify and replace very tiring manual data extraction procedures.

Broadly the optical techniques employed in fluid-flow measurements can be divided into three categories: (i) flow visualisation through the injection of tracer particles, (ii) measurement of frequency shift of scattered illumination from an injected tracer medium in the flow field, and (iii) measurement of index of refraction of the fluid or its spatial derivatives. The present thesis utilizes the method belonging to the third category to study buoyancy-induced convection in a Rayleigh-Benard configuration. Optical methods which utilize the dependence of refractive index of light on quantities such as density, concentration and temperature can be configured in many different ways. Three popular routes are:

1. Shadowgraph, where the reduction in light intensity on beam divergence is employed. This specifically measures the variation of the second order derivative of the index of refraction normal to the light beam.
2. Schlieren, where the deflection of light in a variable refractive-index field is captured. This technique handles the variation of the first order derivative of the index of refraction normal to the light beam.
3. Interferometry, where the image formation is related to changes in the refractive

index with respect to a reference environment. This method responds directly to the refractive index field of the flow system.

For a wide class of applications where temperature differences are within certain bounds, interferometry appears to be a versatile tool for accurate measurement of two-dimensional unsteady temperature fields, and with some modification, for velocity fields. In fact, if refraction errors are taken care of, the method adopted in the present study is a promising tool for measurements including high temperature gradients. Many applications that involve free and forced convective heat transfer are included in this category. One large-scale application worth mentioning is the satellite-based imaging of the planetary atmosphere using coherent optics. Shadowgraphy and schlieren techniques are well suited to the problem of high temperature/density gradients such as flames and shocks.

Information about temperature is present in interferometry in the optical path difference between the test and the reference beams and hence their phase. This necessarily requires a coherent and monochromatic light source. In contrast the schlieren and shadowgraph techniques do not rely on coherence though a monochromatic source is needed. The requirement of a coherent light source and coherent optics makes interferometry expensive compared to the other refractive index-based methods. However interferometry can generate accurate and unambiguous data. For a purely two-dimensional flow field with the light ray direction oriented at normal incidence, interferometry generates interference patterns representing either isotherms or the temperature profile depending on the optical adjustment. If the flow field is three-dimensional interferometry still gives an overall idea of the flow mechanism in terms of an average effect along the direction of the light ray. Hence interferometry has the advantage of visualising the thermal phenomenon under study while the experiment is in progress in a more appealing way compared to the schlieren and shadowgraph techniques. All the three methods belonging to the class of refractive index-based methods are capable of being used in real-time applications. Since each of them produces an integrated effect of a three-dimensional field in the form of a two-dimensional image it is possible to employ the tomographic method to reconstruct the three-dimensional field of refractive index or its derivative. As far as experiments are concerned interferometry is more complex compared to the other two methods.

Optical techniques can be used for validating different numerical solutions. If the three-dimensional field from a numerical solution is computed, schlieren, shadowgraph

and interferometric images can be numerically constructed and can be compared with those in the respective experiments.

The present thesis is an application of the interferometry coupled with the method of tomography to measure the three dimensional temperature field in a buoyancy-driven convective flow system. The goal of tomography is to reconstruct a two dimensional function from a set of its line integrals available from a few angles. Subsequently a three dimensional field can be reconstructed either by sequential two dimensional reconstruction or from a set of surface integrals available from various angles.

The problem undertaken in the present study is Rayleigh-Benard convection in a geometry that is square in plan. Rayleigh-Benard convection is of interest in a variety of engineering applications and has a great scientific importance. It has direct relevance to atmospheric convection. Its importance can be seen from geophysical studies to astronomical research. The importance of Rayleigh-Benard convection is very strongly felt for theoretical as well as fundamental reasons. The equations governing the problem are coupled non-linear partial differential equations. These equations have been used by many workers to study the transition from laminar to turbulent convection and the associated bifurcation sequences. Three dimensional temperature measurement in a Rayleigh-Benard system at intermediate Rayleigh numbers has been reported in the present work.

Consider a layer of fluid confined between two large horizontal plates whose density decreases with increase of temperature. If the temperature of the upper plate is greater than the temperature of the lower plate, there will be a stable stratification and the thermal arrangement of the fluid layer is stable. The hot fluid being lighter will float over the heavier cold fluid. The heat transfer across the fluid layer will be only through the process of conduction. When the enclosed fluid layer is heated from below and cooled from above, an unstable stratification of the fluid layer is produced. The cold heavy fluid is thus above the light hot fluid. The fluid layer thus has a natural tendency to readjust towards a stable configuration. The driving force responsible for the convective motion is buoyancy. When the buoyancy force is below a certain threshold the viscous forces between the fluid layers act as internal friction and inhibit fluid motion. Heat transfer across the fluid layer is then purely by conduction. Once the threshold value of buoyancy is exceeded, convective motion starts. The resulting flow pattern depends on the strength of buoyancy, fluid properties and the geometry of the confining boundaries.

Pattern formation due to convection in fluids was first observed by Weber in 1831. He reported a flow pattern appearing as an assembly of polygonal cells developed in droplets of an alcohol-water solution containing a tracer and present in air. Thermal convection and the associated flow pattern was first observed by Benard in 1901 as a hexagonal planar structure. Later Chandrasekhar, 1961 studied the stability of the hexagonal roll structure. The earlier studies of Weber in 1831 are now referred as Benard-Marangoni convection. The basic instability here is not due to the gravitationally unstable density gradient created in Rayleigh-Benard convection but due to the surface tension gradients at the free surface. In 1916, Rayleigh showed that convection starts after a critical temperature difference between the two horizontal walls has been exceeded. Rayleigh's work is the first theoretical explanation for buoyancy-induced fluid movement as observed by Benard in 1901¹. Hence the fluid motion in a differentially, heated fluid layer has been called Rayleigh-Benard convection.

Rayleigh-Benard convection in the simplest form can be defined as a horizontal fluid layer confined between a pair of parallel infinite plates, heated from below and cooled from the top. The heated-from-below situation produces a top heavy arrangement which is an unstable configuration. As a consequence, the fluid inside the cavity has a tendency to move towards a stable configuration. In practice, the assumption of infinitely long plates has to be restricted to long but finite plates. Hence side walls have to be employed and these are kept insulated. The presence of a large width-to-height ratio is an approximation to an infinite horizontal fluid layer.

The non-dimensional parameter Rayleigh number is a relative measure of the strength of the buoyancy force to viscous force. More appropriately, it can be understood as the ratio of the gravitational potential energy to be gained by reversing the unstable stratification caused by the thermal gradient, to the energy required by the fluid to overcome viscous dissipation and thermal diffusion. The Prandtl number is a second dimensionless quantity arising in thermal convection. It is a measure of ratio of the molecular diffusivity of momentum to that of thermal energy and is a fluid property. Flow transitions are generally documented in terms of Rayleigh number and Prandtl number. The Rayleigh number is defined as:

$$Ra = \frac{g\beta(T_{hot} - T_{cold})h^3}{\nu\alpha} \quad (1.1)$$

¹There is recent evidence that Benard's experiments were also influenced by surface tension.

and the Prandtl number:

$$\text{Pr} = \frac{\nu}{\alpha} \quad (1.2)$$

In the present work a Mach-Zehnder interferometer has been employed to collect the line-of-sight projections of the temperature field inside a Rayleigh-Benard setup. The geometry is square in plan and two different aspect ratios (width of the fluid layer to the height of the fluid layer) have been considered. The fluid employed is air. The line-of-sight projections of the the cavity have been collected in the form of interferograms. The projections of the temperature field has been collected from various angles by rotating the test cell. Various image processing operations and interpolation have been employed to extract quantitative data from the interferograms. The three dimensional temperature field has been reconstructed using tomographic algorithms and heat transfer studies have been subsequently carried out. From the reconstructed temperature field it has been possible to visualize the flow field. A variety of cross-checks have been implemented to gain confidence in the experimental data.

1.1 Literature Review

Application of computerised tomography for measurements in heat and mass transfer has been a topic of research over approximately 40 years. Though the method of tomography and the procedure for data extraction were not the same as it is today, yet the possibility of using this idea can be seen in publications way back in 1940. There has been a revival in the subject in the last two decades owing to parallel technological growth for example, in computing resources, data storage and instrumentation.

1.1.1 Interferometric Tomography in Heat and Mass Transfer

Application of interferometry for qualitative analysis of the two dimensional flow field is well known (Goldstein, 1983). The extension to three dimensional problems is of more recent origin. Snyder (1988) studied tomographically the instantaneous species concentration in a co-flowing jet of neutrally buoyant argon-helium mixture flowing into air. Watt and Vest (1990) studied the structures of a turbulent helium jet using interferometric techniques, with the aid of computer tomography. The recording media in this study

was a hologram. The authors used a pulsed ruby laser to record the holograms. Subsequently, a helium-neon laser was used for reconstruction of the phase information from the holograms. Tolpadi and Kuehn (1991) measured the three-dimensional temperature field in a conjugate conduction-convection problems using interferometric projections. Holograms were recorded and quantitative projection data was retrieved from the holograms. Bahl and Liburdy (1991a) reported their work on reconstruction of three-dimensional temperature distribution above a horizontal heated disk exposed to air. Holographic interferometry with tomography was employed by the workers. Bahl and Liburdy (1991b) have considered various reconstruction algorithms that can be applied to multi-directional interferometric projection data for tomographic reconstruction and presented the effect of noise on reconstructions. The authors have shown a relationship between the noise level in the projection data and the required number of iterations that should be allowed on the noisy data. Michael and Yang (1992) have studied Rayleigh-Benard convection with water as the fluid in a small cavity using interferometric tomography. The formation of longitudinal rolls was detected in the reconstructed three dimensional temperature field. Mayinger (1993) has discussed the different optical image-forming techniques and their use in heat transfer studies. Experimental arrangements and computer-aided data processing have been discussed in the context of tomographic studies. Mayinger (1994) has reviewed different optical measurements techniques and application of tomographic algorithms to evaluate three dimensional fields. Dietz and Balkowski (1997) have considered the bending of light ray due to refraction and suggested an approach to estimate the refraction errors in classical interferometry in strongly refracting fields. More recently Subbarao *et al.* (1997a-b) have considered a wide variety of algebraic reconstruction techniques and their application to limited-data tomography. The authors have recommended that the MART family of algorithms are superior compared to other ART and the optimization family of algorithms. The authors have shown that these algorithms can reconstruct a field (like temperature in Rayleigh-Benard convection) within certain errors even from as few as two orthogonal projections. Three dimensional measurements using tomography for heat and mass transfer studies and an application of the Sobolov space-based error analysis for the reconstructed field has been reviewed by Munshi (1997).

1.1.2 Rayleigh-Benard Convection

A large amount of literature is available in the field of Rayleigh-Benard convection. The studies extend over a wide range of Rayleigh number, Prandtl number and a variety of geometries. Computational studies are quite abundant, whereas not many experimental studies have been reported. Most literature in this area is again dedicated to cavities which are small in size. The available literature on intermediate and large aspect ratio cavities is less compared to small aspect ratio cavities. The aspect ratio is defined as the ratio of horizontal width of the cavity to the vertical depth of the fluid layer. It is a maximum for an infinite fluid layer. The objectives of the published research is to identify the critical Rayleigh number when flow undergoes a transition from one configuration to another. When Rayleigh number is below the first critical value, the buoyancy forces are not sufficient to overcome the viscous forces between the fluid layer. Hence true convection starts only above a particular Rayleigh number. The critical Rayleigh number for the onset of convection in an infinite fluid layer does not depend on the Prandtl number of the fluid, whereas all subsequent transitions are a strong function of the Prandtl number. The critical Rayleigh number at the onset of convection is dependent on the geometry of the cavity. It decreases with the increasing aspect ratio. This part of transition from no motion to onset of convection has been verified by many researchers and the transition Rayleigh number presented for different aspect ratio boxes are in good agreement with experiments.

The study of Rayleigh-Benard convection can be broadly divided into three main categories from the point-of-view of the size of the cavity, namely small ($\approx 2-10$), intermediate ($\approx 10-30$) and large ($\approx 30-60$) aspect ratio. Reported behaviour of convection in these ranges of aspect ratios is different. This is because the side walls play a role in stabilising the convection pattern. Within each range of aspect ratio, the flow transitions strongly depend on the Prandtl number of the fluid and the geometrical structure of the side walls. The published work on each of the three ranges of aspect ratio is scattered and not uniform. A large amount of literature is available for the low aspect ratio enclosures. This is because numerical calculations are easier to perform over a small domain. Experiments with small aspect ratio enclosures are also time effective. Further, this helps analysts to compare their results with published experiments.

For an increase in Rayleigh number above the critical, flow undergoes a sequence

of bifurcations and finally resulting in turbulence. In a bifurcation, the flow undergoes a complete change in its structure. For example an increase in Rayleigh number may result in the formation of plumes starting from longitudinal rolls. If an increase in Rayleigh number corresponds only to a continuous increase in heat transfer rate across the fluid layer or an increase in velocity of the convecting fluid, it is not a bifurcation.

For a given aspect ratio, there is a minimum temperature difference to be maintained between the two horizontal plates of the cavity so that there is onset of convection. If this temperature difference is small, the relevant properties of the fluid change very little over the height of the fluid layer. For a numerical study, the Oberbeck-Boussinesq approximation can be applied to the governing equations. This approximation assumes that the fluid properties are independent of temperature except in the buoyancy term of the Navier-Stokes equation, where density is a function of temperature. Stability analysis for this set of equations predicts the formation of a straight roll pattern in a finite aspect ratio cavity via a continuous transition from the no-motion state. On the other hand if the temperature difference between the two plates is not small, the fluid properties are dependent on the variation of the temperature along the vertical axis. This is generally referred to as a non-Oberbeck-Boussinesq case. The onset of convection is known to occur in the form of hexagonal cells as in the case of an infinite fluid layer, and there is a discontinuous transition from the state of no-motion.

When Rayleigh number is very close to the critical value for the onset of convection, hexagonal convection cells have been observed both experimentally and numerically for small and intermediate aspect ratio boxes. Numerical studies also show the following: For liquids, the fluid particles within the hexagonal cells have an upward motion in the center, while for gases the particles have a downward motion in the center.

For an increase in Rayleigh number, the formation of stable two dimensional longitudinal rolls are seen. The two dimensional rolls slowly deform to three dimensional rolls with temperature variation along the roll axis with further increase in Rayleigh number. The three dimensional rolls are steady over a range of Rayleigh numbers. For further increase in the Rayleigh number, adjacent rolls start to merge leading to a reduction in the number of rolls. The flow switches to a time-dependent regime at higher Rayleigh numbers and slowly approaches the turbulent state.

The roll structure is the most stable pattern for convection near the critical Rayleigh

number for onset of convection. There is a growing tendency of these rolls to terminate their axis perpendicular to the wall. For low Prandtl number fluids this results in curved rolls because of bending of rolls near the corner of the rectangular cavity. The curvature in the rolls induces large-scale convection. This is called the skewed varicose instability. Formation and movement of defects in the rolls leads to time dependence of the flow pattern. The time dependent flow field can follow several routes to chaos. Some of the known routes to chaos are through the evolution of a quasi-periodic state, or through intermittency. The chaotic convection leads finally to the turbulent state. For the large aspect ratio enclosure, some studies beyond the critical Rayleigh number for the onset of convection show that the flow is always non-periodic and time dependent.

The intermediate aspect ratio enclosure shows many interesting phenomena compared to small aspect ratio cavity. Reported work in this range of aspect ratio are only a few. The evolution of time dependence and the nature of bifurcations sequence in intermediate aspect ratio boxes is more complex compare to low or a very high aspect ratio box. Unlike the low aspect or a very high aspect ratio box, there is no general agreement in the literature for the intermediate range. The intermediate aspect ratio boxes, to a degree of approximation simulate the condition of a infinitely extended horizontal fluid layer, since the effect of side walls on the fluid convection is less compared to low aspect ratio boxes. Studies however show that the lateral walls do play a role in determining the long-time flow patterns. Studies in Rayleigh-Benard convection in intermediate aspect ratio boxes have not been widely reported.

The available literature for low and intermediate aspect ratio boxes is presented below in detail.

1.1.3 Experimental Studies in Rayleigh-Benard Convection

For small Rayleigh numbers the flow is generally stable to all disturbances. As the Rayleigh number increases the flow become unstable to specific forms of disturbances. Over certain ranges of Rayleigh numbers, the disturbances perturb the flow pattern but the system slowly returns to the stable state, that is the disturbances do not grow with time. As the Rayleigh number is further increased, the flow becomes unstable to all disturbances and becomes chaotic. The flow in Rayleigh-Benard convection system undergoes a number of discrete transitions and the flow structure in each of the transitions remains

stable over a range of Rayleigh numbers.

Krishnamurti (1970a,1970b) has given a regime diagram for the different transitions in a Rayleigh-Benard convection system as a function of Rayleigh number and Prandtl number. This is one of the earliest experimental studies where a number of different fluids were experimented with and a variety of cavity sizes were considered. In these experiments, the bottom plate was made of a low conductivity methyl methacrylate layer sandwiched between two high conductivity aluminium plates. An electric heater was employed for heating and chilled water for cooling the plates. Flow was visualized by tracer particles and the heat transport was measured by means of thermocouples located in the confining horizontal plates. The associated flow field was observed through the records of tracer particles injected in the fluid. The data for heat flux from the walls corresponding to different Rayleigh number was also reported. Owing to the experimental method adopted, this work has a large uncertainty for low Prandtl number fluids such as gases. The main conclusion of the author is that flow undergoes a sequence of transitions from steady two dimensional flow to steady three dimensional flow, time dependent flow and till it finally becomes turbulent. Each transition in the flow configuration is marked by a change in slope of the heat flux curve. Specifically four distinct changes in the slope of the heat flux curve were seen, each one marking a bifurcation of the flow field. Above the third change in heat flux curve the corresponding flow patterns were found to be time dependent, with the movement of hot or cold spots along the cells. The presence of a strong hysteresis effect was also observed in both wall heat flux and flow patterns.

In a subsequent study Krishnamurti (1973) extended the flow regime diagram in the direction of the Prandtl number axis, namely $2.5 \times 10^{-2} < Pr < 0.85 \times 10^4$. For low Prandtl number fluids the change in the slope of the heat flux curve associated with bifurcations in the flow pattern was again observed. The general observation was that there was an increase in the slope of the heat flux curve in the presence of a bifurcation. However, for low Prandtl number fluids there was a decrease as well as an increase in the slope of the heat flux curve with an increase of Rayleigh number. For air, the increase in slope of the heat flux curve was found at Rayleigh numbers of 1700 and 6000. These two points correspond respectively to the onset of convection and time-dependent oscillations in the cavity. A decrease in slope was observed at a Rayleigh number of 10000 and again at a Rayleigh number of 17000. The response time for the low Prandtl number fluid, specifically for air was found to be very long compared with other higher Prandtl

number fluids. When Rayleigh number was increased by a small amount it was found that the steady state for the new Rayleigh number was achieved after a longer time as compared to other fluids. This can be explained because the thermal diffusion time decreases in comparison to the viscous diffusion time as the Prandtl number decreases. By considering cavities of rectangular cross-section in plan, Krishnamurti (1973) has shown that rolls parallel to the shorter side of the cavity are stable. A couple of experiments were also performed in circular cavity of different sizes. The interior rolls were never seen to be axisymmetric while those near the side walls had defects and were seen to meet the side boundaries mostly at right angles.

Ahlers and Behringer (1978) used a cylindrical geometry cavity for experimentation on Rayleigh-Benard convection with different fluids. The largest aspect ratio employed was 57 and Prandtl numbers of 4.40 and 2.94 were employed. The authors have reported that after the onset of convection the flow field was nonperiodic. For cavities with an aspect ratio in the range of 2 to 6 and for a Prandtl number of ≈ 0.8 , the flow field was seen to be following two different routes to the turbulent state. For the cavity size of aspect ratio of ≈ 5 , the flow was seen to become nonperiodic after staying over a range of Rayleigh numbers in the periodic state. For a small cavity, with an aspect ratio of ≈ 2 , the flow field passed through a quasiperiodic state between a time dependent and a nonperiodic state.

Gollub and Benson (1980) conducted experiments with water as the working fluid in a small aspect ratio cavity. Copper plates were used to develop the cavity of the dimension $9.3 \text{ cm} \times 6.7 \text{ cm}$. The two plates were separated by plexi-glass spacers. The surroundings of the cavity was evacuated to avoid convective heat loss from the sides of the cell. The surroundings surfaces were kept at the average of the two plate temperatures to minimize radiative heat loss. The temperatures of the plates were electrically controlled. Laser Doppler velocimetry was employed for flow mapping and local velocity measurement in real time.

The experiments of Gollub and Benson (1980) showed four distinct routes leading to chaos. One of the routes to chaos observed was the sequence steady-periodic-quasi periodic-chaotic-turbulent. At a Rayleigh number of 46000 the flow was seen to become periodic from a steady state with one dominant frequency along with its harmonics. At a Rayleigh number of 54000 the flow turned quasi periodic with two distinct frequencies and harmonics. With further increase in Rayleigh number, the ratio between the two main

frequencies decreased until the phase locking between the two frequencies took place. At phase locking one of the harmonics of each of the frequencies are equal. For example in one of the experiment of Gollub and Benson (1980) the phase locking occurred at a frequency when $1/7$ th of one main frequency become equal to the $1/3$ rd of the other. This locking behaviour was not reproducible in their experiments. Locking could occur at other harmonics as well. Once there is a phase locking, strong mixing of the fluid is induced and spectral peaks at all the multiples of the lock frequency are strong. As the Rayleigh number is increased further, the noise band slowly starts to broaden and at Rayleigh number of 78000 the flow was seen to be aperiodic. A second route to chaos found was steady-periodic-sub harmonic bifurcations-quasi periodic-chaotic-turbulent. The formation of subharmonic bifurcations gives rise to $1/2$ or $1/4$ of the main periodic frequencies. This is also known in the literature as the period doubling phenomena. The quasi periodic state can have three distinct frequencies rather than two. This gives rise to a third route to chaos. In the fourth, an intermittent noise appears in the quasi periodic state. The effect of this is a dynamical behaviour of switching between non-periodic (turbulent) state to the quasi periodic state. This has been observed in a low Prandtl number fluid (liquid helium) and also in water (Prandtl number = 5.0). The time-mean flow was found to be stable in the form of rolls in all the measurements.

Kim and Viskanta (1984) have reported the effect of wall conductance on buoyancy-driven convection in a two dimensional rectangular cavity. The study includes both experimental as well as numerical investigations. The fluid considered was air. The size of the cavity employed for experimentation had a cross-section of 3.6 cm \times 3.66 cm, and a length of 6 cm \times 6 cm. The walls were made of Lexan. A Mach-Zehnder interferometer with 25 cm optics was used for data collection. Three different configurations for convection in enclosures were considered, the side walls being conductive in all the three cases. Of the three, one of the problems considered was Rayleigh-Benard convection. In the experiments, the fluid showed circulation inside the cavity. The conducting walls were seen to conduct heat to and from the system. The direction of heat transfer from the conducting side walls showed a wave like behaviour. Near the bottom wall there was an addition of heat to the system by the conducting side walls. The vertical conducting walls had a stabilizing effect on the flow. Perfect energy balance was not seen between the two horizontal walls, the Nusselt number on the top wall being lower than the bottom wall.

The change of wavenumber or the loss-of-roll in Rayleigh-Benard convection is a phe-

nomenon observed continuously over a range of Rayleigh numbers. For a fixed Prandtl number and a range of Rayleigh numbers the roll pattern is the most stable form of convection. Thus, subsequent to an instability the roll pattern is most likely to return though with a change in the structure. Different types of instability mechanisms that change the wavelength of the roll system are discussed by Busse (1985). The zigzag instability bends the longitudinal rolls in a wave-like fashion. This is followed by a lengthening of the boundaries between the rolls, resulting in an increase in the wavenumber of the roll system. Experimentally, it has been observed that new rolls are formed in two directions enclosing angles of 40° and 140° with the direction of the original rolls (Busse, 1985). The cross-roll instability occurs in the form of T-shaped rolls formation and gives rise to three dimensional convection. The cross-roll instability can also lead to knots appearing on the boundaries of the rolls. Another important instability mechanism that is responsible for the loss-of-roll phenomena is the skewed-varicose instability. The roll structure gets distorted along the axis of the roll. The roll size also changes along the axis of the roll. A subharmonic wave develops which later cause the pairing of two of the distorted rolls. The skewed-varicose instability is the main cause for the loss-of-roll phenomena in a low Prandtl number fluid.

Kolodner *et al.* (1986) have observed the loss-of-roll phenomena in an intermediate aspect ratio box. A constant heat flux boundary was used in the experiment instead of the isothermal boundary condition. However, according to the authors, isothermal boundary conditions would have produced the same experimental observations. The authors used a copper bottom plate and a sapphire top plate with horizontal walls of acrylic plastic. The top plate was cooled with flowing water and the bottom plate was electrically heated. Optical access from the top of the apparatus allowed visualization. A shadowgraph technique was employed for this purpose. Visualization from the side walls gave images of the horizontal view. These images were projected to a screen and the entire flow process was recorded on video tapes.

Kolodner *et al.* (1986) report that the loss of rolls followed from a 10-roll system to 6-roll via an 8-roll system. The 10-roll pattern for fluids in the range $2 < \text{Pr} < 20$ reduced to an 8-roll pattern at a Rayleigh number of around 10000. The pattern was seen to be distorted for further increase in Rayleigh number. The loss of rolls was again observed at a Rayleigh number of around 20000. The final 6-roll pattern was found at a Rayleigh number of 68000. The flow became time dependent at a Rayleigh number of

approximately 30000. Kolodner *et al.* (1986) also observed the disappearance of a single roll rather than a pair of rolls. The removal of a pair of rolls, whenever it occurred, took place near the central region of the cavity, while the loss of a single roll took place near the side walls.

Kirchartz and Oertel (1988) have shown for a box of small aspect ratio the transition from 4-rolls to 3 and finally to 2-rolls. The cavity was developed using copper plates. The upper plate was thermostat controlled using chilled water and the bottom plate was electrically heated. Perfectly conducting side walls were setup by employing borders made of quartz. Differential interferometry along with a scanning mirror and laser Doppler anemometer were employed to study the phenomena.

Michael and Yang (1992) have reconstructed the three dimensional temperature field from its interferometric projections and have seen the presence of rolls in a water filled cavity of aspect ratios 8.7 and 9.0. The two horizontal confining walls of the cavity were made of aluminium. The top plate was cooled using constant temperature water flowing over the aluminium sheet. The bottom plate temperature was maintained using three electric foil heaters connected in series. Two sides of the vertical side walls were made from delrin and the other two sides were made from 25 mm thick optical flats. Three thermistors were used in each aluminium plate to measure the temperature of the plates. A Mach-Zehnder interferometer with 20 cm diameter optics and a Helium-Neon laser of 10 mW power were employed for collecting the projection data. Wedge fringe setting of the interferometer was used to record the convection pattern inside the cavity. For the tomographic reconstruction of the three dimensional temperature field the authors employed the corresponding numerical solution of the physical problem as an initial guess to the reconstruction algorithm. Their results show the formation of T-defects in the longitudinal rolls near the region of the short side of the box. The movement of hot and cold spots along the roll was observed.

Muralidhar *et al.* (1996) have studied transient convection in a two dimensional square cavity. The fluid considered was air. Rayleigh numbers in the range of 10^4 to 10^5 were employed. The cavity had a width of 74 cm and the aspect ratio considered was unity. The horizontal surfaces were developed using brass sheets. The vertical side walls employed were made of a low thermal conductivity material such as perspex. The isothermal conditions on the brass sheets were obtained by flowing water at constant temperature through them. A Mach-Zehnder interferometer was employed to map the

thermal field. These experiments showed that the flow was mostly bicellular during the early transient period whereas it became unicellular at steady state. The Nusselt number in the cavity was found to be maximum at the steady state. The growth of Nusselt number when the flow approaches steady state from the transient was not monotonic. The associated thermal field was found to be symmetric with respect to the vertical axis at the lowest Rayleigh number studied that is 8.79×10^4 . The symmetry was lost at higher Rayleigh numbers. The initial growth in Nusselt number was seen to be rapid followed by a slow transient till the Nusselt number stabilized at steady state at its maximum value. This was explained in terms of the boundary layer near the hot and cold walls of the cavity during the initial stages. The corners of the cavity were found to be region of high heat transfer for short time but regions of low heat transfer at steady state.

Mavetty and Leith (1998) have studied heat transfer in Rayleigh-Benard convection with air in intermediate aspect ratio boxes. The test cell was made of three layers of materials. The plates comprised of a 15 mm thick paraffin-filled foamed aluminium slab with aluminium tubes embedded and 3.2 mm wide heat flux gauges. A 0.8 mm thick aluminium plate was present over all this to bound the air layer. The aluminium plates were chrome-plated to minimize the radiation heat transfer effects. A set of 36 gauge copper-constantan thermocouples were fixed to the aluminium sheet to record the temperature. Four differential thermocouples were present within the air layer to record the temperature information in the cavity. The bifurcations in the flow field up to a Rayleigh number of 12000 were investigated in terms of the behaviour of the growth of heat flux. The flow field was seen to be steady upto a Rayleigh number of 10000. The loss-of-roll phenomena was detected from the change in the slope of the heat flux curve. The growth of heat flux in larger systems having a higher aspect ratio showed a linear variation with Rayleigh number while it was quadratic in moderate sized containers.

The construction of apparatus used for the study of flow and heat transfer in Rayleigh-Benard convection in the last two decades has been presented in a review paper by de Bruyn *et al.* (1996). Non-uniformities of the heat input to the two horizontal plates and the conductivity of the side walls are major concerns while making a convection test cell. In most of the experiments reported the top plate temperature was held fixed and the bottom plate temperature was controlled by varying the heat input. The experimentalist thus obtained the required temperature difference across the cavity. In most experiments the cooling of a surface was produced by passing water at a low temperature over the flat

horizontal plates. The water temperature was kept constant using a heat removal device. For heating, some experiments used an electrical resistance supplied with an electrical input while others passed hot water over the surface. Uniformity and flatness of the two bounding horizontal surfaces was another issue where care had to be taken. Sagging of the horizontal surfaces was a frequently-faced problem.

1.1.4 Theoretical Aspects of Rayleigh-Benard Convection

Catton (1972) is one of the earliest to observe through a numerical study the effect of lateral adiabatic side walls on a Rayleigh-Benard system. The effect of adiabatic side walls on the critical Rayleigh number at the onset of convection as a function of the aspect ratio was studied. A fully three dimensional flow configuration was generated using trial functions which were in the form of rolls parallel to the shorter side of the container. Keeping the smaller aspect ratio fixed and increasing the other caused a stretching of the rolls. The stretched rolls require more energy to be sustained. Hence the system was seen to move towards a new equilibrium with a greater number of rolls.

Grotzbach (1982) has performed a direct numerical simulation of the Rayleigh-Benard convection problem under both laminar and turbulent conditions. The fluid considered was air. The cavity was an infinite parallel plates channel. Skewed-varicose instability was seen at a Rayleigh number of 4000. For a Rayleigh number of 7000, the velocity field was unsteady and three dimensional. The isotherms drawn on one of the vertical planes showed a well-defined roll structure². The next Rayleigh number considered by Grotzbach (1982) was 87300. At this Rayleigh number the velocity field was found to be completely chaotic but the isotherms drawn on the vertical planes showed an orderly structure, but changed slowly with time. For a Rayleigh number of 381225 the isotherms drawn on the vertical planes also showed chaotic behaviour. One conclusion that can be derived from the work of Grotzbach is that, even if the associated velocity field is chaotic the interferograms of the flow field may still show structured but time dependent isotherms.

²The fringes seen in an interferogram obtained from a Mach-Zehnder interferometer in the infinite fringe setting correspond to isotherms of the line-averaged temperature field along the direction of the ray. Since the isotherms corresponding to the three dimensional velocity field reveal a roll structure it is expected that the interferograms recorded in the present work can be associated with a three dimensional velocity field. Since perfect steady state in the velocity field was not observed in the simulation mild unsteadiness in the experimental fringes can be expected.

In a numerical simulation, Kessler (1987) observed the exchange of mass between adjacent rolls. The location of the upward and downward flow was seen to undergo periodic motion. The fluid from the outer roll slowly moved towards the smaller inner roll. The inner roll moved faster compared to the outer roll. Slowly the inner roll expanded and reached a maximum size after which the mass transfer process reversed from the inner to the outer rolls. The oscillations of the roll showed a maximum strength at the center of the box and gradually decreased towards the side walls. The horizontal size of a roll was not fixed and changed strongly along the roll axis. Since the radius of the roll changed along its axis an inertial force which induces an axial velocity to the convecting flows was observed. For air, this mechanism was seen to maintain the oscillations in the flow. For fluids of higher Prandtl number, the inertial force decreased and the oscillatory motion of the rolls were different. Kessler (1987) performed calculations at a higher Rayleigh number to see how the flow behaves after the oscillatory convection is initiated in a small aspect ratio box. At a Rayleigh number of 38000 and a Prandtl number of 0.71 only one main frequency along with its harmonics were seen. This structure of the flow remained stable upto a Rayleigh number of 60000. For increase in Rayleigh number additional frequencies and their harmonics were seen. When the side walls are changed to conducting from adiabatic, the flow patterns were altered. Subharmonic frequencies and their combination with the main frequencies were introduced. The flow was stable up to a Rayleigh number of 56000. Hysteresis effect were also observed.

Yang and Mukutmoni (1993) have shown that, for rectangular enclosures of small aspect ratio, the sequence of transitions depends strongly on the initial conditions. They have shown a methodology to simulate the Rayleigh-Benard convection in a small cavity with an appropriate experiment. A close comparison between theory and experiments is likely to enhance the reliability of the information generated.

Since Rayleigh-Benard convection is strongly nonlinear, the initial guess of the flow condition is a major factor in the simulation as well as experiments. With these inherent limitations computational studies continue to help in understanding transition and the instability mechanisms. Since there is a strong hysteresis involved the comparison of experiments with numerical work becomes difficult. Most of the experiments may have followed a different path while increasing or decreasing the Rayleigh number. Hence even at a fixed Rayleigh number, all other parameters being equal one may see a different flow configuration in an experiment in comparison to a simulation case, since the size of the

step change in Rayleigh number matters. A sudden jump in Rayleigh number from one value to another may result in a different set of bifurcations compared to a gradual change in the Rayleigh number.

There are several papers reporting the formation of stable two dimensional rolls through numerical studies. Flow in small and intermediate aspect ratio enclosures was investigated more recently in a series of papers by Mukutmoni and Yang (1993-1995). In Mukutmoni and Yang (1993a), steady roll formation has been demonstrated. The rolls are generally parallel to the shorter side of the cavity. It is because this orientation minimizes the ratio of the rate of production of the potential energy by buoyancy to the rate of viscous dissipation of kinetic energy. However stable longitudinal rolls parallel to the longer side of the cavity are also documented in the literature both experimentally as well as numerically, at much higher Rayleigh numbers.

The two dimensional rolls bifurcate to a state of three dimensionality with increase in Rayleigh number. Three dimensional rolls become unstable and a periodic motion of the roll system begins along the axis of the rolls for further increase in Rayleigh number. The critical Rayleigh number for the onset of oscillatory rolls is shown to be in the range of Rayleigh number of 30000 for air ($Pr=0.71$) (Mukutmoni and Yang, 1993a and Kessler, 1987). This critical Rayleigh number increases with the increase of Prandtl number. The frequency of oscillation is not a strong function of the Rayleigh number (Mukutmoni and Yang, 1993a), but increases slowly as we increase the Rayleigh number. There is no general agreement in the literature about the Prandtl number dependence of the Rayleigh number for the onset of oscillatory convection (Busse, 1985). Krishnamurti (1970b, 1973) has suggested a value of Rayleigh number 5.5×10^4 as a transition Rayleigh number for the start of oscillatory convection that is independent of Prandtl number for $Pr > 50$. Other studies have shown that there is a continuous increase in the critical Rayleigh number for the onset of oscillatory convection as the Prandtl number increases (Busse, 1985).

Mukutmoni and Yang (1993b) have shown that there will be an additional frequency of half of the fundamental frequency added to the oscillatory motion between a Rayleigh number of 35000 to 36000 for a fluid of Prandtl number 2.5. The second bifurcation for the same fluid was observed between Rayleigh number of 47000 to 48000 when another additional frequency was observed. More and more frequencies of oscillations were seen as the Rayleigh number was increased. The flow finally became chaotic at a Rayleigh number of around 50000.

Mukutmoni and Yang (1994) have shown that rolls parallel to the longer side of the cavity are stable below a critical Rayleigh number. They have concluded that long rolls are like a metastable state and could become unstable to certain disturbances. Kolodoner *et al.* (1986) have also seen rolls parallel to the longer side in their experiments with an intermediate aspect ratio cavity.

Hernandez and Frederick (1994) have studied the spatial and temporal features of three dimensional Rayleigh-Benard convection in air with varying aspect ratio. The cavity aspect ratio was changed from 1 to 5. The authors concluded that beyond an aspect ratio of 5 the flow field was not stable for any Rayleigh number greater than 8000. This result is seen to be in disagreement with many other numerical as well as experimental observation where for the same fluid and at a higher aspect ratio the flow was stable for higher Rayleigh numbers (Kolodoner *et al.* (1986), Mukutmoni and Yang (1995a)). Most evident in the study is that the flow pattern and heat transfer rates are a strong function of the aspect ratio. When the aspect ratio was systematically increased the flow pattern went through a bifurcation sequence from unicellular at an aspect ratio 1 to multicellular and finally to a toroidal flow structure. The toroidal structure was found to consist of concentric rolls. It was observed that new rolls kept forming from the cavity center. When the new roll is formed, the velocity of the fluid at the vertical axis (upward or downward) first increases with aspect ratio. After it reaches a maximum, it decreases to form a cycle. The initial increase in the velocity is related to the fact that the critical Rayleigh number for onset of convection decreases with increase of aspect ratio. This permits a higher velocity at a higher aspect ratio. The later decrease in the velocity is because of the cross-sectional expansion of the central flow caused by the increase of the aspect ratio. The corresponding heat transfer field was also observed to change significantly with the aspect ratio of the cavity. With increase in aspect ratio, the average Nusselt number of the cavity increased rapidly but later grew at a slower rate as the flow became multicellular. When the aspect ratio was increased with the number of rolls kept a constant, for example an increase in aspect ratio from 1 to 2, the overall average Nusselt number increased. This fact is also related to the increase in the vertical velocity of the fluid and the increase in the flow area. When the aspect ratio increased from 2 to 3, the number of rolls increased from one to two. This resulted in a decrease in the Nusselt number momentarily. This is because the flow structure was found to switch its direction in the central region of the layer from upward to downward flow with a higher downward velocity. This velocity slowly decreased and the Nusselt number was found to increase for further increase in

aspect ratio. The change in aspect ratio from 4 to 5 was related to the change in roll number from 2 to 3 leading to an increase in Nusselt number. This was again due to the change in the direction of vertical upward flow at the center of the cavity.

Hernandez (1995) has studied the influence of heating rate on the convection pattern for air in cavities of aspect ratios 1.21 and 2. The heating rate was introduced by a time dependent Rayleigh number in the range of 10^3 to 10^4 . The cavity side walls were respectively assumed to be perfectly conducting and adiabatic in two sets of calculations. The steady state flow configuration in the cavity was found to be two counter-rotating rolls. With different heating rates, a fixed Rayleigh number was arrived at. At this point, it was found that the rolls in the central region of the layer had a downward motion and near the side walls, had an upward motion. When the heating rate was increased the fluid was found to be rising in the central region and descending near the side walls. The system thus went through a flow transition with the heating rate as a parameter. The author carried out a systematic analysis to find the range of heating rates within which the transition took place. It was found that with increasing final Rayleigh number of the system, the heating rate at which the transition took place also slowly increased.

The transition with respect to the heating rate parameter can be explained as follows. Assuming that the fluid near the side walls (assumed perfectly conducting) has an upward motion, increasing the heating rate will lead to a portion of the cold fluid coming from the upper horizontal wall near the transition heating rate to flow towards the center of the box in a diagonal path. This will start cooling the central portion of the box. Therefore, the local temperature will reduce in the central region. This will cause a flow of high temperature fluid towards the central region of the box, leading to a flow reversal in the center of the cavity. The diagonal paths of the fluid are thus caused by the thermal characteristics of the side walls.

When the side walls are given an adiabatic boundary condition, no change in the flow pattern is observed at different heating rates. The hot fluid is always found to be rising at the center of the box. For a Rayleigh-Benard system with adiabatic side walls the convective motion starts when the Rayleigh number reaches the critical value for onset of convection. When the side walls are conducting a rising flow near the side walls and a downward flow near the center of the cavity can be seen even when the Rayleigh number is below the critical value. However this state of weak convection is not seen when the Rayleigh number increases beyond the critical value for onset of convection.

This is because with increasing Rayleigh number, buoyancy is introduced into the system which neutralizes the weak circulation and a perfect conduction regime is restored. This conduction regime stays till the critical Rayleigh number is reached. Then the convective pattern starts either with a rising flow at the center or with downward flow. This is decided by the relative strengths of the buoyancy forces generated by the side walls before the onset of convection and by the center of the cavity at the critical Rayleigh number.

Mukutmoni and Yang (1995a) have demonstrated the loss-of-roll phenomena as the Rayleigh number is increased in an intermediate aspect ratio box. They have simulated the experimental conditions of Kolodner *et al.* (1986) and the transition from 10-rolls to 6-rolls was investigated. The 10-roll pattern was generated at a Rayleigh number of 10000 and then Rayleigh number was increased to 17000. The authors found a solution with an 8-roll pattern. The 8-roll pattern was found to be three dimensional only near the isothermal walls. The mechanism of roll transition in the numerical data was not found to be strictly identical to that obtained from the flow visualization experiment of Kolodner *et al.* (1986). However with a closer look at the experimental data, their simulation was able to produce the real physical phenomena. When the Rayleigh number was stepped up from 10000 to 17000, a periodic thickening and thinning of the rolls were seen. This is a signature of the skewed-varicose instability. Two rolls at the center disappeared and slowly the system came back to a stable configuration. The authors have concluded that the skewed-varicose instability originally proposed by Busse (1985) is ideally for an infinite layer, whereas the effect of lateral walls does modify the details of the mechanism of the transition process. The authors found that a vertical vorticity component plays a crucial role in the transition process. The spike observed in the vertical vorticity during the transition process indicates a rotation of the pattern around a vertical axis which is referred as swirl. In the original model of skewed-varicose instability (Busse, 1985) it was expected that the vertical vorticity would be absent. Numerical calculations of Mukutmoni and Yang (1995a) showed that the transition from 10-rolls to 8-rolls is via an instability of skewed-varicose type with swirl.

When the Rayleigh number was increased from 17000 to 24000, Mukutmoni and Yang (1995a) observed non-roll patterns. The transition process started again with the skewed-varicose instability leading to a distortion of the 8-rolls system. Slowly the roll boundary merged in a fashion to create a polygonal planform structure. The final state of the structure was found to be polygonal cells with slow steady oscillations. During the

transition process the vertical vorticity was observed and spikes were found. For a change in Rayleigh number from 17000 to 20000 (instead of 24000) the bifurcations observed were different from the polygonal planform solution. A T-shaped roll pattern was observed and perfect steady state was not reached, the flow continuing to evolve at a slow rate. This indicated that the rate of change of Rayleigh number plays a major role in the type of bifurcation experienced by the flow field.

Mukutmoni and Yang (1995b) have numerically simulated the experiment conducted by Gollub and Benson (1980). The authors have shown that flow reversal to a steady state at higher Rayleigh number is possible. They have started with a two counter-rotating rolls structure at a Rayleigh number of 40000 in a small aspect ratio box filled with a fluid of Prandtl number 5. The Rayleigh number was increased in steps of 10000. The flow field was found to be unsteady at a Rayleigh number of 50000. At a Rayleigh number of 60000 the time signal from a point for the velocity field was collected and analysed. The flow was found to be periodic with a well-defined fundamental frequency. At Rayleigh numbers of 70000 and 80000 the system was seen to go through a transition and the resulting field was found to be in the quasi-periodic state. The appearance of new frequency independent of the main fundamental but lower than it, is the reason for quasi-periodic flow. The phase trajectories were found to be in the form of a torus as expected. In comparison, the trajectories at a Rayleigh number of 60000 when the flow was periodic were found to be simple closed curves. The above bifurcation sequences were observed in the experiment of Gollub and Benson (1980) as well. Mukutmoni and Yang (1995b) also examined the spatial distribution of the frequencies. All variables over the fluid layer in the cavity were found to have the same dynamical behaviour. With further increase in Rayleigh number (100000) the flow field reversed from quasi-periodic to a steady state. This transition to steady state from a quasi-periodic flow can be explained on the basis of the increasing complexities in the spatial structure of the flow. Thus the flow field undergoes a change in the spatial pattern that stabilises the unsteady convection. The flow was seen to become oscillatory again when the Rayleigh number was increased to 120000.

The loss-of-roll phenomena has also been documented by other workers. Lin *et al.* (1996) have numerically shown that for an intermediate aspect ratio box and for a fluid of Prandtl number 3.5 the rolls near the side walls gradually weaken and contract. Meanwhile the rolls next to the weakening rolls expand slowly. After some time the rolls near the short sides disappear. The remaining number of rolls in the box readjust and

there is an increase in the size of all the rolls. The authors found another route for loss of rolls in air. The skewed-varicose instability was found to cause distortion of the longitudinal rolls. With time the distortion of the shape and size became larger and two rolls adjacent to each other merged to form a single roll. This resulted in the loss of a single roll. Once a roll was lost, the rolls near the central region of the cavity readjusted to a stable and straight pattern whereas the rolls near the side walls remains unstable and irregular.

1.1.5 Tomographic Algorithm

A considerable amount of literature is presently available in the area of tomographic algorithms. These algorithms work with a set of projections of the field being investigated and reconstruct it to a certain degree of approximation (Herman, 1980). They can be broadly classified as: (a) Transform methods and (b) Series expansion methods. The latter has been developed with a view towards handling a limited number of projections. Hence in interferometry, applied to measurement of temperature fields in fluids, the series expansion method is best suited. Censor (1983) has reviewed the series expansion methods in terms of their rate of convergence and accuracy. Gull and Newton (1986) discuss the use of maximum entropy principle in tomographic reconstruction. A method of encoding prior information about the unknown field is discussed. Verhoeven (1993) has reported the performance of the state-of-the-art implementation of a MART (Multiplicative Algebraic Reconstruction Technique) algorithm to multidimensional interferometric data. Subbarao *et al.* (1997a) have compared ART (Algebraic Reconstruction Technique), MART and entropy algorithms for three dimensional reconstruction of temperature fields. A detailed calculation of errors has been presented. The principal finding of their study is that MART gives the best all-round performance even with as few projections as two.

1.2 Objectives of the Present Work

The present study is concerned with mapping the full three dimensional temperature field in a Rayleigh-Benard convection setup of intermediate aspect ratio using interferometry. The cavity dimensions are 50 cm \times 50 cm in plan and the vertical depth of the fluid layer is adjustable. Two different aspect ratios have been employed. Rayleigh numbers

of 13900, 34800 and 40200 have been selected for the experiments. The aspect ratio at a Rayleigh number of 13900 was 25, while at 34800 and 40200, it was 18.6.

The thermal field has been mapped using a Mach-Zehnder interferometer. The interferograms have been obtained as a collection of fringe patterns. The interferograms give line-averaged information along the direction of the light ray. Hence they represent a projection in that direction. The interferograms can also be used to identify the flow pattern prevailing within the cavity. The three dimensional temperature field has been obtained from the interferograms using the method of tomography.

The first objective of the present study is to obtain the three dimensional temperature field in the fluid layer in a non-intrusive manner. The reconstructed temperature field thus obtained gives a clue to the pattern formation in the fluid. The temperature field available in three dimensions can be used for understanding the heat transfer aspects of the convection phenomena. Accordingly, Nusselt numbers have been computed and presented as an average along a view angle, as a total average over the cavity and also as a distribution of the local Nusselt number over the confining horizontal plates.

A major source of error in processing interferograms is the fringe thinning process. To keep this error under control, a thinning algorithm dedicated to interferometry is required. The second objective of the present work is the development of a versatile thinning algorithm for interferometric fringes.

Tomography is an inverse technique that, in mathematical terms, leads to an ill-posed matrix inversion problem. It is now known that the inversion process can amplify errors in the input data, arising from interferometry as in the present study. The third objective of the present work has been to assess errors in the reconstructed field in relation to those in the interferograms. This has been accomplished by examining a variety of algorithms available in the literature. This process has led to the development of alternative algorithms suitable for interferometry.

Chapter 2

Description of Experiments

Experiments in Rayleigh-Benard convection are necessarily exploratory in nature. From a theoretical view point the convection patterns are governed by a set of non-linear coupled partial differential equations. The solution of this mathematical problem is intrinsically complicated on one hand and on the other it is very sensitive to initial and boundary conditions. Further, the forcing function such as the step change in Rayleigh number place an important role in the pattern formation in the fluid layer. In light of this, theoreticians and numerical analysts are forced to assess their results against benchmark experiments.

A Rayleigh-Benard experimental setup is apparently simple in design. Nominally it comprises of two horizontal surfaces of high thermal conductivity which are maintained at different temperatures. The vertical side walls are perfect insulators and the focus of the experiments is on the flow patterns that emerged in the fluid contained in the enclosed volume. A careful thought is sufficient to indicate the large number of difficulties experienced during experimentation. For example, uniformity and constancy of surface temperatures, parallelism of the walls defining the fluid layer and properties of the insulating surfaces are all factors that determine the quality of the experiment and its suitability for comparison with theory. Further, extraneous factors such as building vibrations, air currents and changes in the ambient temperature have a strong bearing on the quality of the recorded data. Thus Rayleigh-Benard experiments have to be conducted with due care and precautions.

While the present work adopts the optical route for determining the temperature

field, other approaches have been proposed in this regard. For example, the temperature field can be obtained by scanning the fluid layer using a thermocouple. This approach has a serious drawback since the presence of the probe can distort the flow pattern, not just locally but over the entire cavity. The probe intrusion problem is particularly serious at high Rayleigh numbers. A second technique that has been widely employed involve the use of tracer particles in the fluid. This method has been found to be successful mainly in liquids and less so in gases. In any case, the tracer route identifies the velocity field in the fluid but not the temperature field which is the focus of the present work. A subtle point to be noted in the context of flow visualization by tracer is the following: Since the particles respond to velocity, small time-dependent fluctuations are immediately noticed and portray an image of chaotic convection even at moderately low Rayleigh numbers. The tracer route has a fundamental drawback of not generating information regarding three dimensionality of the flow field. In this context, interferometric tomography adopted in the present study has the following definite advantages: (a) Clearly identifiable fringe patterns are formed. (b) These remains stable over a higher range of Rayleigh numbers. (c) Three dimensional information about the temperature field can be extracted from the interferograms. Thus it is possible to deduce the shape of the structures that form in the fluid layer at various Rayleigh numbers. (d) Local as well as global heat transfer rates can be determined.

2.1 Test Cell for Rayleigh-Benard Convection

The apparatus used to study convection in the horizontal layer of air is shown in Figure 2.1. The fluid layer (interchangeably called the cavity) was 500 mm \times 500 mm in plan, the vertical depth being adjustable. The fluid layer was confined by two aluminium plates, 5 mm thickness above and below. The flatness of these plates was carefully established against a reference face plate. After assembly the fluid layer thickness was uniform to within ± 1 mm. Both surfaces were maintained at uniform temperatures by circulating a large volume of water over them. For the upper plate, a tank-like construction enabled extended contact between the flowing water and the the aluminium surface. For the lower plate, special arrangement was required to maintain contact between water and aluminium. The flow of water below the lower surface was pressurized and the presence of baffles introduced a tortuous path, thus increasing the effective interfacial contact area.

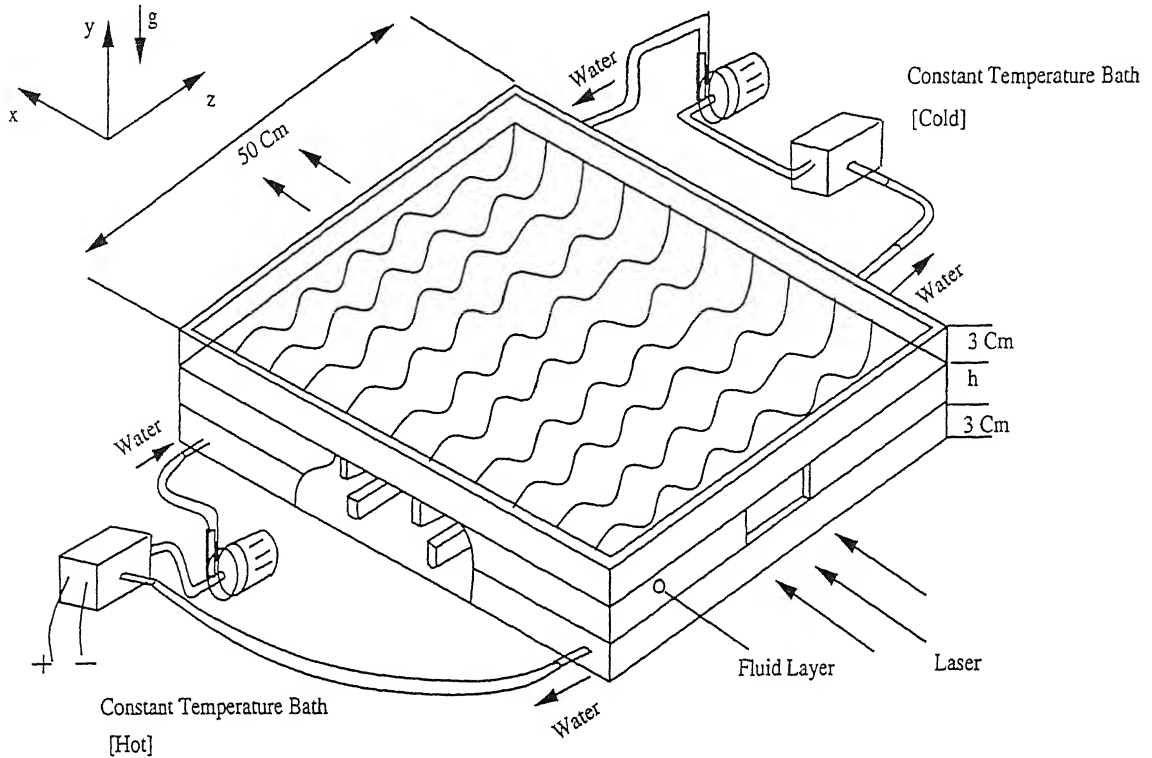


Figure 2.1: Schematic of the Apparatus for Rayleigh-Benard Convection.

The side walls comprised of two layers of perspex sheets, each 10 mm thick. The side walls were simply joined with the upper aluminium surface and did not carry any load. The weight of the upper aluminium surface and the water contained in it was directly transmitted to the lower tank by four short pillars at the four corners. It was thus possible to develop a cavity with an adjustable aspect ratio. A provision was made to accommodate a small window in the perspex side wall for the recording of the interferograms.

A traversing mechanism is needed to mount the apparatus in which the desired experiment is in progress. In practice, the optics and the light source cannot be moved to scan the flow field. The traversing mechanism enables translation and rotation of the test cell and thus plays a central role in instrumentation. The base of the traversing mechanism is padded with a rubber sheet of 30 mm thickness to damp any external vibration from reaching the test cell. The traversing mechanism is schematically shown in Figure 2.2. In axial tomography the angle of rotation is very important. While the object rotates, it is actually the rotation of the table-top of the traversing mechanism. Hence one has to ensure that the center of the rotation of the test cell equal to the center of rotation of the table-top of the traversing mechanism. This is an issue of alignment and carefully

implemented in the present work.

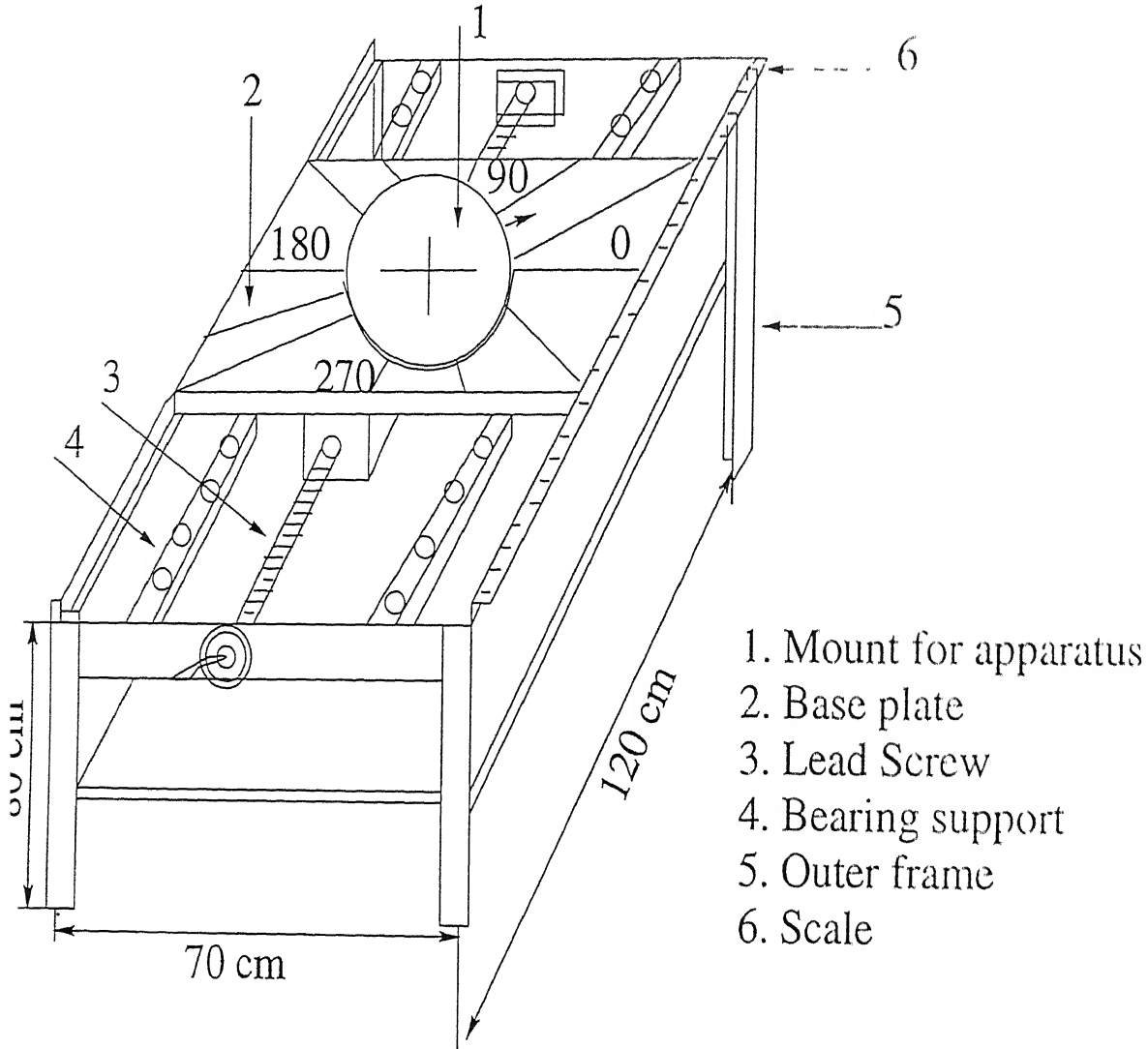


Figure 2.2: Schematic of the Traversing Mechanism

The top wall of the cavity was cooled and the bottom wall heated by pumping water continuously from constant temperature baths. Special attention was given to ensure that isothermal conditions prevailed at the aluminium plates. This was achieved by circulating a large volumetric flow rate of water. Specifically, the temperature drop between the incoming and outgoing fluid on both the hot and the cold side was found to be negligible. To lower the plate temperature below the ambient value a constant temperature bath (Huber, model: variostat) was employed. The specification of the constant temperature bath is given in Table 2.1. For the hot surface, a large tank with a 2 kW heater employing a pump capable of generating 9 m(H₂O) head was used. Temperature control

of the hot plate was accomplished by on-off control of the heater operated by a timer switch.

Table 2.1: Specifications of the constant temperature bath (huber model: variostat)

Operating temperature range	-30 ⁰ C to 150 ⁰ C
Temperature stability at -10 ⁰ C	0.01 K
Temperature adjustment	Digital
Temperature indication	Digital
Temperature sensor	pt100
Force pump capacity	10 liters/min (max)
Suction pump capacity	7 liters/min (max)

Temperatures of both aluminium surfaces were monitored by 24 gauge chromel-alumel thermocouples fixed on the side exposed to the flowing water. The temperatures sensed by these thermocouples were read by a 30 channel temperature recorder. A separate thermocouple was used to monitor the ambient temperature. The constancy of the wall temperature was estimated to be $\pm 0.2^{\circ}\text{C}$ for the complete duration of the experiment. The entire test cell was placed inside a chamber made of a plastic sheet to eliminate the influence of external air currents.

A variety of tests were carried out to ensure that the convection patterns in the fluid layer were insensitive to external disturbances such as floor vibration and the flowing water. It was thus established that air convection was driven by the temperature difference alone. The experiment was conducted beyond 4 hours to eliminate the initial transients and obtain a dynamic steady state. In the present work, the experiments were started with the fluid layer and the bounding walls, all at the ambient temperature. The increment in Rayleigh number from 0 to the final Rayleigh number was applied in one step as follows. The walls were respectively cooled and heated by circulating water from constant temperature baths. Since the deviation from the ambient temperature of each of the walls was practically equal, both walls reached steady state around the same time. The hot and cold walls bounding the cavity were found to reach steady state in about 30 minutes whereas the convection pattern reached steady state in 3 to 4 hours. The variation of wall temperatures with time could be fitted as an exponential function, characteristic of cooling/heating of lumped masses.

Two different vertical depths were used in the present experiments to generate the

Rayleigh numbers used. For a Rayleigh number of 13900, the vertical depth was 20 mm. For the higher Rayleigh numbers of 34800, 40200 and 51800, the vertical depth was increased to 26.8 mm. The aspect ratio was thus maintained at 25 and 18.6 respectively. The aspect ratio is defined as the ratio of horizontal width of the fluid layer to the vertical height of the fluid layer. The lowering of the aspect ratio was seen to reduce the extent of unsteadiness in the convection pattern at the higher Rayleigh numbers. The hot and the cold wall temperatures for the four Rayleigh numbers were maintained as 30.5 and 13.4°C for $Ra=13900$, 33.5 and 15.1 °C for $Ra=34800$, 33.5 and 12.4°C for $Ra=40200$ and 38.8 and 10.4°C for $Ra=51800$. The ambient temperature was 21.7°C in all the experiments.

2.2 Mach-Zehnder Interferometer

The Mach-Zehnder interferometer has been used as a primary instrument in the present work for temperature measurement in the fluid layer. Figure 2.3 is a schematic drawing of the interferometer. The optical components present in it namely the beam splitters BS1 and BS2 and mirrors M1 and M2, are inclined exactly at an angle of 45° with respect to the laser beam direction. The first beam splitter BS1 splits the incoming collimated beam into two equal parts, the transmitted and the reflected beams. The transmitted beam (2) is labelled as the test beam and the reflected beam (1) as the reference beam. The test beam passes through the test region where the convection process is in progress. It is reflected by the mirror M2 and recombines with the reference beam on the plane of the second beam splitter (BS2). The reference beam undergoes a reflection at mirror M1 and passes through the reference medium unaltered and is superimposed with the test beam at BS2. The two beams on superposition at the second beam splitter BS2, produce an interference pattern. This pattern contains the information of the variation of refractive index in the test region. For measurements in air, the reference medium is simply the ambient. For liquids, a compensation chamber is required to introduce an appropriate reference environment. The mirrors and beam splitters employed in the present configuration are of 150 mm diameter. The beam splitter has 50% reflectivity and 50% transmittivity. The mirrors are coated with 99.9% pure silver and employ a silicon dioxide layer as a protective layer against oxidation.

The Mach-Zehnder interferometer can be operated in two modes, namely (a) Infinite fringe setting and (b) Wedge fringe setting. In (a) the test and reference beams are

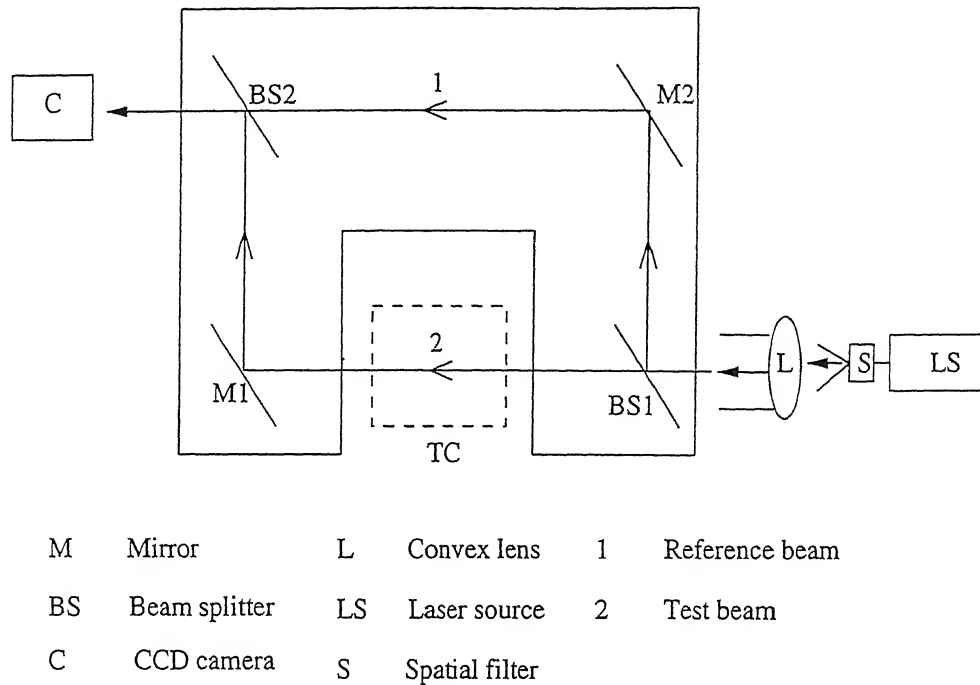


Figure 2.3: Schematic Drawing of the Mach-Zehnder Interferometer

set to have identical geometrical path lengths and fringes form due to density and is temperature changes alone. Since each fringe is a line of constant phase, it is also a line of constant refractive index, a line of constant density and hence temperature and hence an isotherm. It can also be shown that the fringe thickness is an inverse measure of the local temperature gradient (being small where gradients are high). The infinite fringe setting is employed for high-accuracy temperature measurements in the fluid. In (b), the mirrors and beam splitters are deliberately misaligned to produce an initial fringe pattern of straight lines. When a thermal disturbance is introduced in the path of the test beam, these lines deform and represent temperature profiles in the fluid. The wedge fringe setting is commonly employed for heat flux measurements.

2.2.1 Laser Source

A 35 mW, continuous wave (632.8 nm) He-Ne laser is employed as the coherent light source for the interferometer. This laser is sturdy in construction, economical and stable in operation. The original laser beam is of 2 mm diameter. A spatial filter is required to expand the beam to any convenient size. In the present study, the expanded beam

diameter is 70 mm. The spatial filter is a lens-pinhole arrangement with two adjustable screws. The distance between the pin hole and the lens is also adjustable. These screws determine the inplane location of the pin hole and have to be adjusted so that the small laser beam is focussed on the pin hole and the outgoing beam is expanded. A plano convex lens has been used to produce a collimated beam for the camera. The specifications of the laser used in the present study is given in Table 2.2.

Table 2.2: Specifications of the Helium Neon laser

Make	Spectra-physics
Model	Spectra-physics 127
Output power	60 mW (maximum), 35 mW average output
Wavelength	632.8 nm
Color	Orange red
Coherence length	20 cm - 30 cm
Power consumption	≈ 1.0 kW of electrical power
Efficiency	0.01 - 0.1 %
Beam diameter	1.25 ± 0.10 mm
Beam divergence	0.66 ± 0.06 mrad
Amplitude noise, 10 Hz -2 MHz	$< 1\%$ rms
Amplitude ripple, 45 Hz -1 kHz	$< 1\%$ rms
Life time	≈ 20000 hours of operation

2.2.2 CCD Camera

A CCD (charged coupled device) camera (Pulnix, model: T5 565) of spatial resolution of 512×512 pixels has been used to capture the interferometric images. The fringes formed at the second beam splitter of the Mach-Zehnder interferometer is projected over a screen. The selection of the screen and collection of interferometric images from it is a very important step since the clarity in the images will reduce the uncertainty in the subsequent calculations. For this purpose a tracing paper has been used to display the interferometric images. The attenuation of the laser beam through the thickness of the paper was found to be small. It was observed that two screens used together when physically disturbed led to distinctly clear images on the video monitor. This effect can be understood as a spatial averaging of the image over the two screens which makes the fringe pattern smooth and clear.

The CCD camera is connected to a PC-based image processing system through an 8 bit A/D card (PIP 1024 MATROX). The fringe pattern is stored in an integer matrix form with intensities varying between 0 to 255 (the gray scale), where 0 indicates black and 255 indicates white. With the present set up the image acquisition speed is at video rates, namely 50 frames per second. The digital output of the CCD camera is projected on to a high resolution video monitor to visualize and focus the fringe patterns.

2.2.3 Pneumatic Isolation Mount

The optical components of the interferometer are extremely sensitive to vibrations. This can be experienced from the fringes which formed on the screen. To avoid ground vibration from reaching the optics, the entire interferometer is placed over four pneumatic isolation mounts. These mounts are connected to an air compressor for pressurization. Once the mounts are pressurized the entire interferometer floats over the mounts. This stabilizes the interferometric images and facilitates image acquisition. An air compressor of rated capacity 10 atmospheres is used throughout the experiment to pressurize the mounts. The operating pressure for the mounts are 5 kg/cm^2 . Hence a regulator valve was used to supply air to the mounts at the right pressure. The compressor was located sufficiently away from the interferometer to protect it from vibrational noise.

2.2.4 Temperature Recorder

The thermocouples which are used to monitor the temperature of the two horizontal aluminium surfaces of the cavity and the ambient temperature were connected to a 30 channel temperature recorder. The temperature of the plates were monitored throughout the experiment. The specifications of the temperature recorder used in the present study are listed in Table 2.3.

2.3 Alignment of the Interferometer

Before the start of the experiment the interferometer has to be aligned. Though the initial alignment of the interferometer is generally not disturbed from one experiment to

Table 2.3: Specifications of the Temperature Recorder

Make	NEC San-ei Instruments, Ltd.
Model	8H10
Display	Digital
No. of channels	30
Measuring range	-200°C to 1370°C
Resolution	0.1°C

ie other, some fine tuning is essential to ensure that the interferometer is operating at s highest sensitivity. The initial alignment of the interferometer is carried out as per the llowing steps.

1. The light output of the spatial filter is adjusted so that the diffraction rings which appear with the expanded beam vanish. This requires adjustment of the screws on the spatial filter. In most experiments, the diffraction ring formed a complete circle and remained at the periphery of the expanded beam.
2. The laser power output is measured using a light meter. The laser power output is generally not a stable quantity and changes with time. This change in power output is not a transient phenomena but it decreases steadily and slowly with hours of operation. In the present work, the laser output was in the range 30-32 mW over two years.
3. The plano-convex lens is adjusted from the pinhole of the spatial filter so that the distance of separation is the focal length of the lens. This produces a parallel laser beam needed for the experiments.
4. All the optical components of the interferometer are adjusted till their centers fall on a horizontal plane. Once this is accomplished, the first beam splitter (BS1) is adjusted till it is exactly at 45° to the incoming light rays. All the remaining optical components are then made parallel to each other by adjusting one at a time. The mirrors and beam splitters being of 150 mm in diameter, the expanded beam of 70 mm diameter is made to pass through the central portion of the optical components.
5. Adjustment for the infinite fringe setting is delicate and requires effort. In the infinite fringe setting, the initial field of view is one of complete brightness since

interference is constructive. The geometrical and the optical path lengths of the test and reference beams are then the same in the absence of any thermal disturbances in the path of the test beam. Owing to imperfect adjustment of the mirrors and beam splitters by screws movement the exact infinite fringe setting in a theoretical sense may not be realized. As the interferometer approaches the infinite fringe setting the distance between the fringes increases and the number of fringes decreases. In the present work, it was possible to reduce the number of fringes to unity at the start of all the experiments (Figure 2.4).

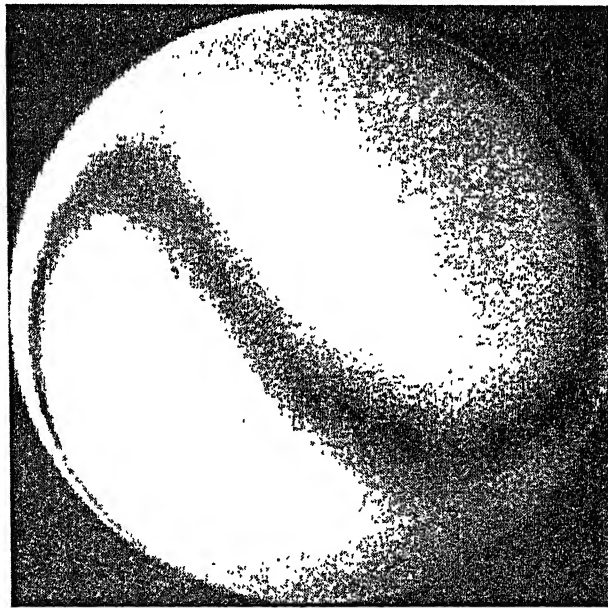


Figure 2.4: Infinite Fringe Setting of the Interferometer

To illustrate fringe formation in the infinite fringe setting, a candle flame was put on the path of the test beam and the interferogram was recorded. The candle flame in the infinite fringe setting is shown in Figure 2.5. The fringes can be seen to correspond to isotherms around the candle flame.

The wedge fringe setting is comparatively easier to set up than the infinite fringe setting. Here the initial fringes form due to deliberate misalignment between the optical components. The orientation of the fringes can be changed by adjusting the inclination of the optical components. Initially the fringes are adjusted so that they are perfectly straight. Figure 2.6 shows the initial wedge fringe setting of the interferometer. If a thermal disturbance is introduced in the path of the test beam, the fringes get displaced

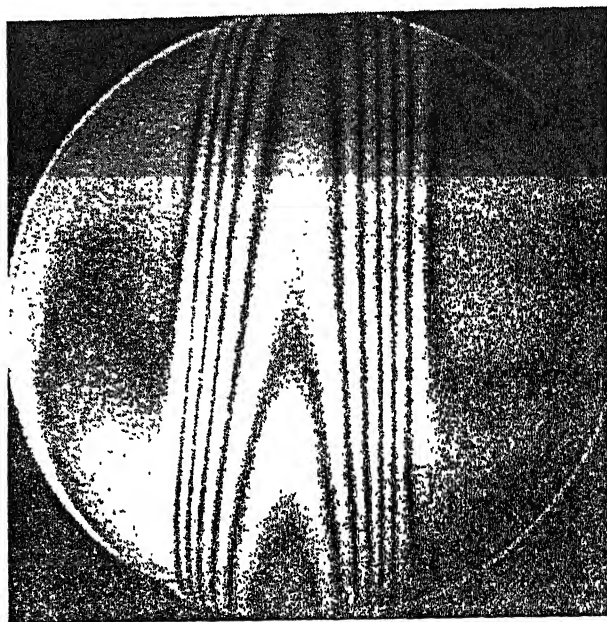


Figure 2.5: Candle Flame in the Infinite Fringe Setting of the Interferometer

to an extent depending on the nature of the temperature profile. Hence the fringes in the wedge fringe setting of the interferometer are representative of the temperature profile in the medium under study. The candle flame experiment is shown in the wedge fringe setting mode in Figure 2.7. Here the fringes are the temperature profile inside the flame. Note the symmetry in the temperature profile along the centerline of the flame.

2.4 Recording Interferometric Projections

The method of axial tomography requires the projection data of the field to be reconstructed from various angles. The experiments were hence conducted by rotating the Rayleigh-Benard convection test cell with reference to the light source. The position of the light source and the detector remained fixed in all the experiments. The experiments were conducted at various angles and for each angle the full width of the fluid layer was scanned. The width of the fluid layer being $500 \text{ mm} \times 500 \text{ mm}$ in plan, requires several translation of the traversing mechanism to scan the complete fluid layer along one angle of projection. This is because the diameter of the laser beam is only 70 mm. To record a projection at each location of the test cell, the flow field was allowed to pass through the initial transients and interferograms were recorded after 4 hours from start of the ex-

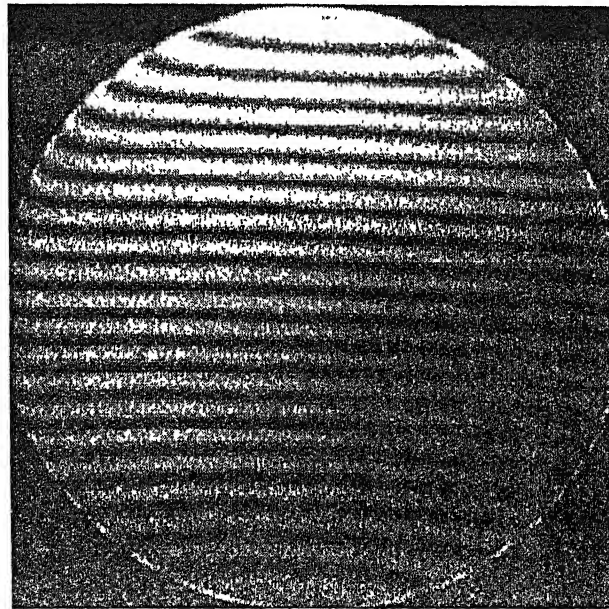


Figure 2.6: Wedge Fringe Setting of the Interferometer

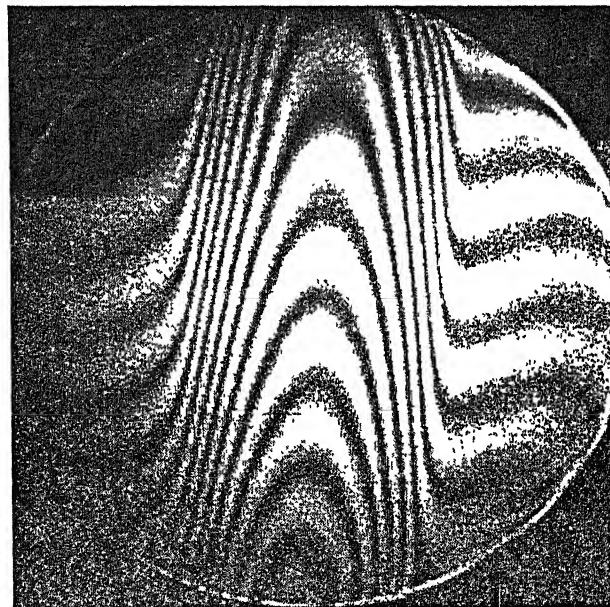


Figure 2.7: Candle Flame in the Wedge Fringe Setting of the Interferometer

periment. The projection field recorded in the form of images were later joined together to generate one complete image corresponding to a given projection angle. Each angle of rotation is known as a projection angle or a view angle. The definition of the view angle θ is shown in Figure 2.8.

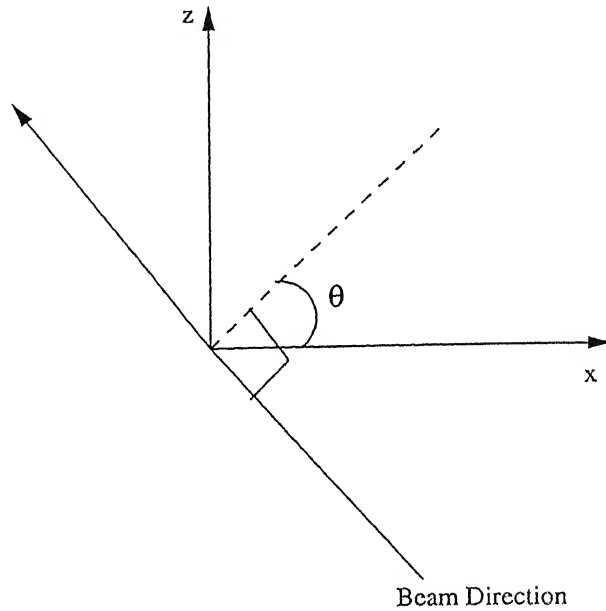


Figure 2.8: Definition of View Angle

For the lowest Rayleigh number studied ($Ra=13900$) experiments were conducted at six different view angles namely 0° , 30° , 60° , 90° , 120° and 150° . For all other higher Rayleigh numbers projections of the temperature field were recorded in the form of interferometric fringes from only two orthogonal view angles of 0° and 90° . At a Rayleigh number of 34800 and 40200, the fringes exhibited some time dependence. Specifically, the flow was seen to switch between two states in a fully repeatable manner. Of the two states, one was more dominant than the other and this mode alone has been analyzed in the present work. The unsteadiness in the flow field was seen to introduce uncertainty in the projection data, particularly with an increasing number of projections. A large uncertainty in projection data would be amplified during reconstruction, particularly with a large number of view angles. To keep the reconstruction errors below an acceptable limit, only two views (0° and 90°) have been employed in the analysis. This is however not a serious limitation since a numerical analysis of the MART family of algorithms has shown two orthogonal projections to produce meaningful results. This aspect is discussed in detail in Chapter 6.

The process of joining adjacent images for a given view angle led to uncertainties, particularly at higher Rayleigh numbers. This was due to unsteadiness in the flow patterns. The problem was circumvented by snapping several images from the camera at each location and considering only those which formed a continuous pattern.

2.5 Uncertainty and Measurement Errors

Errors in the experimental data are associated with misalignment of the apparatus with respect to the light beam, image processing operations including filtering, thinning and assigning temperature to fringes, error amplification during three dimensional reconstruction and the intrinsic uncertainty in the convection process itself. Errors related to refraction effects have been found to be quite small. All experiments were conducted several times to establish the repeatability of the fringe patterns. The uncertainty in Rayleigh number is related to the flatness of the two horizontal confining walls which decides the height of the fluid layer and the constancy of temperature on the horizontal walls which prescribes the temperature difference across the fluid layer. Hence there is a variation of Rayleigh number from point to point in the fluid layer. The average uncertainty level in the Rayleigh number is expected to be less than ± 1000 . Experience with Rayleigh-Benard experiments for $Ra > 3 \times 10^4$ show uncertainty levels in the local wall Nusselt number of upto 20%, primarily due to mild unsteadiness in the flow pattern (Muralidhar *et al.*, 1995). Time-dependent movement of fringes was not a source of uncertainty in the present work at a Rayleigh number of 13900. However, at a Rayleigh number of 40200 two sets of convection patterns were seen to be formed. Analysis has been carried out for the fringe patterns that formed for most part of the experiment. At both Rayleigh numbers, the plate-averaged Nusselt number is found to be in good agreement with published correlations and is discussed in Chapter 6. The width-averaged temperature profile that represents energy balance across the cavity was also found to be unique and well-defined. Hence the results obtained in the present work can be taken to be qualitatively meaningful.

There are two edge effects that interfere with the recorded data in the present design of the test cell. These are described below:

1. While scanning the temperature field using a laser, the test beam encounters a sudden change in temperature as it enters the fluid layer. This introduces a bending in the laser due to a large temperature gradient. The same effect is expected when the beam comes out of the test cell into the ambient. The bending of laser beam due to these changes in temperature gradients at the two ends will be equal and opposite under ideal conditions. Hence theoretically the effect is nullified. In practice this may lead to a small error in the projection data.

the projections were recorded after allowing sufficient time to avoid the transients in the fluid layer. However the time required for reaching the thermal equilibrium in the vertical insulated side walls is expected to be much larger, perhaps 10-12 hours. It is expected that transients in the side walls will not interfere the fluid motion in the core of the cavity. Hence the edge effects arising from the insulated side walls are neglected in the present study.

Chapter 3

Image Processing and Fringe Thinning

The recording of fringe patterns using a CCD camera results in storing the images as a string of numbers in the form of a matrix. Each number corresponds to an intensity level. In the present study, an 8-bit analog-to-digital converter was employed. Hence the resulting images are discretized into 256 gray levels. An intensity level of 0 indicates black whereas 255 is white. Availability of the images on a gray scale is of help in data processing and the automation of the fringe extraction process. With these aids interferometry coupled with tomography for temperature measurement becomes a less tiring and cumbersome tool and certainly more interesting.

The fringe patterns recorded using the interferometer need to be converted into temperature records for tomographic calculations. Quantitative evaluation of the interferograms requires that the fringe skeleton be determined first. From the thinned fringes, temperature information can be generated since, a fringe is an isotherm and the same temperature prevails over its entire length. This step requires the following operations: (1) processing of the fringe images (**image processing**) (2) identifying intensity minima within fringes (**fringe thinning**) (3) measuring distances between fringes and determining fringe order in terms of temperature units (**quantitative evaluation**) and (4) transferring the temperature information available at the fringes to a superimposed uniform grid (**interpolation**). In most experiments, these four steps are difficult since operations such as locating fringe minima and edges result in ambiguity. One of the factors that cause difficulty in image analysis is *speckle*, a form of noise. Elaborate procedures must be em-

played to remove speckle from interferometric images. Examples of filtering strategies are Fourier-filtering using band-pass filters, histogram specification and Laplacian smoothing (Gonzalez and Woods. 1993). The strategies involved in processing the interferograms from the initial stage as a digitized image to finally a fringe skeleton are discussed in the present chapter.

3.1 Image Processing

Images of fringe patterns collected using the CCD camera and the A/D card tend to be noisy. While a collection of fringes indicates a smooth wave-like variation of light intensity, experimental interferograms will have a superposition of higher harmonics of small amplitude. This is a source of ambiguity since it is now quite difficult to identify intensity maxima and minima. Noise can thus be defined as extraneous and unwanted intensity variation which is superimposed over the useful portion of the data. Noise is generated at different stages of the experiment: the imperfection of the optical components, noise in the CCD array, digitization and lastly the flow and thermal fields under study also contribute to noise owing to edge effects due to refraction and nonuniform scattering and absorption. However, in the experience of the author, speckle is the major source of noise in interferometry. It is a superposition of diffraction patterns over the basic interference pattern that constitutes the signal in the present discussion. Speckle arises from imperfection of optical surfaces. The presence of microscopic unevenness on the surface of the optical elements leads to diffraction. The diffracted rays in turn interfere and generate local fringe patterns and corrupt the global intensity distribution. Thus speckle is characterized by high-wavenumber fluctuations in the intensity data. To recover the original intensity variation, there is a need to filter the image, remove noise and extract the signal.

Image processing applications are required to remove the noise present in the images on one hand and enhance the quality of the images on the other. Further, in experiments fringes are bands of finite thickness, and isotherms are associated with the minimum or maximum intensity level within a dark or a bright band. The process of replacing the fringe bands by curves passing through minimum or maximum intensity locations is called fringe thinning. Hence, the next objective of image processing is the generation of a thinned image. In summary, image processing operations in interferometry can be divided into three categories: (a) filtering, (b) image enhancement, and (c) thinning. These steps

are discussed below.

3.1.1 Filtering of Images

Once the image is stored in digital form, the image is available as a matrix of integers. These fall in the range 0-255 and represent light intensity at spatial locations on the image. Speckle can be removed using Fourier filtering, median filtering and averaging. However Fourier filtering has been seen to be best suited for interferometric fringes. Median filtering has been applied locally to an image for better smoothing as an operation after the Fourier filtering.

For the Fourier filtering operation the image is first transformed to the wavenumber space with a two dimensional Fourier transform operation. Here the wavenumber is a kind of a spatial frequency, defined as the number of intensity cycles per pixel. Intuitively one can view the low wavenumber harmonics as information and those at a high wavenumber as noise. In the wavenumber space a two dimensional symmetric band-pass filter can be used to effectively set the high wavenumber components to zero. The size of the band-pass filter is decided by its ability to remove noise without appreciable loss of signal, typically less than 5% . An inverse two dimensional Fourier transform restores the image in filtered form in the spatial domain. The symmetricity of the filter referred above is related to the problem of aliasing with discrete Fourier transforms. The decision on the size of the band pass filter has to be found by trial-and-error. Since the light source and optics employed for all the experiment were identical noise pattern in the images is expected to be invariant. Hence the same band pass filter was used for all filtering operations. The fast Fourier transform (FFT) algorithm (Gonzalez and Woods, 1993, Jain, 1989) was employed for the calculation of the discrete Fourier transform of the image data.

The one dimensional version of FFT is briefly presented here. Any waveform with a zero mean can be looked upon as a combination of a number of sinusoids. Hence the wavenumber of each of these sinusoids with their corresponding amplitude are representative of the signal in the wavenumber space. The Fourier transform of a function transforms the information about the signal in the time domain to the wavenumber domain. Let $f(x)$ be a continuous function of a real variable x . Then Fourier transform of $f(x)$ can be defined as

$$F(\omega) = \int_{-\infty}^{+\infty} f(x) \exp(-j2\pi\omega x) dx \quad (3.1)$$

where ω represents the wavenumber, defined here as the reciprocal of wavelength. j represents the imaginary number, defined as $j = \sqrt{-1}$. The function $f(x)$ can be recovered by an inverse Fourier transform as:

$$f(x) = \int_{-\infty}^{+\infty} F(\omega) \exp(j2\pi\omega x) d\omega \quad (3.2)$$

In a discrete calculation, the function is available at $N-1$ intervals as f_0, f_1, \dots, f_{N-1} with a spacing $\Delta x = L/(N-1)$ where L is the length of the signal. The reciprocal of L can be viewed as the wavenumber of the fundamental harmonics in the wavenumber space. The above definition of Fourier transform can be modified as

$$F(\omega) = \frac{1}{N} \sum_{i=0}^{N-1} f_i \exp\left(\frac{-j2\pi\omega i \Delta x}{N}\right) \quad (3.3)$$

where ω is also a discrete variable, in the range $1/L$ to N/L . The spacing $\Delta\omega$ is the minimum wavenumber that can be measured, that is $1/L$. Hence the wavenumbers are discretized into $N-1$ intervals. Similarly the inverse discrete Fourier transform can be defined as

$$f(i\Delta x) = \sum_{\omega=0}^{N-1} F(\omega) \exp\left(\frac{j2\pi\omega i \Delta x}{N}\right) \quad (3.4)$$

The use of the fast Fourier transform algorithm requires that the sampling of the continuous function be made over 2^m divisions, where m is an integer. Hence 2^m is an even number and can be expressed as

$$N = 2M \quad (3.5)$$

where M is an integer. Equation 3.3 can now be written in the form

$$F(\omega) = \frac{1}{2M} \sum_{i=0}^{2M-1} f_i \exp\left(\frac{-j2\pi\omega i\Delta x}{2M}\right) \quad (3.6)$$

The right hand side of this equation can be split as

$$\frac{1}{2} \left[\frac{1}{M} \sum_{i=0}^{M-1} f_{2i} \exp\left(\frac{-j2\pi\omega 2i\Delta x}{2M}\right) + \frac{1}{M} \sum_{i=0}^{M-1} f_{(2i+1)} \exp\left(\frac{-j2\pi\omega (2i+1)\Delta x}{2M}\right) \right] \quad (3.7)$$

Hence

$$F(\omega) = \frac{1}{2} \left[\frac{1}{M} \sum_{i=0}^{M-1} f_{2i} \exp\left(\frac{-j2\pi\omega 2i\Delta x}{M}\right) + \frac{1}{M} \sum_{i=0}^{M-1} f_{(2i+1)} \exp\left(\frac{-j2\pi\omega (2i+1)\Delta x}{M}\right) \exp\left(\frac{-j2\pi\omega}{2M}\right) \right] \quad (3.8)$$

Breaking the discrete values of the function into odd and even terms one gets

$$F_{even}(\omega) = \frac{1}{M} \sum_{i=0}^{M-1} f_{2i} \exp\left(\frac{-j2\pi\omega 2i\Delta x}{M}\right) \quad (3.9)$$

$$F_{odd}(\omega) = \frac{1}{M} \sum_{i=0}^{M-1} f_{2i+1} \exp\left(\frac{-j2\pi\omega (2i+1)\Delta x}{M}\right) \quad (3.10)$$

Equation 3.8, can now be put in the form

$$F(\omega) = \frac{1}{2} \left[F_{even}(\omega) + F_{odd}(\omega) \exp\left(\frac{-j2\pi\omega}{2M}\right) \right] \quad (3.11)$$

Noting that

$$\begin{aligned} \exp\left(\frac{-j2\pi(\omega + M)}{M}\right) &= \exp\left(\frac{-j2\pi\omega}{M}\right) \\ \text{and } \exp\left(\frac{-j2\pi(\omega + M)}{2M}\right) &= -\exp\left(\frac{-j2\pi\omega}{2M}\right) \end{aligned}$$

one can derive

$$F(\omega + M) = \frac{1}{2} \left[F_{\text{even}}(\omega) - F_{\text{odd}}(\omega) \exp\left(\frac{-j2\pi\omega}{2M}\right) \right] \quad (3.12)$$

Equations 3.11 and 3.12 are central to the success of the FFT algorithm. They show that the actual Fourier transform can be computed for two halves of the series (odd and even) and that of the original series can be determined by recombination. Each half of the full series can be further divided into even and odd parts. This breaking up into even and odd parts can be repeated till we reach a stage where only one term remains in each of the series. Equation 3.6 can be used to show that the Fourier transform of only one term is the term itself. Hence Equations 3.11 and 3.12 can be used to compute the Fourier transform of the original series.

The FFT algorithm for calculation of the Fourier transform of a discrete set of data requires only $N \log_2 N$ number of calculations (multiplications and additions). The discrete Fourier transform using direct Fourier transform formula requires N^2 number of calculations. N represents the number of discrete data points. The FFT algorithm has a requirement of 2^m number of data points, m being an integer. If the number of points is not equal to integer power of 2, FFT can still be used to compute the Fourier transform of the series of data. This is achieved by adding 0 to the series of data on both sides of the series so that the nearest integer power of 2 number of data can be obtained. This method of adding zero to a series of data, so that FFT can be applied on it is known as zero padding. In the present work, the image obtained are of the size of 512×512 pixels. Hence for FFT applications no zero padding was required.

The computer implementation of the FFT algorithm discussed above is briefly discussed here. The major point to be taken care of during the implementation of the FFT algorithm is to arrange the discrete data in the order for successive applications of Equations 3.11 and 3.12. The ordering procedure is also referred as butterfly algorithm. The butterfly algorithm for ordering of the discrete data for implementation of the FFT algorithm is shown schematically in Figure 3.1. The figure shows an example of 8-point Fourier transform. The input data, to the algorithm are $\{f_0, f_1, \dots, f_7\}$. This set of data can be break into two series of data as the odd and even series. The odd series is $\{f_1, f_3, f_5 \text{ and } f_7\}$ and the even series is $\{f_0, f_2, f_4 \text{ and } f_6\}$. Each of these 4-points series can be splitted further as odd and even series with 2-points data. These are $\{f_0, f_4\}$.

$\{f_1, f_5\}$ as the even series and $\{f_2, f_6\}$, $\{f_3, f_7\}$ as the odd series. No further splitting is required, since in a 2-points data series is having one even and one odd term. Hence the input series to the algorithm requires the ordering as:

$$\{f_0, f_4, f_2, f_6, f_1, f_5, f_3 \text{ and } f_7\}$$

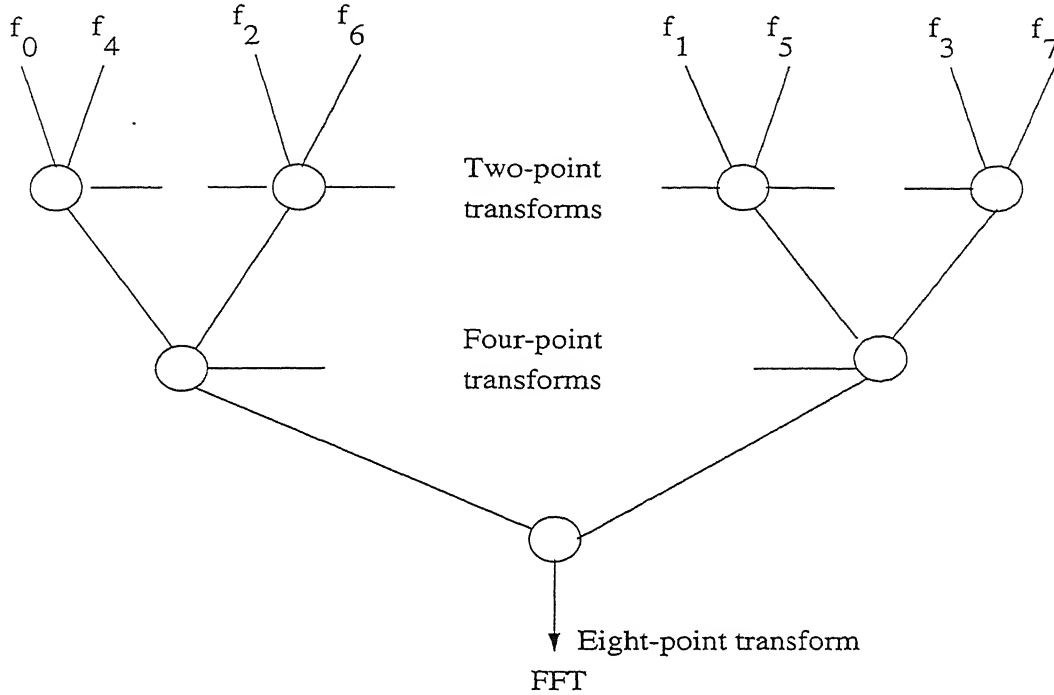


Figure 3.1: Schematic of Butterfly Algorithm, for Implementation of FFT

The butterfly algorithm for ordering operates as shown in Figure 3.1. The first step is calculation of the four 2-points transforms. The next step uses these results to obtain two 4-points transforms. The third step uses these results to produce the final 8-points transform. This reordering of data follows a simple rule of the corresponding binary number. This is known as bit-reversal. If n represents the argument value in the actual series of input data, the corresponding argument of the data in the reordered series can be directly obtained by expressing the number n in its binary form and then reversing the bits from left-to-right and then obtaining the corresponding number. For example the 4th element of the 8-points series considered above in the input data is f_3 . The number 3 (argument of the 4th element) can be expressed as a binary number as 011. Applying the bit-reversal rule the modified binary number is 110 which corresponds to an argument of 6. Hence the data f_3 will occupy the position of argument 6 in the reordered data, that is the 7th element from the beginning.

The one dimensional FFT algorithm discussed above can be extended to a two dimensional FFT algorithm. To this end the one dimensional FFT was implemented successively in the two directions to obtain the two dimensional Fourier transform. The inverse Fourier transform was obtained in the similar way by adopting successively the one dimensional inverse FFT. The number of arithmetic operations in one dimensional FFT being $N \log_2 N$, that for two dimensional FFT is clearly $2N^2 \log_2 N$.

The application of Fourier filtering to digitized interferograms is discussed below. Figure 3.2 shows an interferogram as recorded using a CCD camera. This interferogram has been collected in the infinite fringe setting of the inteferometer and the thermal disturbance introduced is the convective field of the Rayleigh-Benard experiment. The interferogram has been recorded at a 90° view angle and corresponds to a physical dimension of 6.5 cm of the test cell. The interferogram shown in Figure 3.2 is a portion of the total image that appears on the screen (512×512 pixels). The number of pixels in the interferogram in Figure 3.2 are 451 (width) \times 246 (height). This is because the laser beam diameter on the reference beam was 7 cm, whereas the test beam that passes through the window of the Rayleigh-Benard setup was 6.5 cm (width) \times 2.0 cm (height). For Fourier filtering the total image was used, since data was available at 2^N points in both the directions. No zero padding was thus required.

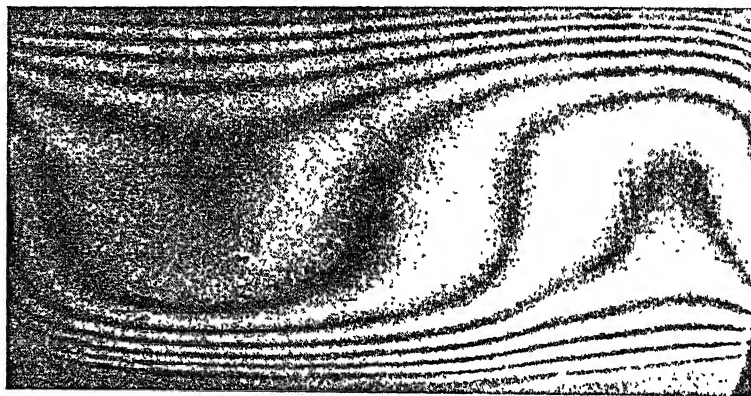


Figure 3.2: An Original Interferogram

Since the fringe images captured are formed due to the principle of interference, it is expected that the intensity variation along a column of the image has a cosine square variation. In practice, the intensity variation is a superposition of a range of wavenumbers. The higher harmonics in the intensity variation correspond to unwanted information generated through the speckle. Since in Rayleigh-Benard convection the

temperature gradient exists in the vertical direction, it is mainly required to filter the noise present along the vertical coordinate of the cavity, namely the columns of the two dimensional image. The two dimensional Fourier transform of the intensity function is shown in Figure 3.3. A symmetric band pass filter for low pass operation over the one dimensional Fourier transform is shown schematically in Figure 3.4. The peaks at the two extreme ends of the amplitude variation along the wavenumber axis represent information without the noise part of the input signal. The band pass filter is symmetric about the Nyquist wavenumber to take care of the aliasing error which is inherent to FFT. Since the image size is 512×512 pixels, this corresponds to a numerical value of 256 in both directions. The band pass filter has been chosen as a square of size 100×100 . The band pass filter is symmetric with respect to both x and y directions.

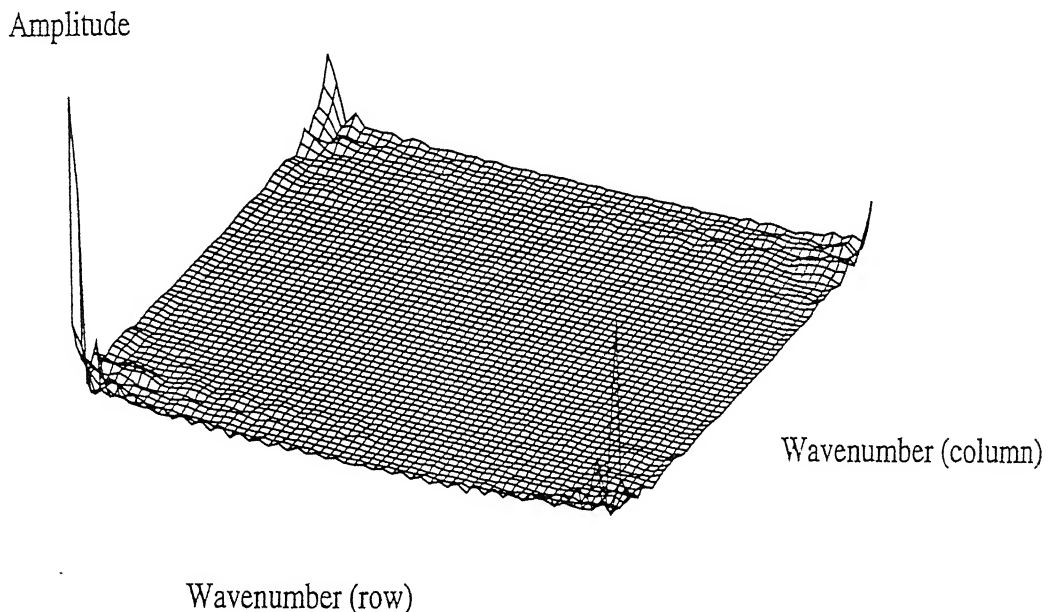


Figure 3.3: Two Dimensional Fourier Transform of the Intensity Function

Figure 3.5 shows the intensity variation in one of the column of the image in both original and the filtered interferograms. To maintain clarity of the figure the actual intensities in the original and in the filtered interferograms have been displaced. The intensity distribution of the filtered interferogram is seen to be smooth compared to the original interferogram. Figure 3.6 shows the filtered interferogram of the same image. From Figures 3.2 and 3.6 it can be readily observed that there is an enhancement of fringe information since the position of the minima and maxima are now clearly recognised. Filtering removes the high wavenumber components of the intensity distribution and

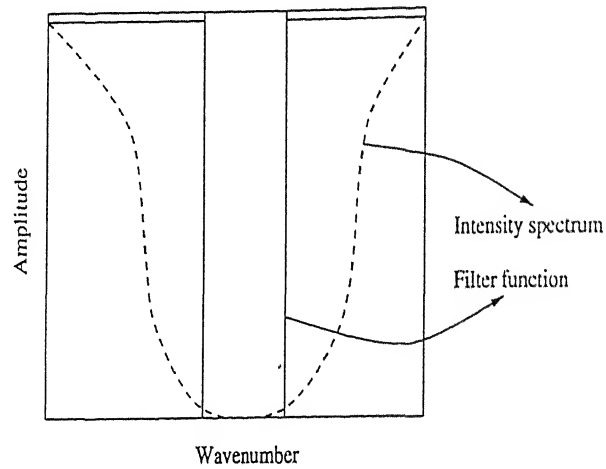


Figure 3.4: Schematic of an One Dimensional Band Pass Filter

thereby removes unwanted noise in the image data. At the same time the fringe edges becomes blurred. This is due to the fact that the edge of the fringe bands corresponds to high wavenumbers. Filtering may result in loss of this contrast. The visual appearance of a filtered image may not be good compared to the unfiltered image. But the filtered image is definitely an improvement over the unfiltered image in terms of the noise content. Image processing operations can be unambiguously applied to the filtered image.

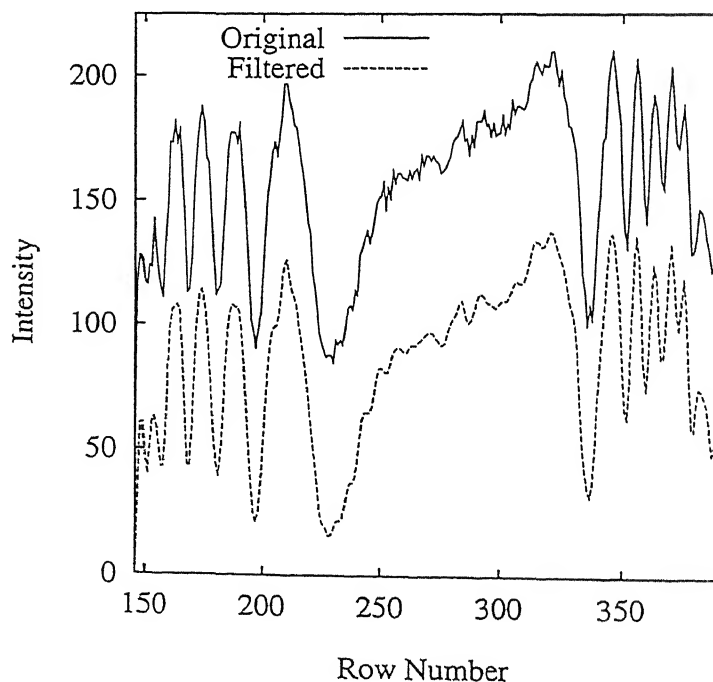


Figure 3.5: Original and Fourier Filtered Intensity Distribution

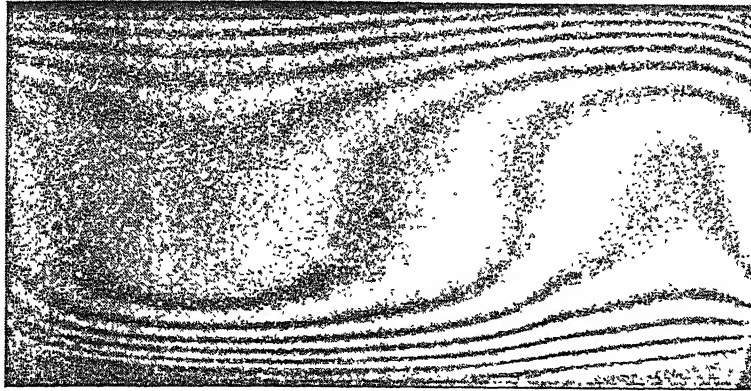


Figure 3.6: Filtered Interferogram

3.1.2 Image Enhancement

The Fourier filtered images are generally blurred owing to loss of contrast. Hence, further operations are required to enhance the quality of the image. In particular, edge enhancement and contrast improvement are essential for analyzing the interferograms. While various techniques are available in the literature for improving the images, the image enhancement techniques are problem-specific. The method of image enhancement for optical images generated from an interferometer may be completely different from the images obtained from a satellite.

The techniques for image enhancement can be classified as spatial domain and wavenumber space methods. Spatial domain methods deal with the gray value at a pixel directly whereas the wavenumber space techniques manipulate the wavenumber spectra obtained from the Fourier transform of the image. The spatial domain enhancement techniques process the image over a point or a mask. Strategies that have proved to be useful for improving the appearance of the images are: (a) specification of probability density function, (b) median filtering and (c) edge enhancement. These are described in the following sections.

Specification of probability density function (PDF)

Specification of a probability density function (specifically a histogram) for intensity variation over the pixels belongs to the point processing approach in the spatial domain. The area enclosed by each strip of a histogram gives an estimate of the probability of occur-

rence of that gray level in the image. A plot of this function for all gray levels (0-255) provides a complete description about the appearance of an image. Once the histogram of an image is obtained, it can be forced to follow a predetermined shape, whose functional form depends on the problem being studied. A strategy where all gray levels have equal probability density will reduce noise and produces an image with high contrast. This process is called histogram equalization.

Let I be the intensity level in the image and T a function which transforms I to a new value J , that is

$$J = T(I) \quad (3.13)$$

The function T is such that, for every intensity level in I there exist an intensity level in J . The bounds within which I is defined, hold for J . The function T is monotonic. Let $P_I(I)$ and $P_J(J)$ are the probability density function of I and J . Since the distribution I is known, hence $P_I(I)$ is also known. The probability density function of J is given by,

$$P_J(J) = [P_I(I) \frac{dI}{dJ}]_{I=T^{-1}(J)} \quad (3.14)$$

To implement histogram equalization, $P_J(J)$ in the transformed image is forced to be unity for all values of J . It can be shown that the transformation

$$J_k = T(I_k) = \sum_{m=0}^k \frac{L_m}{L} \quad (3.15)$$

produces an intensity distribution where the probability density function $P_J(J)$ is 1 for all values of J . Here L is the number of intensity levels in the image and L_m is the number of pixels having the intensity level m .

Figure 3.7 shows a contrast improved image obtained from histogram equalization corresponding to the interferogram shown in Figures 3.2 and 3.6.

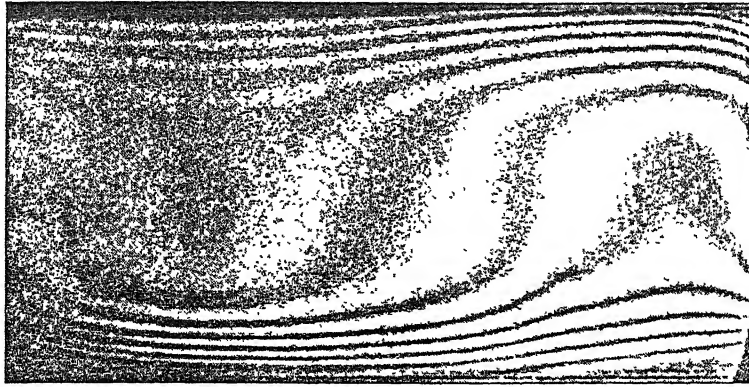


Figure 3.7: Contrast-improved Interferogram, (Histogram Equalization)

Median filtering

A median filter is a smoothing operator and is employed in the spatial domain, that is the image itself. However it involves mask processing. A mask is collection of pixels around the point whose intensity is being adjusted. The intensity at the point under consideration is readjusted to be in consonance with the neighbouring intensities. The purpose of this filter is to remove noise locally at selected regions of the image. To this end the gray level of each pixel is replaced by the median of the gray levels in its neighbourhood as defined by the mask. This step can be applied once or twice and results in the removal of localized patches present in the image. One of the advantages of using the median filter is that it removes noise but preserves the edges and other sharp details in the image. Figure 3.8 shows a median-filtered interferogram obtained by median filtering twice the entire Fourier-filtered image of Figure 3.6. The intensity distribution on a particular column for the Fourier-filtered and the median-filtered interferograms are compared in Figure 3.9. It can be seen that fringe minima positions are untouched but median-filtering has produced more smoothing over the Fourier-filtered image. From Figure 3.8 it can be readily seen that there is no loss of edge information of the fringe band.

Edge enhancement

Along with the noise, edges of fringes are also equivalent to the high wavenumber portion of the image spectrum because of the accompanying sharp change in the gray level. During Fourier-filtering, the high wavenumber part of the spectrum is set to zero and in this process some edge information is lost and the edges become blurred. Since the



Figure 3.8: Median-filtered Interferogram

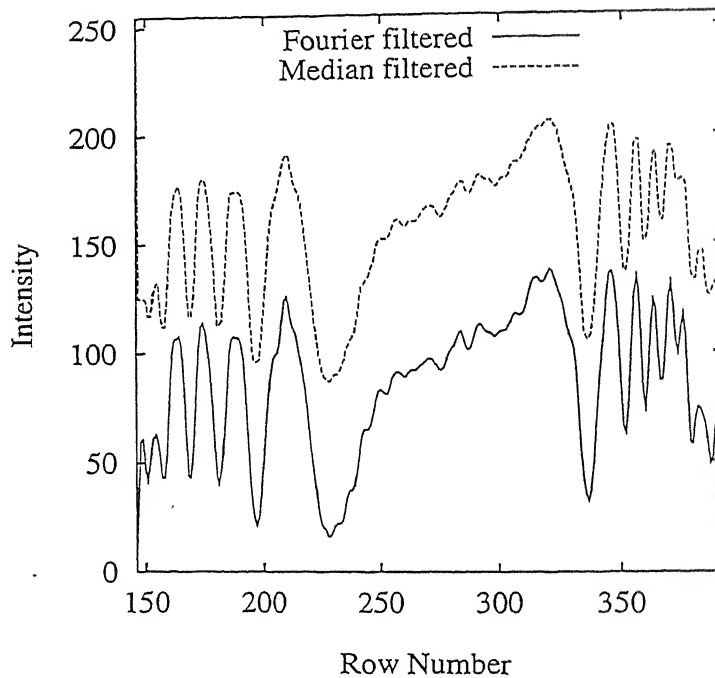


Figure 3.9: Intensity Distribution in Fourier-filtered and Median-filtered Interferogram

fringe thinning operations are carried out within the fringe band, a proper definition of fringe thickness is required. Hence the edges of the fringes need to be sharpened. This is accomplished as follows. A high-pass spatial filter is first applied to the image. The shape of the impulse response required to implement a high-pass filtering operation on the image should have positive coefficients near the center, and negative coefficient near the boundary. In the present study a 3×3 mask with a coefficient of 8 at the center and -1 at all other locations is used. A fraction of the original image is then added to this high-pass filtered image to obtain a high-boost image. The original image restores

partially the lost low frequency components in the high-pass filtered image. The superposition of the two images is accomplished as:

$$\text{High-boost image} = (A-1) \text{ Original Image} + \text{High-pass filtered image}, A > 1$$

For optical images obtained from the interferometer, a value of A between 1.0 to 3.0 gives good results depending upon the initial quality of the image. Gray levels greater than 255 are reset to 255. This is acceptable because fringe thinning employs intensity minima alone and maxima are only of peripheral interest. Since a spatial filter was used to expand the laser beam diameter to 7 cm, the average intensity level over the image is not constant. For precise adjustment of the spatial filter one would expect a Gaussian profile in the average intensity variation over the image, with the peak at the center. However, a slight misalignment of the pinhole location inside the spatial filter results in a noticeable shift of the center of the peak from the center of the image. To accommodate this effect, a dynamic change in the factor A was implemented. The fraction of image to be added back to the high-pass filtered image was reduced in low contrast (brightly illuminated) areas compared to the high contrast (less illuminated) parts of the image. Hence this fraction is a maximum at the outer edge of the image where the average intensity level is small and the contrast is good. The fraction to be added is a minimum at the center of the image where the average intensity level is generally high. The variation in the fraction of original image to be added to the high-pass filtered image was chosen to be linear from the edge of the image to its center.

Figure 3.10 shows the 3×3 template used for preparing the high-boost image. Figure 3.11 shows the high-boost image with edge enhanced properties as compared to the image shown in Figure 3.2. The use of edge enhancement is essential when the thinning has to be accomplished using the edge-detected image. Figure 3.12 shows a comparison of the intensity variation in the Fourier filtered interferogram and in the high-boost image. The stretching of contrast is clearly visualized here. However the process of high pass filtering has introduced spikes in the intensity data. Since the high-boost image is required only for manual fringe thinning operation these spikes donot create any further uncertainty in the data reduction process. Instead the improvement in contrast helps in eye judgement. The intensity variation shown in Figure 3.12 also shows that the positions of fringe minima are not altered in the high-boost image.

-1	-1	-1
-1	8	-1
-1	-1	-1

Figure 3.10: Template for High-boost Image Preparation

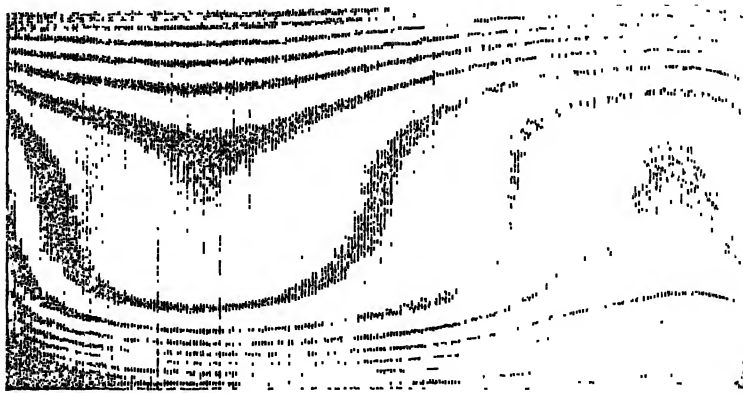


Figure 3.11: Contrast Improved Interferogram, (High Boost image)

3.2 Fringe Thinning

Fringe thinning is one of the most important operation in the extraction of quantitative data from interferograms. Fringe thinning is a process of extraction of the set of points of minimum or maximum intensities in the dark and bright bands of the fringes. When the interferometer is operated in the infinite fringe setting, each fringe is a locus of points having an identical path difference. This can be interpreted as follows: For rays having a certain path difference, the corresponding pixels in the interferometric image will have identical light intensity. One of the direct ways to locate a typical locus of points is to connect all minimum intensity pixels within a dark band or the maximum intensity pixels within a bright band. The minimum intensity will appear at a point of complete destructive interference and hence will have a zero intensity. Similarly, a maximum in intensity will appear at a point where interference is constructive. In experiments, the original as well as partially processed images have superimposed noise. Hence the distribution of

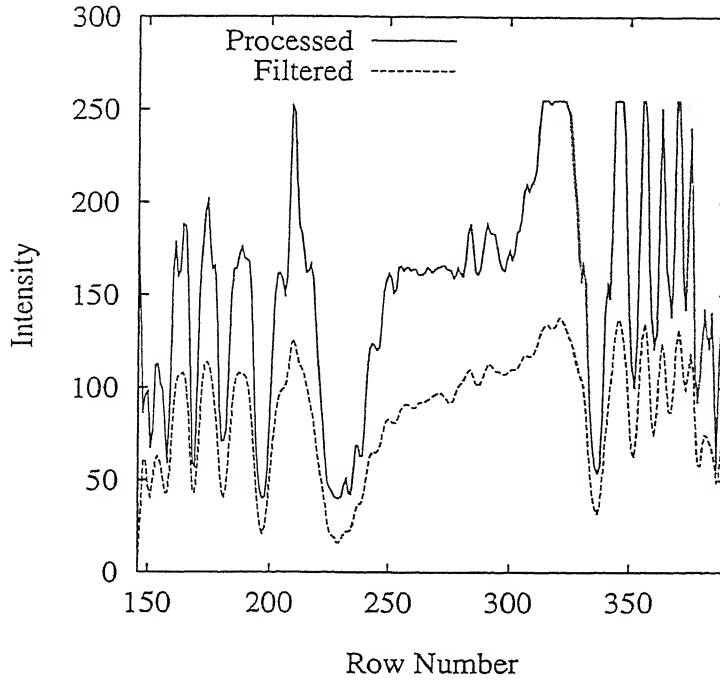


Figure 3.12: Contrast Improved Interferogram, (High Boost image)

intensity across fringes will exhibit ambiguity. Specifically, the minimum intensity will not strictly be a zero and the maximum intensity in 8-bit digitization will not be 255. Hence the strategy that is employed is to trace the intensity minima within dark bands and maxima within bright bands, rather than search for points of known intensity. This is the closest approximation that can be achieved to track a series of pixels having low or high intensities. When a laser is used as a light source, one must also take into account the overall Gaussian profile of the light output. Hence, determination of extrema in intensity becomes a local operation in the image domain. Subsequently, the locus of minima or maxima need to be connected within a fringe band across the width of the image, to get a curve on which temperature itself or a temperature-dependent function is a constant. It is clear that under experimental conditions, only intensity minima can be traced since intensity itself is not precisely defined. In practice, one observes a greater noise level in the high intensity regions, possibly related to device saturation in the recording medium. This makes locating intensity maxima a difficult task. Hence, fringe thinning operations referred in the present work are related to the location of intensity minima in the dark fringe bands alone.

Several fringe thinning methods are available in the literature. Most of the fringe

tracing algorithms that have been suggested are problem-specific and cannot be accepted as being generally valid. A large number of published algorithms are based on edge detection by global thresholding but these are specific to a class of problems and appear to be inapplicable for interferometric images. In the presence of a non-uniform average level of illumination with superimposed noise, the opinion of the present author is that the task of automatic extraction of the fringe skeleton is difficult. This has been experienced even with the well-behaved fringe tracing algorithms given by Robinson (1983) and Krishnaswamy (1991) for interferometric fringes and by Ramesh and Singh (1995) for photoelastic fringe patterns. Funnel (1981) has suggested an easy-to-implement but not a fully automatic technique to trace the fringes. His method is likely to yield good results for low-quality images. In the present study, an algorithm that is similar in approach to that proposed by Funnel (1981) has been developed. This algorithm is automatic in the sense that no user input is required at any intermediate stage of the calculation. It is based on the actual two-dimensional gray level variations and the fringe skeleton is traced by searching along the minimum intensity direction while simultaneously maintaining connectivity of the points traced. Two other thinning methods pursued in this work are (a) midpoint search and (b) free hand drawing using options available on a PC.

The implementation of the three fringe thinning algorithms suitable for interferograms recorded using the Mach-Zehnder interferometer are presented in this section.

3.2.1 Automatic Fringe Thinning Algorithm

The algorithm under discussion is similar to the one proposed by Funnel (1981), but in view of certain differences in the details, the full algorithm is presented below. Once a single point is specified the present algorithm does not require a user's intervention while the tracing is in progress. It is in this respect the algorithm is fully automatic. It consists of tracing of the fringes in the direction of the minimum intensity. The direction is decided by using the intensity information over a template of pixels. The computer code developed in the present study can run using different sizes of templates and handle complex fringe shapes. The input required for the code is the starting point for each fringe selected for each of the fringes.

The algorithm uses the following ideas. The direction of the tracings are defined as: (a) forward and (b) backward (Figure 3.13). The turning of fringes by more than

$\pm 90^\circ$ results in a change of direction and is a special case. Such areas of the fringes where a turning is there has to be pre-defined in the form of a rectangle covering the area. These cases are classified into four categories depending on the angle of turning: (a) while in forward direction turning backward up, (b) while in forward direction turning backward down, (c) while in backward direction turning forward up and (d) while in backward direction turning forward down (Figure 3.14). To locate the point of minimum intensity, eight directions of movement (1-8) are defined (Figure 3.15). The direction in which the minima should be searched is located by placing a template whose size is user-specified at the concerned pixel. The choice of size of the template is related to the fringe thickness. The near wall fringes in the present study were very thin owing to large heat flux. Hence the choice of template size was limited to the minimum possible, namely a 3×3 square. Use of bigger template is likely to interfere with neighbouring fringes and is hence undesirable. However a large template can be used when the fringe bands spread over several pixels. Use of template as big as 7×7 and 9×9 results in an average direction of minimum intensity and tends to produce a smooth tracing. Local unphysical variations can be bypassed by using a large template. Hence a 5×5 template appears to be an optimal choice for interferometric fringes.

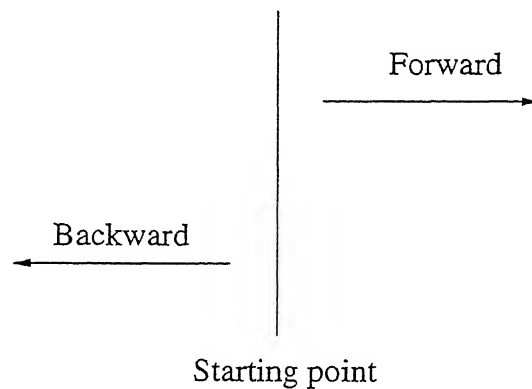


Figure 3.13: Two Major Directions for Tracing of Fringes

The direction in which the fringe is to be traced is determined as follows. The sum of the intensities in all the eight directions are computed and the two sequences of numbers along which the minima occur are searched. The directions producing the minimum intensity sums are accepted as the minimum intensity directions within a fringe band. One of these is the previous direction already identified. Hence the new direction is the one along which the fringe curve has to be extended. In practice the two intensity sums may not be identical since the average intensity level of the image is not constant.

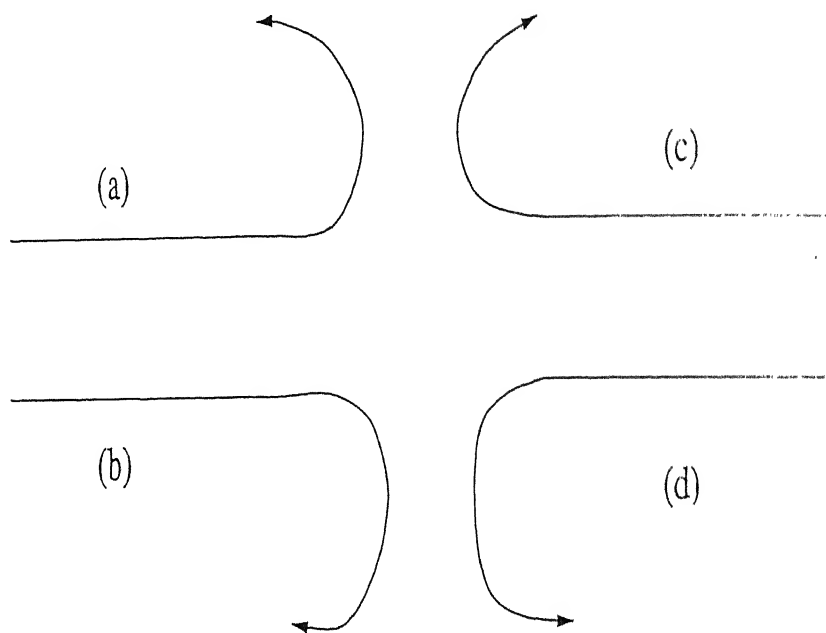


Figure 3.14: Four Possible Turning Options for Fringes

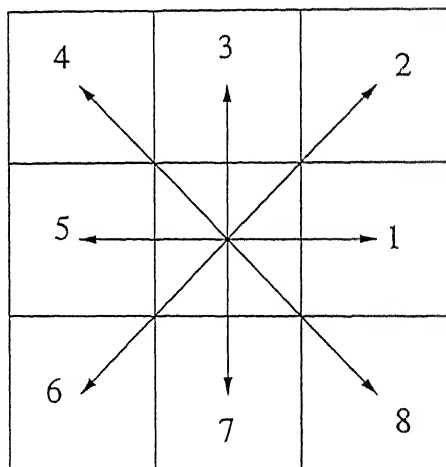


Figure 3.15: Eight Possible Directions for Movement

Any given pixel will be connected to two neighbouring pixels in a thinned image. Hence the past direction of movement has to be preserved to decide the future connecting points. Because of residual noise present in the image, it is likely that a pixel may show two new directions in addition to its last movement. In such a case the sum of intensity which is closer to that of the previous direction is ignored and the other direction is accepted as the direction for the next movement.

The above algorithm can produce loops if precautions are not taken. If a fringe

is in the forward tracing mode and the special turning case is not supplied, the fringe is forced to move in the specified direction of (1,2,3,7 and 8) and not (4,5 and 6), the backward direction (Figure 3.15). Similarly in backward tracing, the direction (1,2 and 8) is not allowed. If one of the directions that is not permissible during forward tracing is encountered as the final direction of movement, a loop-like structure is formed. Tracing may not be completed in some cases. To avoid the formation of loops the nearest forward direction needs to be found iteratively, till one advances to the next pixel. This is accomplished as follows. Once a reverse direction of movement is encountered, the nearest possible direction is adopted in its place. For example, if the direction of movement is 4 while the tracing is in the forward direction, the direction nearest to 4 is 3. Similarly 7 can be replaced by 6. If the direction found is 5, then both 3 and 7 are equally likely. In such a case, the most unbiased estimate to 5 is direction 1.

Reallotment of a direction as described above may result in a wrong movement. For example, the direction of movement identified may be one of the previously detected points on the thinned image. In such a case the above steps are repeated and the next closest direction is searched. If the new pixel located falls in one of the four special cases for turning, the image is rotated by 90° in the clockwise direction. Then depending on one of the four cases, one may have to move temporarily in forward or backward directions. During implementation, the code is prepared in a modular fashion to trace forward and backward fringes. Rotation of the image enables one of the modules to be used without any change in the marked areas of the fringes.

The boundaries of the image, i.e. the window size are to be prescribed as an input to the computer code. On reaching the boundary, control in the computer code is transferred to the starting point so that the rest of the fringe in the opposite direction can be traced.

The algorithm used for fringe tracing is summarized below:

1. Initialize the thinned image as white (intensity 255).
2. Read the image containing the interferogram including the boundary.
3. Read the starting point data for all the fringes to be traced in the image.
4. Specify the desired template size at the starting point.
5. Specify the initial direction of movement to the right or left.

6. Obtain the intensity sums in the eight directions and find the two minima.
7. Start tracing in the direction of the minimum intensity.
8. At the boundary, transfer control to starting point.
9. Start tracing in the opposite direction till the boundary is reached.
10. Assign a gray level of 0 to the traced pixels.
11. Repeat the process for all the fringes.

Interferograms of the Rayleigh-Benard convection at a Rayleigh number of 13900 and from two different view angles of 0° and 90° have been chosen to demonstrate the working of the fringe thinning algorithms. Figure 3.16 shows the thinned image developed using the procedure given above. Figure 3.17 shows the superposition of the fringe skeleton and the interferograms. The agreement can be seen to be satisfactory. The fringe immediately adjacent to the top wall (90°) could not be resolved in the sense that a minimum intensity direction could not be identified in certain parts of the image. This could have been taken care of by manually joining the two halves of the fringe. Instead, to force the worst-case scenario the unresolved fringe has been taken to be lost. As discussed later, this was not seen to introduce errors in the tomographically reconstructed temperature field. A quantitative evaluation of the thinning process is taken up in Appendix A .

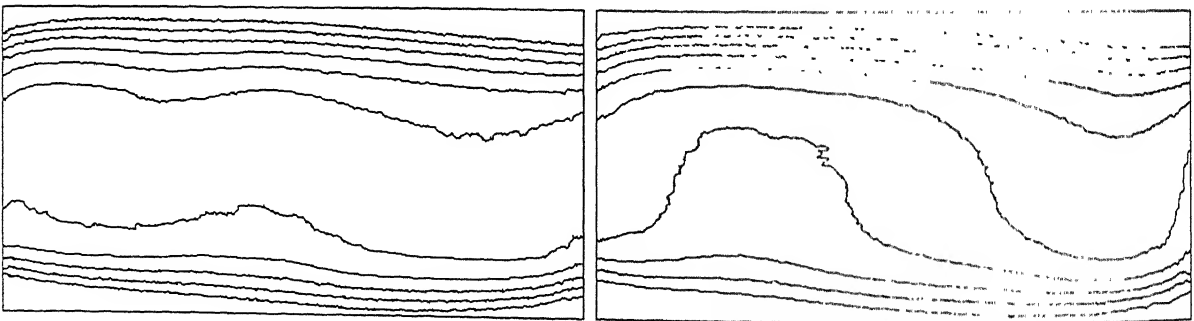


Figure 3.16: Thinned Images, Automatic Fringe Thinning Algorithm

3.2.2 Curve Fitting Approach

In this method, the intensity minima are assumed to coincide with the center of the fringe bands. Specifically, the variations in the gray levels are not made use of. This is

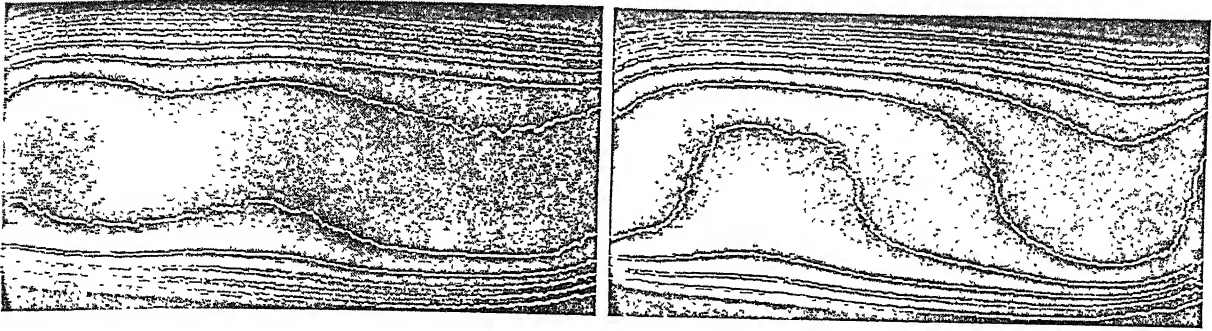


Figure 3.17: Superimposed Thinned Images (Automatic Fringe Thinning Algorithm) with Original Images

equivalent to the classical microscope route of fringe analysis. A few points within each band are collected using a pixel viewing utility. The number of points to be collected over an entire fringe depends on the nature of the function to be fitted through the fringe curve. A greater number of points is chosen in the region of sharp changes in the fringe slope. Relatively fewer points are chosen when the fringe shape varies uniformly or is a constant. In the present work, a cubic spline has been fitted through sets of four points while maintaining slope continuity between adjacent data sets. While this method has the disadvantage of not identifying the minimum intensity location, it does offer certain advantages. These are 1. thinning of all fringes with no loss and 2. smoothness of the fringe skeleton.

Figure 3.18 shows the thinned images obtained using the curve fitting approach corresponding to the thinned images in Figure 3.16. In the interferogram for the 90° projection, an extra fringe can be seen to be captured. This could not be resolved using the automatic fringe thinning approach. Figure 3.19 shows the thinned images superimposed with the original interferograms. The match is again seen to be good.

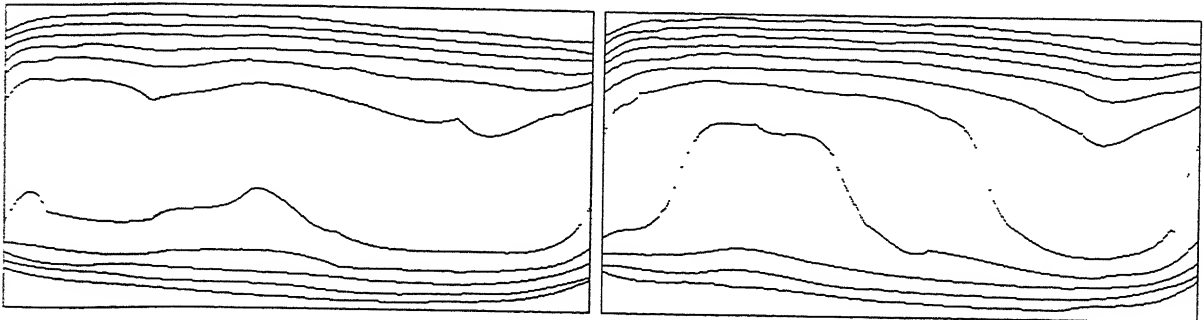


Figure 3.18: Thinned Images, Curve Fitting Method for Fringe Thinning

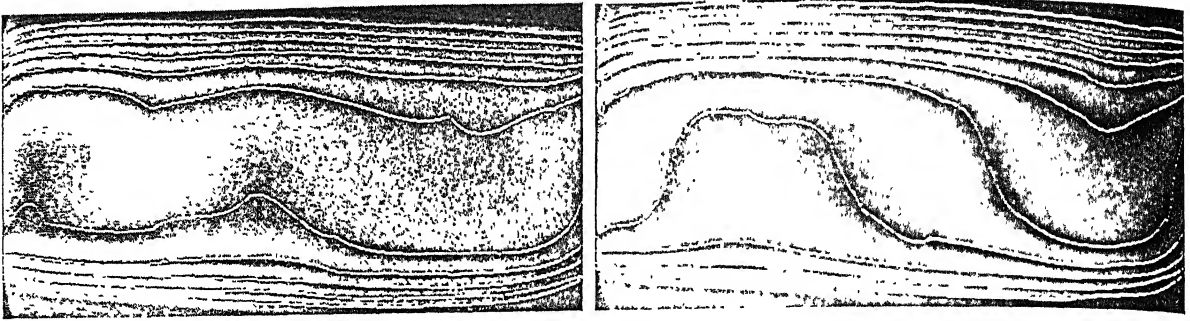


Figure 3.19: Superimposed Thinned Images (Curve fitting method) with Original Images

3.2.3 Paint-brush Drawing

This is a free-hand drawing technique where the midpoints within a dark band of the interferogram are approximately located and joined by a smooth curve. It relies exclusively on eye judgement. The paint-brush utility of the Windows-95 operating system has been employed in this study. The image containing the fringe curves and the original image are subtracted to get the fringe skeleton. Figure 3.20 shows the thinned images corresponding to the thinned images shown in Figure 3.16. Using the manual, user-interactive approach, the 90° projection has an extra fringe over the image generated by the automatic thinning method (Figure 3.16). The superposition of the original interferogram and the fringe skeleton is shown in Figure 3.21. The paint-brush approach has the disadvantage of not locating the minimum intensity location, but can be advantageous under certain conditions. It does not require code development and hence is reasonably fast.

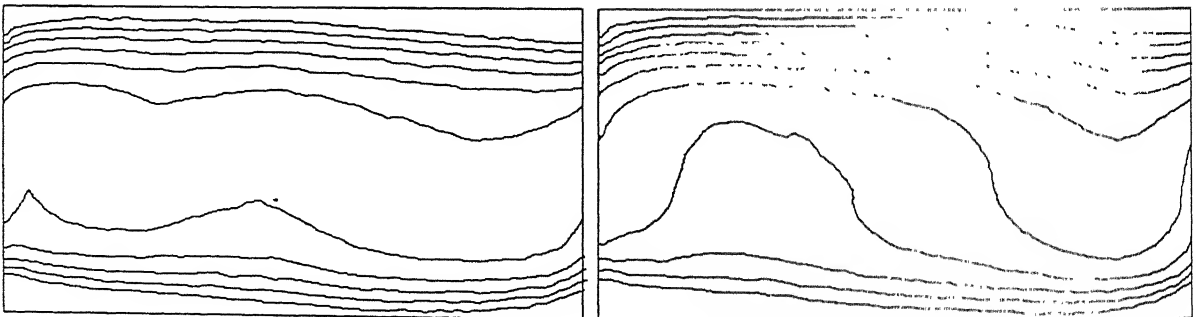


Figure 3.20: Thinned Images, Paint-brush Drawing Method for Fringe Thinning

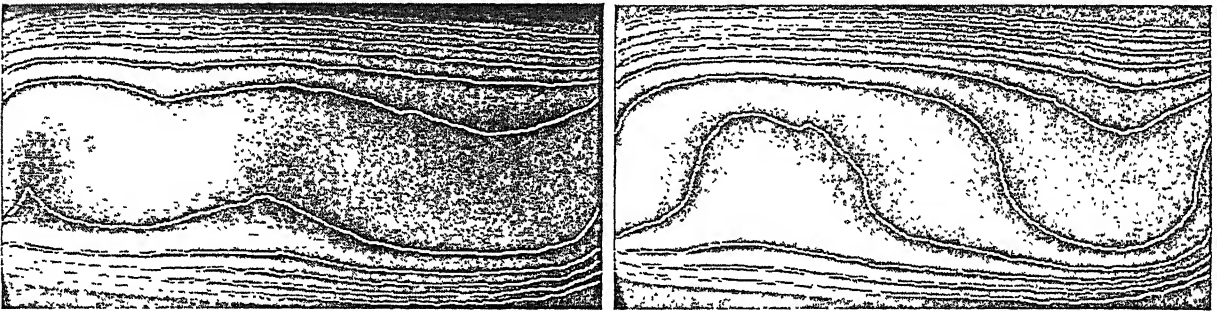


Figure 3.21: Superimposed Thinned Images (Paint-brush method) with Original Images

Chapter 4

Interferometry and Evaluation of Interferograms

Principles of interferometry and the evaluation of interferograms for the determination of fringe temperature are discussed in the present chapter. The concepts of interferometry with reference to temperature field in the infinite fringe setting of a Mach-Zehnder interferometer have been discussed. The fringes in the interferograms have been identified as isotherms or isofunctions in the more general context. The methodology adopted to calculate the fringe temperature and the transfer of data to a two dimensional grid through interpolation have been discussed.

4.1 Interferometry

In the infinite fringe setting, the optical path difference between the test and the reference beam is zero in the absence of any thermal disturbance. Hence interference is constructive and a bright field-of-view is obtained. The image obtained is practically fringe-free (Figure 2.4) but may show imperfections associated with the spatial filter and the interferometer optics in the form of a broad fringe. When nonisothermal conditions prevail in the path of the test beam (example a candle flame) each ray of light undergoes a change of phase, depending on the extent of change of the refractive index of the medium. Hence an optical path difference is established between the test and the reference beams, resulting in a fringe pattern (Figure 2.5). In the wedge fringe setting, the optical components

(primarily BS2, in Figure 2.3) are deliberately misaligned to produce a set of line fringes of any convenient spacing (Figure 2.6). In the presence of a thermal disturbance the fringes would be displaced towards regions of higher temperatures, thus producing a fringe pattern that resembles the temperature profile itself (Figure 2.7).

In the present work, attention is restricted to image patterns that form in the infinite fringe setting. Here, the test beam records information about the variation of the refractive index of the fluid. To make temperature measurement possible, the refractive index variation must be related to that of temperature. The relationship between the refractive index n and temperature T is established as follows. For gases, the relationship

$$\frac{n - 1}{\rho} = \text{constant} \quad (4.1)$$

called the Gladstone-Dale equation holds, where ρ is density (Goldstein, 1983). Hence $dn/d\rho = \text{constants}$. For moderate changes in temperature, typically ≤ 20 K and nearly uniform bulk pressure, density varies linearly with temperature as

$$\rho = \rho_0(1 - \beta(T - T_0)) \quad (4.2)$$

It follows that dn/dT is also a constant, being purely a material property. Hence changes in temperature simultaneously result in changes in refractive index and from principles of wave optics, lead to changes in the phase of the wave. This is the origin of fringe formation in interferometric images.

If temperature differences within the physical region being studied are large, two factors arise which limits the usefulness of interferometry. These are: (1) the linearity of relationship between density and temperature and (2) beam deflection due to a refractive index gradient. These factors complicate the data reduction process and make interferometry more of a qualitative tool. However, fringes continue to form and images can be used for flow visualization. In the present study, temperature differences between the test section and the ambient are small and the linear relation between refractive index and temperature has been taken to be valid.

Let $n(x, y)$ and $T(x, y)$ be the refractive index and temperature fields respectively in the physical domain being studied in a two dimensional horizontal plane. A three dimensional region can be visualized as a collection of two dimensional horizontal planes. Let n_0 and T_0 be the reference values of n and T respectively as encountered by the

reference beam. Let L be the total geometric path length covered by the test and reference beams. The interferogram is a fringe pattern arising from the optical path difference

$$\Delta PL = \int_0^L (n(x, y) - n_0) ds \quad (4.3)$$

which in terms of temperature is

$$\Delta PL = \frac{dn}{dT} \int_0^L (T(x, y) - T_0) ds \quad (4.4)$$

The integral is evaluated along the path of a light ray given by the coordinate s . Neglecting refraction effects, this path will be a straight line and the integral evaluation is greatly simplified. The fringes seen on the interferograms are locus of points having the same optical path difference. Hence on any given fringe the optical path difference ΔPL is a constant and

$$\int_0^L (T(x, y) - T_0) ds = \frac{\Delta PL}{dn/dT} = \text{constant}$$

Hence

$$\int_0^L T(x, y) ds - T_0 L = \text{constant}$$

The integral $\int_0^L T(x, y) ds$ is defined as $\bar{T}L$, where \bar{T} is the average value of $T(x, y)$ over the length L of the laser beam through the test cell. This is also the line integral of the function $T(x, y)$. Hence

$$L(\bar{T} - T_0) = \text{constant} \quad (4.5)$$

In the infinite fringe setting Equation 4.5 holds good for all fringes. When L is constant for all the rays, Equation 4.5 implies that \bar{T} is a constant over the fringe and hence each fringe represents a locus of points over which the the average of the temperature field along the direction of the ray is a constant, hence fringes are isotherms.

Consider a geometry where the length of the ray through the test cell changes for each ray. The line integral of the function $T(x, y)$ ($= \bar{T}_2$) at a location which corresponds to a length L_2 can be given in terms of the line integral of the function $T(x, y)$ ($= \bar{T}_1$) at some other location corresponding to a ray length of L_1 as

$$\bar{T}_2 = T_0 + \frac{L_1}{L_2} (\bar{T}_1 - T_0) \quad (4.6)$$

Since the change in path length per fringe shift is a constant, the temperature drop per fringe shift is also a constant. Defining the function $L(\bar{T} - T_0)$ in Equation 4.5 as $f(\bar{T}, L)$, the fringe temperature on two successive fringes for same value of L can be given as;

$$\begin{aligned} \text{fringe 1: } f_1(\bar{T}, L) &= \frac{\Delta PL}{dn/d\bar{T}} \\ \text{fringe 2: } f_2(\bar{T}, L) &= \frac{(\lambda + \Delta PL)}{dn/d\bar{T}} \end{aligned}$$

where λ is the wavelength of the laser used. From these two equations, the temperature drop per fringe shift can be calculated as

$$\Delta T_\epsilon = \frac{1}{L} (f_2(\bar{T}, L) - f_1(\bar{T}, L)) = \frac{\lambda/L}{dn/d\bar{T}} \quad (4.7)$$

The interferograms reflect the equation

$$\Delta PL = \frac{dn}{dt} \int_0^L (T - T_0) ds$$

and hence the line integral of the temperature field. The set of all line integrals (an interferogram, in the present study) defines a projection of the temperature field. The interferograms can be numerically processed so that the left side of the above equation is a known quantity. The mathematical problem now is one of solving the temperature field from its projections. If the original field is three dimensional, its projection is a field in a dimension reduced by unity, i.e., two for the present case. It is theoretically possible to record a large number of projections of the test field at various angles and reconstruct the original temperature function with accuracy. This process of three dimensional reconstruction from two dimensional projections is called tomography and discussed in Chapter 5 of this thesis.

The above derivation of temperature difference between successive fringes will be modified in the presence of a strongly refracting field. In the present context a strongly refracting field will arise when a large transverse temperature gradient is present. The light ray will not travel in a single horizontal plane, and depending on the sign of the temperature gradient, the ray will bend in the vertical plane owing to refraction effects. Refraction, thus will introduce an additional optical path length to the test beam. Refraction effects can be precisely computed and accounted for. The extent of refraction determines the type of the three dimensional reconstruction algorithm that can be used in a particular experiment. In the present work, refraction errors were found to be negligible and hence a sequential plane-by-plane reconstruction approach was adopted.

An estimate of the increase in path length due to refraction is developed here. Consider the path of the light ray AB through a test cell (Figure 4.2) when it is affected by the refraction effects. Let α be the bending angle at a location P of the test cell. The optical path length from A to B is given by;

$$\begin{aligned} AB &= \int_0^L n(x, y, z) ds \\ &= \int_0^L n(x, y, z) \frac{dz}{\cos \alpha} \end{aligned}$$

Here y is a coordinate parallel to the gravity vector and z is parallel to the direction of propagation of light. Assuming α is small, $\cos \alpha$ can be expressed as,

$$\cos \alpha = (1 - \alpha^2)^{1/2}$$

using first two terms of the binomial expansion

$$\cos \alpha \approx 1 - \frac{\alpha^2}{2}$$

Hence the optical path length is given by

$$AB = \int_0^L n(x, y, z) \left(1 - \frac{\alpha^2}{2}\right)^{-1} dz \quad (4.8)$$

$$= \int_0^L n(x, y, z) \left(1 + \frac{\alpha^2}{2}\right) dz \quad (4.9)$$

The angle $\alpha(z)$ at any location z can be calculated as described below.

Consider Figure 4.1 where two wave fronts are at time τ and $\tau + \Delta\tau$ is shown. At time τ the ray is at a position z . After a time interval of $\Delta\tau$, the light has moved a distance of Δz . Hence

$$\Delta z = \Delta\tau \frac{c_0}{n}$$

where c_0 is the velocity of light in vacuum. There is a gradient in n along the y direction. The gradient in n results in a bending of the wave front due to refraction. The distance $\Delta^2 z$ is given by,

$$\Delta^2 z = \Delta z_y - \Delta z_{y+\Delta y}$$

$$\begin{aligned}
&\approx \Delta z_y - \Delta z_y + \frac{\Delta}{\Delta y} (\Delta z) \Delta y, \\
&= -c_0 \frac{\Delta 1/n(x, y, z)}{\Delta y} \Delta \tau \Delta y
\end{aligned}$$

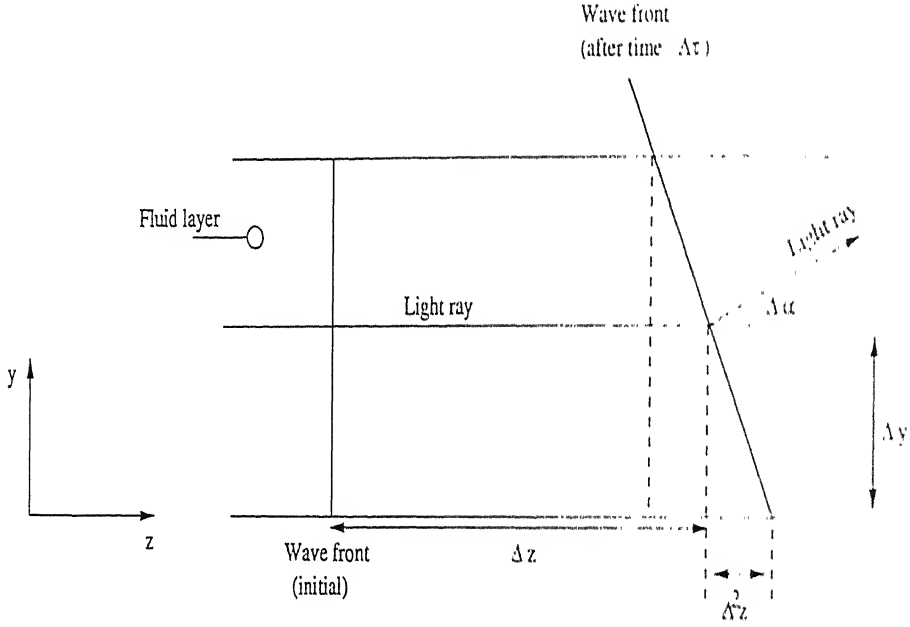


Figure 4.1: Calculation of Bending Angle of Light Ray due to Refraction effects

Let $\Delta\alpha$ represent the bending angle at a fixed location z . For a small increment in the angle, $\Delta\alpha$ can be expressed as

$$\begin{aligned}
\Delta\alpha &= \tan(\Delta\alpha) = \frac{\Delta^2 z}{\Delta y} \\
&= -c_0 \frac{\Delta 1/n(x, y, z)}{\Delta y} \Delta \tau \\
&= -n(x, y, z) \Delta z \frac{\Delta 1/n(x, y, z)}{\Delta y}
\end{aligned} \tag{4.10}$$

In the limiting case,

$$d\alpha = \frac{1}{n(x, y, z)} \frac{\partial n(x, y, z)}{\partial y} dz \tag{4.11}$$

Hence the cumulative bending angle at any location along the z axis is

$$\alpha(z) = \int_0^z \frac{1}{n(x, y, z)} \frac{\partial n(x, y, z)}{\partial y} dz$$

$$= \frac{1}{\bar{n}(x, y, z)} \frac{\partial \bar{n}(x, y, z)}{\partial y} z$$

where $1/\bar{n}(x, y, z)$ and $\partial \bar{n}(x, y, z)/\partial y$ is the average line integral along the path of the ray over a distance 0 to z .

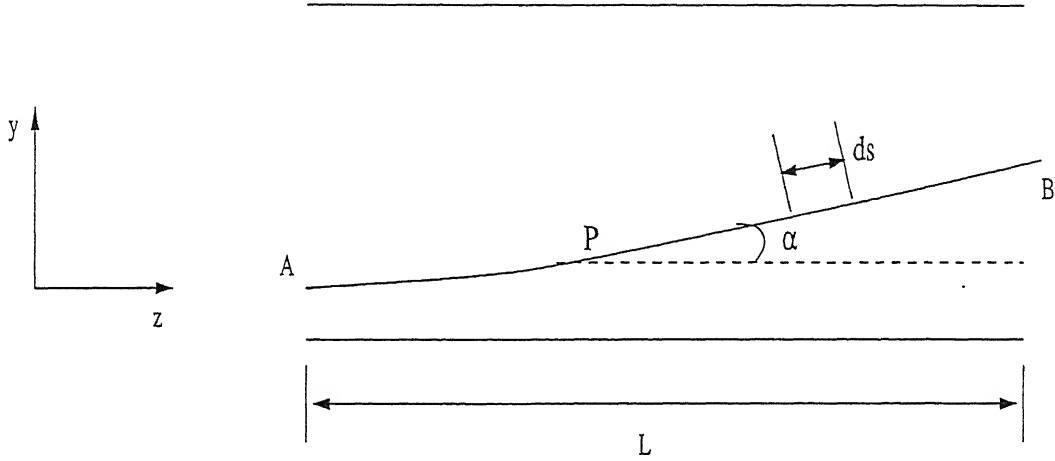


Figure 4.2: Bending of Light Ray in the Fluid Medium due to Refraction Effects

From Equation 4.9

$$\begin{aligned} AB &= \int_0^L n(x, y, z) \left(1 + \frac{1}{2} \frac{1}{\bar{n}^2} \left(\frac{\partial \bar{n}}{\partial y} \right)^2 z^2 \right) dz \\ &= \bar{n}(x, y, z) L + \frac{1}{6 \bar{n}(x, y, z)} \left(\frac{\partial \bar{n}}{\partial y} \right)^2 L^3 \end{aligned}$$

where $\bar{n}(x, y, z)$ is the average line integral of $n(x, y, z)$ over the complete length L . Similarly the expressions $1/6\bar{n}$ and $\partial \bar{n}/\partial y$ represent average line integrals over the length L .

The optical path of the reference beam is simply,

$$\text{Reference path} = \int_0^L n_0 dz = n_0 L \quad (4.12)$$

Hence the difference in the optical path length in the presence of refraction effects is

$$\Delta PL = \bar{n}(x, y, z) L + \frac{1}{6 \bar{n}(x, y, z)} \left(\frac{\partial \bar{n}}{\partial y} \right)^2 L^3 - n_0 L$$

$$\begin{aligned}
&= (\bar{n}(x, y, z) - n_0)L + \frac{1}{\bar{n}(x, y, z)} \left(\frac{\partial n}{\partial y} \right)^2 L^3 \\
&= (\bar{T}_1(x, y, z) - T_0)L \frac{dn}{dT} + \frac{1}{\bar{n}(x, y, z)} \left(\frac{\partial n}{\partial y} \right)^2 L^3
\end{aligned}$$

where $\bar{T}_1(x, y, z)$ represents the average line integral of the temperature field along the direction of the ray at a given point on the fringe. The corresponding ray over the next fringe corresponds to an additional path of λ . Hence this can be written as

$$\Delta PL + \lambda = (\bar{T}_2(x, y, z) - T_0)L \frac{dn}{dT} + \frac{1}{\bar{n}(x, y, z)} \left(\frac{\partial n}{\partial y} \right)^2 L^3$$

where $\bar{T}_2(x, y, z)$ represents the average line integral of the temperature field along the direction of the ray at a point on the next fringe. The successive temperature difference between two fringes is

$$\lambda = (\bar{T}_2(x, y, z) - \bar{T}_1(x, y, z))L \frac{dn}{dT} + \frac{1}{\bar{n}(x, y, z)} \left(\frac{dn}{dT} \right)^2 \left(\left(\frac{\partial T}{\partial y} \right)_2^2 - \left(\frac{\partial T}{\partial y} \right)_1^2 \right) L^3 \quad (4.13)$$

and the temperature drop per fringe shift is

$$\Delta T_\epsilon = \frac{\lambda - \frac{1}{\bar{n}(x, y, z)} \left(\frac{dn}{dT} \right)^2 \left(\left(\frac{\partial T}{\partial y} \right)_2^2 - \left(\frac{\partial T}{\partial y} \right)_1^2 \right) L^3}{L \frac{dn}{dT}} \quad (4.14)$$

Since the gradient in the temperature field is not known before the calculation of the fringe temperature the factor $\left(\frac{\partial T}{\partial y} \right)_2 - \left(\frac{\partial T}{\partial y} \right)_1$ must be calculated from a guessed temperature field. Thus, the final calculation of ΔT_ϵ relies on a series of iterative steps with improved estimates of the temperature gradients.

The refraction errors in the present set of experiments can be shown to be quite small. As a conservative estimate, the temperature gradient term can be replaced by its value at the wall. This would give an upper bound on the refraction error. The following numerical values have been used: $\lambda = 632.8$ nm, $L = 0.5$ m (that is the dimension of the test cell in the present study), dn/dT for air at 20°C and 1 bar is -0.927×10^{-6} (°C)⁻¹ and refractive index of air at 20°C as 1.0. The contribution of the refractive index term in Equation 4.13 can be evaluated as 2.617×10^{-8} m. This value is small as compared to the wavelength ($=6328 \times 10^{-8}$ m).

The number of fringes expected in a projection can be estimated directly from the relation,

$$\text{Number of fringes} = \frac{T_{hot} - T_{cold}}{\Delta T_\epsilon}$$

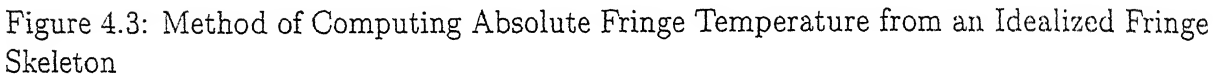
This number when calculated without considering the refraction effect was seen to be satisfied in all the experiments reported in the work. This also indicates that refraction errors in the present work are negligible.

4.2 Evaluation of Interferograms

The thinned fringes carry essentially the information of the path integrated temperature field. Hence, to extract temperature profiles and heat transfer rates from the interferogram, the fringe skeleton rather than the fringe bands is needed. In the context of three dimensional reconstruction of the temperature field, the line integral of the temperature field is required over a uniform grid so that tomographic algorithms can be applied. Consequently the calculation of temperature associated with the fringes is the most important step in interferometry. The methodology adopted for the calculation of fringe temperature is presented in this section. The technique has been discussed in the context of Rayleigh-Benard experiment.

For definiteness, consider the fringe skeleton as shown in Figure 4.3. The upper and lower walls as shown in the figure have known temperatures. It is possible that high temperature gradients near the wall produce a large number of thin fringes. Hence during the recording and processing of the interferogram a few near wall fringes could be lost. The loss of near wall fringes could be due to the finite resolution of the CCD camera, and loss of signal information during filtering and other image processing operations. The first fringe seen in a thinned interferogram near the wall will thus be of arbitrary order. One cannot assign a temperature to the fringes directly from the wall temperature by using Equation 4.7 though the wall itself is an isotherm. Even when no near-wall fringe is lost, assigning a temperature to the first fringe is not straight-forward since the wall (though an isotherm) need not be a fringe, i.e. a site for destructive interference. The following procedure has been adopted in the present work to derive temperature values at the fringes.

Two regions on the interferograms were selected, one where the fringes are close to the cold wall (marked I in Figure 4.3) and the other where the fringes are close to the hot wall (marked II in Figure 4.3). Two sets of independent calculations were performed to obtain all the fringe temperatures in the interferogram. The estimates of fringe tem-


$$T(y) = a + by + cy^2 \quad (4.15)$$
$$\Delta T_\epsilon = T_2 - T_3 = b(y_2 - y_3) + c(y_2^2 - y_3^2) \quad (4.16)$$

$$\Delta T_\epsilon = T_3 - T_4 = b(y_3 - y_4) + c(y_3^2 - y_4^2) \quad (4.17)$$

The local wall temperature gradient is simply $(\partial T / \partial y)_{y=y_1}$. From equation 4.15, this gradient can be expressed as $(b + 2cy_1)$. The gradient in the temperature field very near the wall is likely to be constant since conduction heat transfer is dominant. Hence the gradient in temperature field at the first fringe (fringe marked 2 in Figure 4.3) is expected to be same as the gradient at the wall in region I. The gradient in temperature field at

the first fringe is $(b + 2cy_2)$. The wall temperature gradient is allotted as an extrapolation step, the average of the two gradients. Once the gradient at the wall is known, the first fringe temperature near the cold wall can be calculated as

$$T_2 = (y_2 - y_1) \frac{(b + 2cy_1) + (b + 2cy_2)}{0.5} + T_1 \quad (4.18)$$

Since ΔT_ϵ , the temperature difference between successive fringes is known, the subsequent fringe temperatures are found out simply adding or subtracting the amount from the first fringe temperature depending upon the sign of the temperature gradient. Since the image is available in the form of a matrix, the above procedure for calculating the fringe temperature can be implemented at any column. The column where the near-wall fringes are dense (as in regions I and II) is preferred for this purpose. Column-to-column variation in the computed fringe temperatures was found to be generally small for the interferograms recorded in the experiments.

4.3 Temperature Data over a Grid by Interpolation

Once the absolute fringe temperatures are obtained, this data must be transferred to a two dimensional uniform grid over the fluid region. This is required to apply tomographic algorithms for the reconstruction of three dimensional temperature field. The data transfer is achieved by interpolation as described below. The 9 different points where the fringes intersects the column (Figure 4.4) are first mapped to a uniform rectangular grid using a quadratic polynomial as a basis. Temperature at any point (such as P, Figure 4.4) can be computed by using quadratic interpolation again (Lapidus and Pinder, 1982). Interpolation using a higher order scheme, even with quadratic basis produces oscillations in the interpolated data. The interpolated value in the interior may exceed the values at boundary points and is undesirable. Though rare, this may occur when the data spacing is large. In the present study, such overshoot and undershoot have been taken care of by using universal limiters (Leonard and Niknafs, 1991). The limiter used is one dimensional in the sense that it is applied only along the vertical direction. Once the interpolated value at a point on the superimposed grid is obtained, its value is compared with the two nearest vertically separated fringes. If the interpolated temperature is outside the range of the two fringe temperatures, the limiter is switched on to force the interpolated value to be one of the temperatures closest to the interpolated value. Interpolation errors in the present work was found to be negligible ($< 0.1\%$).

The collection of thinned images from the Rayleigh-Benard experiment at a 90° projection angle is shown in Figure 4.5. Interpolation has been carried over the entire image by superimposing a two dimensional grid on it. The grid has 120 points along the horizontal and 21 points along the vertical direction. Once the interpolation is complete isotherms have been drawn to represent the fringes in the original image. This is shown in Figure 4.6. It can be seen here that the temperature data on the grid follows closely the pattern of the original thinned image and interpolation errors are negligible. The isotherms based on the interpolated grid data is seen to capture as well the lost fringe in the interferogram. Hence the isotherms in Figure 4.6 show all the fringes with continuity throughout the width of the cavity.

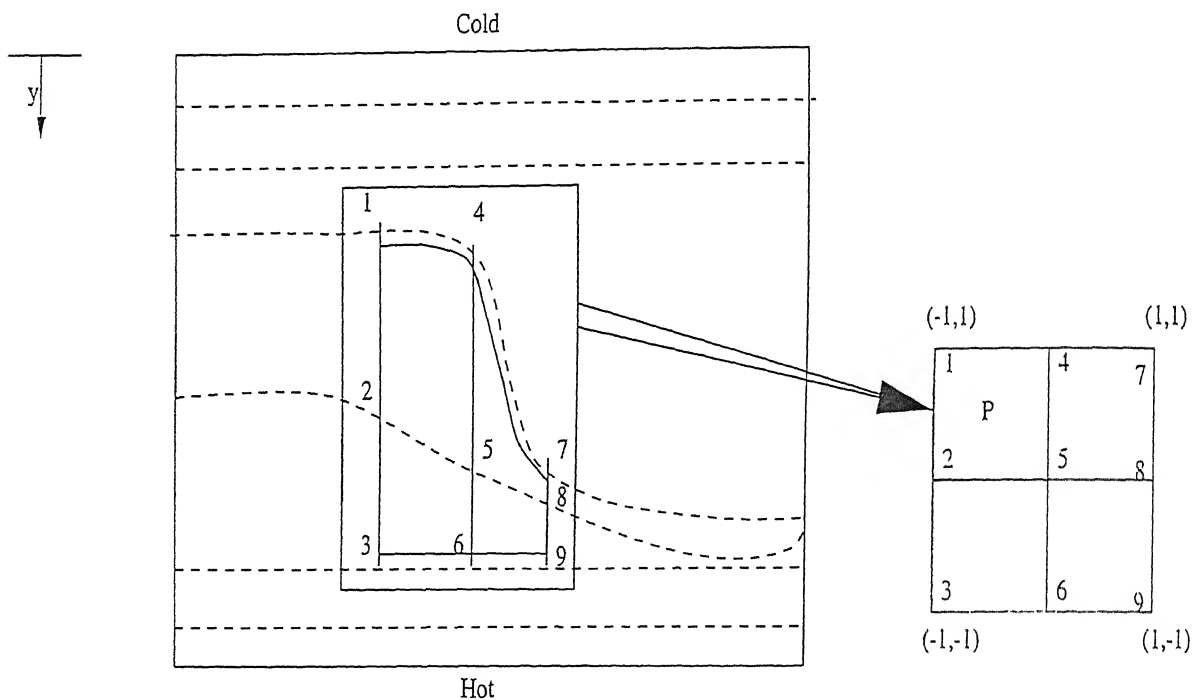


Figure 4.4: Data Transfer to a 2 Dimensional Grid for the Idealized Fringe Pattern

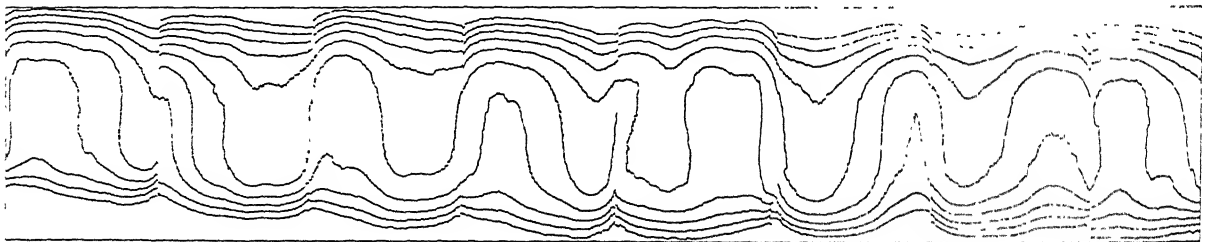


Figure 4.5: Collection of Thinned Images, $Ra=13900$

The correctness of fringe thinning, assigning fringe temperatures and a check on

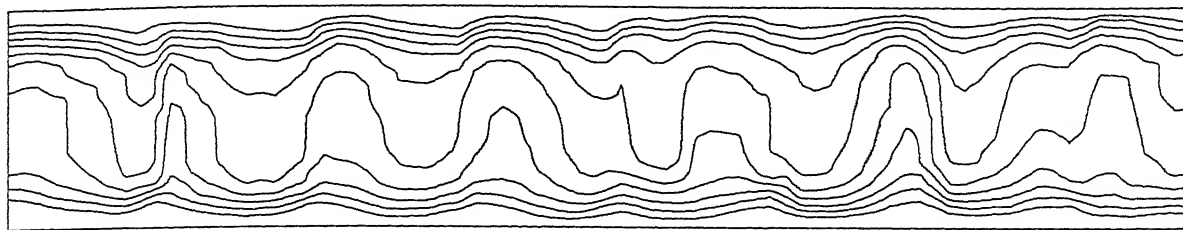


Figure 4.6: Isotherms Obtained from Interpolated Temperature Data, $Ra=13900$

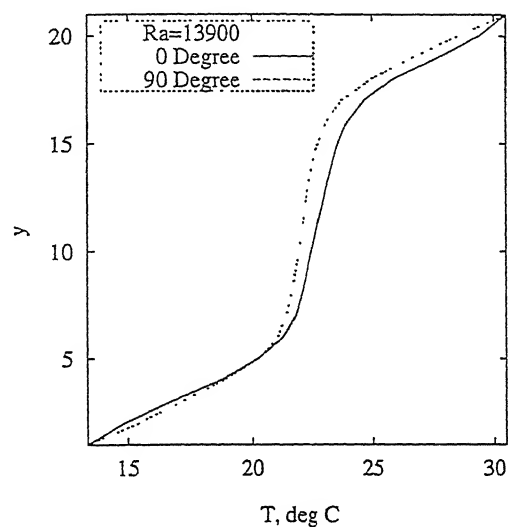


Figure 4.7: Width-averaged Temperature Profile from the Interferograms, $Ra=13900$

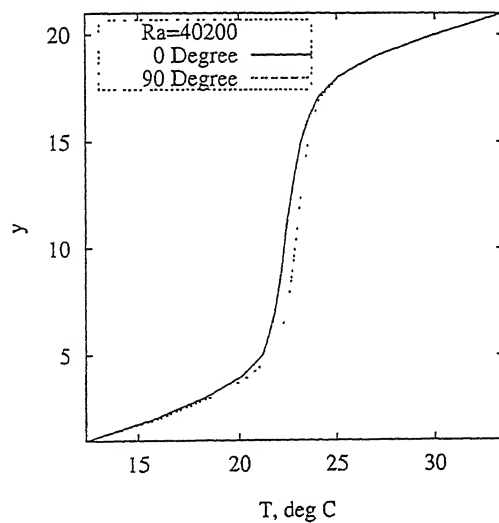


Figure 4.8: Width-averaged Temperature Profile from the Interferograms, $Ra=40200$

the magnitude of interpolation errors have been examined by using the following result: At steady state, the width-average of the line integrals of temperature field plotted as a function of the vertical coordinate is independent of the projection angle. This is because the total energy transferred across the cavity is unchanged from one horizontal plane to the next. Figure 4.7 shows the variation of line integrals of the temperature field averaged over a horizontal plane as a function of the vertical coordinate. The line integrals are simply the temperature as computed from the interferograms. The y coordinate is measured from the cold top wall. Both 0 and 90° projections have been shown and Rayleigh number is 13900. The corresponding graph for $Ra=40200$ is shown in Figure 4.8. The S-shaped curve, characteristic of buoyancy-driven convection can be seen in all the figures. The curves for the two projections match closely and their slopes at the hot and cold walls are practically equal. The S-shaped curve for the angular projections have not been shown since the corresponding projection data does not span the entire width of the test cell. This point is discussed in Chapter 6. Temperatures in the 0 and 90° data have been subsequently corrected to ensure that between the two projections, the S-shaped curve is strictly unique. This step did not alter the isotherms in the projection data to any significant degree, but was expected to improve performance of the tomographic inversion process.

Chapter 5

Tomographic Reconstruction of the Temperature Field

The three dimensional temperature field can be reconstructed from its interferometric projections using principles of tomography. Tomography is the process of recovery of a function from a set of its line integrals evaluated along some well-defined directions. In interferometry, the source of light and the detector (CCD camera) lie on a straight line, and a parallel beam of light is used. This configuration is called *transmission* tomography in a parallel beam geometry (Herman, 1980). Tomographic algorithms used in interferometry reconstruct two dimensional fields from their one dimensional projections. As discussed in Chapter 4, this is permissible when refraction errors are small. Reconstruction is then applied sequentially from one plane to the next till the third dimension is filled.

Tomography can be classified into: (a) transform (b) series expansion and (c) optimization methods. Transform methods generally require a large number of projections for a meaningful answer (Lewitt, 1983). In practice, projections can be recorded either by rotating the experimental set up or the source-detector combination. In interferometry, the latter is particularly difficult and more so with the Mach-Zehnder configuration. With the first option, it is not possible to record a large number of projections, partly owing to inconvenience and partly due to time and cost. Hence, as a rule, requiring a large number of projections is not desirable with interferometry and one must look for methods that converge with just a few projections. Limited-view tomography is best accomplished using the series expansion method (Censor, 1983). As limited data tomography does not have a unique solution, the algorithms are expected to be sensitive to the initial guess of

The problem of reconstruction thus is a problem of inversion of a rectangular matrix. Iterative techniques that are used in the tomography can be viewed as developing a generalized inverse of the matrix $[w_{ij}]$. This matrix in a typical laser tomography problem has large dimensions. For the problem under study, the greatest matrix size encountered was 560×14400 . This is a sparse matrix with many of its element being zero. General purpose matrix libraries cannot be used to invert such matrices since they are highly ill-conditioned and rectangular in structure. The tomographic algorithms can be seen as a systematic route towards a meaningful inversion of the matrix equation 5.2.

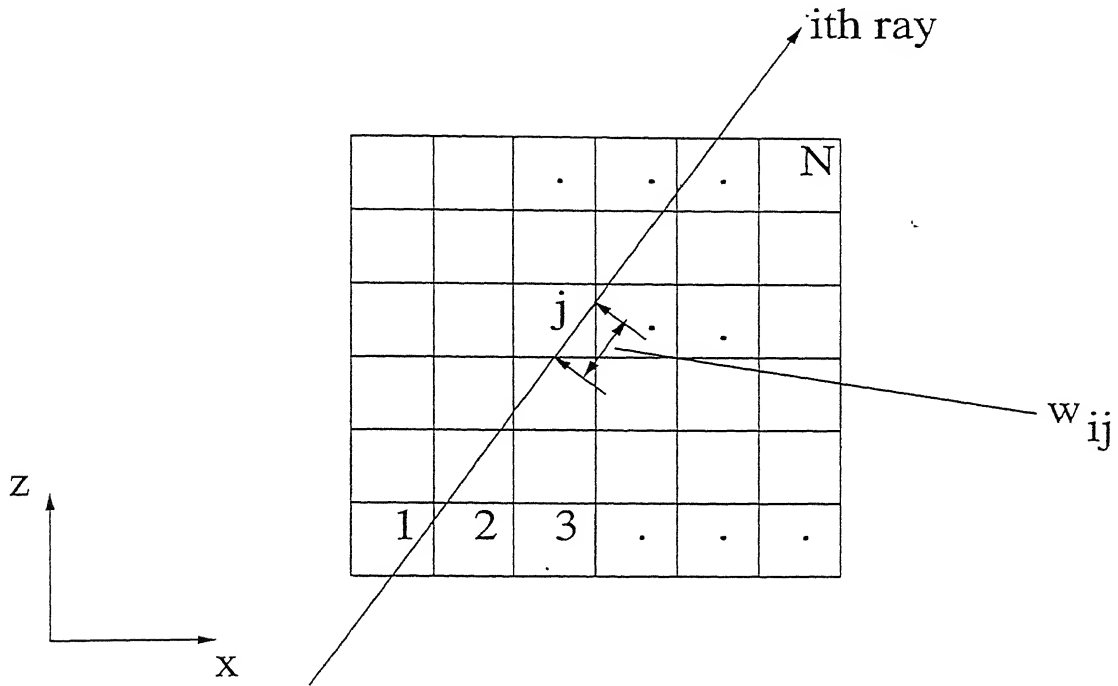


Figure 5.1: Discretization of a Horizontal Plane of the Fluid Layer

Series expansion methods being discussed in the present chapter can be classified into: ART (Algebraic Reconstruction Technique) and MART (Multiplicative Algebraic Reconstruction Technique). The optimization techniques for reconstruction are discussed with reference to maximization of the entropy and minimization of the energy functions.

Algebraic techniques are frequently used tomographic algorithms concerning problems where the projection data is limited. The procedure of the algorithms differs only in two ways: (1) the method of updating the field parameters in each iteration and (2) the sequence of operations. The most general procedure is based on the comparison of the estimated projection from an initial guess with the measured projection data obtained

through experiments. This gives a correction term for the field variables. The value of the field variables are then updated. Once an iteration is over, the field value obtained differs from the measured projection values. The extent of the difference is then calculated. If the difference is within acceptable limits of the prescribed convergence criteria, the field value taken at that stage to represent the reconstructed field. Otherwise the iterations continue till the convergence criteria are satisfied. Since the original field is unknown, an estimate of the number of iterations is found by using test functions that are similar in nature to the original field. The test functions are also perturbed with noise to gauge the sensitivity of the algorithms to issues such as initial guess and errors in the projection data. This method can only be adopted where an exact estimate of noise in the projection data and a good knowledge of the original field is known beforehand. Slight variations in the noise level and nature of distribution of the noise in the projection data can alter the convergence rates.

Tomographic algorithms used in the present work are iterative in nature and intermediate steps may also involve iterations in the form of FOR loops. To identify the beginning and the ending of each iterative loop, start and close labels with statement numbers have been indicated in the description of each algorithm. These algorithms are briefly surveyed in the following sections.

5.1 ART

Various ART algorithms are available in the literature owing to their origin from Kaczmarz (1937) and Tanabe (1971). They differ from each other in the way the correction is applied. Those presented below have been tested successfully in the context of interferometry.

5.1.1 Simple ART

Mayinger (1994) has suggested this algorithm. The corrections are applied through a weight factor, computed as an average correction along a ray. The comparison of the calculated projections with the measured projection data gives the total correction to be applied for a particular ray. The average correction is the contribution to each cells falling in the path of the ray. This is computed by dividing the total correction obtained

with the length of the ray. The calculated projections are computed once for a particular angle, and though the field values continuously updated the calculated projections remains unchanged till the completion of all the rays for a given angle. This algorithm will be referred to as ART1 in future discussions.

Let $\phi_{i\theta}$ be the projection due to the i th ray in the θ direction of projection and \tilde{f}_i be the initial guess of the field value. Numerically the projection $\tilde{\phi}_{i\theta}$ using the current field value is defined as:

$$\tilde{\phi}_{i\theta} = \sum_{j=1}^N w_{i\theta,j} f_j \quad i\theta = 1, 2, \dots, M_\theta \quad (5.3)$$

Calculate the total value of weight function ($W_{i\theta}$) along each ray as:

start: 1 For each projection angle (θ):

start: 2 For each ray ($i\theta$):

start: 3 For each cell (j):

$$W_{i\theta} = \sum_{j=1}^N w_{i\theta,j}$$

close: 3

close: 2

close: 1

start: 4 Start iterations (k):

start: 5 For each projection angle (θ):

start: 6 For each ray ($i\theta$):

Compute the numerical projection (Equation 5.3)

close: 6

start: 7 For each ray ($i\theta$):

Calculate the correction as:

$$\Delta\phi_{i\theta} = \phi_{i\theta} - \tilde{\phi}_{i\theta}$$

Calculate the average value of correction as:

$$\overline{\Delta\phi_{i\theta}} = \frac{\Delta\phi_{i\theta}}{W_{i\theta}}$$

close: 7

start: 8 For each ray ($i\theta$):

start: 9 For each cell (j):

If $w_{i\theta,j}$ is non-zero then:

$$f_j^{new} = f_j^{old} + \mu \overline{\Delta\phi_{i\theta}}$$

where μ is a relaxation factor.

close: 9

close: 8

close: 5

Check for convergence as:

If

$$\text{abs}[\frac{f^{k+1} - f^k}{f^{k+1}}] \times 100 \leq e]$$

(where e is the prescribed convergence criteria, say 0.01%)

STOP:

Else: Continue

close: 4(k)

5.1.2 Gordon ART

The ART algorithm contributed by Gordon *et al.* (1970) is considered. Mayinger's ART (Section 5.1.1) is similar to this original version under the condition that no two rays simultaneously pass through a particular cell for a given projection. In this method corrections are applied to all the cells through which the i th ray passes, using the weight factor which is exactly the proportion of w_{ij} to the total length of the ray. The calculated projections gets updated after calculations through each ray. This will be referred to as ART2.

Calculate the total value of weight function ($W_{i\theta}$) along each ray as:

start: 1 For each projection angle (θ):

start: 2 For each ray ($i\theta$):

start: 3 For each cell (j):

$$W_{i\theta} = \sum_{j=1}^N w_{i\theta,j} \times w_{i\theta,j}$$

close: 3

close: 2

close: 1

start: 4 Start iterations (k):

start: 5 For each projection angle (θ):

start: 6 For each ray ($i\theta$):

Compute the numerical projection (Equation 5.3)

Calculate the correction as:

$$\Delta\phi_{i\theta} = \phi_{i\theta} - \tilde{\phi}_{i\theta}$$

start: 7 For each cell (j):

If $w_{i\theta,j}$ is non-zero then:

$$f_j^{new} = f_j^{old} + \mu \frac{\Delta\phi_{i\theta} \times w_{i\theta,j}}{W_{i\theta}}$$

where μ is a relaxation factor.

close: 7

close: 6

close: 5

Check for convergence as:

If

$$\text{abs}\left[\frac{f^{k+1} - f^k}{f^{k+1}}\right] \times 100 \leq e$$

STOP:

Else: Continue

close: 4

5.1.3 Gilbert ART

Gilbert (1972) has developed independently a form of ART known as SIRT (Simultaneous Iterative Reconstruction Algorithm). In SIRT, the elements of the field function are modified after all the correction values corresponding to individual pixels have been calculated. This will be referred to as ART3. The numerically generated projections are computed once for all the angles and gets updated only after the completion of calculations through all the rays. For each ray from all angle, all the cells will be examined to look for those rays which passes through a particular cell. For each cell, the rays which passes through will contribute a correction which will be decided by the weigh factor w_{ij} . The algebraic average of all these corrections will be implemented on the cell. Calculate the total value of weight function ($W_{i\theta}$) along each ray as:

start: 1 For each projection angle (θ):

start: 2 For each ray ($i\theta$):

start: 3 For each cell (j):

$$W_{i\theta} = \sum_{j=1}^N w_{i\theta,j} \times w_{i\theta,j}$$

underline close: 3

close: 2

close: 1

start: 4 Start iterations (k):

start: 5 For each projection angle (θ):

start: 6 For each ray ($i\theta$):

Compute the numerical projection (Equation 5.3)

Calculate the correction as:

$$\Delta\phi_{i\theta} = \phi_{i\theta} - \tilde{\phi}_{i\theta}$$

close: 6

close: 5

start: 7 For each cell (j):

Identify all the rays passing through a given cell (j) (let M_{c_j} be the total number of rays passing through the j th cell) and corresponding $i\theta$, $w_{i\theta,j}$, $W_{i\theta}$ and $\Delta\phi_{i\theta}$.

Apply correction as:

$$f_j^{new} = f_j^{old} + \frac{1}{Mc_j} \sum_{Mc_j} \mu \frac{wi_{\theta, j} \Delta \phi_{i\theta}}{W_{i\theta}}$$

μ is the relaxation factor.

close: 7

Check for convergence as:

If

$$\text{abs}[\frac{f^{k+1} - f^k}{f^{k+1}}] \times 100 \leq e$$

STOP:

Else: Continue

close: 4

5.1.4 Anderson ART

Anderson and Kak (1984) proposed a variation in the ART algorithm. In short this algorithm is known as SART (Simultaneous Algebraic Reconstruction Technique). The method of implementing correction is similar to ART1. The only difference this algorithm has from ART1 is in the calculation of correction for each cell. The weight factor used here is the exact intersection of a ray with the concerned cell. In contrast ART1 use the average correction for all the cells. This will be referred to as ART4. The algorithm is given below.

Calculate the total value of weight function ($W_{i\theta}$) along each ray as:

start: 1 For each projection angle (θ):

start: 2 For each ray ($i\theta$):

start: 3 For each cell (j):

$$W_{i\theta} = \sum_{j=1}^N w_{i\theta, j} \times w_{i\theta, j}$$

close: 3

close: 2

close: 1

start: 4 Start iterations (k):

start: 5 For each projection angle (θ):

start: 6 For each ray ($i\theta$):

Compute the numerical projection (Equation 5.3)

close: 6

start: 7 For each ray ($i\theta$):

Calculate the correction as:

$$\Delta\phi_{i\theta} = \phi_{i\theta} - \tilde{\phi}_{i\theta}$$

start: 8 For each cell (j):

If $w_{i\theta,j}$ is non-zero then:

$$f_j^{new} = f_j^{old} + \mu \frac{\Delta\phi_{i\theta} \times w_{i\theta,j}}{W_{i\theta}}$$

where μ is a relaxation factor.

close: 8

close: 7

close: 5

Check for convergence as:

If

$$\text{abs}\left[\frac{f^{k+1} - f^k}{f^{k+1}}\right] \times 100 \leq e$$

STOP:

Else: Continue

close: 4

5.2 MART

When the corrections in the iterative algorithms are multiplicative rather than additive, the algorithms are grouped under the family of MART (Verhoeven, 1993). Golden *et al.* (1970), Gordon and Herman (1974) and Lent (1977) suggested different forms of MART. The MART algorithm presented below are similar to the set considered by Verhoeven (1993).

The major difference between ART and MART algorithms are the method of computing the corrections. While ART uses the difference between the calculated projections and measured projections MART uses the ratio between the measured projections and the calculated projections. Hence the corrections applied to each cell during calculations are via multiplications. The structure is similar to Gordon's ART (ART2).

Calculate the total value of weight function ($W_{i\theta}$) along each ray as:

start: 1 For each projection angle (θ):

start: 2 For each ray ($i\theta$):

start: 3 For each cell (j):

$$W_{i\theta} = \sum_{j=1}^N w_{i\theta,j} \times w_{i\theta,j}$$

close: 3

close: 2

close: 1

start: 4 Start iterations (k):

start: 5 For each projection angle (θ):

start: 6 For each ray ($i\theta$):

Compute the numerical projection (Equation 5.3)

Calculate the correction as:

$$\Delta\phi_{i\theta} = \frac{\phi_{i\theta}}{\phi_{i\theta}}$$

start: 7 For each cell (j):

If $w_{i\theta,j}$ is non-zero then:

MART1:

$$f_j^{new} = f_j^{old} \times (1.0 - \mu \times (\Delta\phi_{i\theta}))$$

MART2:

$$f_j^{new} = f_j^{old} \times (1.0 - \mu \times \frac{w_{i\theta,j}}{(w_{i\theta,j})_{max}} \times (1.0 - \Delta\phi_{i\theta}))$$

MART3:

$$f_j^{new} = f_j^{old} \times (\Delta\phi_{i\theta})^{(\mu w_{i\theta,j} / (w_{i\theta,j})_{max})}$$

where μ is a relaxation factor.

close: 7

close: 6

close: 5

Check for convergence as:

If

$$\text{abs}\left[\frac{f^{k+1} - f^k}{f^{k+1}}\right] \times 100 \leq e$$

STOP:

Else: Continue

close: 4

5.3 AVMART

The MART algorithms discussed above has been modified in the present work to form a new approach to applying the corrections. The performance evaluation presented in Appendices B and C show that the modified algorithm is superior to original MART. The newly developed algorithm has been named as AVMART (Average MART). This algorithm is similar to the MART but the corrections are applied by considering all the rays from all the angles passing through a given pixel. Instead of a single correction as obtained from individual rays a correction that is the average of all the rays is used. This route of average corrections is expected to behave well in the presence of noisy projection data. The difference between the conventional MART and the present implementation is the following: The correction at each pixel is updated on the basis of the N th root of the product of all the corrections from all the N rays and view angles passing through a pixel. Since an average correction is introduced, the algorithm is insensitive to noise; further, no relaxation parameter is required to stabilize the iterations. The statement of the AVMART algorithm is presented below.

Calculate the total value of weight function ($W_{i\theta}$) along each ray as:

start: 1 For each projection angle (θ):

start: 2 For each ray ($i\theta$):

start: 3 For each cell (j):

$$W_{i\theta} = \sum_{j=1}^N w_{i\theta,j} \times w_{i\theta,j}$$

close: 3

close: 2

close: 1

start: 4 Start iterations (k):

start: 5 For each projection angle (θ):

start: 6 For each ray ($i\theta$):

Compute the numerical projection (Equation 5.3)

Calculate the correction as:

$$\Delta\phi_{i\theta} = \frac{\phi_{i\theta}}{\bar{\phi}_{i\theta}}$$

close: 6

close: 5

start: 7 For each cell (j):

Identify all the rays passing through a given cell (j). Let Mc_j be the total number of rays passing through the j th cell and corresponding $i\theta$, $w_{i\theta,j}$, $W_{i\theta}$ and $\Delta\phi_{i\theta}$.

Apply correction as:

AVMART1:

$$f_j^{new} = f_j^{old} \times \left(\prod_{Mc_j} (1.0 - \mu \times (\Delta\phi_{i\theta})) \right)^{1/Mc_j}$$

AVMART2:

$$f_j^{new} = f_j^{old} \times \left(\prod_{Mc_j} (1.0 - \mu \times \frac{w_{i\theta,j}}{(w_{i\theta,j})_{max}} \times (1.0 - \Delta\phi_{i\theta})) \right)^{1/Mc_j}$$

AVMART3:

$$f_j^{new} = f_j^{old} \times \left(\prod_{Mc_j} (\Delta\phi_{i\theta})^{(\mu w_{i\theta,j} / (w_{i\theta,j})_{max})} \right)^{1/Mc_j}$$

close: 7

Check for convergence as:

If

$$\text{abs}\left[\frac{f^{k+1} - f^k}{f^{k+1}}\right] \times 100 \leq e$$

STOP:

Else: Continue

close: 4

5.4 Maximum Entropy

Based on ideas from information theory, one can perform image analysis and construct meaningful tomographic algorithms. Suppose there is a source which generates a discrete set of independent messages r_k with probabilities p_k . Then the information associated with r_k is defined logarithmically as

$$I_k = -\ln p_k \quad (5.4)$$

The entropy of the source is defined as the average information generated by the source and can be calculated as

$$\text{entropy} = - \sum_{k=1}^L p_k \ln p_k \quad (5.5)$$

When the source is the image, the probability can be replaced by the gray level f_j , for the j th pixel and entropy can be redefined as

$$\text{entropy} = - \sum_{j=1}^N f_j \ln f_j \quad (5.6)$$

For natural systems, the organisation of intensities over the image can be expected to follow the second law of thermodynamics namely,

$$f_j : - \sum_j f_j \ln f_j = \text{maximum}$$

This is the basis of the MAXENT algorithm. For interferometric images, one can view the pixel temperature as the information content and entropy built up using the pixel temperature values. In the absence of any constraint, the solution of the above optimization problem will correspond to a constant temperature distribution, more generally a uniform histogram in terms of probabilities. Hence, the MAXENT algorithm is properly posed along with the projections as constraints.

Requiring that the entropy of the system be a maximum along the interferometric projections as constraints is known as the Maximum entropy optimization technique

(MAXENT). It produces an unbiased solution and is maximally non-committal about the unmeasured parameters (Gull and Newton, 1986). This technique is particularly attractive when the projection data is incomplete (Censor, 1983). The algorithm is described below :

Consider a continuous function $f(x, y, z)$ with the condition $f(x, y, z) \geq 0$. In the present context, entropy technique refers to the optimization of the functional

$$F = - \sum_{j=1}^N f_j \ln | f_j | \quad (5.7)$$

subject to a set of constraints. In MAXENT the collected projection data and any other *a priori* information about the field to be reconstructed can be viewed as the constraints over which the entropy is to be maximized. A typical maximum entropy problem can be stated as :

$$\begin{aligned} &\text{Maximize} \quad (- \sum_{j=1}^N f_j \ln | f_j |) \\ &\text{subject to} \quad \phi_i = \sum_{j=1}^N w_{ij} f_j \\ &\quad \text{and} \quad f_j \geq 0 \end{aligned}$$

Different techniques are available in the literature for optimizing a functional over some constraints. One of the most popular is the Lagrangian multiplier technique. The method of solving the optimization problem using the Lagrangian technique is given in Appendix D.

The MART algorithms have been shown to converged to the solution of entropy optimization algorithm in the literature (Herman, 1980 and Censor, 1983). A necessary condition for which this is true is that the feasible set of solution which satisfies the projection data should be nonempty. However this is only a necessary condition and not sufficient.

5.5 Minimum Energy

The MAXENT algorithm can be generalized for any other function in place of entropy. Gull and Newton (1986) have suggested four such functions which can be maximized under the projections as constrained to obtain the tomographic reconstruction. Entropy and energy functions are attractive and natural to use in physical problems. The minimum energy method (MEM) can be implemented in a manner analogous to MAXENT as follows:

$$\begin{aligned} \text{maximize} \quad & \left(- \sum_{j=1}^N f_j^2 \right) \\ \text{subject to} \quad & \phi_i = \sum_{j=1}^N w_{ij} f_j \end{aligned}$$

Compared to MAXENT, MEM has a simpler implementation while using the Lagrangian multiplier technique, since it results in a simple set of linear equations. Gull and Newton (1986) however have recommended the MAXENT over MEM, since they found that the MEM produces a field which is negatively correlated and hence produced a biased solution. The method of minimizing the energy function using the Lagrangian technique is given in Appendix D.

5.6 Testing of Tomographic Algorithms

The algorithms discussed in Sections 5.1 - 5.5 have been tested for variety of cases identified by Subbarao *et al.* (1997a-b). Among the ART, MART and entropy algorithms, these authors have identified MART3 as the best in terms of error and CPU time requirements. The AVMART algorithms have been validated in the present section against the numerically generated three dimensional temperature field in Rayleigh-Benard convection. The model three dimensional temperature field has been generated using the stream function, vorticity and energy equations (Muralidhar and Kulacki, 1987) by a finite difference method. At a Rayleigh number of 13900 longitudinal rolls were seen in this simulation using periodicity conditions on the side boundaries. The two dimensional

temperature field was then spread along the roll axis to fill the cavity. This led to the full three dimensional temperature field characterized by two dimensional longitudinal rolls. The formation of cubic cells at higher Rayleigh numbers has been seen in the experiments of the present work. To obtain cubic cells from the numerical solution, a sine variation along the roll axis of the two dimensional longitudinal rolls was introduced. The knowledge of a temperature field similar to that encountered in the experiments aids in the determination of the proper initial guess and anticipated error levels. This also helps in selecting the proper tomographic algorithm. In the present work each horizontal plane of the fluid layer in the numerical data is discretized into 62×62 grid points. This results in 61×61 cells. Along the vertical direction it is discretized into 11 horizontal planes. The three dimensional reconstruction using AVMART algorithms has been obtained for all the planes. No relaxation parameter was used in the calculation since an average correction was enforced. The errors reported here are on the basis of the entire fluid layer. The three different errors reported are:

$$\begin{aligned}
 E_1 &= \max[\text{abs}(T_{orig} - T_{recon})], & \text{Maximum of absolute difference, } ^\circ C \\
 E_2 &= \sqrt{\frac{\sum[(T_{orig} - T_{recon})^2]}{N}}, & \text{RMS error, } ^\circ C \\
 E_3 &= \frac{E_2}{(T_{hot} - T_{cold})} \times 100 & \text{Normalized RMS error, \%}
 \end{aligned}$$

In these definitions, T_{hot} and T_{cold} are the hot and cold plate temperatures. T_{orig} and T_{recon} are the temperature variables of the original and the reconstructed field respectively. Results for the error level distribution in the fluid layer have also been determined. The distribution of the absolute error as a percentage of the E_1 error has been presented in the three regions, namely, $> 95\%$, 75% to 95% and 50% to 75% .

Figure 5.2 shows the stream lines of the roll pattern generated numerically at Rayleigh number 13900. Figures 5.3-5.4 show the temperature surface and the corresponding isotherms along the mid-plane of the fluid layer. of the fluid layer. It can be seen that the longitudinal rolls pattern is essentially two dimensional while the cubic cell pattern is fully three dimensional.

The projection data of the temperature field has been computed at 4 different angles. They are 0° , 60° , 90° and 150° . The projections data are presented in the form of isotherms in Figure 5.5 for longitudinal rolls in the fluid layer. These projections are similar to

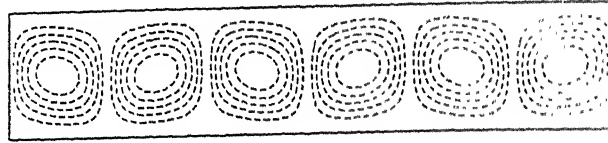


Figure 5.2: Streamlines of the Roll Pattern, Generated for Validation of AVMART algorithms

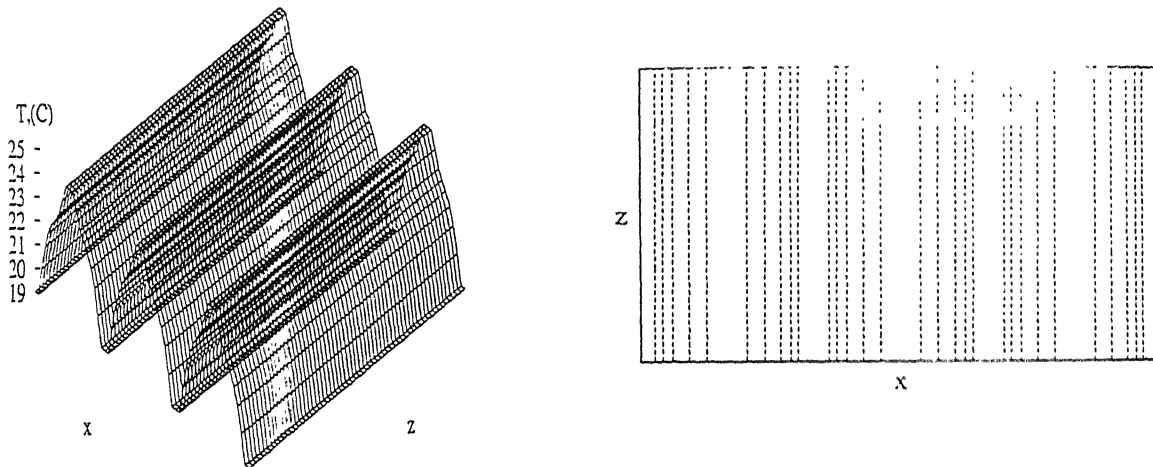


Figure 5.3: Temperature Surface (Left) and Isotherms (Right) of the midplane of the Fluid Layer Corresponding to Two Dimensional Longitudinal Rolls

interferometric projections in the infinite fringe setting. Figure 5.6 shows the projections at 0° , 60° , 90° and 150° for the cubic cell pattern.

5.7 Performance Characteristics of Tomography Algorithms

An evaluation of various algorithms with respect to initial guess and noise in projection data shows AVMART2 to be the best. In the present section, the performance character-

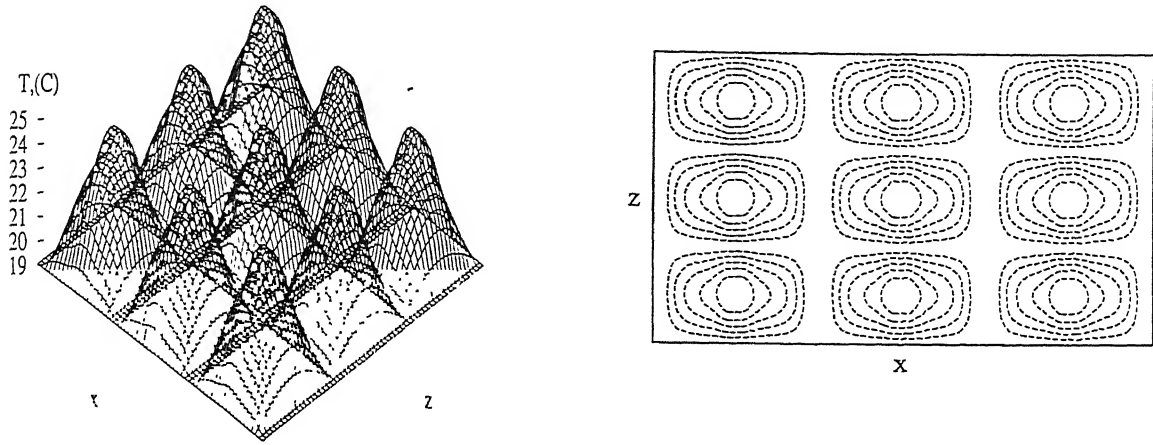


Figure 5.4: Temperature Surface (Left) and Isotherms (Right) of the midplane of the Fluid Layer Corresponding to Three Dimensional Cubic Cells

istics of the tomographic algorithms studied have been summarized. Quantities reported are CPU time, number of iterations and error indices. Results obtained from AVMART2 have been taken as the reference for determination of the three errors E_1, E_2, E_3 and the distribution of the errors in the fluid domain.

The comparison in terms of errors is presented in Table 5.1-5.6. The E_1 errors are found to be large, but confined only to a few points in the entire fluid domain. AVMART2 and AVMART3 give practically the same solution field and hence the errors are small. Among the ART family of algorithms the ART3 is seen to be closest to AVMART2. This is because ART3 incorporates an average correction in an additive sense and is thus similar to AVMART.

The optimization-based algorithms consumed the most CPU time. The MAXENT algorithm did not even converge for any horizontal plane for 2-view tomography after a week of CPU time in DEC 4000/300 computer with 32 MB of RAM and 233 MHz processor. The MEM algorithm comparatively took less time than MAXENT. Three horizontal plane were reconstructed using 2-view and 4-view projection data through this algorithm. With a 2-view projection data (0 and 90°) a field qualitatively similar to other algorithms was obtained.

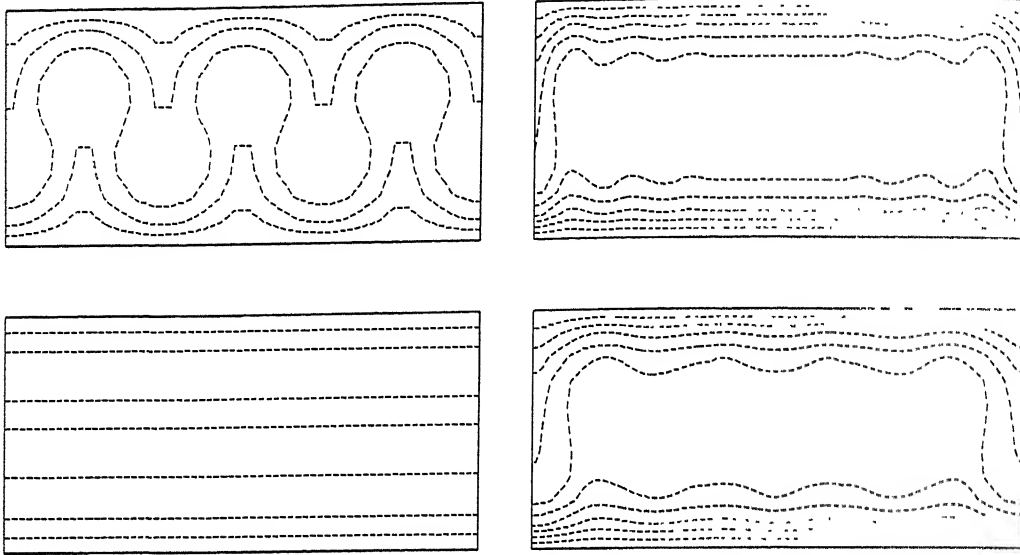


Figure 5.5: Numerically Generated Projection Data Corresponding to Rolls Formation in the Fluid Layer, Top left 0° , Top right 60° , Bottom left 90° and Bottom right 150°

Table 5.1: Reconstruction Errors from Different ART Algorithms: Comparison with AV-MART2

Error	ART1	ART2	ART3	ART4
$E_1, ^\circ\text{C}$	14.03	13.85	4.59	13.84
$E_2, ^\circ\text{C}$	1.93	1.92	0.60	1.92
$E_3, \%$	11.31	11.23	3.50	11.23

All the algorithms described in the chapter were seen to reconstruct the temperature field correctly from perfect projection data. Major differences in CPU time were not seen among the algorithms. Significant differences did show up when the projection data was superimposed with a noise pattern. Some algorithms converged, some did not and in a few cases convergence was delayed and the errors were large. The MART family of algorithms exhibited the best overall behaviour in terms of low errors as well as CPU time under

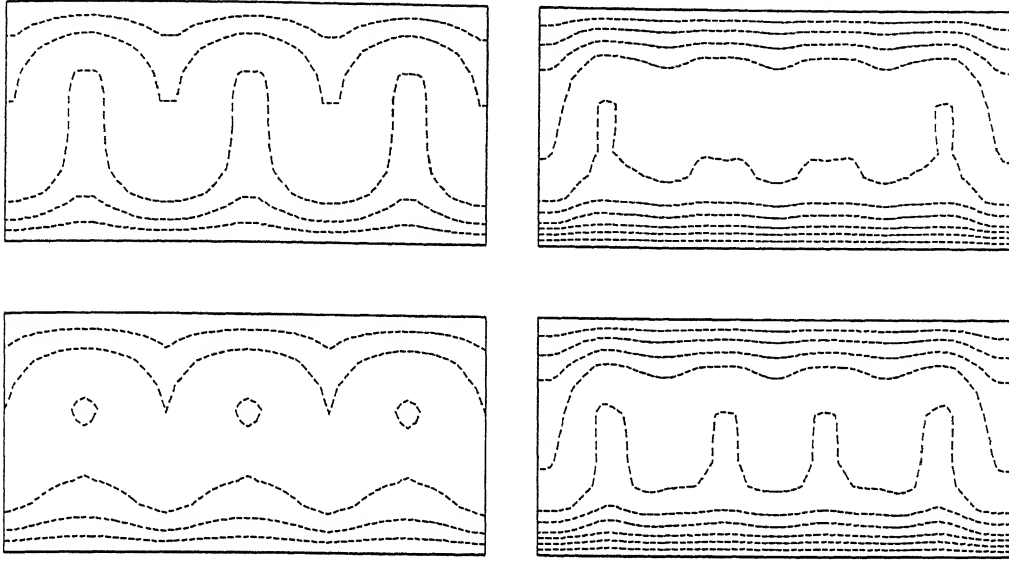


Figure 5.6: Numerically Generated Projection Data Corresponding to Cubic Cells Formation in the Fluid Layer, Top left 0° , Top right 60° , Bottom left 90° and Bottom right 150°

Table 5.2: Fractional Distribution of the E_1 Error over the Fluid Domain.

Number of points (%) having error in the range	ART1	ART2	ART3	ART4
> 95 %	0.001	0.003	0.0006	0.003
75-95 %	0.115	0.133	0.010	0.132
50-75 %	0.635	0.743	0.618	0.742

noisy input conditions.

The MART family requires a relaxation factors and its convergence properties depends strongly on the choice of this factor. The AVMART algorithms (1-3) were developed to reduce the sensitivity of their performance to the relaxation factor. Specifically, this

Table 5.3: Reconstruction Errors from Different MART Algorithms: Comparison with AVMART2

Error	MART1	MART2	MART3
E_1 , °C	17.10	14.53	15.64
E_2 , °C	2.86	2.03	2.28
E_3 , %	16.75	11.86	13.34

Table 5.4: Fractional Distribution of the E_1 Error over the Fluid Domain.

Number of points (%) having error in the range	MART1	MART2	MART3
> 95 %	0.016	0.006	0.007
75-95 %	0.147	0.132	0.137
50-75 %	1.524	0.743	0.795

Table 5.5: Reconstruction Errors from Different AVMART Algorithms: Comparison with AVMART2

Error	AVMART1	AVMART3
E_1 , °C	15.79	0.16
E_2 , °C	1.45	0.008
E_3 , %	8.47	0.05

Table 5.6: Fractional Distribution of the E_1 Error over the Fluid Domain.

Number of points (%) having error in the range	AVMART1	AVMART3
> 95 %	0.003	0.003
75-95 %	0.014	0.004
50-75 %	0.135	0.037

factor was set as unity in all the calculations. The sensitivity of the AVMART algorithms to initial guess and noise in the context of the numerically simulated temperature field is discussed in detail in Appendices B and C. The overall conclusion to emerge from this

Table 5.7: Summary of Performance of AVMART2

Source of data	Size of data $x \times z \times y$	Remarks	No. of views	Relaxation parameter	No. of iterations	CPU (sec)
Numerical	$61 \times 61 \times 11$	Clean	2	1	14	81.2
Numerical	$61 \times 61 \times 11$	Clean	4	1	1	37.8
Numerical	$61 \times 61 \times 11$	Noisy	2	1	15	91.8
Numerical	$61 \times 61 \times 11$	Noisy	4	1	52	933.2
Experimental	$120 \times 120 \times 21$	Processed	2	1	10	600.0
Experimental	$120 \times 120 \times 21$	Processed	4	1	330	97200.0

study is the following. The AVMART algorithms perform better than MART when :

1. the initial guess is unbiased, preferably a constant and
2. the projection data is noisy.

Among the AVMART family the AVMART2 is superior. The performance of AVMART2 for projection data corresponding to roll structure is presented in Table 5.7 for numerical and experimental data.

Chapter 6

Results and Discussion

Results have been presented for three Rayleigh numbers, namely 13900, 34800 and 40200. The flow structure and roll pattern, temperature field over horizontal planes and the wall Nusselt numbers have been reported. Experiments were conducted at a fourth Rayleigh number of 51800 as well. The flow field at this Rayleigh number was found to be completely unsteady with no noticeable periodicity. Hence images even at neighbouring positions were seen to be uncorrelated. Using the present strategy of data collection by scanning different sections of a view angles at different times using a traversing mechanism is inadequate to deal with strongly unsteady phenomena.

Three dimensional temperature field within the fluid layer has been reconstructed using interferometric projections. Results presented in this chapter are obtained using the AVMART2 algorithm discussed in Chapter 5.

6.1 Convection at $Ra=13900$

The experiments at a Rayleigh number of 13900 are considered first. The fringes associated with the convective flow pattern can be interpreted as the line-of-sight projection of the refractive index field. This in turn depends on the the temperature field in the fluid layer. Using the projection data, the three dimensional temperature field has been determined from principles of tomography. Reconstruction of the three dimensional temperature field requires that the projection data employed be complete. In the present

work, this requires the recording of interferograms for the entire width of the fluid layer along different view angles. The laser beam diameter being 70 mm, the flow field of width 500 mm was mapped completely by translating the test cell with the traversing mechanism.

View angles of 0, 30, 60, 90, 120 and 150° have been considered in the present study for the Rayleigh number of 13900. In these experiments, the fringes near the solid surfaces were seen to be stationary. Hence, for a given projection angle, there was no difficulty in maintaining the continuity of fringes from one projection record to the next. Mild unsteadiness however was observed in the fringes near the central region of the fluid layer, midway between the two horizontal walls. To circumvent this difficulty, several images were recorded at a given position and those giving the best continuity were chosen for analysis.

A second difficulty was encountered while recording angular projections. This was due to a reduction in the length of the ray passing through the test cell at angles other than 0 and 90°, particularly towards the corners of the fluid layer. This effect led to a considerable drop in the number of fringes at these locations. The corresponding interpolation errors after transforming the temperature data to a grid were found to be large. For this reason, the segment over the fluid layer where the number of fringes was less than 5 have not been considered for tomographic inversion. Hence for 30, 60, 120 and 150° angles the interferometric projections were collected over the entire fluid layer but only a partial width in the central fluid layer (39 cm out of a total of 68.3 cm) was considered for tomographic inversion.

6.1.1 Interferometric Projections

Figures 6.1-6.6 show the original interferograms as recorded by the CCD camera, before the application of any image processing operations. The collection of three interferograms placed side-by-side is also shown for each projection. Each individual interferograms shown in these Figures corresponds to a width of 6.5 cm of the fluid layer, except for one, which is towards one end.

The collection of interferograms at 0 and 90° projections when considered together, indicates the formation of longitudinal rolls within the fluid layer. The interferograms at

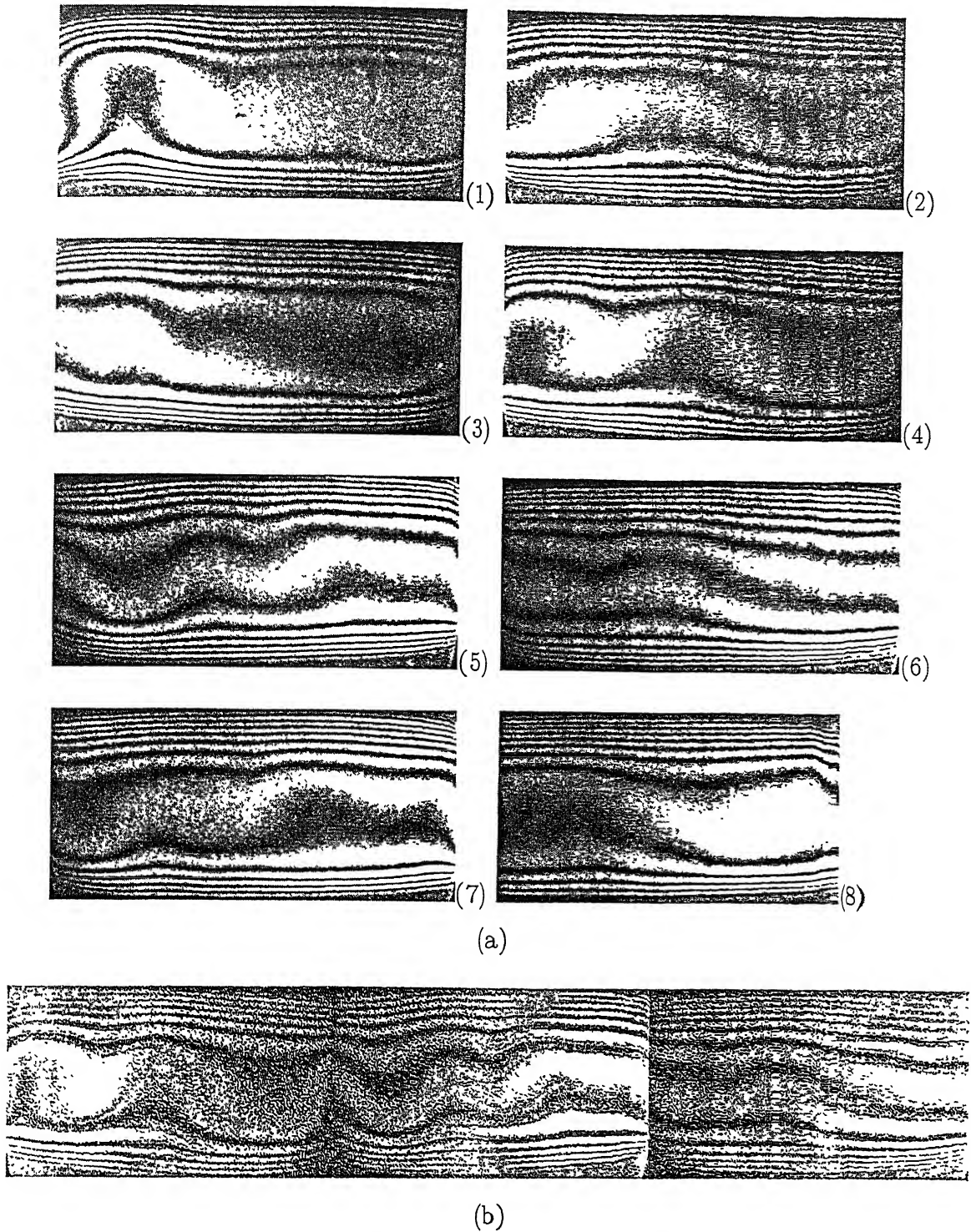


Figure 6.1: (a) Original Interferograms at Neighbouring Locations of the Fluid Layer and (b) Collection of Interferograms, 0° Projection, $Ra=13900$

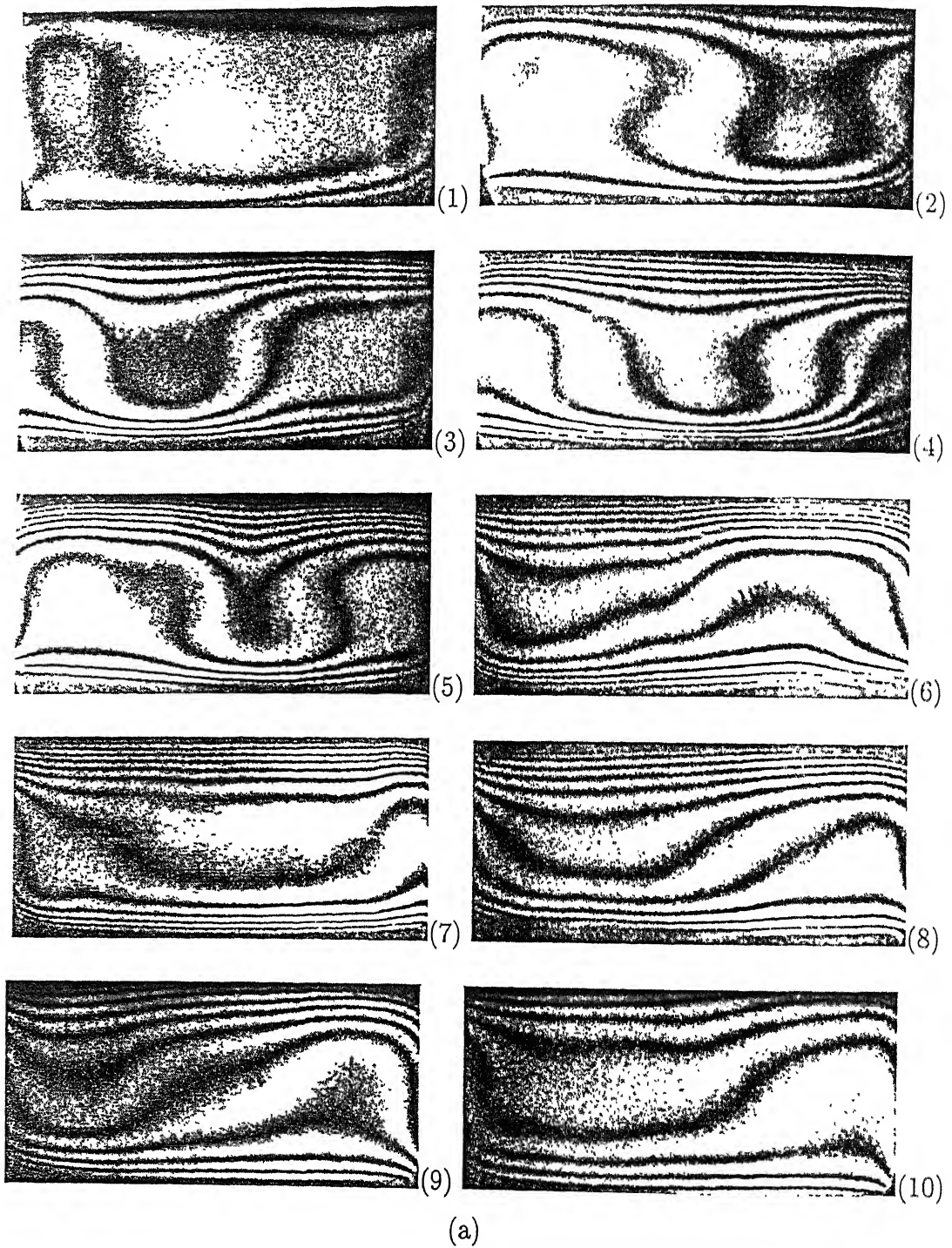


Figure 6.2: for caption see next page

a Rayleigh number of 13900 show a roll-like structure along the 90° view angle that is periodic along the width of the cavity. In contrast, the 0° view angle shows fringes that are less wavy. This shows that the roll structure seen in the 90° projection has little variation

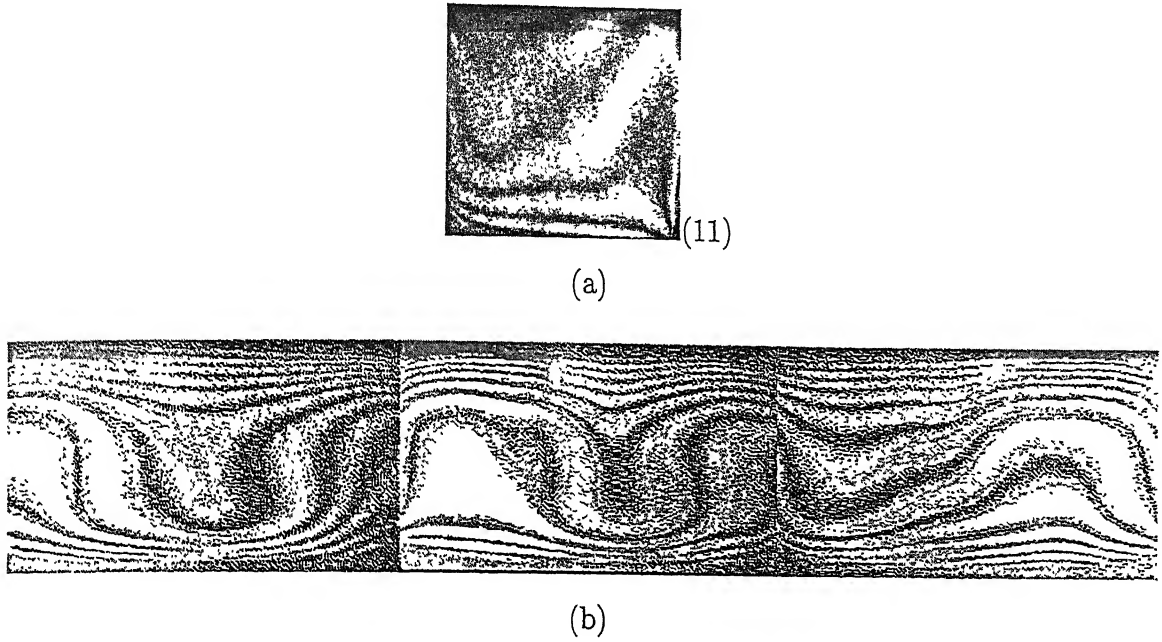


Figure 6.2: (a) Original Interferograms at Neighbouring Locations of the Fluid Layer and (b) Collection of Interferograms, 30° Projection, $Ra=13900$

along the roll axis. Hence the two views taken together qualitatively confirm the formation of two dimensional longitudinal rolls inside the fluid layer with the roll axis oriented along the 90° view angle. This pattern can be more clearly seen from the collection of thinned images in Figures 6.7 and 6.10. Figures 6.8, 6.9, 6.11 and 6.12 show the collection of thinned images¹ at 30° , 60° , 120° and 150° respectively. As one moves through the sequence of interferometric projections, the progressive change from near-straight fringes (0°) to a repeating roll structure (90°) is brought out. The dominant structure in the fluid layer is thus longitudinal rolls, with a superimposed three dimensionality effect. A stronger longitudinal roll pattern was observed by Michael and Yang (1992) in their experiments at $Ra=6000$.

Images of the convective field have been collected in the present work in the infinite fringe setting. Hence, lines of constant phase such as those passing through the intensity minima within a dark fringe band represent contours on which the function $L(T_{avg} - T_{ref})$ is a constant. Here, T_{ref} is the reference temperature, being the ambient value in the experiments. The subscript *avg* stands for the temperature averaged in the direction of the light ray passing through the test cell. When L is a constant for all rays at a

¹The thinned images are presented in a reversed sequence with respect to the interferograms. This step facilitated book keeping in tomography.

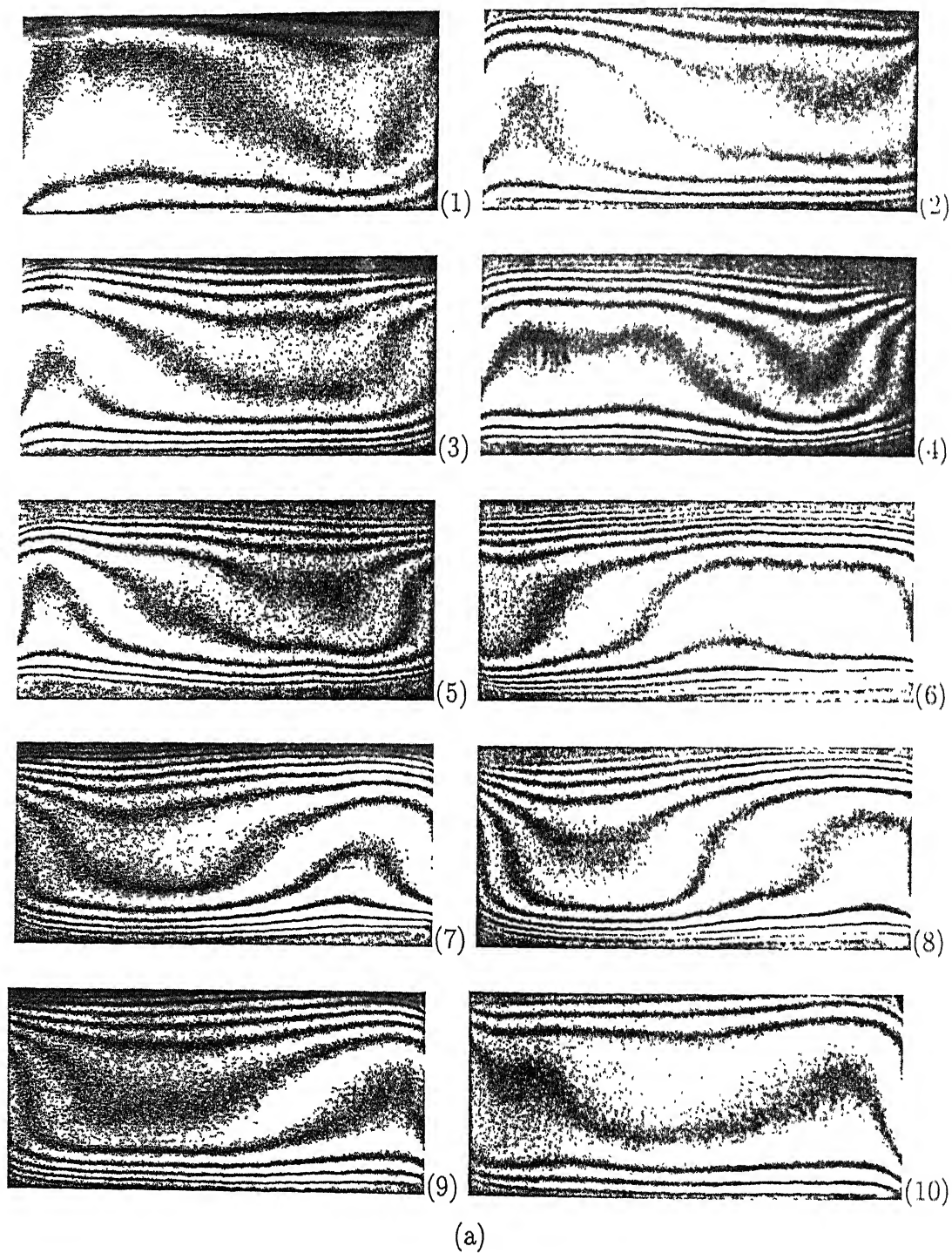


Figure 6.3: for caption see next page

given view angle, as in with 0 and 90° projections, the thinned fringes are isotherms. This interpretation cannot be used for other view angles and temperature will vary along the fringe curves. This factor has been taken care of while plotting the thinned fringes

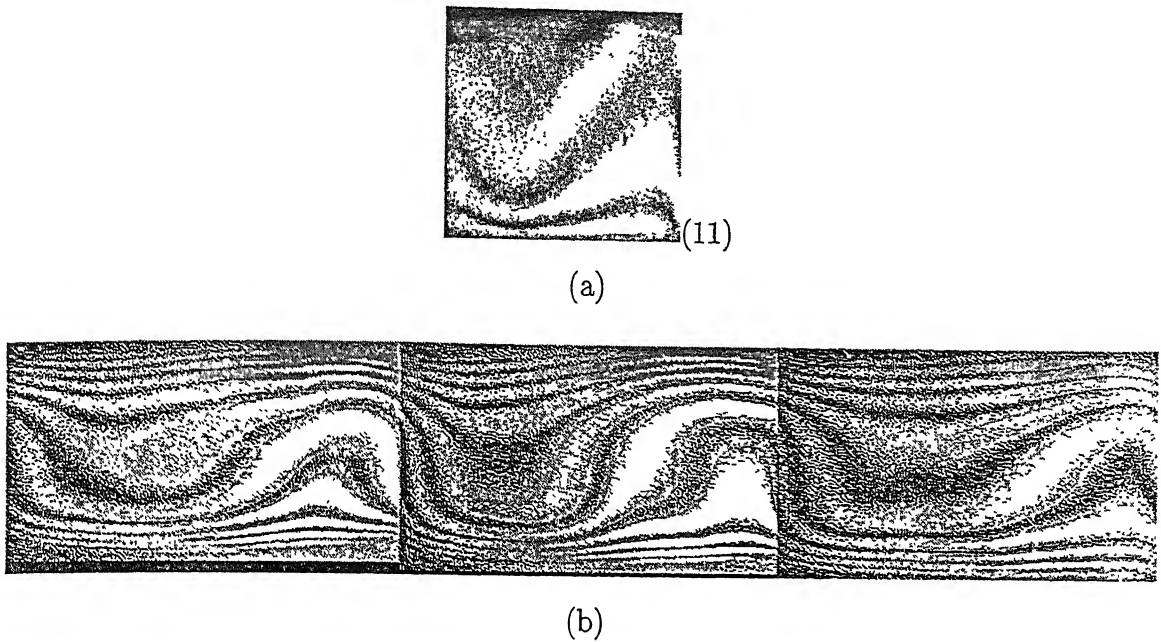


Figure 6.3: (a) Original Interferograms at Neighbouring Locations of the Fluid Layer and (b) Collection of Interferograms, 60° Projection, $Ra=13900$

in Figures 6.7-6.12. Specifically, the temperature data on the uniform grid required for tomography has been used. Hence the contours shown in these figures are truly isotherms.

For a cavity square in plan, the orientation of the rolls is indeterminate in principle, and will depend on mild imperfections in the experimental apparatus and nonuniformities in the thermal boundary conditions. In the present work, the roll axis was deduced to be parallel to the 90° view angle, because nearly straight fringes were observed along the 0° projection. The orientation of the roll axis was found to be repeatable for the experiments carried out over a one year period. Even before performing tomographic inversion, it is possible to count the number of rolls from the interferograms for the 90° projection. The rolls are stacked adjacent to one another, but the roll-width is not a constant. At the onset of longitudinal rolls in the fluid layer, scale analysis suggests the formation of as many rolls as the aspect ratio, 25 in the present experiment. The number of rolls seen in the projection data, Figures 6.4 and 6.10 is 15. The reduction in the number of rolls with increase in Rayleigh number finds support in the work of Kolodner *et al.*, (1986). These authors have reported a decrease in the number of rolls from 10 to 6 in 10:5:1 cavity for a Rayleigh number increasing upto 20000. Despite the presence of a dominant roll pattern, the present experiments also show that the temperature field is fully three dimensional. This is supported by the lack of straightness of the isotherms in the 0° projection.

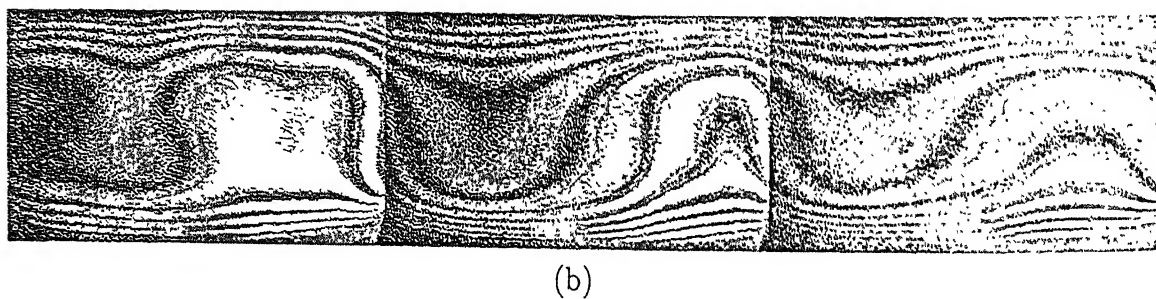
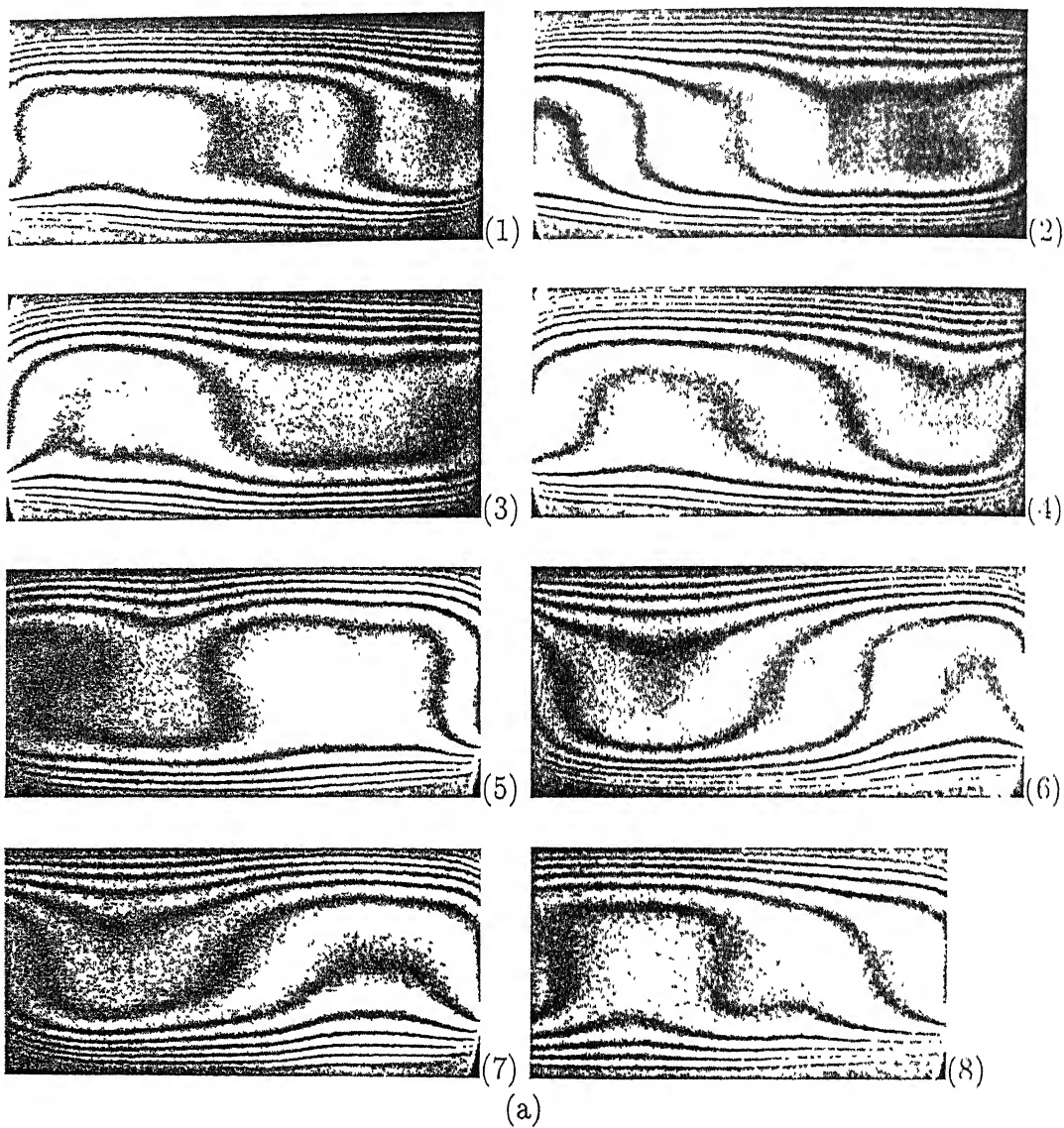


Figure 6.4: (a) Original Interferograms at Neighbouring Locations of the Fluid Layer and
 (b) Collection of Interferograms, 90° Projection, $Ra=13900$

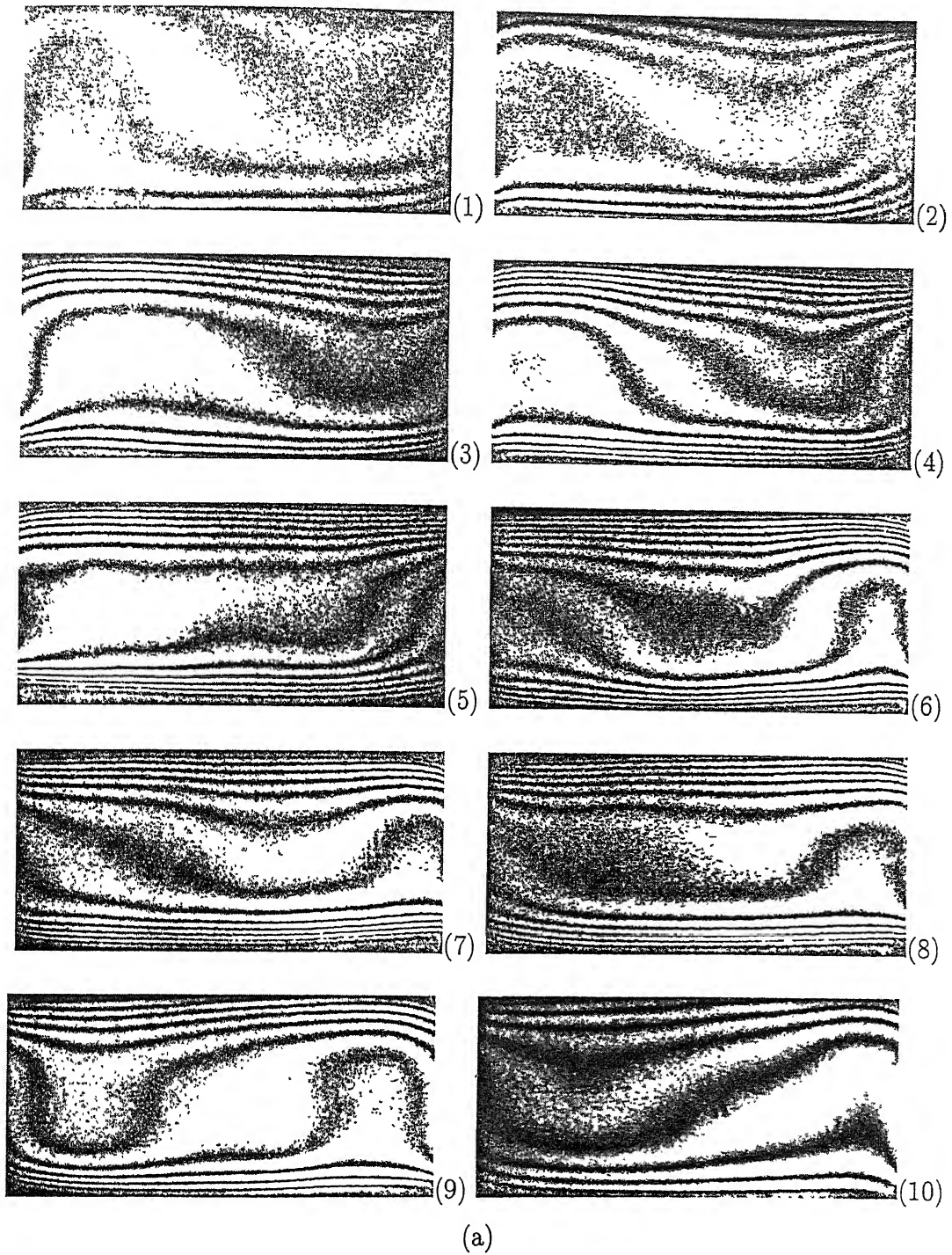


Figure 6.5: for caption see next page

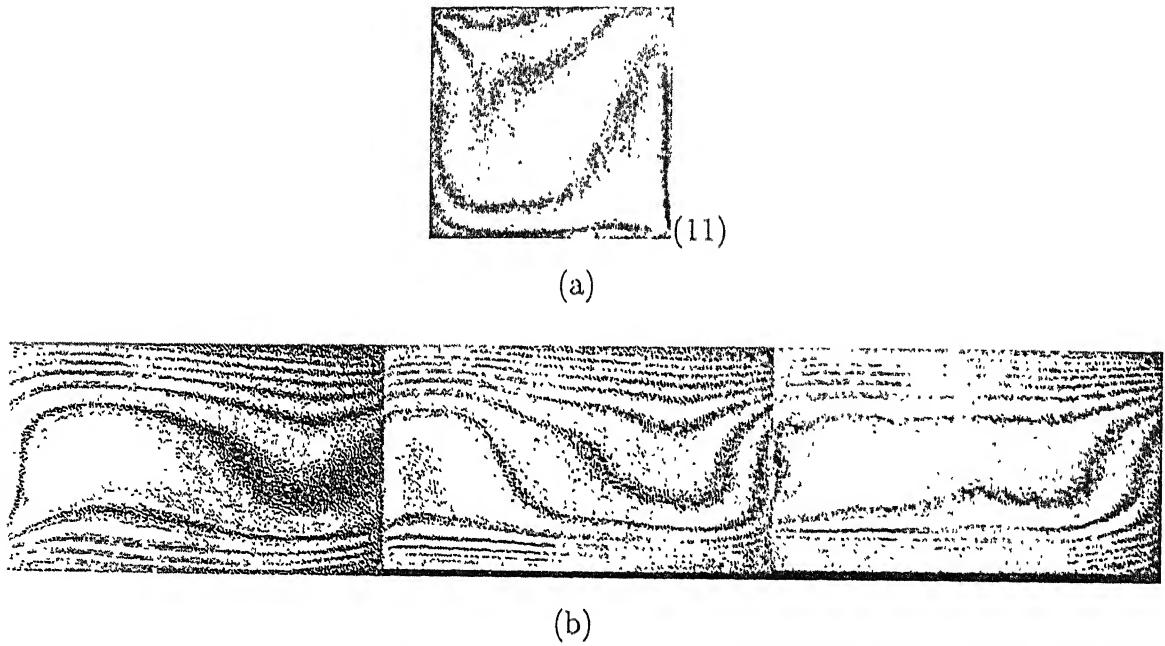


Figure 6.5: (a) Original Interferograms at Neighbouring Locations of the Fluid Layer and (b) Collection of Interferograms, 120° Projection, $Ra=13900$

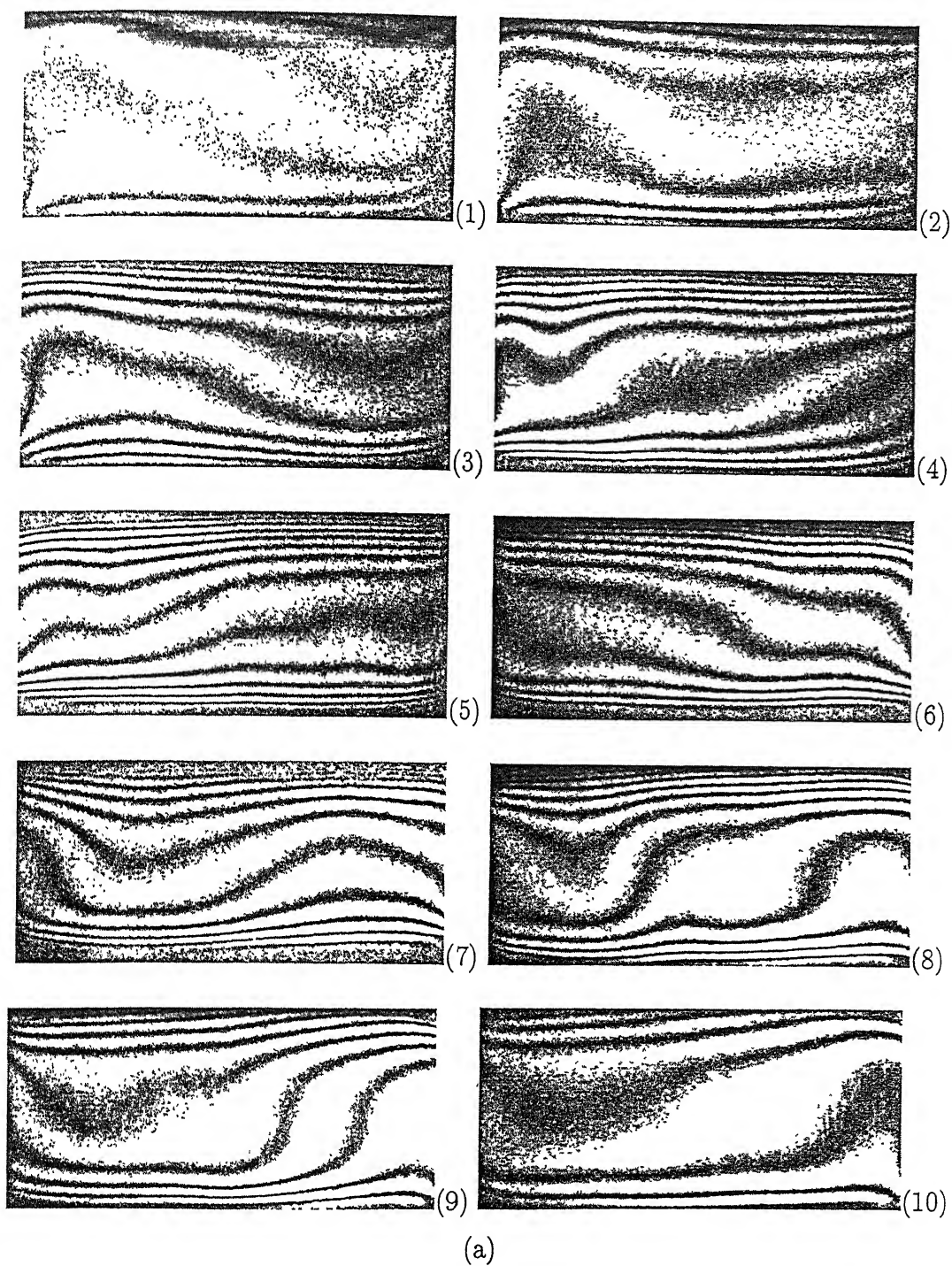


Figure 6.6: for caption see next page

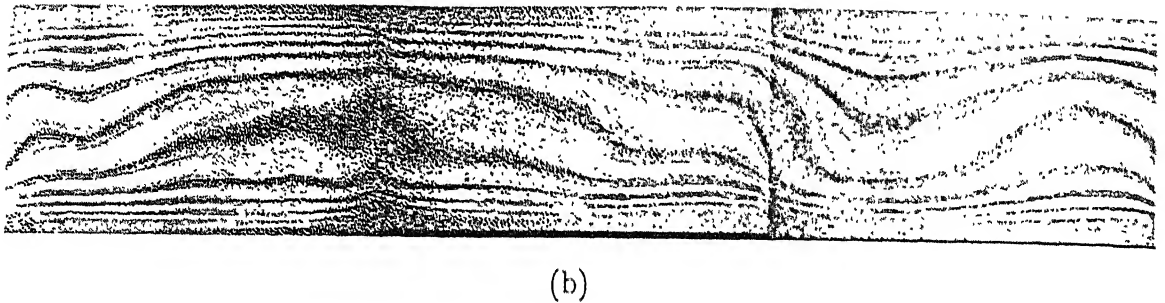
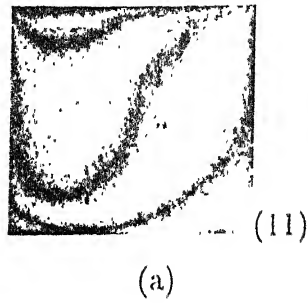


Figure 6.6: (a) Original Interferograms at Neighbouring Locations of the Fluid Layer and (b) Collection of Interferograms, 150° Projection, $Ra=13900$

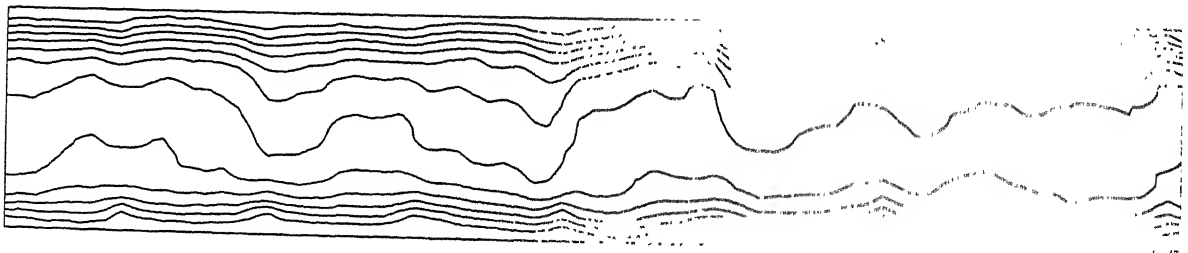


Figure 6.7: Collection of Thinned Images, 0° Projection, $Ra=13900$

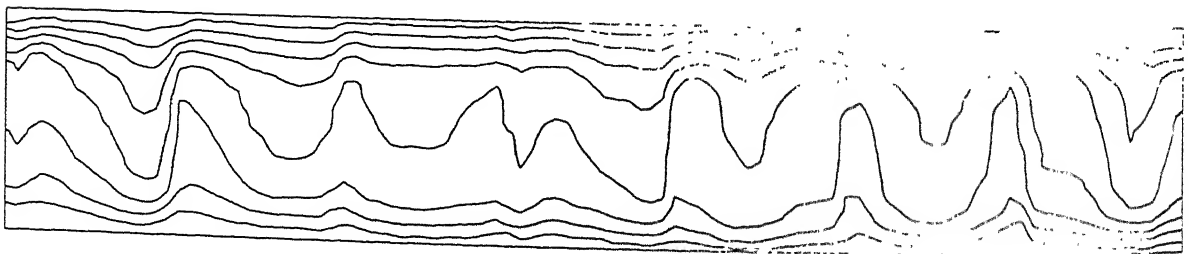


Figure 6.8: Collection of Thinned Images, 30° Projection, $Ra=13900$

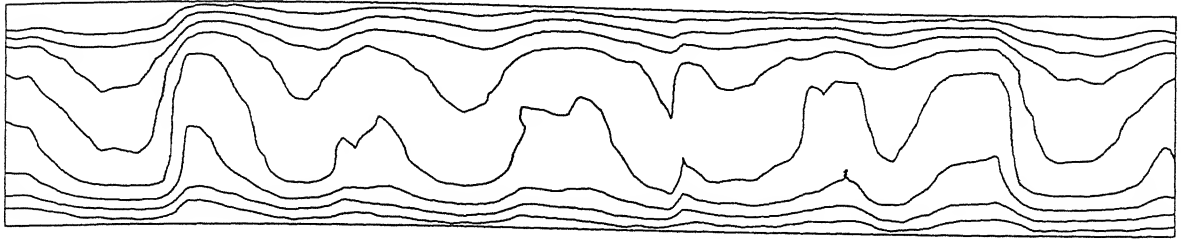


Figure 6.9: Collection of Thinned Images, 60° Projection, $Ra=13900$

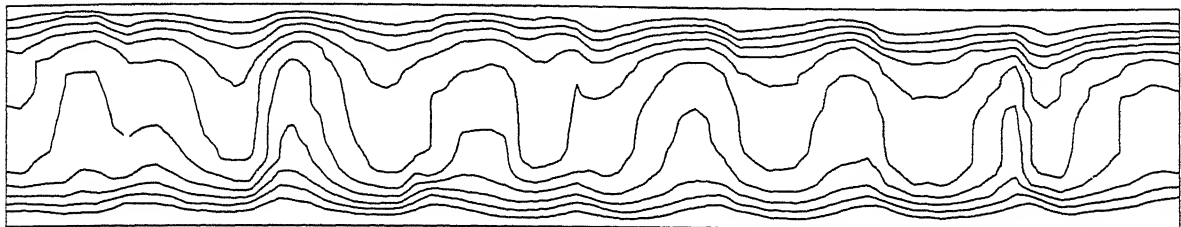


Figure 6.10: Collection of Thinned Images, 90° Projection, $Ra=13900$

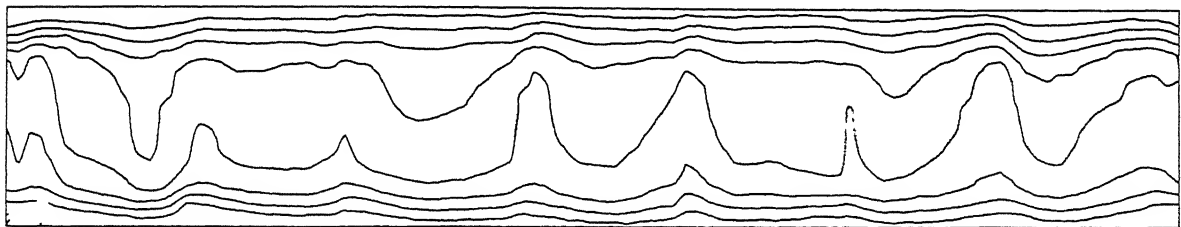


Figure 6.11: Collection of Thinned Images, 120° Projection, $Ra=13900$

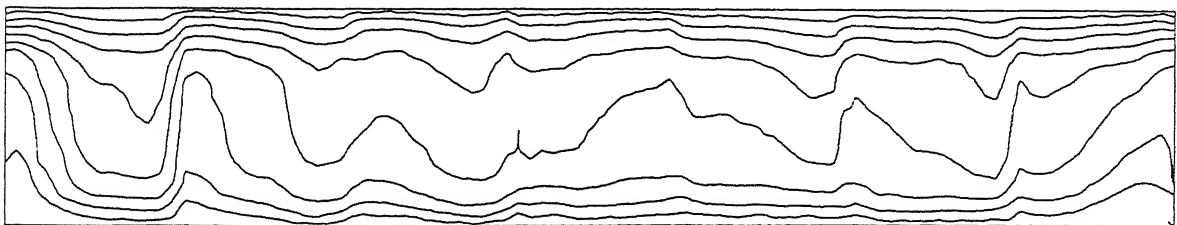


Figure 6.12: Collection of Thinned Images, 150° Projection, $Ra=13900$

6.1.2 Interferometric Tomography with 2 Projections

The results obtained from tomographic inversion of the interferometric data at Rayleigh numbers of 13900 are presented next. The temperature fields over horizontal planes have been obtained first using two views of 0 and 90° projection data. The initial guess for the 2-view reconstruction was assumed as a constant temperature distribution throughout the fluid layer (For a discussion on the role of the initial guess, see Appendix B). The reconstructed three dimensional surfaces representing the true temperature field in the fluid layer are shown in Figures 6.13-6.15 over three horizontal planes of the cavity. These planes correspond to $y/h = 0.15$, $y/h = 0.5$ and $y/h = 0.85$. The ordering of the horizontal planes is from the cooled top plate where $y = 0$. To preserve visual clarity, these surface plots have been partially filtered, without causing any noticeable loss of signal strength. The surfaces shown clearly bring out the formation of longitudinal rolls in the fluid layer. Figures 6.16- 6.18 show the corresponding isotherms over the horizontal planes of the fluid layer.

The utility of the reconstructed field from two projections can be questioned. Experience with tomographic algorithms shows that a structured field can be successfully identified using two views alone. In the present context, one can think of the thermal pattern emerging from 2-views as the dominant trend, with other details surfacing from increasing view angles (Natterer, 1986).

6.1.3 Interferometric Tomography with 4 Projections

Tomographic reconstruction and the computed results for 4-view angles of projection data is presented in this section. The solution obtained from the 2-view reconstruction is used as an initial guess for further calculations. The three-dimensional temperature field for a Rayleigh number of 13900 in the fluid layer was reconstructed successfully using the 0, 30, 90 and 120° projections. The computed field was used as an initial guess for reconstruction using 0, 60, 90 and 150° projections. The final results presented here are on the basis of projection data at 0, 60, 90 and 150°. The selection of the groups (0, 30, 90, 120°) and (0, 60, 90, 150°) ensures that orthogonal sets are employed and the largest possible view angle is involved in reconstruction. The 0 and 90° angles were retained since it is known that the presence of this orthogonal views increase the accuracy of the reconstruction

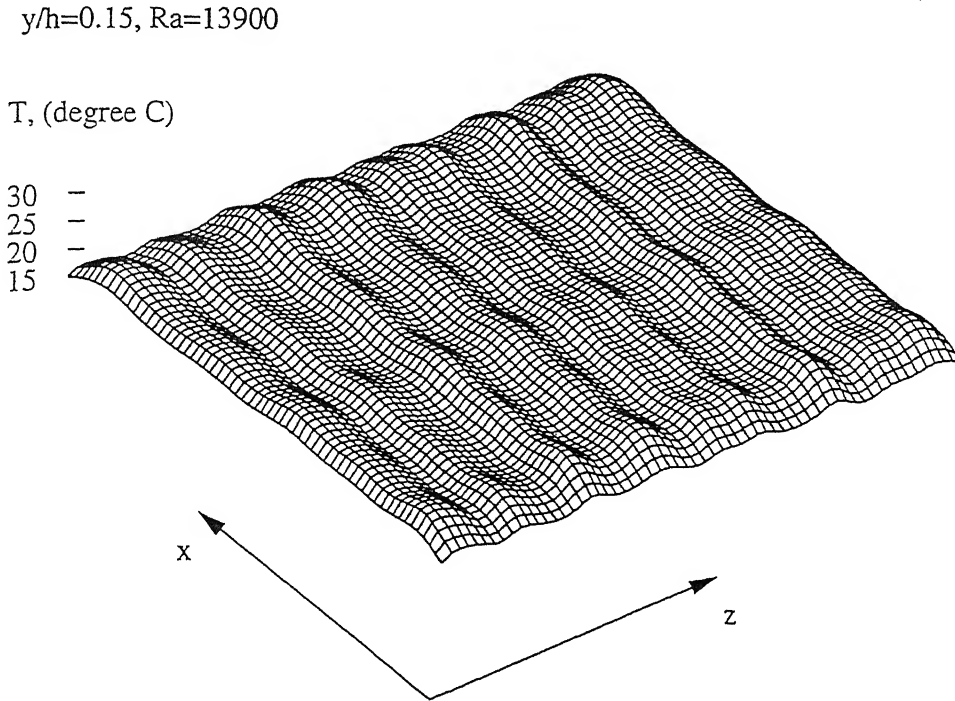


Figure 6.13: Reconstructed Temperature Surface at $y/h = 0.15$, $Ra=13900$, 2-view Tomography

(Subbarao *et al.*, 1997a-b).

The three dimensional temperature field in the fluid layer obtained using 4-views is shown in the form of surfaces in Figures 6.19-6.21. The three horizontal planes of the cavity ($y/h = 0.15$, $y/h = 0.5$ and $y/h = 0.85$) have once again been considered. The nature of the temperature field is three-dimensional but are similar at all the three planes. One can see rolls spreading over the entire length of the cavity. While this is a qualitative trend, distortions can also be seen in the form of nonuniformity in roll width and straightness, and possible interference between neighbouring rolls. Deviation from an ideal longitudinal roll, called *defects* are seen in the temperature surfaces. The formation of T and K type patterns can also be discerned (see Kolodner *et al.*, 1986, for shadowgraph images of these defects at a Rayleigh number of 17000 in an intermediate size cavity for fluids having Prandtl number in the range 2 to 10).

The above aspects are also brought out in the isotherms over horizontal planes of the fluid layer (Figures 6.22-6.24). These figures have also been partially filtered for presentation. While the unfiltered plots strictly satisfy the projection data, the isotherms shown in Figures 6.22-6.24 are quite close. Hence, the resulting influence of the appar-

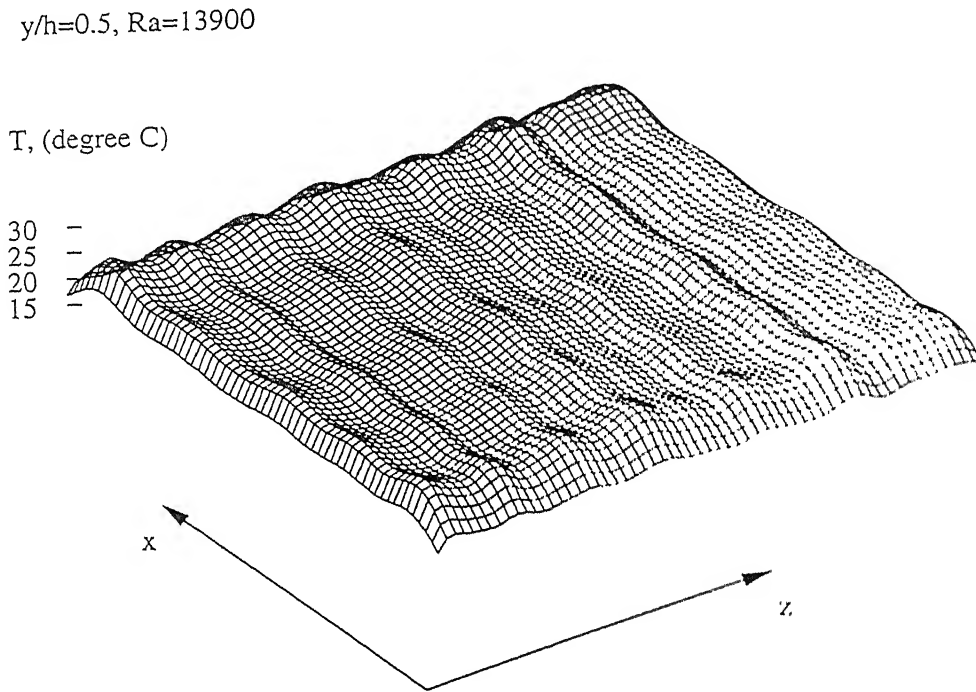


Figure 6.14: Reconstructed Temperature Surface at $y/h = 0.5$, $Ra = 13900$. 2-view Tomography

ently three dimensional flow field in Figures 6.22-6.24 is akin to longitudinal rolls. The isotherms on three different planes obtained with the final set of 4 views (0, 60, 90 and 150 °) are similar in nature except for a change in magnitude of the temperature data. This change in magnitude is related to the gradient in the temperature field along the vertical direction. While the contour plots show three dimensionality, the similarity in the geometry of isotherms suggest the formation of a stable structure in the fluid layer. The situation is analogous to chaotic convection superimposed on a set of stationary rolls observed by Gollub and Benson (1980) at a Rayleigh number of 60000. The result obtained above reveals an unexpected advantage of using interferometry. The projections capture the integrated and hence the average (global) trends in the convective field, while local information can be recovered using tomography. The local temperature field is seen to be complete three dimensional in nature, but there is a stable pattern prevailing over the fluid layer as seen in the temperature surfaces and isotherms. This stable pattern is the roll structure in the fluid layer. Gollub and Benson (1980) have observed time-dependent and non-periodic flow regimes simultaneous with a stable mean flow in the form of rolls. The finding presented here supports their work².

²Gollub and Benson (1980) used Laser Doppler Velocimetry to discriminate between a stable pattern

$y/h=0.85$, $Ra=13900$

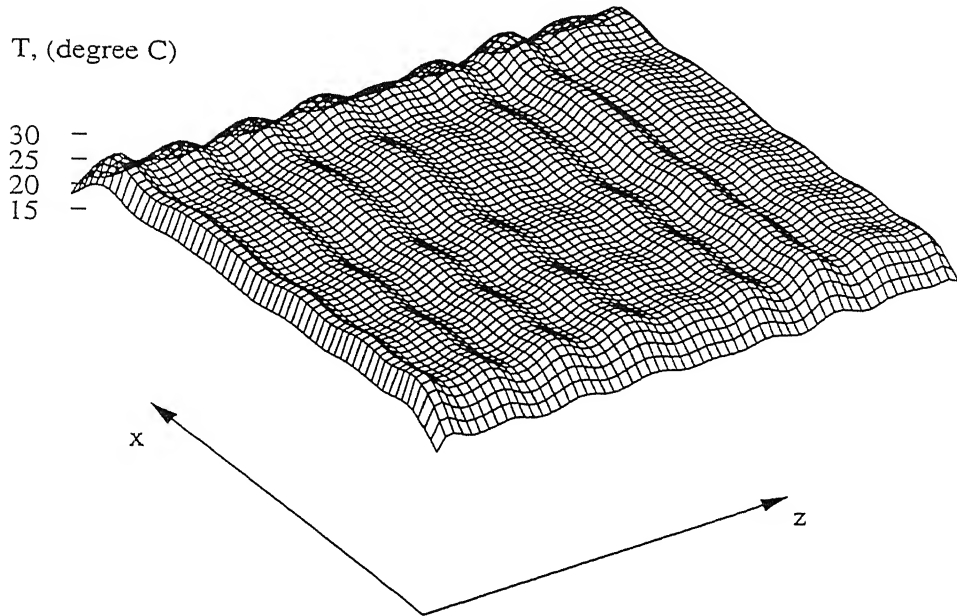


Figure 6.15: Reconstructed Temperature Surface at $y/h = 0.85$, $Ra=13900$, 2-view Tomography

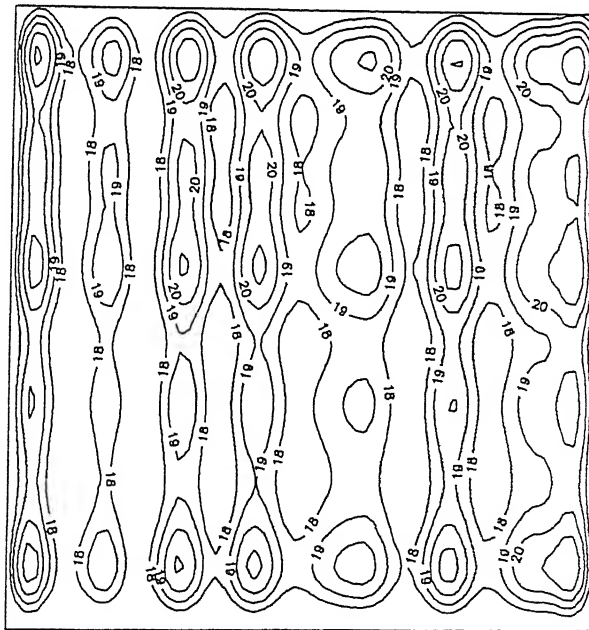


Figure 6.16: Isotherms over a Horizontal Plane, $y/h = 0.15$, $Ra=13900$, 2-view Tomography

and the superimposed disturbances. Their measurements had to scan the flow field point by point. The

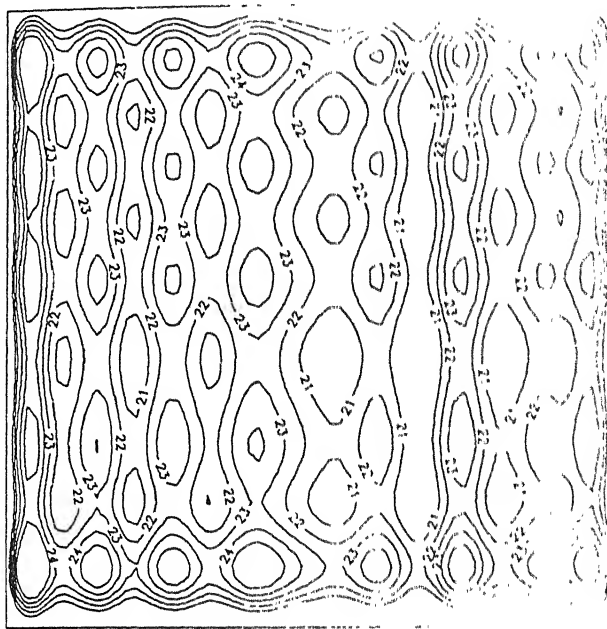


Figure 6.17: Isotherms over a Horizontal Plane, $y/h = 0.5$, $Ra = 13900$, 2-view Tomography

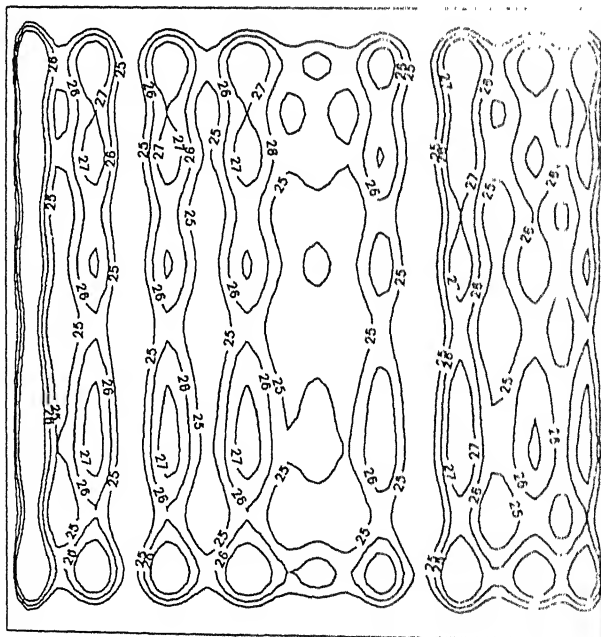


Figure 6.18: Isotherms over a Horizontal Plane, $y/h = 0.85$, $Ra = 13900$, 2-view Tomography

A point-wise comparison between the reconstructed temperature fields obtained from 2-view and 4-view tomography is shown in Tables 6.1-6.2. Though the maximum

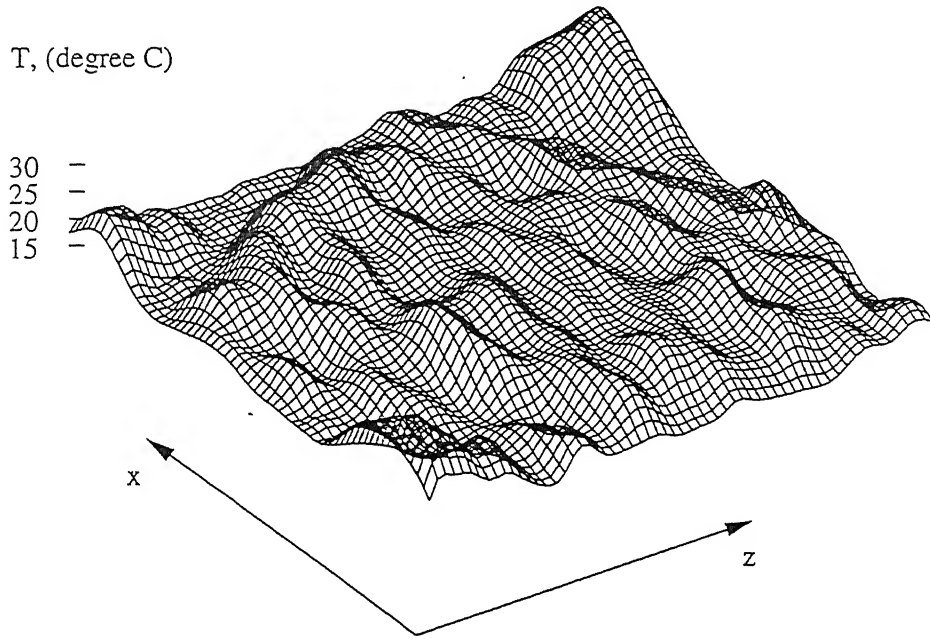
$y/h=0.15, Ra=13900$ 

Figure 6.19: Reconstructed Temperature Surface at $y/h = 0.15$, $Ra=13900$, 4-view Tomography

absolute difference is seen to be quite high, Table 6.2 shows that this is seen at very few points. The number of points in the fluid domain having a difference within 5% of the maximum value was found 0.004% an insignificant number. Hence the large differences in the temperature distribution is confined to a negligible part of the fluid domain. Hence the reconstructed fields with 2 and 4 views are quite close to each other.

Table 6.1: Differences between 2-view and 4-view Tomography in the Reconstructed Temperature Field, $Ra=13900$

$E_1, ^\circ\text{C}$	15.79
$E_2, ^\circ\text{C}$	2.86
$E_3, \%$	16.73

6.1.4 Cross-checks on Reconstructed Temperature Field

A check on the correctness of the reconstructed field was carried out along the following lines. For Rayleigh number of 13900, 6 different sets of projections were collected. Of

$y/h=0.5$, $Ra=13900$

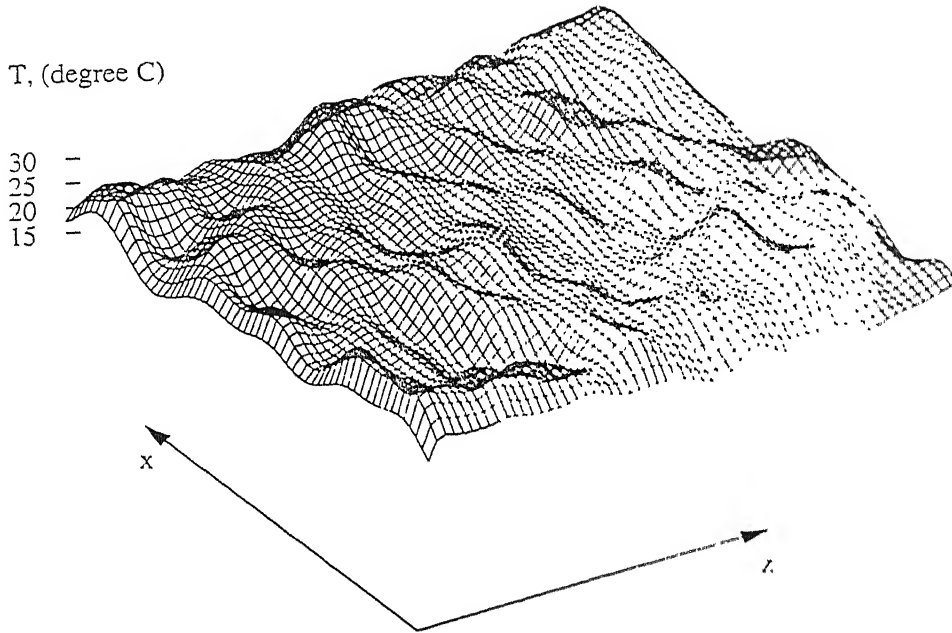


Figure 6.20: Reconstructed Temperature Surface at $y/h = 0.5$, $Ra = 13900$, 4-view Tomography

Table 6.2: Fractional Distribution of the E_1 Error over the Fluid Domain: Comparison between 2-view and 4-view Tomography, $Ra=13900$

Number of points (%) having error in the range	
> 95 %	0.004
75-95 %	0.162
50-75 %	1.103

these, 4 projections were used to reconstruct the three-dimensional temperature field inside the cavity. The reconstructed field was employed to construct the projections numerically at the two angles not included in the tomographic algorithm. These two projections could thus be used for a direct comparison with the experimentally recorded interferograms.

The correct convergence of the computer code that implements the tomographic algorithm has been established in the following manner. Using the computed three di-

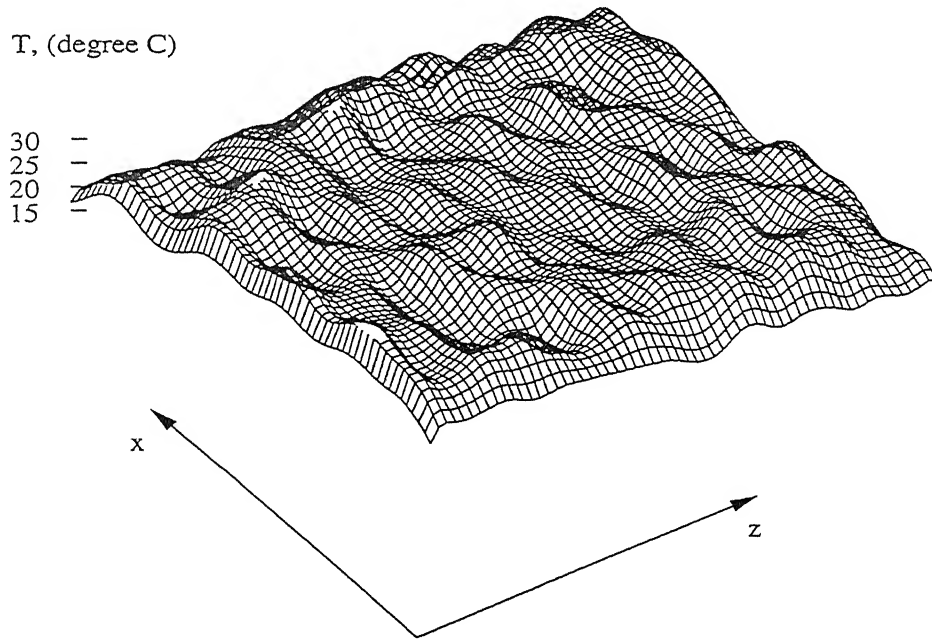
$y/h=0.85$, $Ra=13900$ T , (degree C)

Figure 6.21: Reconstructed Temperature Surface at $y/h = 0.85$, $Ra=13900$, 4-view Tomography

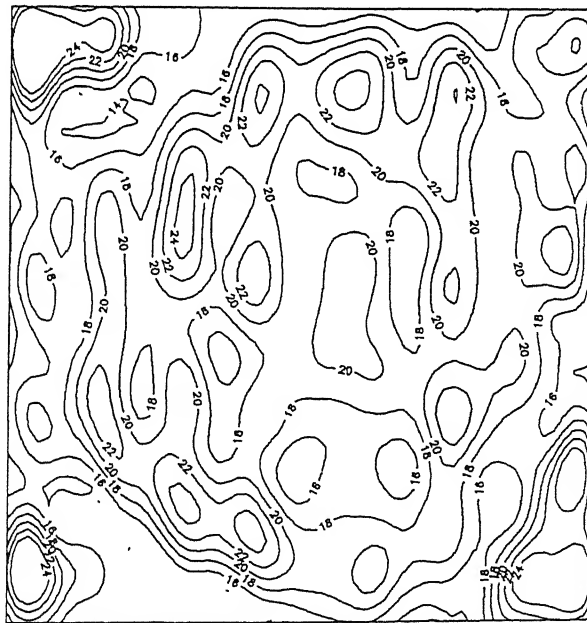


Figure 6.22: Isotherms over a Horizontal Plane, $y/h = 0.15$, $Ra=13900$, 4-view Tomography

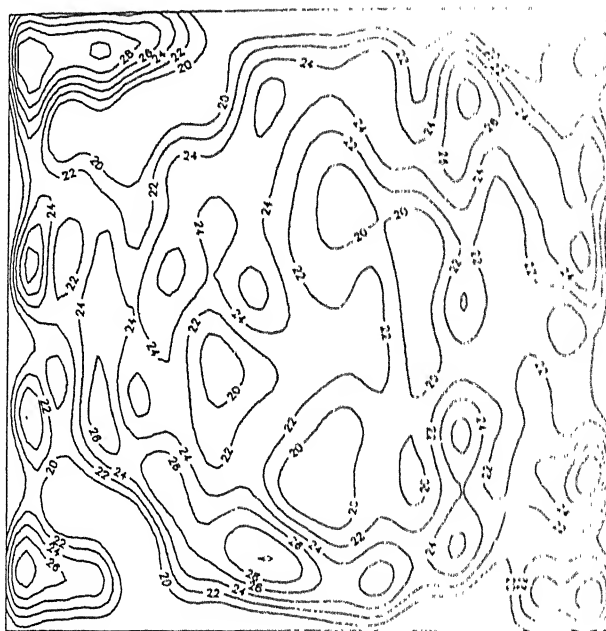


Figure 6.23: Isotherms over a Horizontal Plane, $y/h = 0.5$, $Ra = 13900$, 4-view Tomography



Figure 6.24: Isotherms over a Horizontal Plane, $y/h = 0.85$, $Ra = 13900$, 4-view Tomography

mensional temperature field, the projections at various angles have been recalculated numerically. These have been subsequently compared with the secondary field of isotherms

An exact match to within the convergence criterion was seen for all the view angles employed in the tomographic algorithm. This is proof that the convergence is correctly met.

The comparison of isotherms between experiments and the numerically generated projection data from the three dimensional temperature field at 0° , 60° , 90° , 150° are shown in Figures 6.25-6.28. The comparison is seen to be good. This result has significance for the following reason. In the tomographic algorithm used here (AVMART2), the correction applied to the field variable in a particular iteration is the geometric mean of all the corrections obtained from all the rays. Hence, even after correction, the temperature field is not required to satisfy any particular projection data. The corrections employed are simultaneous and an average effect on the basis of all the projections. The excellent match between the numerically generated data and the individual interferograms indicates (a) the versatility of the algorithm used (b) an excellent correlation among the projections collected at different sections and at different times.

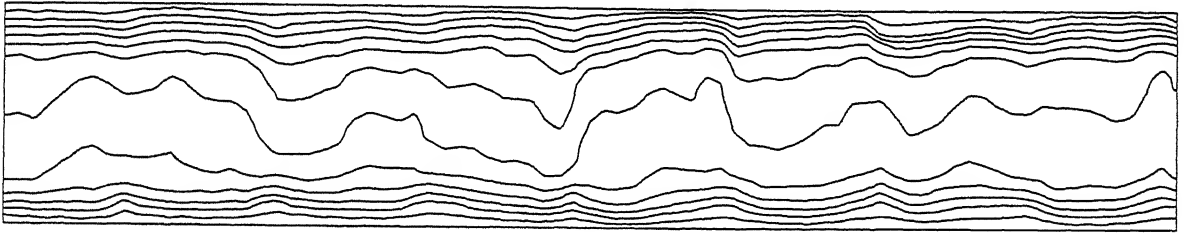


Figure 6.25: Numerically Generated Projection from the Reconstructed Temperature Field, 0° Projection, $Ra=13900$

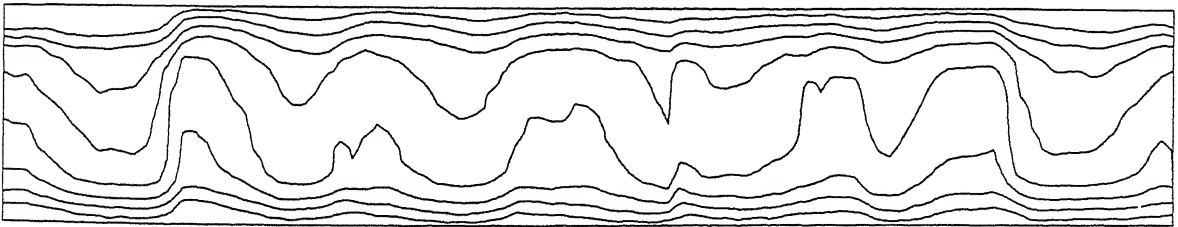


Figure 6.26: Numerically Generated Projection from the Reconstructed Temperature Field, 60° Projection, $Ra=13900$

The comparison between the numerically generated projections and the experimentally recorded interferograms not utilized in reconstruction is now considered. The cross-checks have been carried out at view angles of 30° and 120° in terms of isotherms, Figures

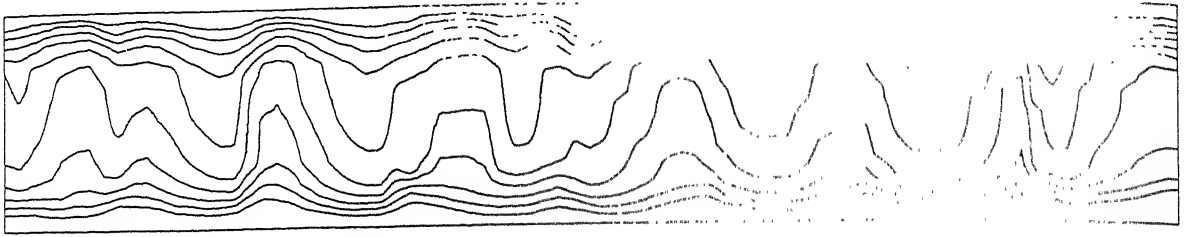


Figure 6.27: Numerically Generated Projection from the Reconstructed Temperature Field, 90° Projection. Ra=13900

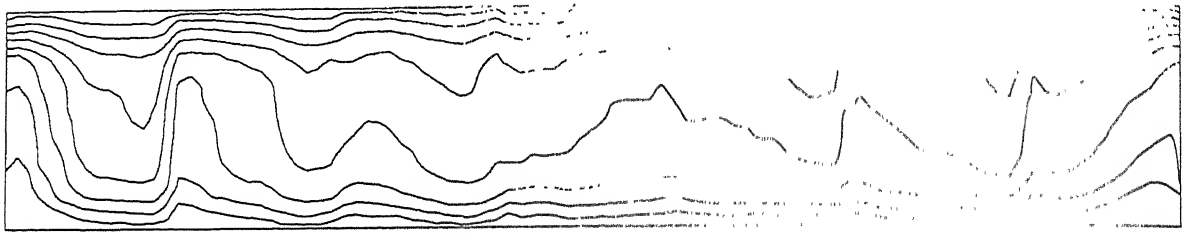


Figure 6.28: Numerically Generated Projection from the Reconstructed Temperature Field, 150° Projection. Ra=13900

6.29-6.30. The close match between the two sets of data confirms the correctness of the reconstructed temperature field.

6.1.5 Local and Average Heat Transfer Rates

Heat transfer rates at the boundary walls are reported in terms of the Nusselt number defined as

$$\text{Nu} = \frac{-h}{T_{\text{hot}} - T_{\text{cold}}} \frac{\partial T}{\partial y} \Big|_{y=0,h} \quad (6.1)$$

The derivative has been calculated by a forward finite difference formula. The local, the line-of-sight averaged (i.e. averaged along a light ray) and the cavity-averaged Nusselt numbers have been reported in the present section. The Nusselt number has been computed using the reconstructed field as well as the projection data. The average Nusselt number for the entire surface has been computed from the width-averaged temperature profile of the projection data. This corresponds to the slope of the S-shaped curve at the bounding planes (Figures 4.7 to 4.8). The average Nusselt number at both the plates have been reported for each angle of projection. The angular projections other than 0 and 90° donot include the entire width of the test cell, but it is expected that the average

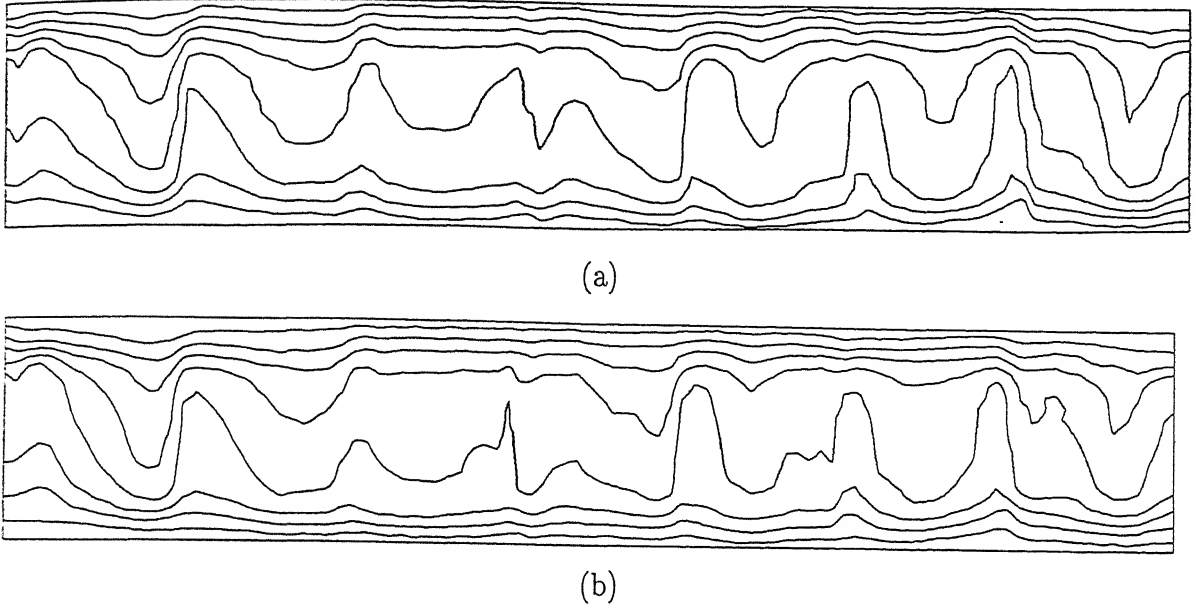


Figure 6.29: (a) Experimentally obtained Projection, (b) Numerically Generated Projection from the Reconstructed Temperature Field, 30°, Ra=13900

Nusselt number over the partial length will be representative of the entire width of the cavity. The average Nusselt number for each of the plates has also been compared with the experimental correlation reported by Gebhart *et al.* (1988). This correlation is based on independently conducted experiments by several authors and has a large uncertainty band (of around 20 %). For air, the correlation is given by:

$$\text{Nu} = 1 + 1.44 \left[1 - \frac{1708}{\text{Ra}} \right] + \left[\left(\frac{\text{Ra}}{5830} \right)^{1/3} - 1 \right] \quad (6.2)$$

A summary of all the Nusselt numbers referred above as a function of the projection angle is given in Table 6.3. The Nusselt number computed from interferometric measurements are within ± 10 % of the globally averaged value of 2.14. The individual plate-averaged Nusselt numbers are 2.16 and 2.12 at the cold and the hot surfaces respectively. Equation 6.2 gives a value of Nu=2.59 at Ra=13900. The Nusselt number obtained from the present set of experiments is thus approximately 17 % below the Nusselt number based on Equation 6.2. The agreement is much closer in the higher Rayleigh number experiment and is discussed later. Within experimental uncertainty, the comparison with previous experiments at the lower Rayleigh number may be taken to be favourable.

The temperature field derived from the interferograms suggest the formation of

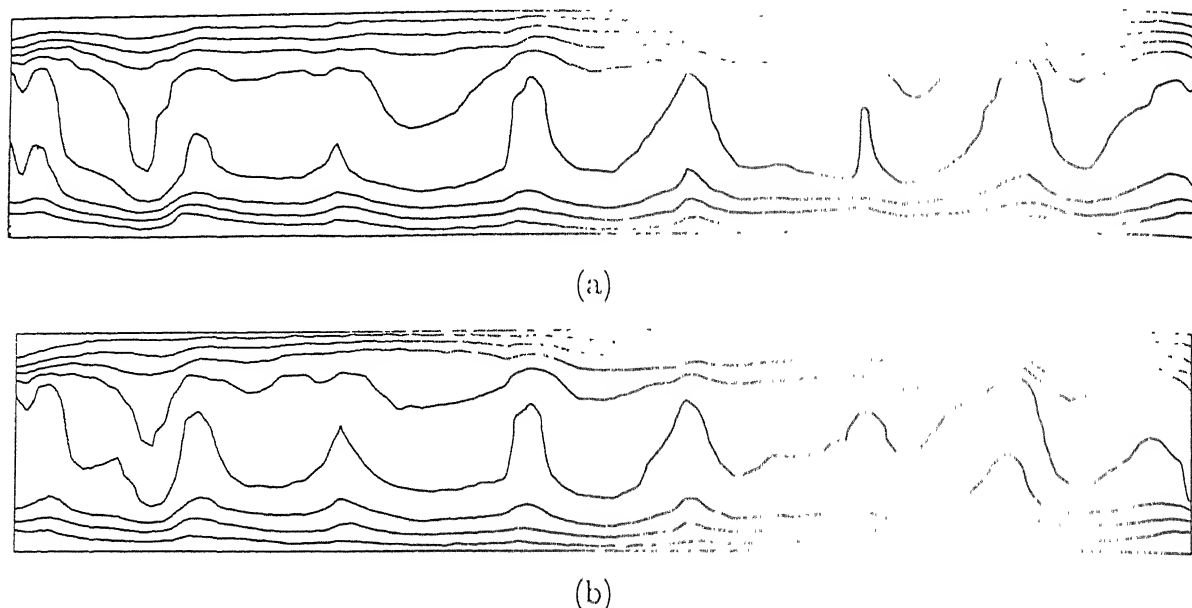


Figure 6.30: (a) Experimentally obtained Projection, (b) Numerically Generated Projection from the Reconstructed Temperature Field, 120° , $Ra=13900$

longitudinal rolls superimposed with three dimensional effects in the cavity. The presence of rolls in the fluid layer can be deduced from the local Nusselt number variation with distance. When the local Nusselt number is computed from the projection data, the value corresponding to the average computed along the light ray within the test cell is obtained. These line-of-sight Nusselt numbers are shown in Figure 6.31 for various projections angles for the top and the bottom plates. The rolls being parallel to the x -axis, the line-averaged Nusselt number along the z -axis that is the 0° projection is expected to show similar trends over both the walls. This is evident in Figure 6.31(a),

Table 6.3: Comparison of Average Nusselt Number with Gebhart *et al.*, (1988), $Ra = 13900$.

Projection Angle in degree	Nu (Cold)	Nu (Hot)	Nu (Average) From All Angles	Nu (Reference)
0	2.18	1.94	2.12 (hot)	2.59
30	2.33	2.02	2.16 (cold)	
60	1.99	2.34	2.14 (cavity)	
90	2.00	2.17		
120	2.19	2.32		
150	2.27	1.95		

where except for a small part of the test cell towards the ends, the local hot and cold wall Nusselt numbers are similar. Along the x -axis, that is the 90° projection, the local Nusselt number at the two walls are expected to show a phase shift. This corresponds to the inclination of the major axis of the roll cross-section with respect to the vertical direction. This shift is seen in Figure 6.31(b). Hence in a qualitative sense the variation of the line-averaged Nusselt number over the two plates supports the equivalent flow pattern in the cavity to be in the form of longitudinal rolls. The local Nusselt number along the direction of the 0° projection angle shows definite variations with distance. This clearly is the three-dimensionality in the longitudinal rolls which are no longer two dimensional at the Rayleigh number studied. The loss of two dimensional structure in the rolls can also be confirmed from other projections (Figures 6.31(c)-6.31(f)). Since the rolls identified in the projection data are parallel to the x -axis, projections symmetric with respect to the 90° axis will be identical at the limit of strict two dimensionality. A comparison of projections obtained from symmetrically placed angles, namely $(30,150)$ and $(60,120)$ shows qualitative similarity. This strengthens the suggestion of rolls, but also highlights their unequal sizes and their three dimensional nature along the roll axis.

The Nusselt number surface obtained from the reconstructed temperature field is shown for each of the hot and cold surfaces in Figure 6.32. Along the roll axis, the Nusselt number surfaces of the top and bottom plates are oppositely oriented. Heat transfer from the lower to the top plate by a buoyancy-driven roll can be associated with the peaks and valleys of the Nusselt number surface.

As stated earlier, interferometric projections at 30 and 120° were not utilized for the final reconstruction. Hence an independent test on reconstruction is a comparison between the line averaged Nusselt number at these angles and the line averaged Nusselt number calculated directly from the projection data. This comparison for both the plates is presented in Figure 6.33. Within experimental uncertainty this comparison is seen to be favourable. Further such comparison with all the angles employed for reconstruction namely 0 , 60 , 90 and 150° were also carried out. The numerically computed line averaged Nusselt number from the reconstructed temperature field and the line averaged Nusselt number as obtained directly from the projection data are shown in Figure 6.34. While the tomographic algorithm produces a temperature field that satisfies the projection data, it can be seen that the Nusselt numbers also shows the consistency in the reconstructed temperature field.

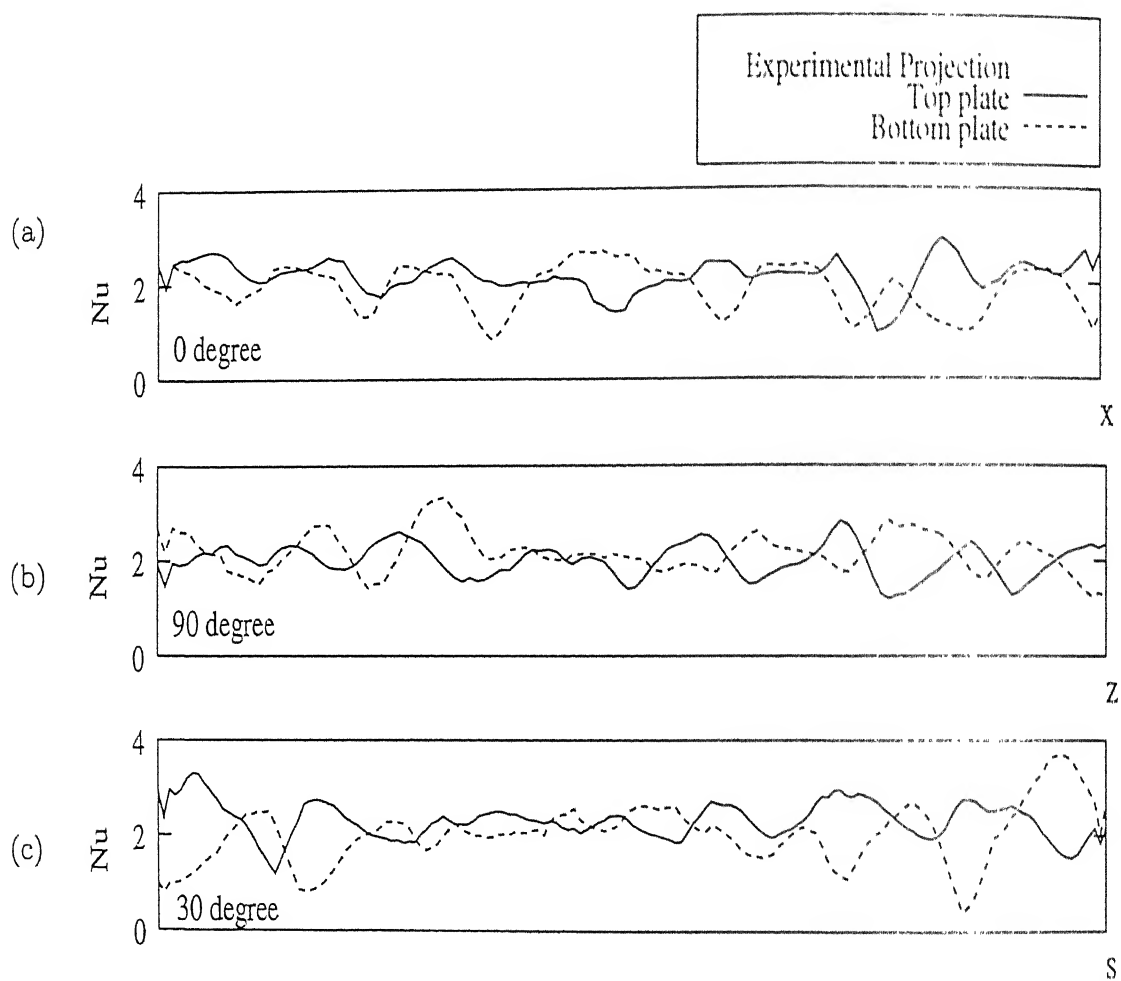


Figure 6.31: for caption see next page

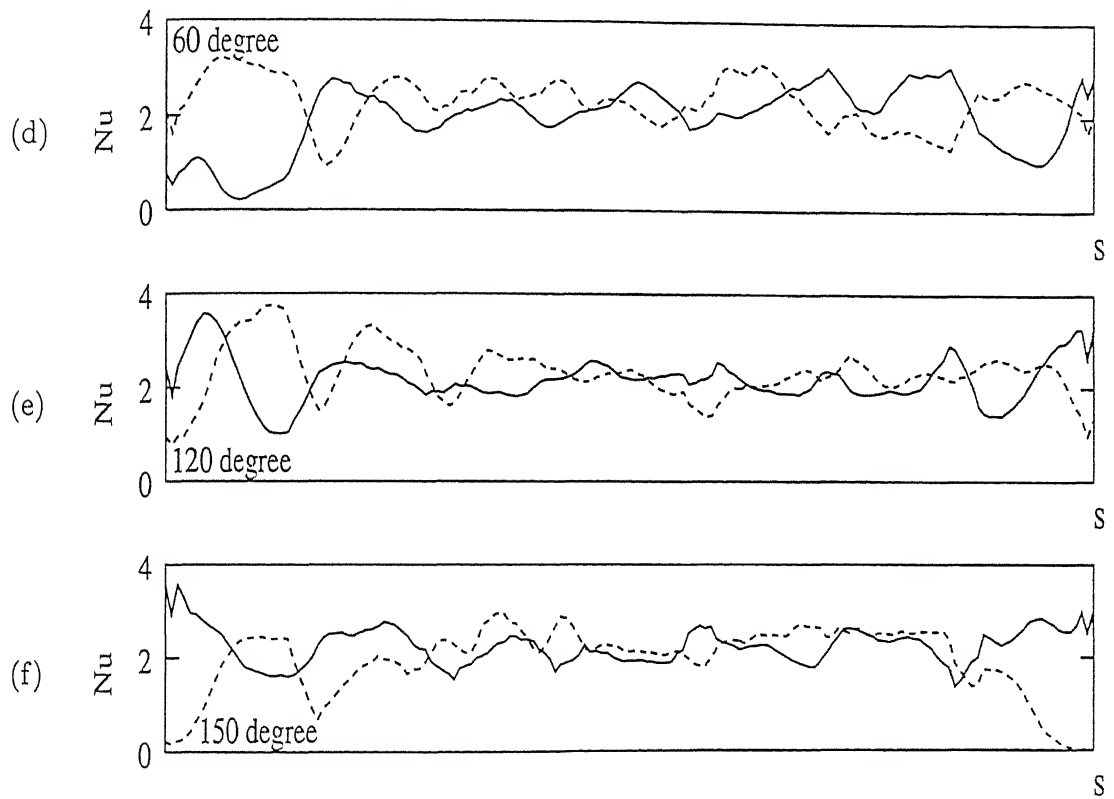
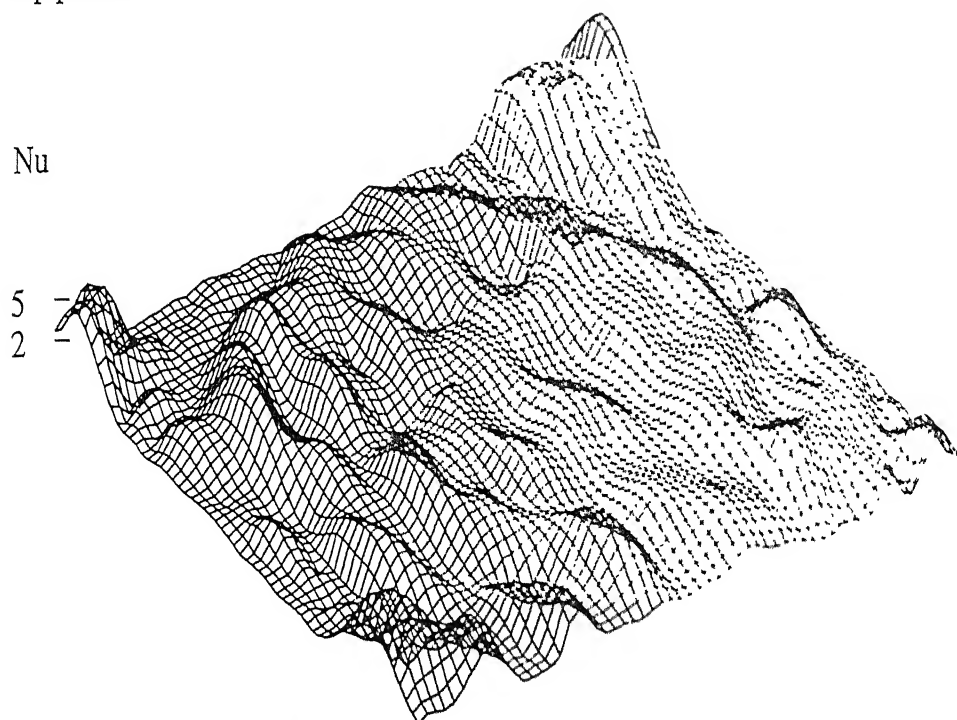


Figure 6.31: Experimentally obtained Line Integrals of the Nusselt Number for both the Plates, $Ra=13900$

Top plate, $Ra=13900$

Nu

5
2



Bottom plate, $Ra=13900$

Nu

5
2

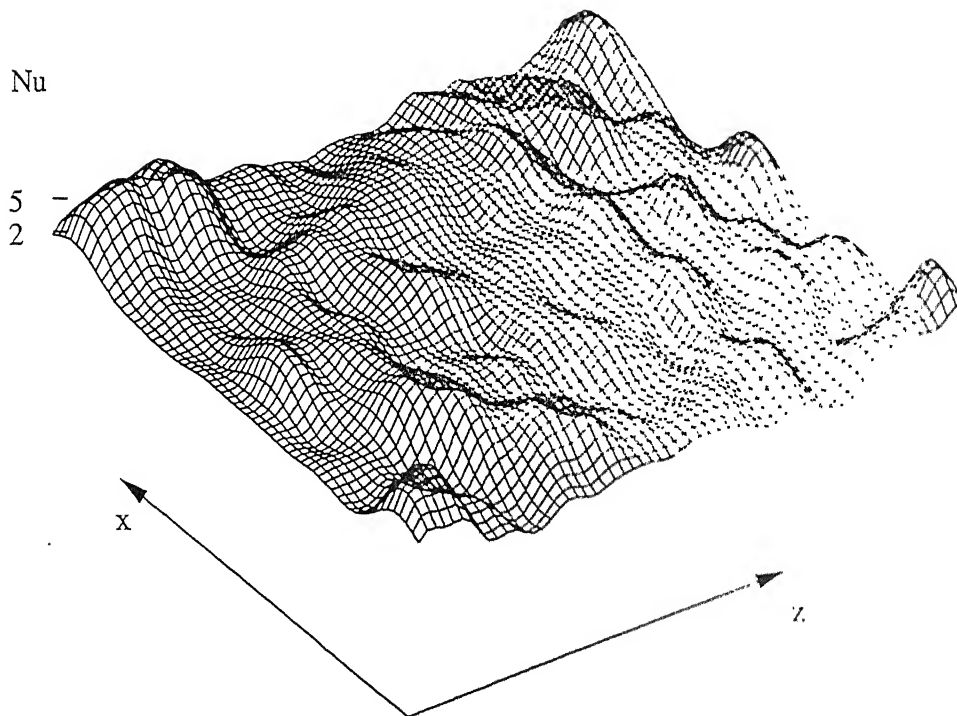


Figure 6.32: Nusselt Number Surfaces for Top and Bottom Plates, $Ra=13900$

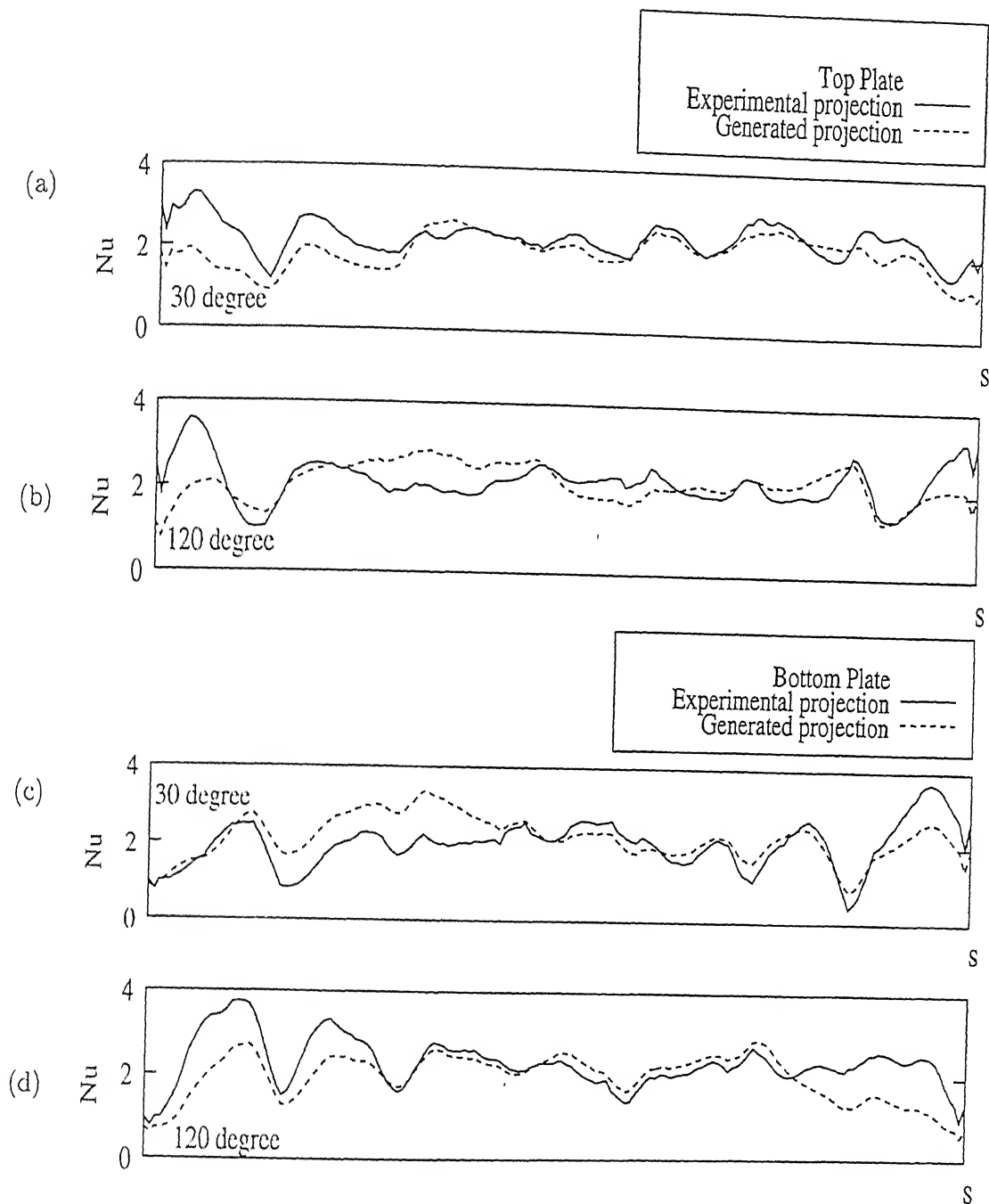


Figure 6.33: Comparison of Experimentally obtained Line Integrals of the Nusselt Number with Numerically Generated Line Integrals of the Nusselt Number for Projection Angles not used in Tomography, $Ra=13900$

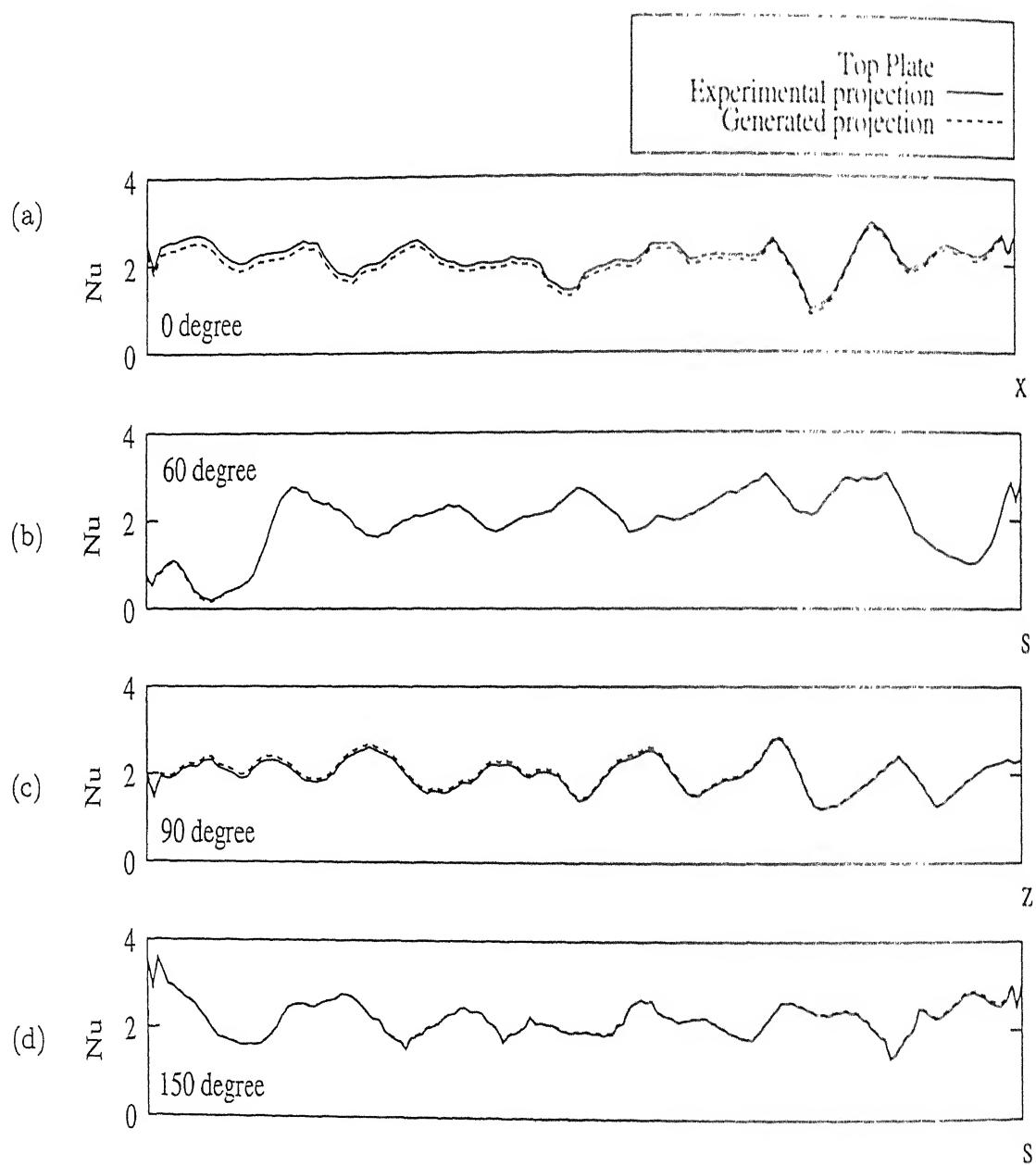


Figure 6.34: for caption see next page

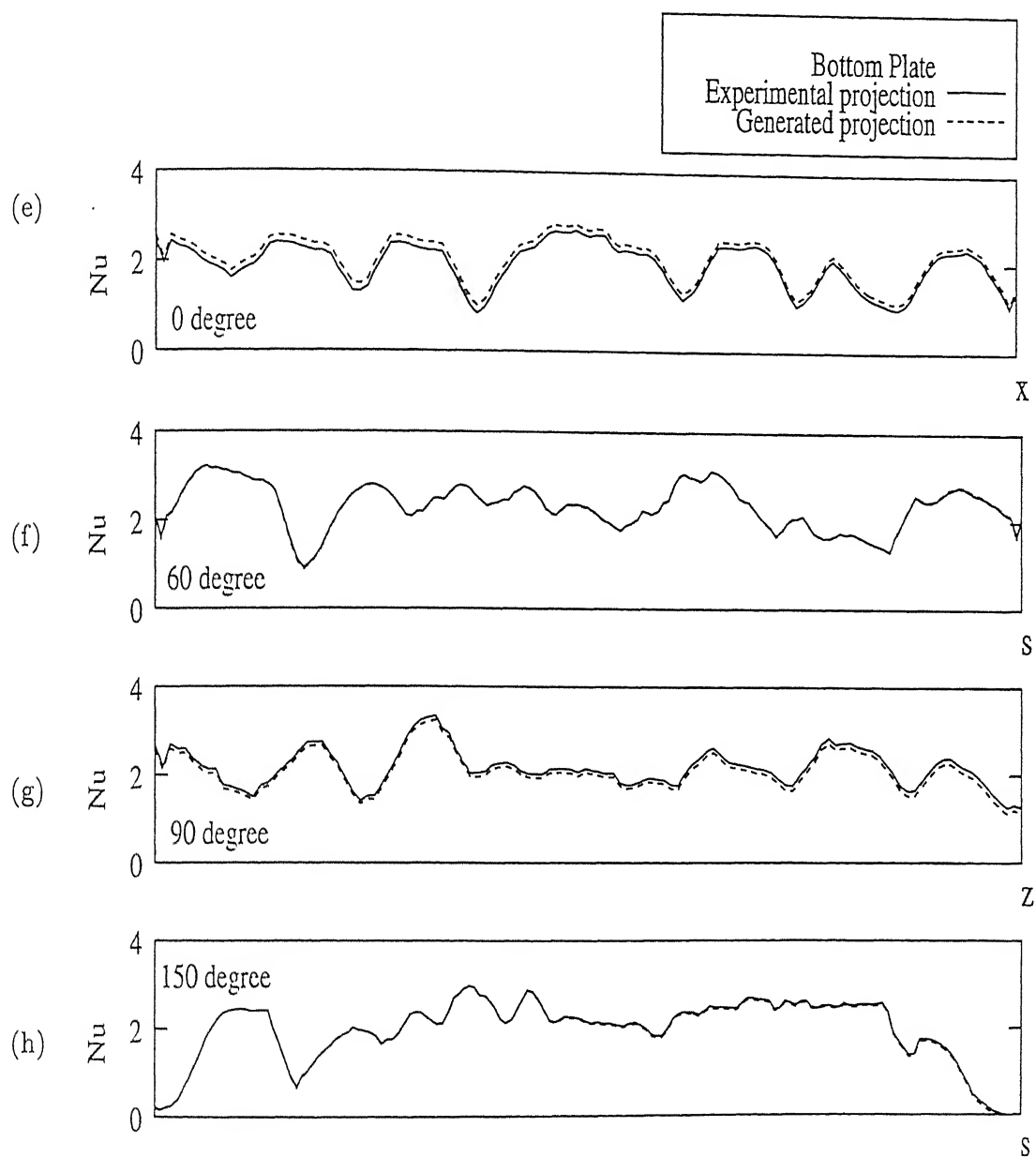


Figure 6.34: Comparison of Experimentally obtained Line Integrals of the Nusselt Number with Numerically Generated Line Integrals of the Nusselt Number from the Reconstructed Temperature Field, $Ra=13900$

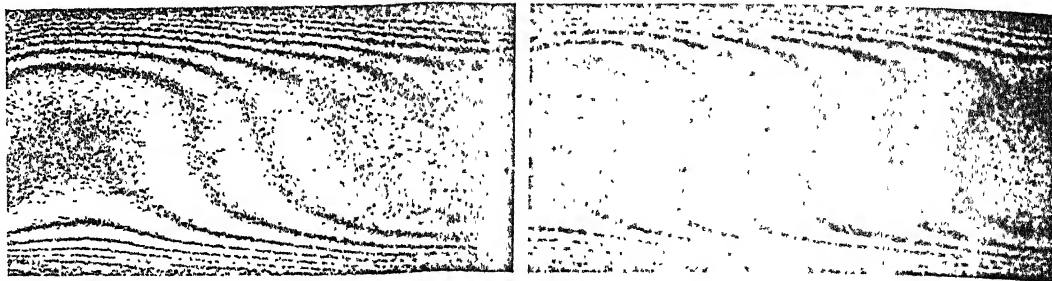


Figure 6.36: Interferograms of the Central Region of the Fluid Layer, 0° Projection (left) and 90° Projection (right), $Ra=34800$

a cubic cell finds support in the numerical calculations of Mukutmoni and Yang (1995). These authors have reported the formation of polygonal cells in this range of Rayleigh numbers for intermediate aspect ratio enclosures.

The cubic cell forms the basis of reconstructing the full three dimensional temperature field. The projection data (within a cell) of 0 and 90° was spread out individually till it filled the apparatus. This was the full field data (for $Ra=34800$) necessary for reconstruction using two projections.

Results of tomographic reconstruction for Rayleigh number of 34800 are presented here. Temperature surfaces and isotherms are shown at selected horizontal planes within

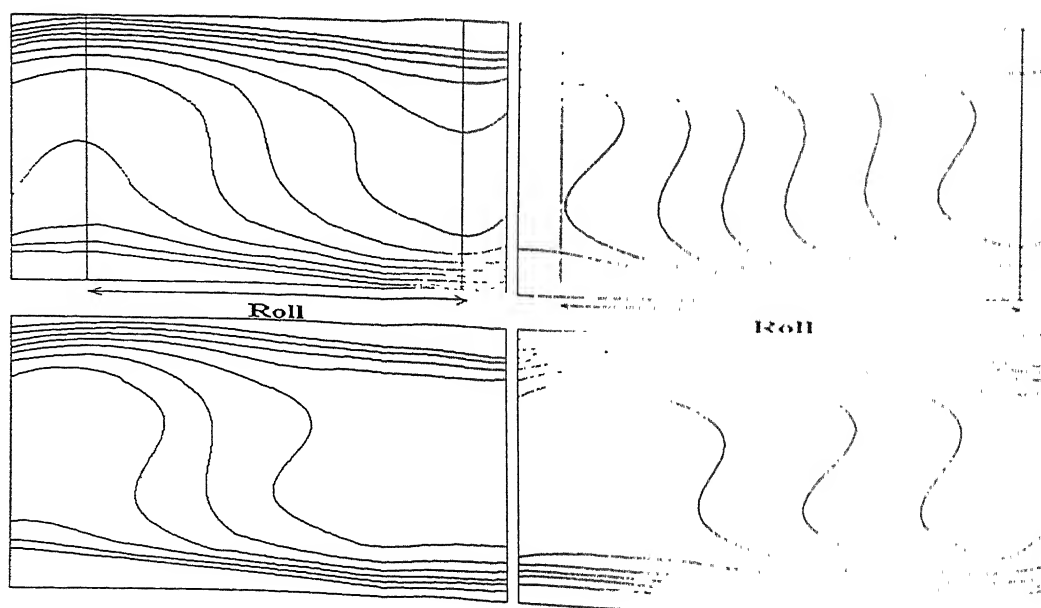


Figure 6.37: Thinned Images, Top left 0°, Top right 90°, Bottom left 30° and Bottom right 60°, $Ra=34800$

the fluid layer in Figure 6.38. To facilitate interpretation of the results, a collection of 4 adjacent cubic cells is considered. The assembly is formed in such a way that the cells have a common vertical axis at the center. The layer height is divided into 21 horizontal planes. Temperature surfaces and isotherms are presented in Figure 6.38 at the 4th, 11th and 18th planes respectively. These planes are located at $y/h = 0.15, 0.5$ and 0.85 measured from the cold top surface. Near the cold wall, the fluid temperature is generally low, except in the middle. The size of the heated region increases as one moves towards the lower hot wall. In any particular cubic cell, (which is one quarter of the region shown in Figure 6.38), the diagonal plane divides the heated fluid on the left and the cooled fluid to the right. It should be noted that this is possible only if the accompanying velocity field is truly three dimensional.

The trajectories of fluid particles as they move among the cubic cells is of special interest in visualizing the flow field. To this end, the following observations have been noted. For the assembly of 4 cells, there exists in Figure 6.38 an isolated vertical region at the center which is at a higher temperature compared to the rest of the fluid. Secondly, contour plots in Figure 6.38 show that hot and cold fluid lie adjacent to each other within a cubic cell, separated by a diagonal plane. The second observation can be interpreted in the following manner. The fluid motion associated with the thermal field is a roll, moving the hot mass of fluid from the lower surface against the cold top wall, to be followed by the descent of a cold body of fluid. Thus, the assembly of four cells enclose a set of four rolls, all of which raise hot fluid jointly along the central vertical axis. While it is possible to identify a cubic cell that is isolated from a thermal viewpoint, it should be noted that the associated velocity field need not be isolated. In fact, the velocity fields in individual cubic cells will interact and an orderly pattern for flow can be discerned only over a collection of cells.

A flow model that integrates all aspects of the temperature contours shown in Figure 6.38 is the following. The assembly of four cells supports the picture of a central hot plume ascending like a buoyant fountain in the middle and distributing the cold fluid in the four quadrants from above, almost symmetrically. The plume broadens as one approaches the hot wall. The plume model explains the origin of hot and cold fluid lying adjacent to each other in any particular cubic cell. It also explains the consistently high temperatures that prevail along the vertical edge of the cell, the edge being a part of the plume center. As seen in Figure 6.38, the plume cross-section is closer to an ellipse, and not a circle, simply

6.2 Convection at $Ra=34800$ and 40200

Analysis of results from the experiments at a Rayleigh numbers of 34800 and 40200 are presented next. In this range of Rayleigh numbers experiment, formation of a hot buoyant plume arising from the bottom plate and advancing towards the cold top plate has been observed. Since the discussion is based on two views, structures referred below are to be interpreted as representative of the flow field.

In the range (34800 - 40200) of Rayleigh numbers, the fringes exhibited some time dependence. Specifically, the flow was seen to switch between two states in a fully repeatable manner. Of the two states, one was more dominant than the other and this mode alone has been analyzed in the present work. The unsteadiness in the flow field was seen to introduce uncertainty in the projection data, particularly with an increasing number of projections. A large uncertainty in projection data would be amplified during reconstruction, particularly with a large number of view angles. To keep the reconstruction errors below an acceptable limit, only two views (0 and 90°) have been employed in the analysis. For the Rayleigh number of 34800 , the flow field was analysed by considering partial projection data from 0 and 90° angles. This suggested the formation of a buoyant plume in the fluid layer. To get a clear picture of the flow field, a detailed experiment was carried out at a Rayleigh number of 40200 . Here the entire fluid layer was considered and interferometric projections were recorded over the fluid layer by using the traversing mechanism. Since flow field was seen to be time dependent, at each scanning location the most dominant structure observed was stored. Several such projections were recorded at each location. Later on these projections were joined and the set giving the best continuity of the fringes alone were analysed. All data has been recorded after a considerable passage of time, and hence do not contain information about the initial transients.

The switching phenomenon responsible for the formation of two modes of convection in the fluid layer is itself a topic of interest. It is indicative of an intermediate step in transition towards chaos. In the present study, it has not been possible to capture the momentary appearance of the second mode owing to limitations in the instrumentation. A visual examination however showed this mode to comprise of straight fringes. This suggests two dimensionality and hence points at the formation of a longitudinal roll. The estimated time scale of the problem is in the range of 10 seconds, corresponding to a frequency of 0.1 Hz. Frequencies of this order can be seen in the LIDV study of supercritical

Rayleigh-Benard convection of Gollub and Benson (1980). Figure 6.35 shows the modes of switching observed in the fringe pattern.

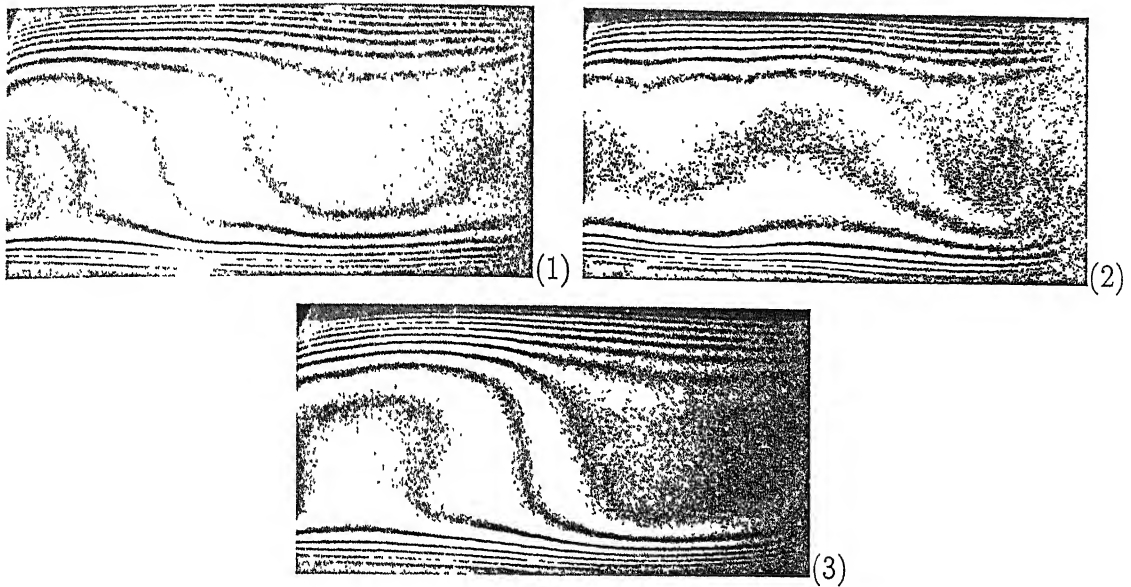


Figure 6.35: The Sequence of Fringe Patterns Formed during the Switching phenomenon, Cubic Cell Pattern (1st) Longitudinal Rolls Pattern (2nd) and back to Cubic Cell Pattern (3rd), $Ra=34800$

The discussion pertaining to the dominant mode of convection in the fluid layer is now taken up at a Rayleigh number of 34800. The original interferograms for the 0° and 90° projections are shown in Figure 6.36. A closer look at the fringe patterns for these projections shows that they indicate the formation of a cubic structure, though not with edges of equal length. The cell boundary for each of the projections can be identified by utilizing fringes that experience maximum displacement from the horizontal surface. The cell boundary is made to pass through the location where the fringe slope is zero. Cell structure thus identified is shown in Figure 6.37. This procedure is meaningful because the cell now encloses a roll, with hot fluid rising along the left boundary and descending along the right. Interferograms of a repeating structure (such as a cubic cell) will show symmetry about the center at other projection angles but will not be repetitive. Hence they cannot be used directly to support the formation of such a structure.

The cell dimensions computed from Figure 6.37 (0° and 90° projection) are 1.75:1:2.01 in the x , y and z directions, y being the vertical. These dimensions are specific to the choice of a Rayleigh number of 34800. One can expect them to be independent of the aspect ratio since the fluid layer studied in the experiment is large. The formation of

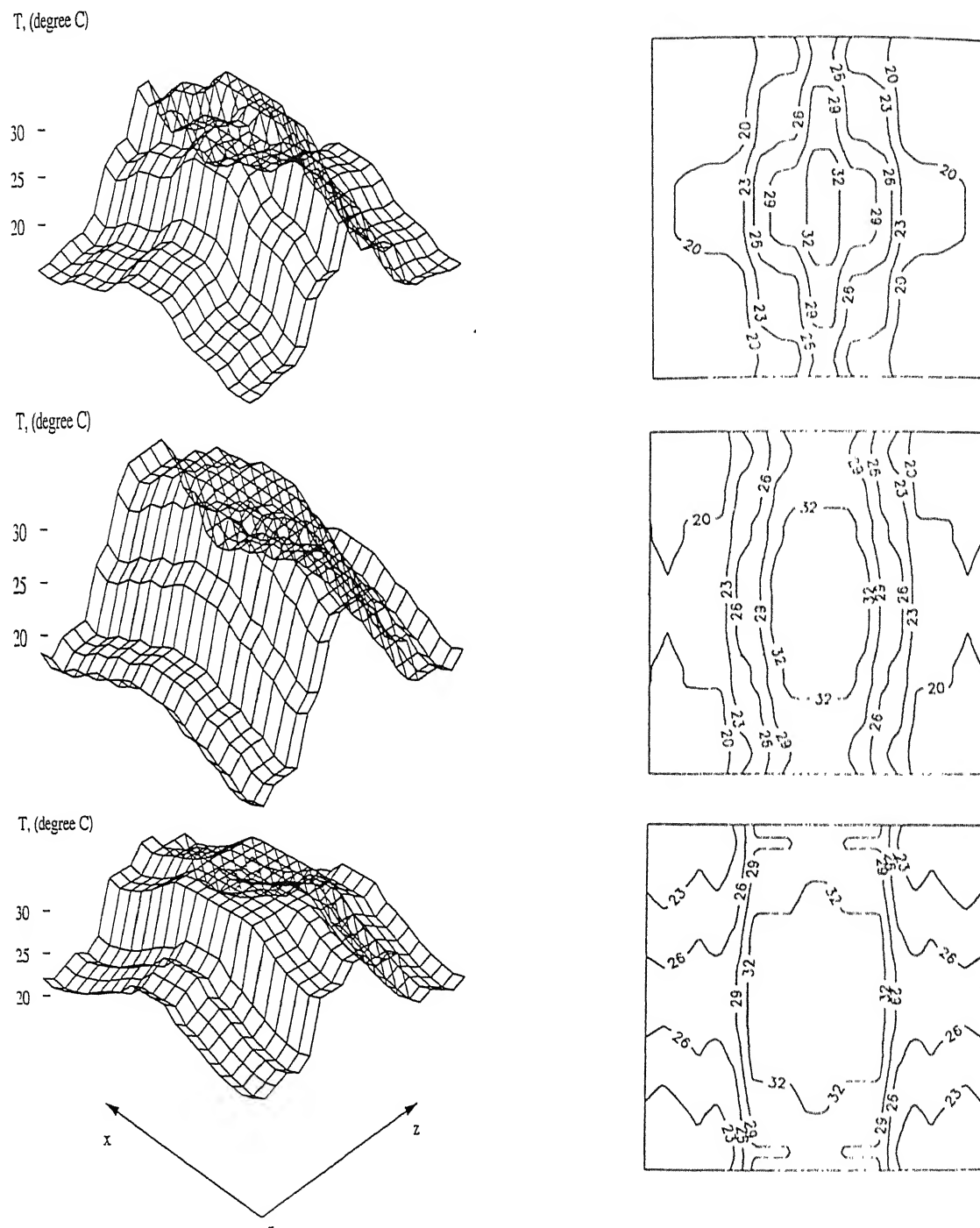


Figure 6.38: Reconstructed Temperature Surfaces and Isotherms over Three Horizontal Planes of the Fluid Layer, $y/h = 0.15$ (top), $y/h = 0.5$ (middle) and $y/h = 0.85$ (bottom), $Ra=34800$

because the cubic cell has unequal edges.

Buoyant plumes have been observed in various studies and is well-documented (Gebhart *et al.*, 1988). Most of the experiments on this subject have employed a direct flow visualization strategy, primarily in liquids. The appearance of a plume in the present experiment from tomographic calculations based on interferometric data (from an arbitrary initial guess of a constant temperature field) reinforces the correctness of the measurement on the whole.

Figure 6.39 shows a comparison between the variation of the line-averaged Nusselt number along the two plates at Rayleigh number of 13900 corresponding to formation of rolls and 34800 corresponding to cubic cells. The data is presented over a collection of 2 rolls and 2 cubic cells. At Rayleigh number of 13900, the shape of the Nusselt number curve correlates well with the identified flow pattern, namely the formation of longitudinal rolls. The Nusselt number variation over the two plates are of opposite orientation, showing the roll to be inclined (Figure 6.39(a)). Along the 0° view angle the Nusselt number variation at the two surfaces are very similar, confirming the formation of a roll that stretches along the length of the cavity (Figure 6.39(b)).

At Rayleigh number of 34800, it is expected that when seen either from 0° or from 90° view angle the Nusselt number of the bottom plate should be maximum on the two sides of the plume and a minimum at the center. An opposite-trend for the Nusselt number is expected at the top plate. These expectations are clearly realized in Figures 6.39(c-d). The Nusselt number surfaces for the hot and the cold surfaces are thus seen to be complimentary.

The local ray-averaged Nusselt numbers presented in Figure 6.39 have been numerically integrated to obtain the global average Nusselt number for each of the plates. This is equivalent to using the width-averaged temperature profile of the projection data. The average Nusselt numbers have been compared with the empirical correlation reported by Gebhart *et al.* (1988) in Table 6.4. Given the uncertainties in the empirical correlation as well as the limited data in the present set of experiments, the overall comparison may be taken as favourable.

The results for the complete experiment at a Rayleigh number of 40200 are presented next. Here the entire fluid layer was mapped along the 0 and 90° projections and 2-view tomography was employed for reconstruction. Besides this, for view angles of 30 and 60° , projections of the near-central region of the cavity over a width of 6.2 cm were

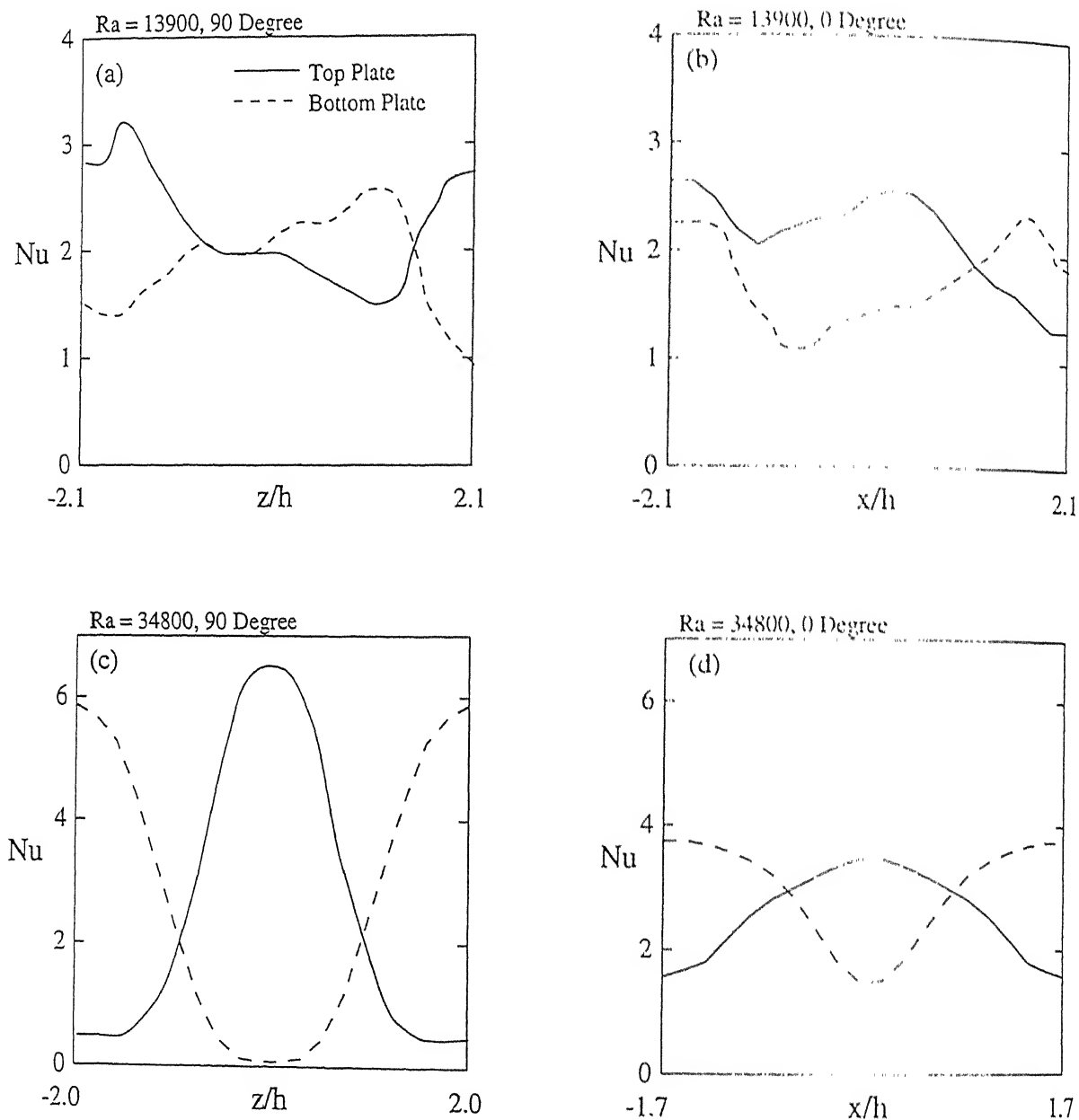


Figure 6.39: Comparison of the Ray-averaged Nusselt Number for the Top and the Bottom Plate

collected to serve as a cross check for the reconstructed field. Figure 6.40 shows the original interferograms at various locations and assembly of a set of three interferograms as seen from the 0° view angle. Interferograms for the 90° view angle is shown in Figure 6.41. Each individual interferogram shown corresponds to a physical dimension of 6.2 cm. Figure 6.42 shows the original interferograms for the 30° and 60° view angles for the central region of the fluid layer covering a width of 6.2 cm. The thinned images corresponding to

Table 6.4: Comparison of the Average of the Ray-averaged Nusselt Number with Gebhart *et al.*, 1988, $Ra=34800$.

Ra	Nu (Cold)	Nu (Hot)	Nu (Av)	Nu (Ref)
13900	2.16	2.12	2.14	2.59
34800	2.52	2.98	2.75	3.18

these interferograms are shown in Figures 6.43-6.44.

The temperature surfaces namely the temperature variation over horizontal planes are shown in Figures 6.45-6.47. Three horizontal planes, namely $y/h=0.15, 0.5$ and 0.85 have been considered. A clearer picture emerges when isotherms at the corresponding planes over an assembly of four adjacent cells is examined. This is shown in Figure 6.48. Here, each cell corresponds to a small portion of the cavity reconstructed from the interferograms. On assembly, the collection of temperature surfaces over the three planes clearly shows the structure of a rising plume. The repeating roll-like structure seen from both the 0 and 90° view angles suggests that a cubic cell exists inside the cavity.

Figures 6.48 shows that the size of the heated region increases as one moves towards the heated lower wall. The buoyant plume rises from the center of the cluster of 4 adjacent repeated cubic cells. Each cubic cell can be visualized as being divided along its diagonal plane with high and low bulk fluid temperatures on each side. Thus, the fluid rising along the center descends uniformly around the plume in the four quadrants. The assembly of four cells enclose a set of four rolls, all of which raise hot fluid jointly along the central vertical axis which after being cooled, descends all around towards the lower surface. This observation is similar to the one seen for a Rayleigh number of 34800 where only partial projection data at limited view angles were employed for reconstruction of the thermal field.

A flow model that integrates all aspects of the temperature contours shown in a schematic diagram in Figure 6.49. This figure shows the hot mass of fluid rising in the form of a buoyant fountain from the center of the four adjacent cubic cells and distributing the cold fluid in the four quadrants from above, almost symmetrically. When viewed from any direction this flow field will show a roll-like repeating structure. The recorded interferograms at 30 and 60° view angles also shows a roll like pattern. The plume cross-section is not seen to be of any definite shape but is closer to an ellipse than a circle.

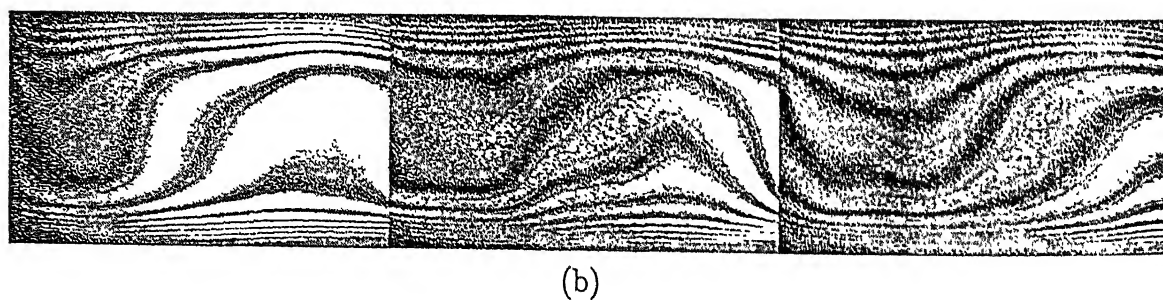
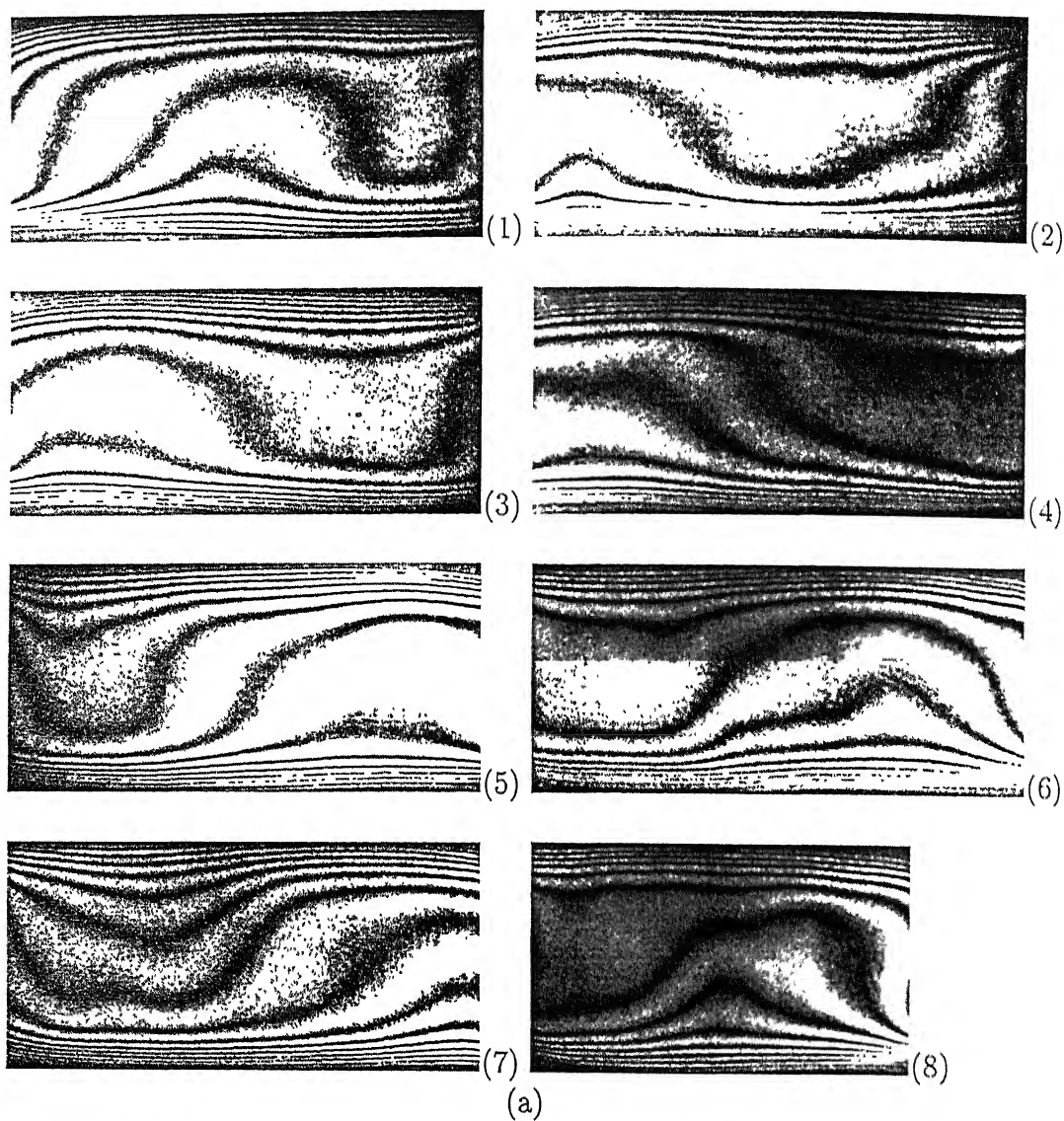


Figure 6.40: (a) Original Interferograms at Neighbouring Locations of the Fluid Layer and (b) Collection of Interferograms, 0° Projection, $Ra=40200$

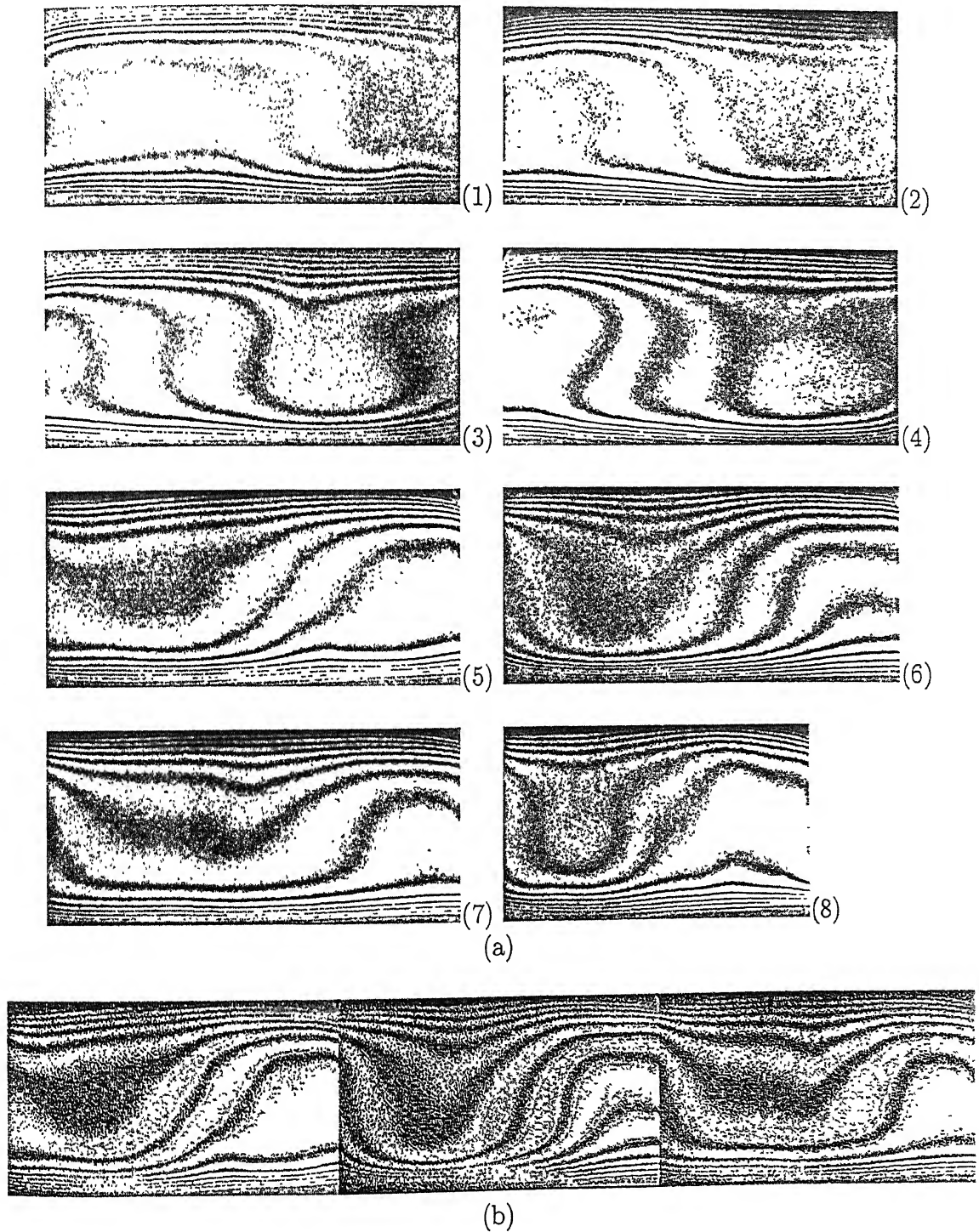


Figure 6.41: (a) Original Interferograms at Neighbouring Locations of the Fluid Layer and (b) Collection of Interferograms, 90° Projection, $Ra=40200$

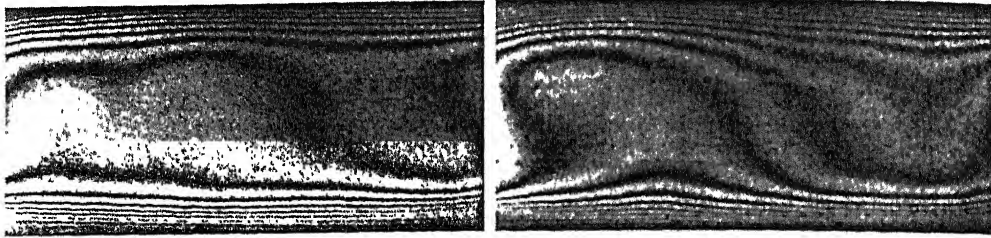


Figure 6.42: Original Interferogram at the Central Layer of Fluid Region, 30° Projection (left) and 60° Projection (right), $Ra=40200$

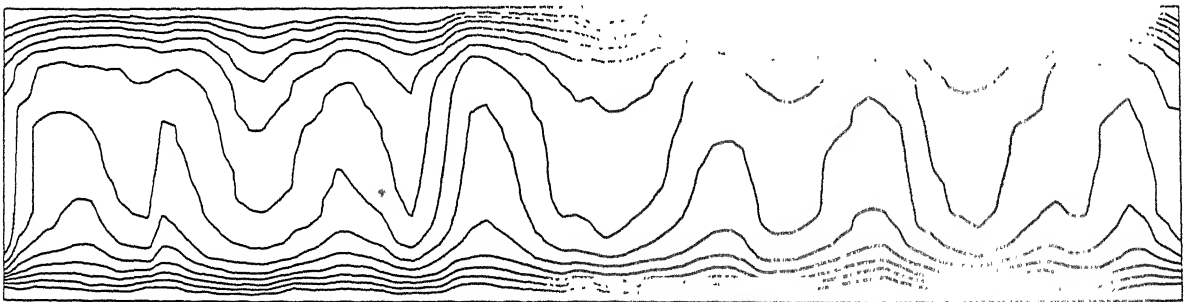


Figure 6.43: Collection of Thinned Images, 0° Projection, $Ra=40200$

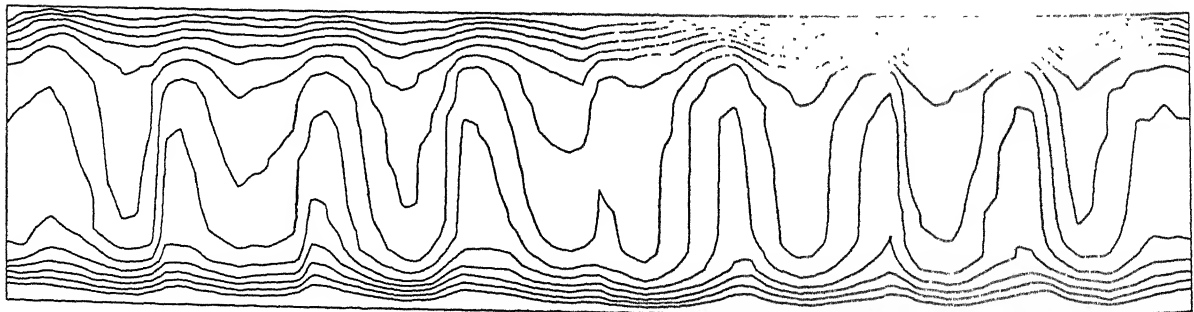


Figure 6.44: Collection of Thinned Images, 90° Projection, $Ra=40200$

$y/h=0.15$, $Ra=40200$

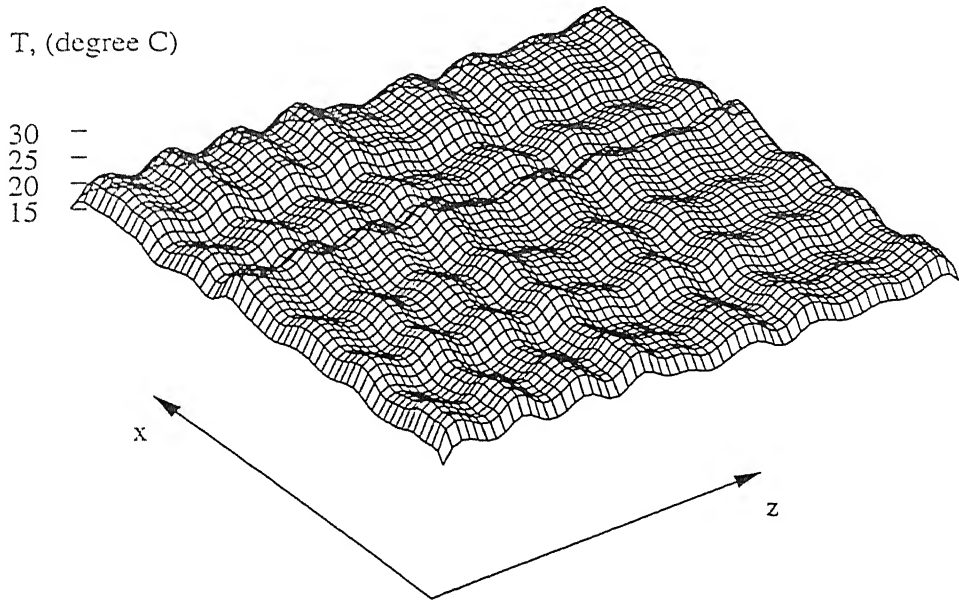


Figure 6.45: Reconstructed Temperature Surface at $y/h = 0.15$, $Ra=40200$

$y/h=0.5$, $Ra=40200$

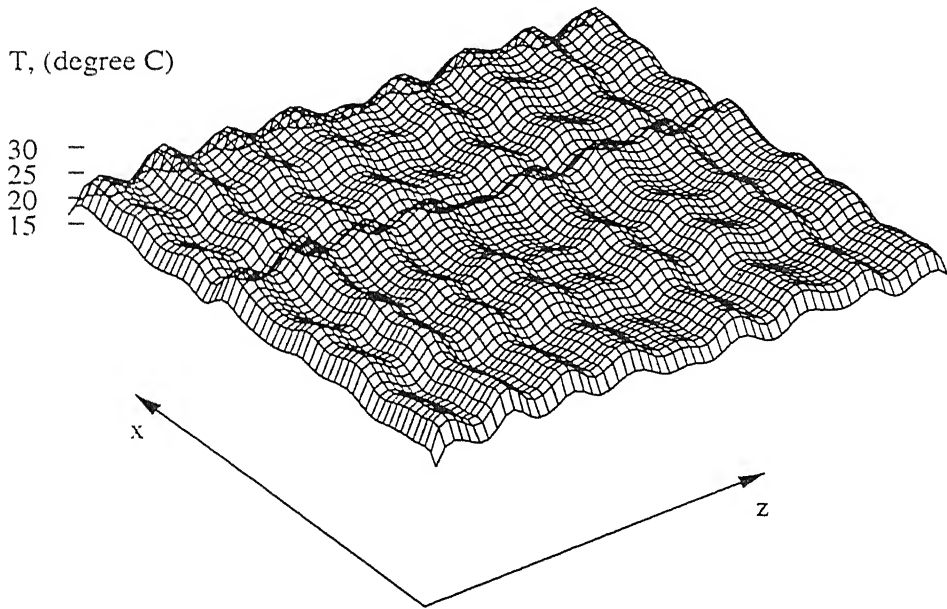


Figure 6.46: Reconstructed Temperature Surface at $y/h = 0.5$, $Ra=40200$

$y/h=0.85$, $Ra=40200$

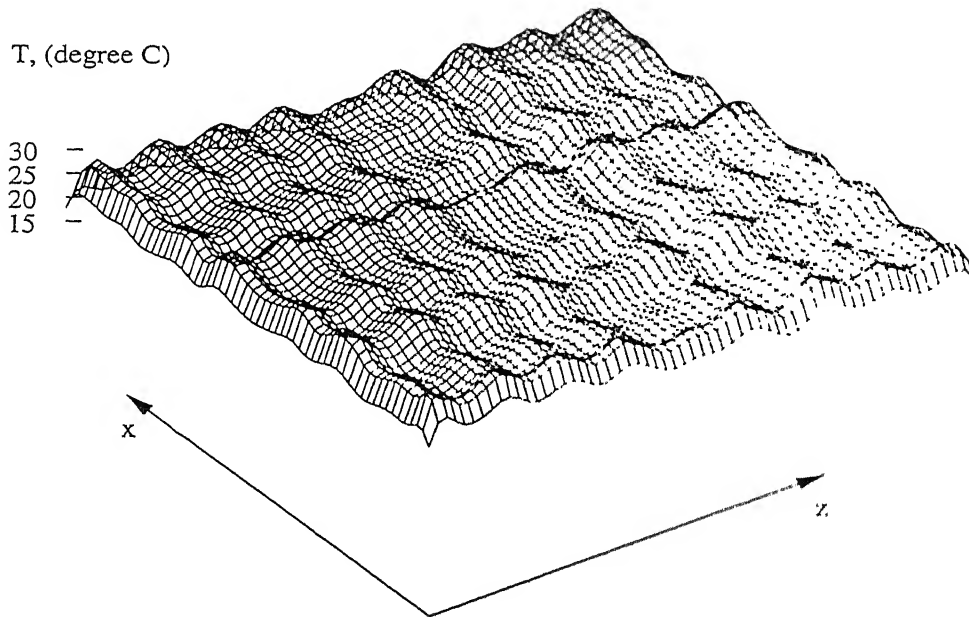


Figure 6.47: Reconstructed Temperature Surface at $y/h = 0.85$, $Ra = 40200$

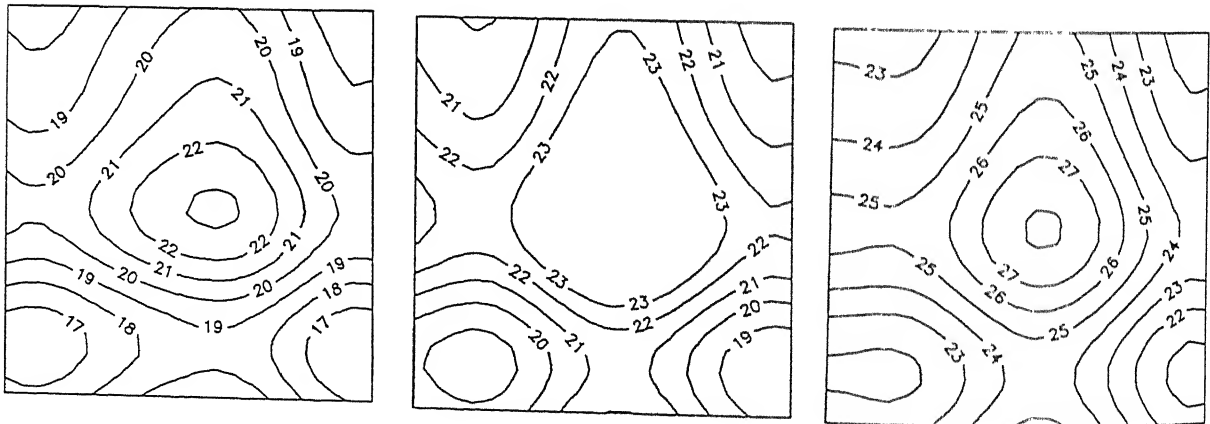


Figure 6.48: Isotherms over a Horizontal Plane at $y/h = 0.15$ (left), $y/h = 0.5$ (middle) and $y/h = 0.85$ (right), $Ra=40200$

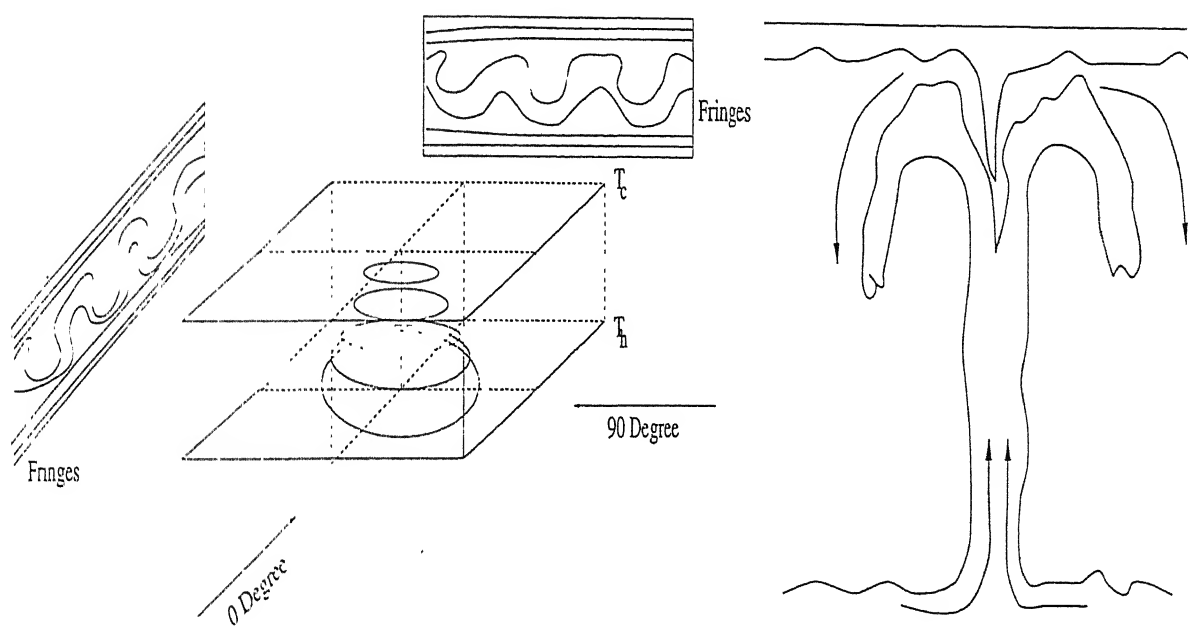


Figure 6.49: Schematic of the Cubic Cells and the Rising Plume Inside the Cavity

6.2.1 Cross-checks on Reconstructed Temperature Field

The cross-check at the Rayleigh number of 40200 for 30 and 60° projections is presented next. The comparison between the experimentally obtained data and the numerically generated projections for a given angle is shown in Figure 6.50. The thinned images shown are isotherms in the central region of the cavity over a width of 6.2cm. The correspondence between the two sets of isotherms is close near the two walls. However the agreement in the region away from the walls is questionable and at best qualitative. This difference can be attributed to two factors: (1) Only two projection angles have been employed for reconstruction. Hence minor details visible from other angles have not been captured. (2) The unsteadiness in the fringe patterns during experiments was mainly confined to the central fringes. This led to partial decorrelation among the images. Thus the reconstructed field in the layers away from the walls is perhaps an average effect of the slow time-dependent fringe oscillations.

6.2.2 Local and Average Heat Transfer Rates

As in Section 6.1.5, wall heat transfer rates are presented in terms of the Nusselt number. Results for Nusselt number at a Rayleigh number of 40200 are presented here. The Nusselt number averaged over the entire surface are given in Table 6.5. These have been compared with the correlation given by Equation 6.2. The agreement between the Nusselt numbers of the present work and Equation 6.2 can be seen to be close. Specifically, the Nusselt number computed from the experiments is within 1.5 % for a Rayleigh number of 40200 and within 14 % for a Rayleigh number of 34800 with respect to the empirical correlation.

The variation of the line-of-sight averaged Nusselt number with distance closely reflects the flow pattern in the cavity. As in the case of $Ra=13900$, these have been computed directly from the interferograms and are shown in Figure 6.51 for $Ra=40200$. Both 0 and 90° projections have been presented.

Since a roll-like structure can be seen from both view angles, the Nusselt number variation is expected to be oppositely oriented for the two active surfaces. This result is clearly brought out in Figure 6.51. The line-of-sight averaged Nusselt numbers were also computed from the reconstructed (fully three dimensional) temperature field. The comparison between the reconstructed and the original local Nusselt numbers is presented

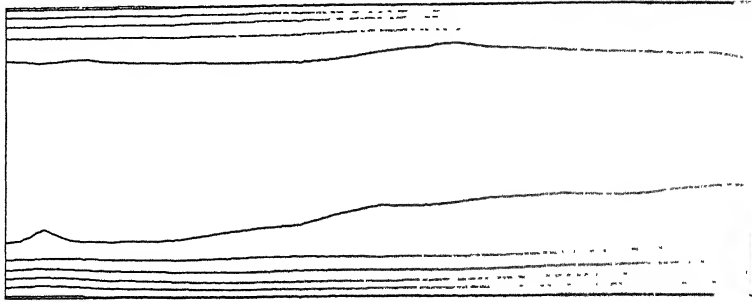
Table 6.5: Comparison of Average Nusselt Number with Gebhart *et al.*, (1988), $Ra = 40200$

Projection Angle in Degree	Nu (Cold)	Nu (Hot)	Nu (Average) From All Angles	Nu (Reference)
0	3.22	3.30	3.32	3.28
90	3.48	3.30		

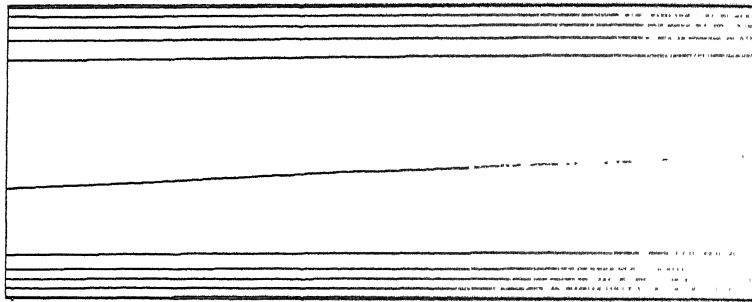
in Figure 6.52. For the 0 and 90° view angles that have been employed in reconstruction, the comparison for both surfaces is excellent. Figure 6.53 also shows the comparison for 30 and 60° view angles that were not used for reconstruction. The comparison is qualitatively good but differences upto 22% are to be seen. The Nusselt number surfaces over the two bounding planes are shown in Figure 6.54. These surfaces are clearly oppositely oriented at the hot and cold walls. This confirms that when visualised from any angle, the resulting fringe pattern will be a roll-like repeating structure. It strengthens the suggestion made earlier that the flow field is in the form of a buoyant plume.

6.3 Convection at $Ra=51800$

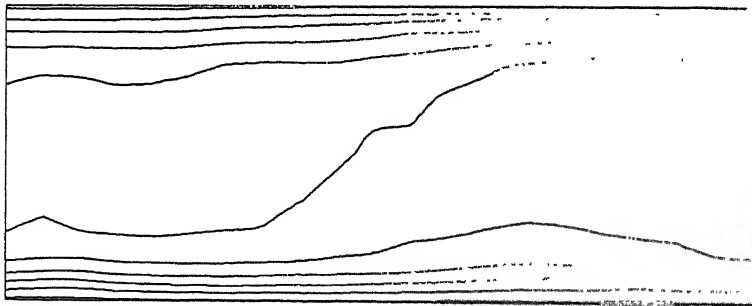
For a Rayleigh number of 51800, the fringes were seen to change continuously from one pattern to another and no specific periodicity was observed. Hence the present strategy of collecting projections of different sections of the fluid layer at different times could no longer be adopted. What is required is simultaneous scanning of the flow field for the entire width of the fluid layer at various angles. The sequence of thinned images obtained at a Rayleigh number of 51800 are shown in Figure 6.55. The total time over which the images were recorded in Figure 6.55 is around 10 minutes, at approximately equal intervals. The temperature field and the associated velocity field at this Rayleigh number is already turbulent. Since the interferometric projections show rapid change in pattern without any noticeable periodicity, one can conclude that no stable mean flow is present.



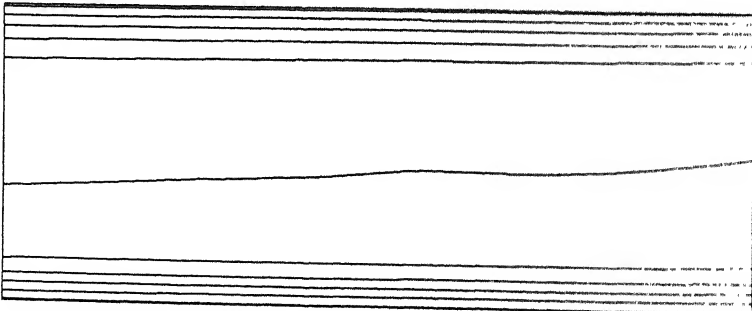
(a) Experimental Projection (30°)



(b) Generated Projection from Reconstructed Temperature Field (30°)



(c) Experimental Projection (60°)



(d) Generated Projection from Reconstructed Temperature Field (60°)

Figure 6.50: Comparison of Experimentally obtained Thinned Images with Generated Projections for Cross-check of Reconstructed Temperature Field, $Ra=40200$

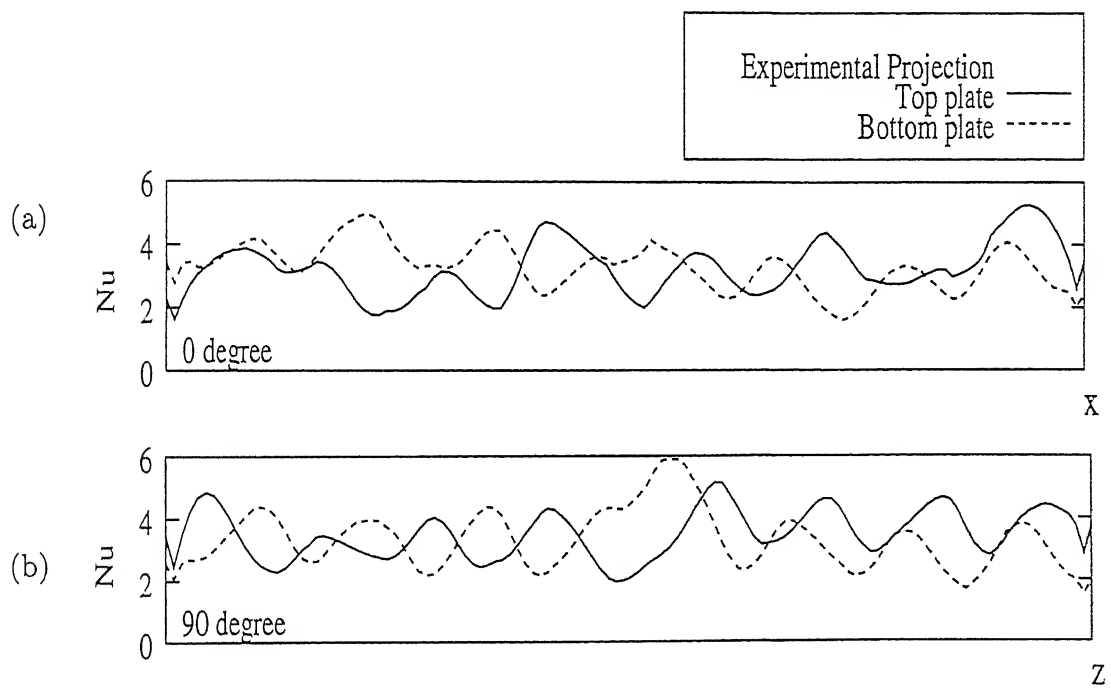


Figure 6.51: Experimentally obtained Line Integrals of the Nusselt Number for both the Plates, $Ra=40200$

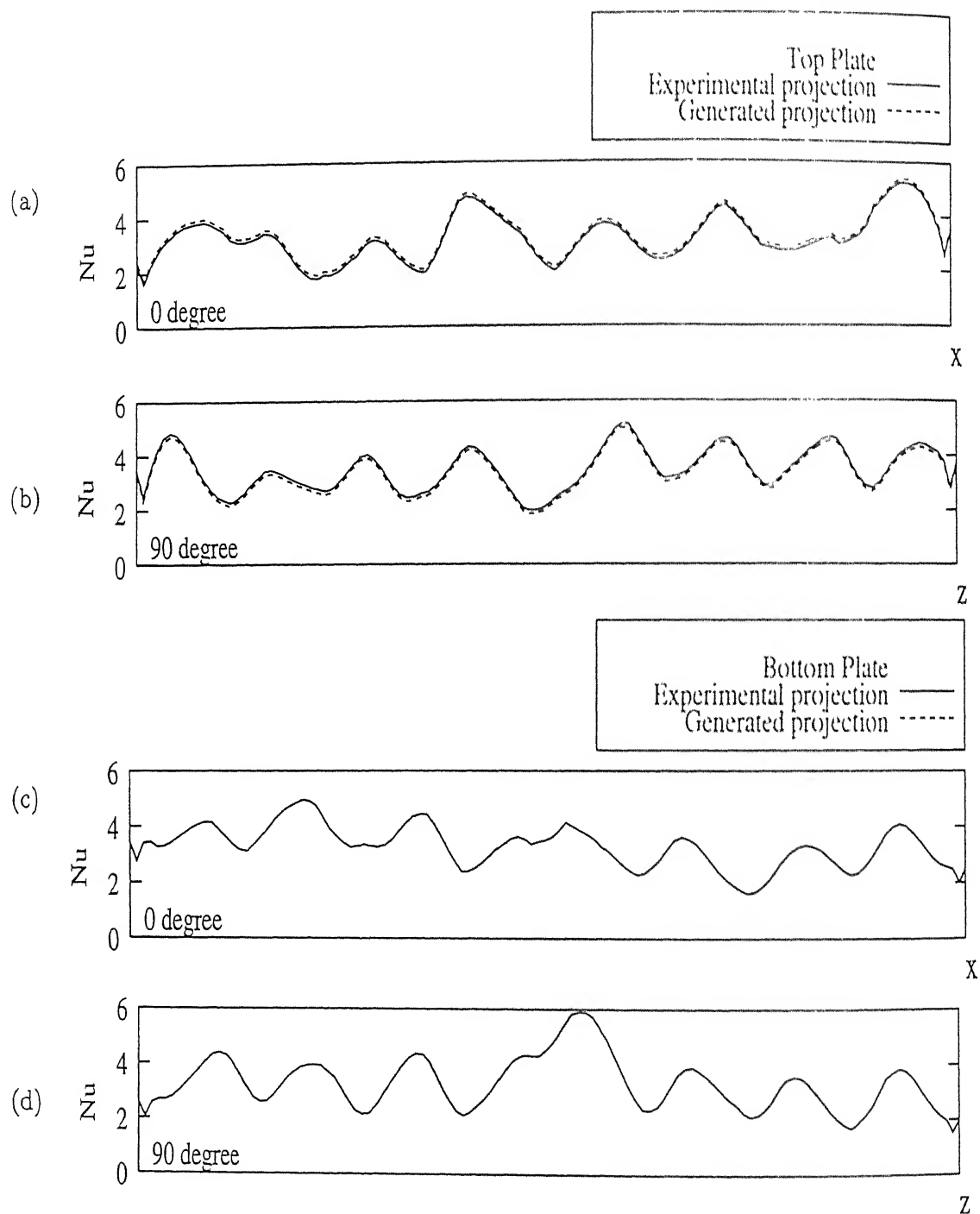
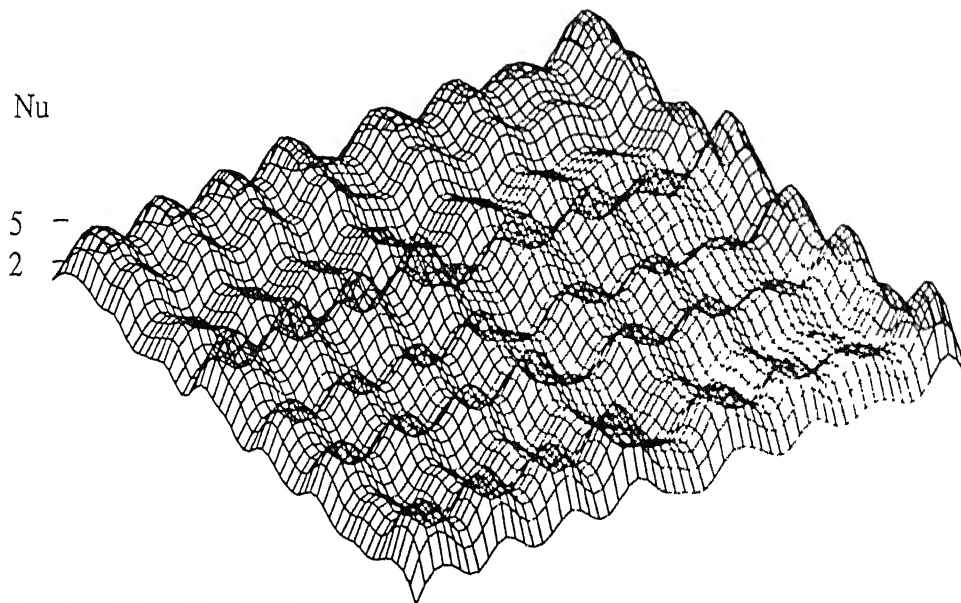


Figure 6.52: Comparison of Experimentally obtained Line Integrals of the Nusselt Number with Numerically Generated Line Integrals of the Nusselt Number from the Reconstructed Temperature Field, $Ra=40200$

Top plate, $Ra=40200$



Bottom plate, $Ra=40200$

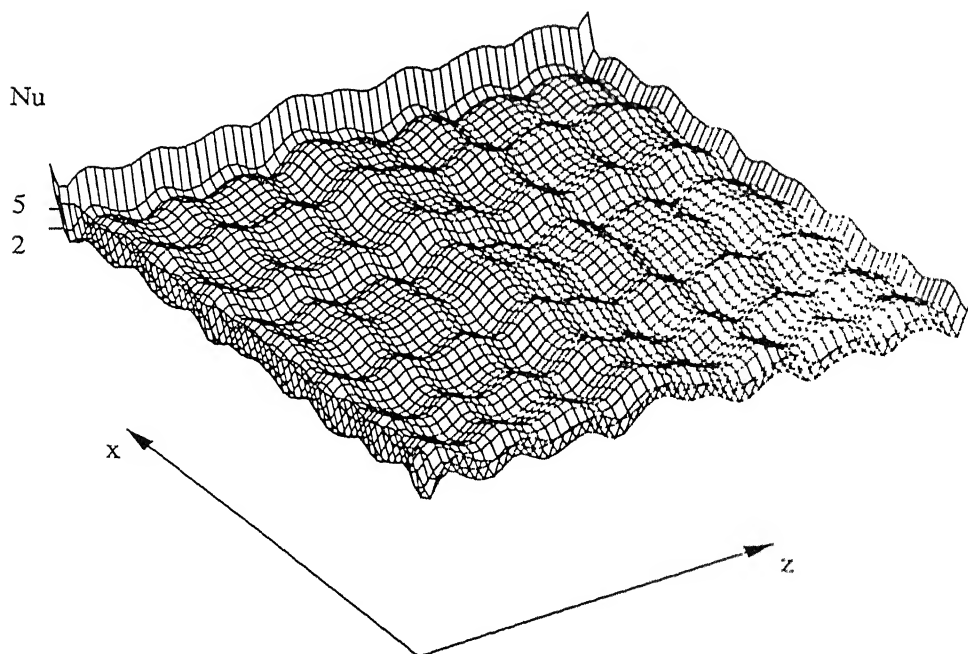


Figure 6.54: Nusselt Number Surfaces for Top and Bottom Plates, $Ra = 40200$
The high Nusselt numbers along the boundary of the lower plate correlates with the low Nusselt numbers of the top plate.

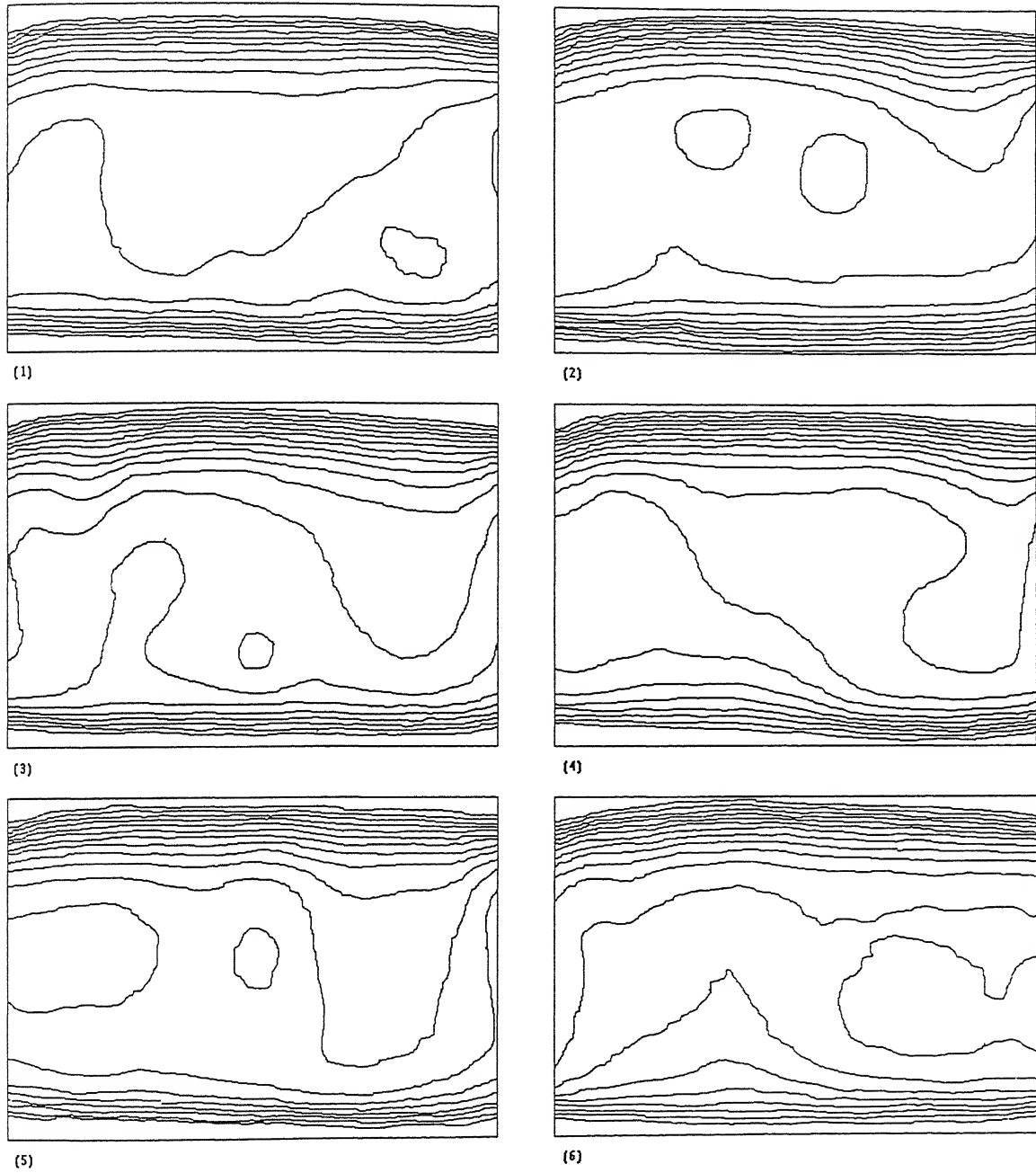


Figure 6.55: Sequence of Fringe Patterns in Unsteady Convection at $Ra=51800$

Chapter 7

Conclusions and Scope for Future Work

7.1 Conclusions

Convection experiments were conducted in an intermediate aspect ratio, differentially heated fluid layer that is square in plan. The thermal field was mapped using a Mach-Zehnder interferometer. The three dimensional temperature field in a fluid layer was reconstructed from its interferometric projections. Four different Rayleigh numbers equal to 13900, 34800, 40200, and 51800 were considered. Tomographic inversion was carried out for three of these Rayleigh numbers namely 13900, 34800 and 40200. The fringes formed at a Rayleigh number of 51800 were found to be unsteady and rapidly moving with time. Hence the corresponding interferograms could not be analysed.

A modified version of the MART algorithm (called AVMART2) was used for tomographic inversion of the interferometric images. The algorithm converged without ambiguity to the final solution and did not display excessive sensitivity to the initial guess, relaxation factor and noise in the experimental data. The reconstructed field was seen to be fully consistent with the projection data. The reconstructed field was also seen to be in good agreement with the projection recorded but not used in the tomography calculations. The three dimensional field was seen to satisfy energy balance checks. The cavity-averaged Nusselt number computed from the interferometric projections was seen to be in reasonable agreement with published correlations, those in turn being based on

a wide variety of experiments.

At a Rayleigh number of 13900, the fringes were seen to be steady near the bounding walls, but mild unsteadiness was observed in the central horizontal layers. At the higher Rayleigh numbers of 34800 and 40200, the unsteadiness was more pronounced, with flow switching between two well-defined states. The interferograms corresponding to the dominant mode have been recorded and analyzed in the present work.

At a Rayleigh number of 13900, the flow field was seen to be organized in the form of a three dimensional structure. A 2-view tomographic calculation showed a set of longitudinal rolls as a dominant pattern in the fluid layer. The rolls could be identified from the orthogonal projections oriented parallel and perpendicular to the roll axis. The number of rolls was smaller than that based on the aspect ratio consideration. The roll also displayed three dimensionality along its axis. The complete reconstruction of the temperature field revealed interference of rolls boundaries and defects along the roll axis for example the formation of T and K patterns have been seen. However the mean flow as recorded by the interferometer was seen to be in the form of longitudinal rolls with superimposed three dimensionality.

At Rayleigh numbers of 34800 and 40200, the thermal field was seen to be organised in the form of cube-like cells that are repetitive over the fluid layer. The analysis of a collection of four cubic-cells revealed a centrally located buoyancy-driven thermal plume rising from the hot plate and descending all around it from the cold wall. The variation of the line-of-sight averaged Nusselt number as a function of a wall coordinate at each of the hot and cold surfaces was seen to be consistent with the proposed flow models at each Rayleigh number.

While the unsteadiness in the convection patterns have not been analyzed in detail, the present work has revealed the following: mild transients at $Ra=13900$, a switching between a dominant and a temporary mode at $Ra=34800$ and 40200 and chaotic convection at $Ra=51800$ indicating intermittency with two degrees of freedom as the possible route to chaos.

A summary figure showing the flow patterns in the fluid layer with increasing Rayleigh number is shown in Figure 7.1.

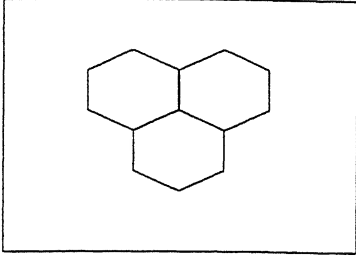
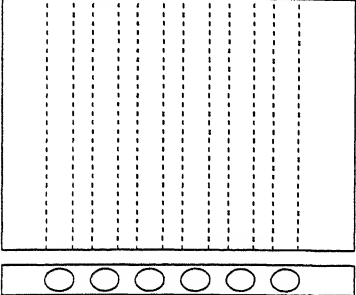
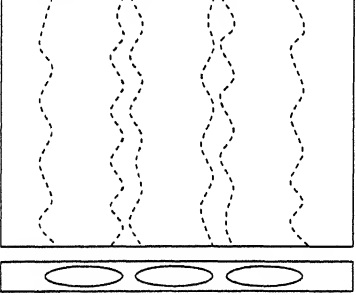
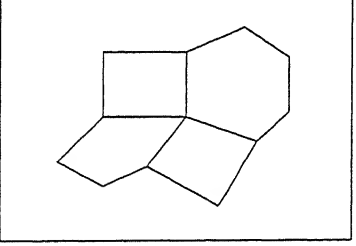
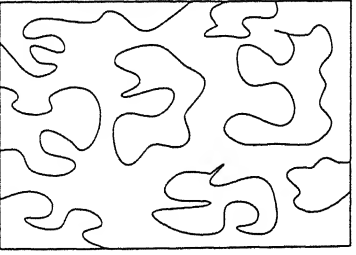
Transitions in Rayleigh-Benard Convection	Remarks	Source
	Onset of convection Hexagonal Cells $Ra > 1707$	Chandrasekhar, 1961
	Longitudinal Rolls Roll Size $\sim h$ Two Dimensional $Ra < 6000$	Krishnamurti, 1970
	Longitudinal Rolls Three Dimensional Roll Size Variable Mild Unsteadiness Loss of Roll $Ra < 15000$	1. Kolodner et al., 1986 2. Present
	Polygonal Cells Unsteady $Ra \sim 30000$	1. Mukutmoni and Yang, 1995 2. Present
	$Ra > 50000$ Completely Unsteady Turbulent	1. Gollub and Benson, 1980 2. Present

Figure 7.1: Summary of Flow Transitions in Rayleigh-Benard Convection

7.2 Scope for Future Work

The findings presented here generate interesting possibilities for research that can lead to a deep understanding of the physics of the Rayleigh-Benard convection. The present experiments show the presence of a mean flow in the form of longitudinal rolls and complete three dimensionality in the reconstructed temperature field. This suggests that the flow field known to be in the form of stable three dimensional rolls at a lower Rayleigh number, slowly undergoes a bifurcation towards a plume-like structure enclosed by cubic cells that are defined by the temperature field. The presence of these hidden rolls superimposed with three dimensional convection cannot be detected by conventional methods. Interferometry is a powerful tool available to reveal such flow configurations. The interferograms contain line-averaged temperature information and the local information can be recovered using tomography. Hence this is a powerful tool to investigate a very sensitive problems of fundamental interest.

There are a quite a few interesting problems that can be addressed in the future. These are:

1. Three dimensional reconstruction of a fully unsteady convective field.
2. Simultaneous reconstruction of temperature on all planes of the fluid layer to include ray-bending effects.
3. Rayleigh-Benard convection in axisymmetric geometries.
4. Interferometry for a two-layer (water-air) system and tomographic reconstruction of temperature at the interface, with and without curvature.
5. Computation of the velocity field from the temperature data.

References

- [1] Ahlers G. and Behringer R.P., 1978, Evolution of Turbulence from Rayleigh-Benard Instability, *Phys. Rev. Lett.* Vol. 40, pp 712-716.
- [2] Bahl S. and Liburdy J.A., 1991a, Measurement of Local Convective Heat Transfer Coefficients Using Three-dimensional Interferometry, *Int. J. Heat Mass Transfer*, Vol. 34, pp 949-960.
- [3] Bahl S. and Liburdy J.A., 1991b, Three Dimensional Image Reconstruction Using Interferometric Data from a Limited Field of View with Noise, *Applied Optics*, Vol. 30, No. 29, pp 4218-4226.
- [4] Busse F.H., 1985, Transition to Turbulence in Rayleigh-Benard Convection in *Topics in Applied Physics, Hydrodynamic Instabilities and Transition to Turbulence*, Edited by Swinney H.L. and Gollub J.P., Springer-Verlag, Berlin.
- [5] Catton I., 1972, The Effect of Insulating Vertical Walls on the Onset of Motion in a Fluid Heated from Below, *Int. J. of Heat and Mass Transfer*, Vol. 15, pp 665-672.
- [6] Censor Y., 1983, Finite Series-Expansion Reconstruction Methods, *Proceedings of the IEEE*, Vol. 71, No. 3, pp 409-419.
- [7] Chandrasekhar S., 1961, *Hydrodynamic and Hydromagnetic stability*, Oxford University Press, London.
- [8] Chu T.Y. and Goldstein, 1973, Turbulent Convection in a Horizontal Layer of Water, *J. of Fluid Mechanics*, Vol. 60, pp 141-159.
- [9] de Bruyn J. R., Bodenschatz E., Morris S. W., Trainoff S. P., Hu Y., Cannell D. S. and Ahlers G., 1996, Apparatus for the Study of Rayleigh-Benard Convection in Gases Under Pressure, *Rev. sci. Instrumentation*, Vol.67(6), pp 2043-2067.

- [10] Dietz G., Balkowski I., 1997, Interferometry and Reconstruction of Strongly Refracting Fields in Two-dimensional Boundary Layer Flow, *Experiments in Fluids*, Vol. 22, pp 423-431.
- [11] Faw R.E. and Dullforce T.A., 1981, Holographic Interferometry Measurement of Convective Heat Transport Beneath a Heated Horizontal Plate in Air, *Int. J. Heat Mass Transfer*, Vol. 24, No. 5, pp 859-869.
- [12] Funnell W.R.J., 1981, Image Processing Applied to the Interactive Analysis of Interferometric Fringes, *Applied optics*, Vol. 20(18), pp 3245-3250.
- [13] Gebhart B., Jaluria Y., Mahajan R.L., and Sammakia B., 1988, *Buoyancy-induced Flows and Transport*, Hemisphere Publishing Corporation, New York.
- [14] Gilbert, P.F.C., 1972, Iterative Methods for Three-dimensional reconstruction of an Object from its Projections, *J. Theoretical Biology*, Vol. 36, pp 105-117.
- [15] Goldstein R.J. (Editor), 1983, *Fluid Mechanics Measurements*, Hemisphere Publishing Corporation, New York.
- [16] Gollub J.P. and Benson S.V., 1980, Many Routes to Turbulent Convection, *J. of Fluid Mechanics*, Vol. 100(3), pp 449-470.
- [17] Gonzalez R.C. and Woods R.E., 1993, *Digital Image Processing*, Addison-Wesley Publishing Company, USA.
- [18] Gordon R., Bender R. and Herman G.T., 1970, Algebraic Reconstruction Techniques (ART) for Three-dimensional Electron Microscopy and X-ray Photography, *J. of Theoretical Biology*, Vol. 29, pp 471-481.
- [19] Grotzbach G., 1982, Direct Numerical Simulation of Laminar and Turbulent Benard Convection, *J. of Fluid Mechanics*, Vol. 119, pp 27-53.
- [20] Gull S.F. and Newton T.J., 1986, Maximum Entropy Tomography, *Applied Optics*, Vol. 25, pp 156-160.
- [21] Hauf, W. and Grigull, U. , 1970, Optical Methods in Heat Transfer, in *Advances in Heat Transfer*, Ed(s). J.P. Hartnett and T.F. Irvine, Jr., Vol. 6, pp 134-362.
- [22] Herman G.T., 1980, *Image Reconstruction from Projections*, Academic Press, New York.

- [23] Hernandez R., Frederick R.L., 1994, Spatial and Thermal Features of Three Dimensional Rayleigh-Benard Convection, *Int. J. Heat and Mass Transfer*, Vol. 37, No. 3, pp 411-424.
- [24] Hernandez R., 1995, Influence of the Heating Rate on Supercritical Rayleigh-Benard Convection, *Int. J. Heat and Mass Transfer*, Vol. 18, No. 16, pp 3035-3051.
- [25] Jain A.K., 1989, *Fundamentals of Digital Image Processing*, Prentice-Hall International Editions, USA.
- [26] Kaczmarz M.S., 1937, Angenaherte Auflosung Von Systemen Linearer Gleichungen, *Bull. Acad. Polonaise Sci. Lett. Classe Sci. Math. Natur. Serier*, Vol. A35, pp 355-357.
- [27] Kessler R., 1987, Nonlinear Transition in Three-dimensional Convection, *Journal of Fluid Mechanics*, Vol. 174, pp 357-379.
- [28] Kim, D.M. and Viskanta, R., 1984, Study of the Effects of Wall Conductance on Natural Convection in Differently oriented Square Cavities, *J. Fluid Mechanics*, Vol. 144, pp 153-176.
- [29] Kirchartz K.R. and Oertel H. (Jr), 1988, Three-dimensional Thermal Cellular Convection in Rectangular Boxes, *Journal of Fluid Mechanics*, Vol. 192, pp 249-286,
- [30] Kolodner P, Walden R.W, Passner A. and Surko C.M., 1986, Rayleigh-Benard Convection in an Intermediate-aspect-ratio Rectangular Container, *Journal of Fluid Mechanics*, Vol. 163, pp 195-226.
- [31] Krishnamurti R., 1970a, On the Transition to Turbulent Convection. Part 1: The Transition from Two To Three Dimensional Flow, *Journal of Fluid Mechanics*, Vol. 42, Part 2, pp 295-307.
- [32] Krishnamurti R., 1970b, On the Transition to Turbulent Convection. Part 2: The Transition to Time Dependent Flow, *Journal of Fluid Mechanics*, Vol. 42, Part 2, pp 309-320.
- [33] Krishnamurti. R., 1973, Some Further Studies on the Transition to Turbulent Convection, *J. Fluid Mechanics*, Vol. 60, pp 285-303.

- [34] Krishnaswamy S., 1991, Algorithm for Computer Tracing of Interference Fringes, *Applied optics*, Vol. 30(13), pp 1624-1628.
- [35] Lapidus L. and Pinder G.F., 1982, *Numerical Solution of Partial Differential Equations in Science and Engineering*, John Wiley and Sons, New York.
- [36] Lauterborn W. and Vogel A., 1984, Modern Optical Techniques in Fluid Mechanics, in *Annual Review Fluid Mechanics*, Vol. 16, pp 223-244.
- [37] Lewitt R.M., 1983, Reconstruction Algorithm-Transform Methods, *Proceedings of IEEE*, Vol. 71, pp 390-408.
- [38] Lin T.F., Yu C.H., Su H.L., 1996, Evolution of Roll Patterns in Rayleigh-Benard Convection in a Rectangular Layer: A Numerical Study, *Numerical Heat Transfer, Part A*, Vol. 29, pp 165-179.
- [39] Maveety, J.G. and Leith, J.R., 1998, Heat Transfer in Rayleigh-Benard Convection with Air in Moderate Size Containers, *Int J. Heat and Mass Transfer*, Vol. 41, pp 785-796.
- [40] Mayinger F., 1993, Image-Forming Optical Techniques in Heat Transfer: revival by Computer-Aided Data Processing, *ASME J. Heat Transfer*, Vol. 115, pp 824-834.
- [41] Mayinger F. (Edited), 1994, *Optical Measurements: Techniques and Applications*, Springer-Verlag, Berlin.
- [42] Michael Y.C. and Yang K.T., 1992, Three-Dimensional Mach-Zehnder Interferometric Tomography of the Rayleigh-Benard Problem, *ASME J. Heat Transfer*, Vol. 114, pp 622-629.
- [43] Mukutmoni D. and Yang K.T., 1993a, Rayleigh-Benard Convection in a Small Aspect Ratio Enclosure: Part 1 - Bifurcation to Oscillatory Convection, *J. of Heat Transfer*, Vol. 115(5), pp 360-366.
- [44] Mukutmoni D. and Yang K.T., 1993b, Rayleigh-Benard Convection in a Small Aspect Ratio Enclosure: Part 2 - Bifurcation to Chaos, *J. of Heat Transfer*, Vol. 115(5), pp 367-376.
- [45] Mukutmoni D. and Yang K.T., 1994, Flow Transitions and Pattern Selection of the Rayleigh-Benard Problem in Rectangular Enclosures, *Sadhana*, Vol. 19(5), pp 649-670.

- [46] Mukutmoni D. and Yang K.T., 1995a, Pattern Selection for Rayleigh-Benard Convection in Intermediate Aspect Ratio Boxes, Numerical Heat Transfer, Part A, Vol. 27, pp 621-637.
- [47] Mukutmoni D. and Yang K.T., 1995b, Thermal Convection in Small Enclosures: An Atypical Bifurcation Sequence, Int. Journal of Heat and Mass Transfer, Vol. 38, No.1, pp 113-126.
- [48] Munshi P., 1997, Application of Computerized Tomography for Measurements in Heat and Mass Transfer, Proceedings of the Third ISHMT-ASME Heat and Mass Transfer Conference and Fourteenth National Heat and Mass Transfer Conference, Edited by Biswas G., Murthy S.S., Muralidhar K., Dhir V.K., Narosa New Delhi, pp 97-105.
- [49] Muralidhar K. and Kulacki F.A., 1987, Stability of Mixed Convective Flow. Int. J. Heat Fluid Flow, Vol. 8, pp 228-234.
- [50] Muralidhar K., Patil V.B. and Kashyap R., 1996, Interferometric Study of Transient Convection in a Square Cavity, J. of Flow Visualization and Image Processing, Vol. 2, No. 4, pp 321-333.
- [51] Natterer, F., 1986, *The Mathematics of Computerized Tomography*, John Wiley & Sons, New York.
- [52] Ramesh, K. and Singh, R.P., 1995, Comparative Performance Evaluation of Various Fringe Thinning Algorithms in Photomechanics, Electronic Imaging, Vol. 4, pp 71-83.
- [53] Robinson D.W., 1983, Automatic Fringe Analysis with a Computer Image-processing System, Applied optics, Vol.22(14), pp 2169-2176.
- [54] Snyder Ray, 1988, *Instantaneous Three-dimensional Optical Tomographic Measurements of Species Concentration in a Co-flowing Jet*, Ph.D Thesis, Department of Aeronautics and Astronautics, Stanford University.
- [55] Subbarao P.M.V, Munshi P. and Muralidhar K., 1997a, Performance Evaluation of Iterative Tomographic Algorithms Applied to Reconstruction of a Three Dimensional Temperature Field, Numerical Heat Transfer, Part B, Vol. 31, pp 347-372.

- [56] Subbarao P.M.V., Munshi P. and Muralidhar K., 1997b, Performance of Iterative Tomographic Algorithms Applied to Non-destructive Evaluation with Limited Data, NDT & E International, Vol. 30, No. 6, pp 359-370.
- [57] Tanabe K., 1971, Projection Method for Solving a Singular System, Numerical Mathematics, Vol. 17, pp 203-214.
- [58] Tolpadi A.K. and Kuehn T.H., 1991, Measurement of Three-Dimensional Temperature Fields in Conjugate Conduction-Convection Problems Using Multidimensional Interferometry, Int. J. Heat Mass Transfer, Vol. 34, No. 7, pp 1733-1745.
- [59] Verhoeven D., 1993, Multiplicative Algebraic Computed Tomography Algorithms for the Reconstruction of Multidirectional Interferometric Data, Optical Engineering, Vol. 32, pp 410-419.
- [60] Watt D.W. and Vest C.M., 1990, Turbulent Flow Visualization by Interferometric Integral Imaging and Computed Tomography, Experiments in Fluids, Vol. 8, pp 301-311.
- [61] Yang K.T. and Mukutmoni D., 1993, Computational Aspects of Studies of Buoyant Enclosure Flows in *Computers and Computing in Heat Transfer Science and Engineering*, Edited by Nakayama Wataru, Yang Kwang-tzu, CRC Press Boca Raton, Florida, pp 23-41.
- [62] Yu C.H. and Lin T.F., 1997, Effects of Aspect Ratio on Vortex Flow Patterns in Mixed Convection of Air Through a Bottom-heated Horizontal Rectangular Duct, Numerical Heat Transfer, Part A, Vol. 31 pp 745-764.

Appendix A

Sensitivity of Reconstructed Field on Fringe Thinning Algorithm

The present appendix is concerned with the sensitivity of the reconstructed field to fringe thinning operations. For this study the experimental data at $Ra=13900$, has been chosen. The interferograms from 0 and 90° projections have been used. The roll size is identified from the fringe pattern and the projection data for one roll is spread to fill the entire width of the fluid layer. All the three methods of fringe thinning discussed in Chapter 3 have been considered.

An implementation of the three thinning algorithms to interferometric fringes revealed the following. The automatic thinning approach is unambiguous and repeatable, in the sense that the thinned fringes do not depend on starting point specified by the user. The curve fitting and paint-brush approaches are sensitive to the user input. On the other hand, they do not require elaborate code preparation time and can be adopted if thinning is only sporadically required.

A preliminary examination of the thinned images (Figures 3.16, 3.18 and 3.20) shows that the three methods produce qualitatively similar results. An independent assessment of these techniques is taken up in the present appendix. The first criterion adopted is the comparison of the width-averaged temperature profile for each projection. Under nominally steady conditions, i.e. after sufficient time is allowed to elapse, the width-averaged temperature profile plotted as a function of the vertical coordinate can be shown to be independent of the projection angle. This is because the total energy transferred

across any horizontal plane in the fluid layer is a constant. These profiles are shown in Figure A.1, for all the three algorithms studied. The S-shaped curve, characteristic of buoyancy-driven convection can be seen in this figure. Within experimental limits, a close match between the 0 and 90° profiles is seen to be realized when the first fringe thinning approach is employed. This match confirms the accuracy of fringe thinning, temperature allocation to fringes and absence of interpolation errors while transferring the data to a rectangular grid. Figure A.1 also shows that the fringe lost during thinning near the top wall does not degrade energy balance. The agreement in case of the curve-fitting method is partial, while it is unsatisfactory with the paint-brush method.

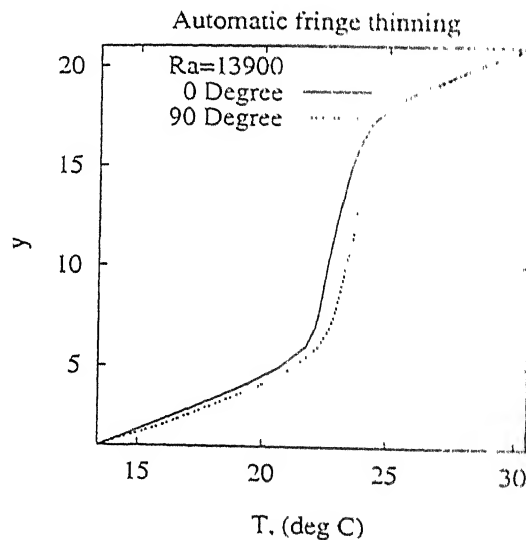


Figure A.1 for caption see next page

The tomographic reconstruction of the temperature field using two projections is considered next. The three fringe thinning algorithms are first qualitatively evaluated. The three-dimensional temperature field in the fluid layer has been reconstructed using the AVMART2 algorithm. The AVMART2 algorithm converged asymptotically to a solution for all the three thinning algorithms. Since a correction corresponding to the average of all the rays passing through a pixel is used, a relaxation parameter of unity was used for reconstruction. A convergence criterion of 0.01 % between successive updates was employed for stopping the iterations. For each horizontal plane, the number of iterations required was in the range 30-50.

Figure A.2 shows the reconstructed temperature surfaces along the central plane for all the three thinning algorithms. These surfaces show the formation of rolls. The rolls show only a minor variation in the z direction and accordingly, may be classified

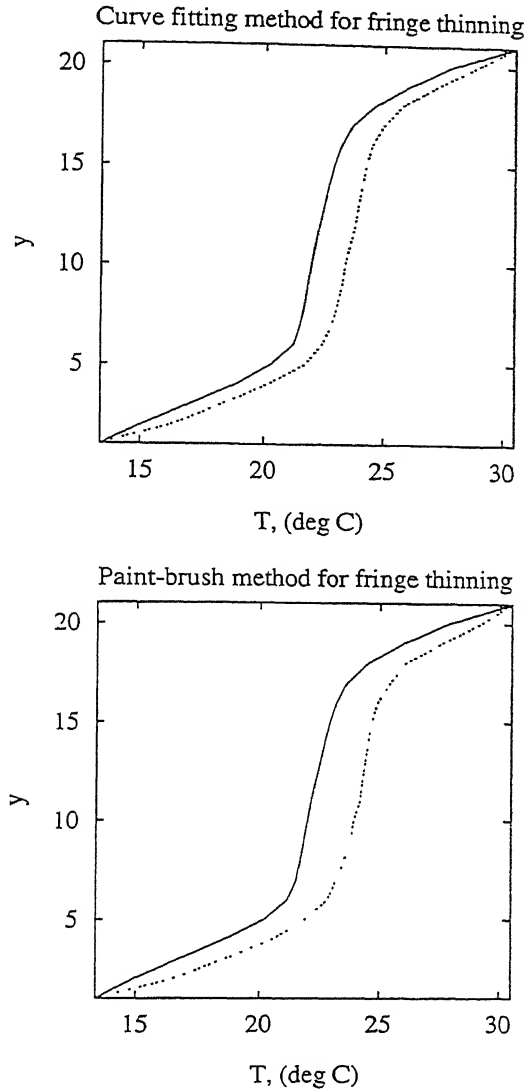


Figure A.1: Width-averaged Temperature Profile of the Projection Temperature Field Inside a Roll

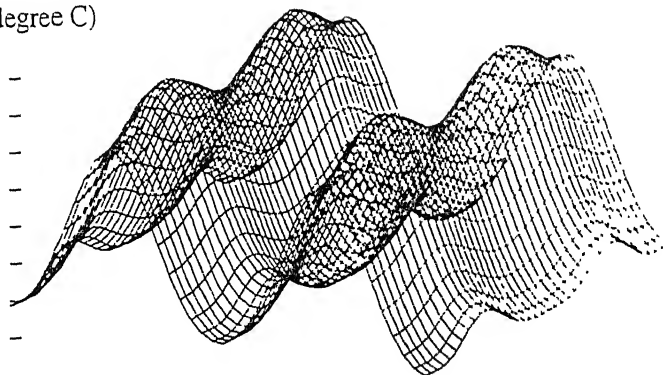
as longitudinal, with the roll axis being parallel to the z coordinate. Since this is a reconstructed result from 2-view tomography, this should be taken as the most dominant pattern prevailing in the fluid layer. Further the projection data employed here is only partial, that is the fringe portion corresponding to a roll pattern is identified and spread so as to get the full field data. Hence the results are shown only for a section of the horizontal plane. Qualitatively all the three methods display similar results for the temperature field.

A quantitative assessment of the reconstructed temperature field is taken up next. To compute errors, a reference solution is required. Since this is not available for experi-

Automatic fringe thinning

T, (degree C)

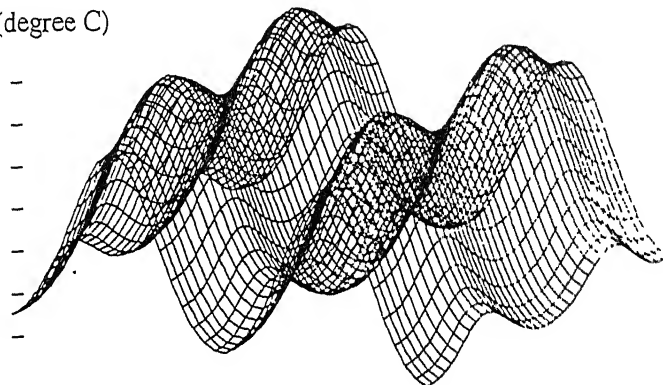
25 -
24.5 -
24 -
23.5 -
23 -
22.5 -
22 -
21.5 -



Curve fitting method for fringe thinning

T, (degree C)

24 -
23.5 -
23 -
22.5 -
22 -
21.5 -
21 -



Paint-brush method for fringe thinning

T, (degree C)

24.5 -
24 -
23.5 -
23 -
22.5 -
22 -
21.5 -

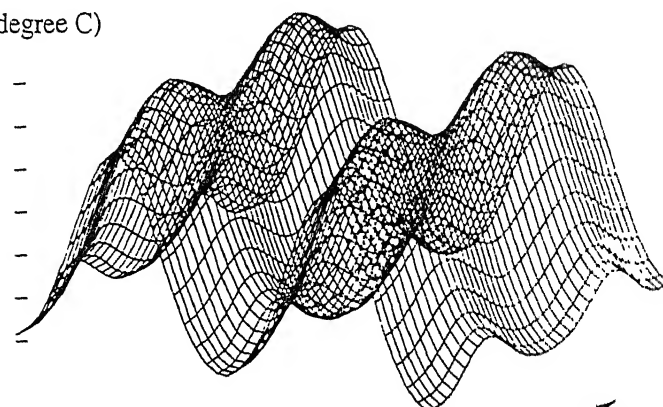


Figure A.2: Reconstructed Temperature Surfaces Within the Cavity at the Central Horizontal Plane

mental data, the following strategy has been adopted. The temperature field obtained by merging the *S*-shaped curves in the two projections has been taken as the reference solution. The temperature field thus developed satisfies exactly the energy balance criterion. Errors have been determined between the temperature field developed from the thinning algorithms and the reference solution. The complete fluid layer has been considered while obtaining these quantities. The errors for each thinning algorithm have been summarized in Table A.1.

An examination of Table A.1 shows that errors associated with the automatic thinning algorithm are uniformly small. The absolute maximum errors with the other algorithms are larger, being in excess of 1 °C. This may not be acceptable in many applications. A comparison of the absolute maximum and RMS errors shows the latter to be smaller, by more than a factor of two. This suggests that large errors are localized over the flow field. The percentage RMS error is truly small for the automatic thinning algorithm, while it is in the range 2-3.5 % for the curve fitting and paint-brush methods. This range may still be acceptable in engineering measurements.

The extent to which large errors are localized over a plane of the fluid layer has been examined next. To this end, the percentage fractional area over which a range of error values are to be found, has been computed (Table A.2). All three algorithms show that the largest errors are confined to only a small area, being 0.19, 0.43 and 0.24 % respectively for the three algorithms. This shows that all three thinning algorithms are acceptable in principle. The final choice depends on the need for a high accuracy measurement on one hand and the time available for code development on the other.

A comparison of the wall heat transfer rates determined from the temperature field is presented next. The average Nusselt number computed from the slope of the *S*-shaped curve shown in Figure A.1. For comparison, the benchmark result for Nusselt number has been taken from Equation 6.2.

Figure A.3 shows the local Nusselt number variation with the *z*-coordinate over one roll for the three thinning algorithms. Both the hot and cold walls have been considered. The view angle is 90° and so the roll formation is visible in this projection. The roll axis being along the 0°, the Nusselt number variation on the two walls are of opposite orientation. The three thinning algorithms qualitatively reproduce similar trends. The Nusselt number profile predicted by the automatic thinning algorithm can be seen to be

the smoothest of the three. Differences among the three algorithm can be seen to have increased in Figure A.3, compared to the errors reported in Table A.2. This is because the Nusselt number is calculated as the derivative of the temperature field. The local Nusselt numbers calculated from the three algorithms are within $\pm 10\%$ of one another.

Table A.3 presents the Nusselt number averaged over a single roll in the fluid layer. The automatic fringe thinning algorithm gives Nusselt numbers that are comparatively close to each other at the two walls. For the 0° projection the average Nusselt number over the two plates differ for curve-fitting and the paint-brush methods. The roll in the present study is seen to be formed parallel to the 0° axis. There is a considerable mismatch in the average Nusselt number over a single roll as viewed along the 90° projection data. The cavity-averaged Nusselt number however is close to the predictions of Gebhart *et al.* (1988).

Table A.1: Reconstruction Errors from the three Fringe Thinning Algorithms.

Error	Automatic fringe thinning	Curve fitting method	Paint-brush method
$E_1, ^\circ\text{C}$	0.034	1.51	1.03
$E_2, ^\circ\text{C}$	0.011	0.60	0.34
$E_3, \%$	0.066	3.51	2.01

Table A.2: Fractional Distribution of the E_1 Error over a Horizontal Plane.

Number of points (%) having error in the range	Automatic fringe thinning	Curve fitting method	Paint-brush method
$> 95\%$	0.19	0.43	0.24
75-95 %	2.09	0.24	2.0
50-75 %	13.4	7.24	4.47

The results presented for complete 4-view tomography in Section 6.1.3 corresponds to the automatic fringe thinning algorithm. In Table 6.3 the total average Nusselt number from 6 different view angles and the cavity Nusselt number is shown. These Nusselt numbers are lower than that predicted by the one-roll data. They are however within the experimental uncertainty of the reference value.

Table A.3: Comparison of Average Nusselt Number Based on the Width of a Single Roll

	Automatic fringe thinning	Curve fitting method	Paint-brush method	Gebhart <i>et al.</i> (1988)
0°, cold	2.37	2.01	1.81	
0°, hot	2.38	3.14	3.11	
90°, cold	2.99	2.53	3.02	
90°, hot	2.41	2.88	2.34	
Cavity average	2.53	2.64	2.57	2.59

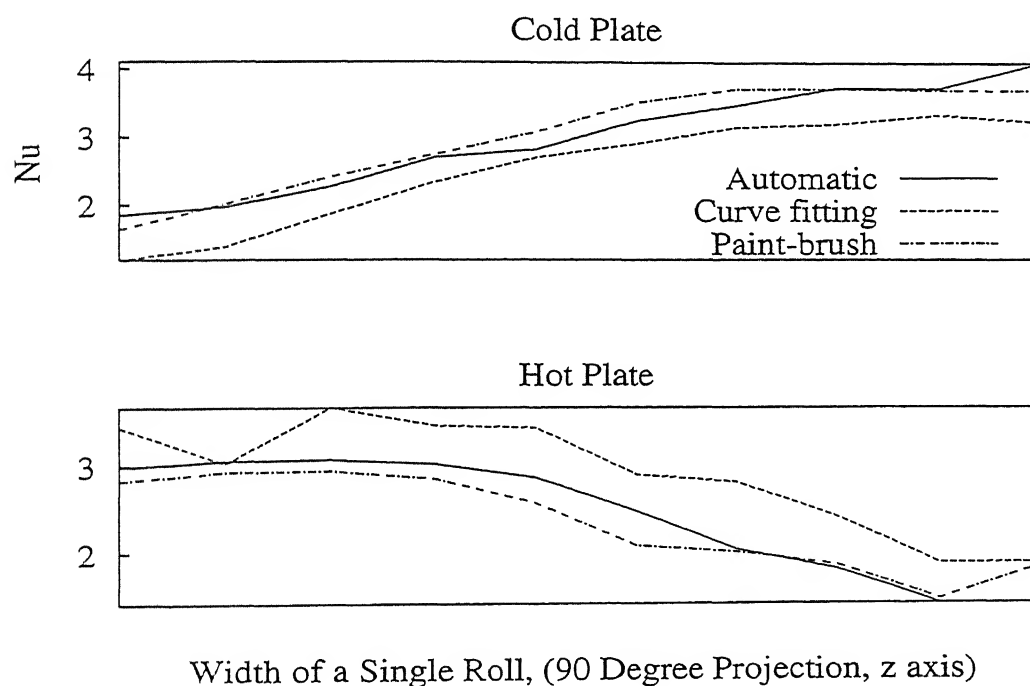


Figure A.3: Local Nusselt Number Variation over the Hot and Cold Plates; Comparison of the three Thinning Algorithms

To summarize, three fringe thinning algorithms based on minimum intensity, curve fitting and paint-brush available on PCs have been compared in the context of tomographic inversion. The main conclusions that have been drawn from this analysis are:

1. The three methods of fringe thinning produce qualitatively similar temperature fields.

2. Quantitative analysis shows differences in the results, but large errors are localized and over 95 % of the fluid region, errors are smaller than 1 %.
3. The loss of a wall fringe during the automatic fringe thinning does not increase errors either in the reconstructed temperature field or the Nusselt number.
4. The automatic fringe thinning algorithm requires the most code preparation time. It is however superior to the other two methods since it is repeatable and takes the minimum computer time for execution. It is also physically meaningful since it closely satisfies the energy balance criterion.

Appendix B

Sensitivity of Tomographic Inversion to Initial Guess

The inversion of limited projection data using algebraic reconstruction techniques forms a mathematically ill-posed problem. As a rule, the number of equations is much smaller than the number of unknowns. This makes the solution-set infinite in the sense that a unique solution is not guaranteed. Different initial guesses will therefore lead to different solutions of this infinite set. In the absence of any knowledge about the field being studied it is a difficult task to prescribe the initial guess. The present appendix is concerned with studying the sensitivity of the AVMART (1-3) algorithms to the initial guess of the temperature field.

B.1 Sensitivity Analysis for Initial Guess with a Two Dimensional Longitudinal Roll Pattern

For sensitivity analysis, four different initial guesses were supplied to two different roll patterns. The flow patterns considered were (1) two dimensional longitudinal rolls and (2) cubic cells in the fluid layer. The sensitivity to two dimensional longitudinal roll pattern is analysed first. The initial guesses used are:

1. Constant temperature distribution (1°C)
2. Constant temperature distribution (100°C)

3. Temperature distribution corresponding to cubic cells pattern
4. Random field between 0 and 1°C ($\text{RMS} = 0.5^{\circ}\text{C}$)

The three AVMART algorithms have been tested for 2 projection angles of 0° and 90° . While working with limited-view tomography, a commonly used strategy is to reconstruct the field with two orthogonal projections and use this as an initial guess for inversions with a higher number of projections. There is also sufficient evidence that two orthogonal projections can elucidate the dominant convection pattern in the fluid layer. Hence the interest in the sensitivity analysis of 2-view tomography.

Figure B.1 shows the reconstructed temperature surface and the isotherms for a constant initial guess of 0°C for AVMART1 algorithm. Figure B.2 and B.3 show the reconstructed surface and isotherms for this initial guess using AVMART2 and AVMART3.

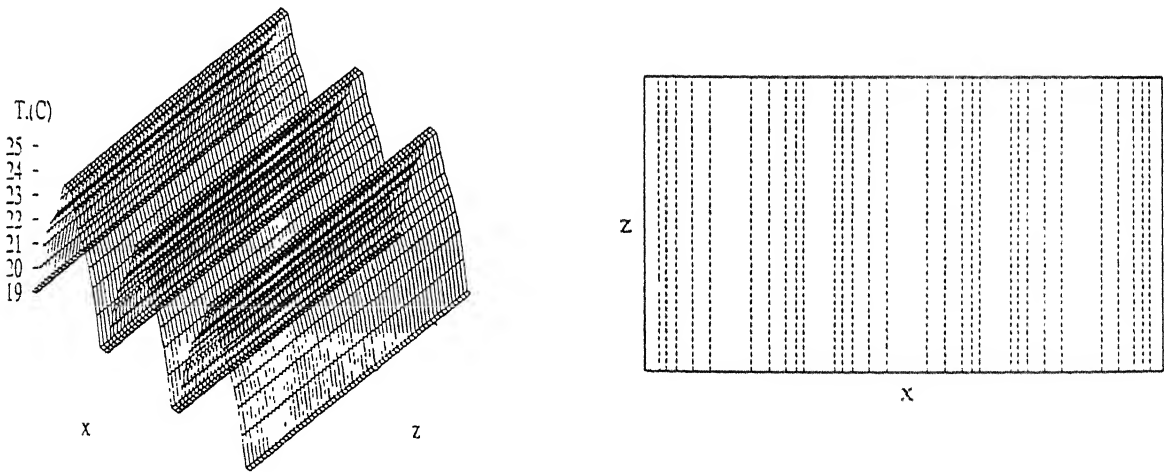


Figure B.1: Reconstructed Temperature Surface (Left) and Isotherms (Right) of the mid-plane of the Fluid Layer using AVMART1, Initial Guess (1), Two Dimensional Longitudinal Rolls.

Qualitatively all the three algorithms are seen to predict similar temperature fields. These are very close to the original field obtained by numerical solution. Table B.1 shows the three different errors E_1 , E_2 and E_3 defined in Chapter 5 and further the average number of iterations per plane and the CPU time required the reconstruction.

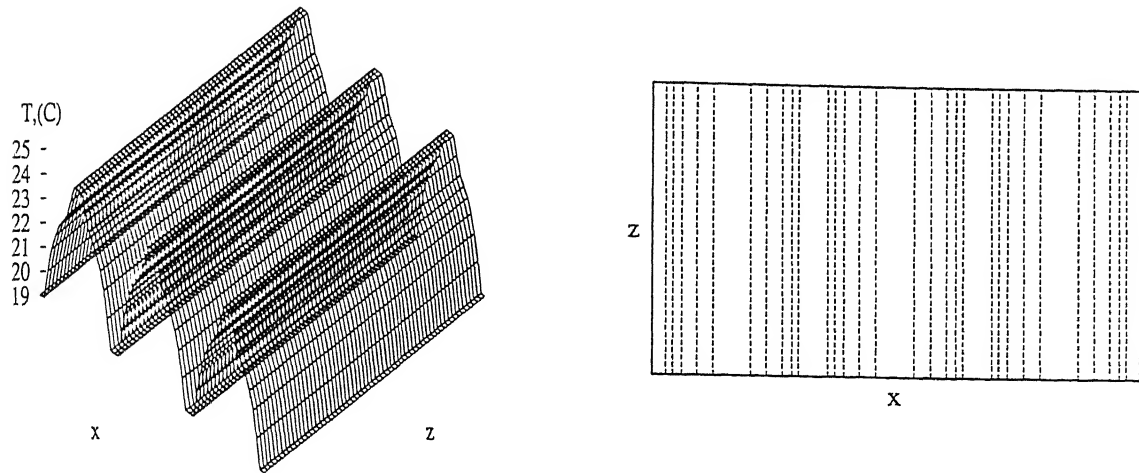


Figure B.2: Reconstructed Temperature Surface (Left) and Isotherms (Right) of the mid-plane of the Fluid Layer using AVMART2, Initial Guess (1), Two Dimensional Longitudinal Rolls.

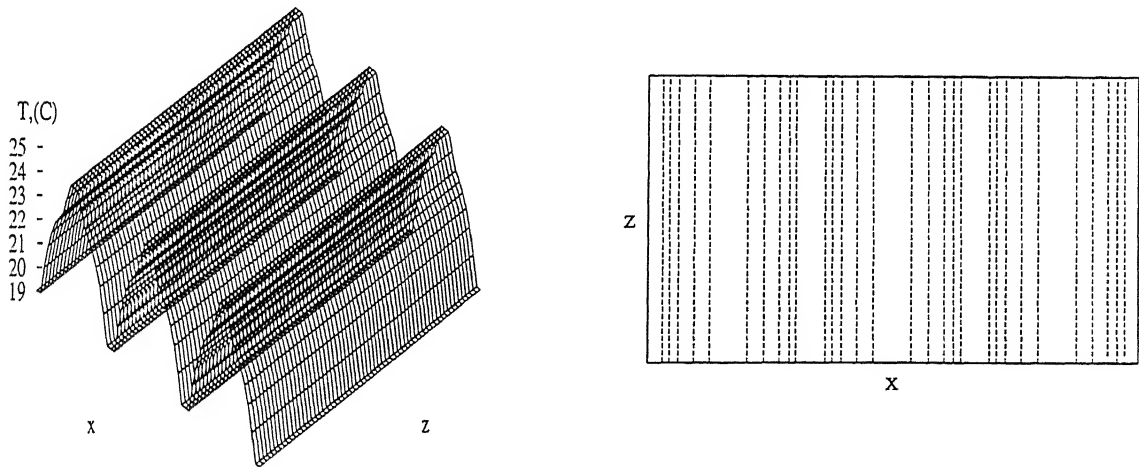


Figure B.3: Reconstructed Temperature Surface (Left) and Isotherms (Right) of the mid-plane of the Fluid Layer using AVMART3, Initial Guess (1), Two Dimensional Longitudinal Rolls.

All the computations were carried out using a 150 MHz Pentium processor with 32 MB RAM. It can be readily seen from Table B.1 that the errors are uniformly small and the

reconstructed temperature field is very close to the original field. Table B.2 shows the distribution of the errors in the fluid domain. It can be inferred that large errors are locally present at only a few points in the fluid domain. AVMART2 predicts a field where the large errors are present at fewer number of points, almost one half of the other two algorithms. The error level is otherwise distributed homogeneously throughout the fluid domain.

Table B.1: Comparison of the Three AVMART Algorithms: Initial Guess (1), Temperature Field in the Form of Longitudinal Rolls

	AVMART1	AVMART2	AVMART3
$E_1, ^\circ\text{C}$	0.0034	0.0079	0.0078
$E_2, ^\circ\text{C}$	0.0016	0.0034	0.0035
$E_3, \%$	0.0094	0.0199	0.0207
CPU (sec)	58.7	81.2	92.6
Number of Iterations	9	13	14

Table B.2: Fractional Distribution of the E_1 Error over the Fluid Domain, Initial Guess (1). Temperature Field in the Form of Longitudinal Rolls

Number of points (%) having error in the range	AVMART1	AVMART2	AVMART3
> 95 %	2.68	1.34	2.68
75-95 %	7.15	7.00	5.66
50-75 %	27.27	19.97	24.74

The results for the second initial guess are presented next. The initial guess for the temperature field was prescribed as a constant but of a different magnitude ($=100^\circ\text{C}$). The results obtained can be seen to be very close to those from initial guess (1). The reconstructed temperature surface and isotherms for the three algorithms are shown in Figure B.4-B.6.

Table B.3 and Table B.4 represents the errors and their fractional distribution over the fluid domain.

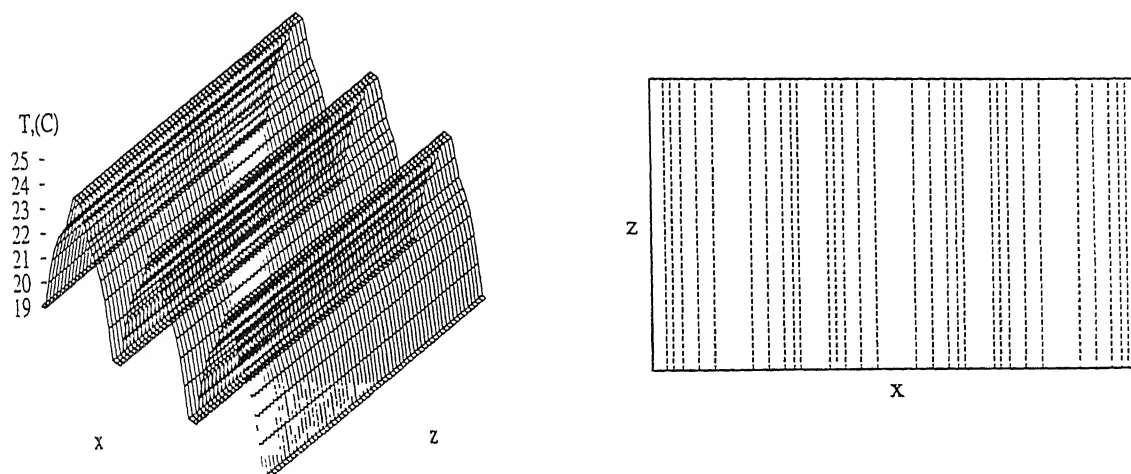


Figure B.4: Reconstructed Temperature Surface (Left) and Isotherms (Right) of the mid-plane of the Fluid Layer using AVMART1, Initial Guess (2), Two Dimensional Longitudinal Rolls.

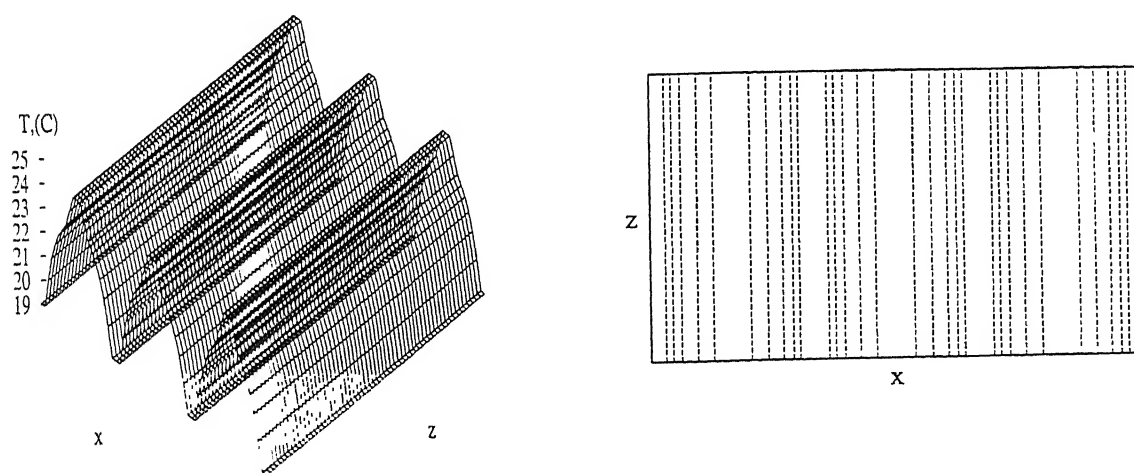


Figure B.5: Reconstructed Temperature Surface (Left) and Isotherms (Right) of the Mid plane of the Fluid Layer Using AVMART2, Initial Guess (Case 2), Two Dimensional Longitudinal Rolls.

The third initial guess considered was a field completely different from the one to be reconstructed. Specifically, the cubic cell pattern was used as an initial guess to

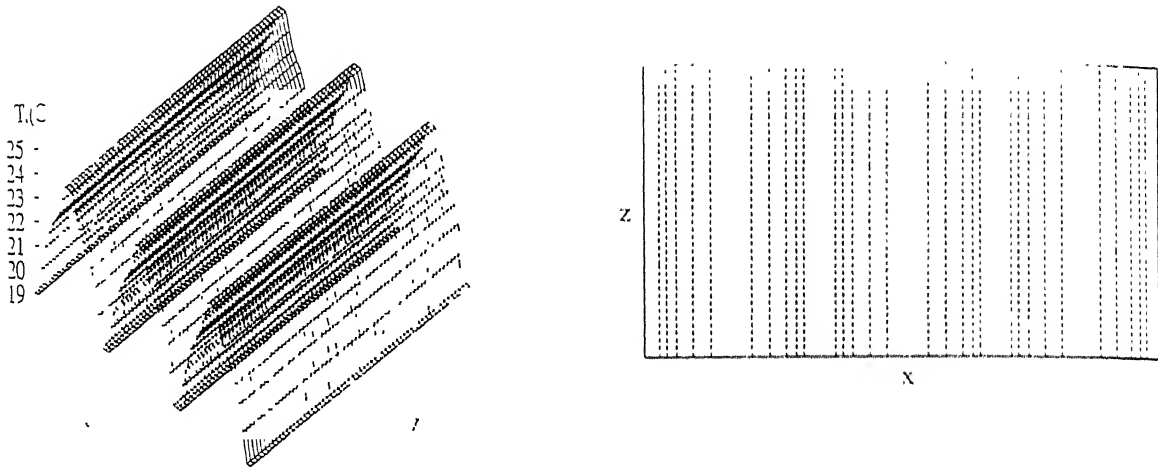


Figure B.6: Reconstructed Temperature Surface (Left) and Isotherms (Right) of the mid-plane of the Fluid Layer using AVMART3, Initial Guess (2), Two Dimensional Longitudinal Rolls.

Table B.3: Comparison of the Three AVMART Algorithms: Initial Guess, (2), Temperature Field in the Form of Longitudinal Rolls

	AVMART1	AVMART2	AVMART3
$E_1, ^\circ\text{C}$	0.0034	0.0075	0.0078
$E_2, ^\circ\text{C}$	0.0016	0.0032	0.0035
$E_3, \%$	0.0094	0.0187	0.0208
CPU (sec)	58.7	92.1	91.6
Number of Iterations	9	14	14

the projection data obtained from two dimensional longitudinal rolls. The reconstructed temperature surface and isotherms are presented in Figure B.7-B.9. The errors as well as the distribution of errors are presented in Table B.5-B.6. One can see that the errors have increased in comparison to the reconstructed field from a constant initial guess. Qualitatively, the structure of the rolls in the reconstructed temperature surface is seen to be distorted to some extent. The converged solution thus retains some of the bias of the initial guess. The resulting temperature field however strictly satisfies the projection data employed, but continues to resemble the cubic cell pattern. The distribution of errors is

Table B.4: Fractional Distribution of the E_1 Error over the Fluid Domain, Initial Guess (2), Temperature Field in the Form of Longitudinal Rolls

Number of points (%) having error in the range	AVMART1	AVMART2	AVMART3
> 95 %	2.68	1.34	2.68
75-95 %	7.15	5.66	5.66
50-75 %	27.27	18.47	26.53

found to be practically identical for all the three algorithms.

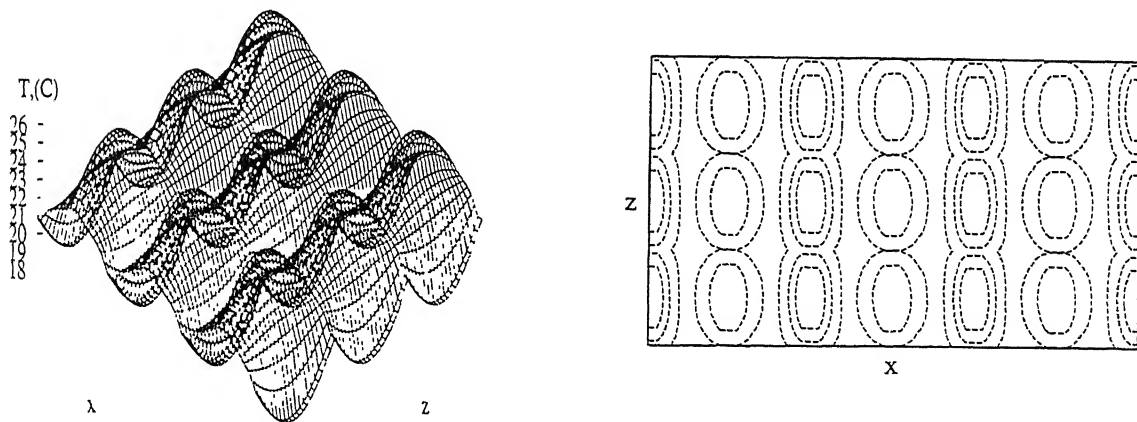


Figure B.7: Reconstructed Temperature Surface (Left) and Isotherms (Right) of the mid-plane of the Fluid Layer using AVMART1, Initial Guess (3), Two Dimensional Longitudinal Rolls

The fourth initial guess is a complete random field. This was established by a random number generator to produce temperature values in the range $0-1^{\circ}\text{C}$. The reconstructed fields for this guess are shown in Figure B.10-B.12. The reconstructed field on close examination was seen to have longitudinal rolls with superimposed noise. This field was filtered using Fourier transforms to improve the visual effect. The rolls structure emerging from the filtered reconstructed field appear distorted. However, compared to the result obtained from the cubic cell pattern, the filtered surface shown in Figure B.13- B.15 is

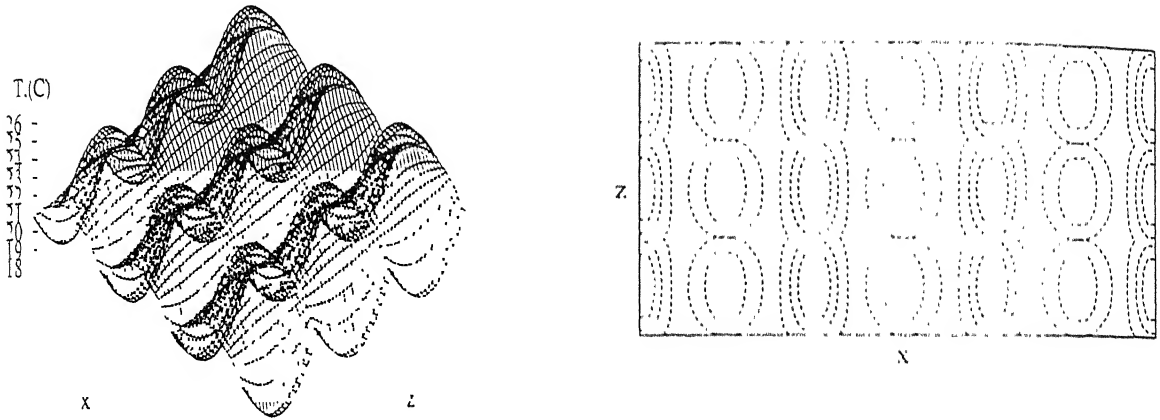


Figure B.8: Reconstructed Temperature Surface (Left) and Isotherms (Right) of the mid-plane of the Fluid Layer using AVMART2, Initial Guess (3), Two Dimensional Longitudinal Rolls

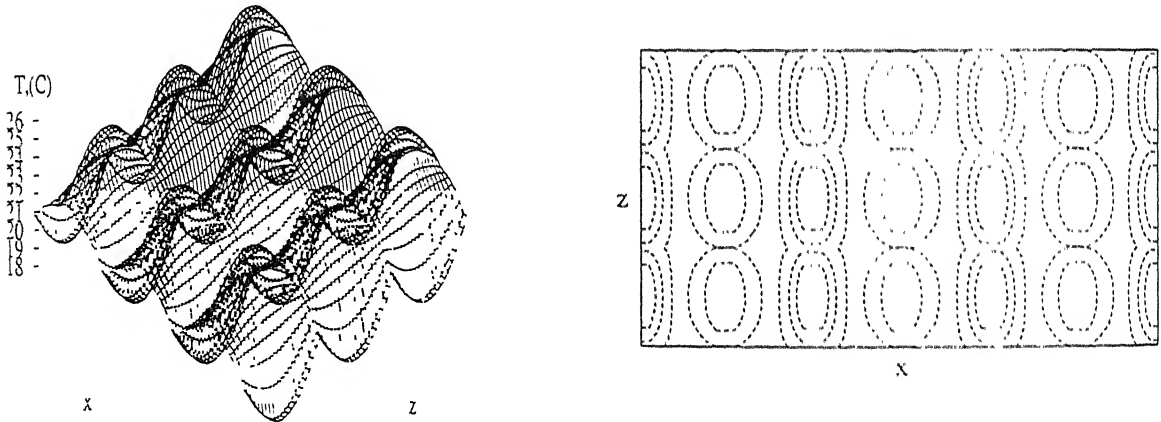


Figure B.9: Reconstructed Temperature Surface (Left) and Isotherms (Right) of the mid-plane of the Fluid Layer using AVMART3, Initial Guess (3), Two Dimensional Longitudinal Rolls

a better representative of the two dimensional longitudinal rolls. The errors are however larger in the present case. The errors as well as the distribution of errors over the fluid

Table B.5: Comparison of the Three AVMART Algorithms: Initial Guess (3), Temperature Field in the Form of Longitudinal Rolls

	AVMART1	AVMART2	AVMART3
E_1 , °C	2.23	2.24	2.24
E_2 , °C	0.52	0.52	0.52
E_3 , %	3.05	3.06	3.06
CPU (sec)	56.7	79.7	81.6
Number of Iterations	9	12	12

Table B.6: Fractional Distribution of the E_1 Error over the Fluid Domain, Initial Guess (3), Temperature Field in the Form of Longitudinal Rolls

Number of points (%) having error in the range	AVMART1	AVMART2	AVMART3
> 95 %	0.17	0.17	0.17
75-95 %	0.47	0.47	0.47
50-75 %	4.07	4.07	4.07

domain are given in Tables B.7-B.8. Among the three algorithms AVMART3 is seen to take less computer time and produces a better estimate of the temperature field.

Table B.7: Comparison of the Three AVMART Algorithms: Initial Guess (4), Temperature Field in the Form of Longitudinal Rolls

	AVMART1	AVMART2	AVMART3
E_1 , °C	11.96	13.33	4.83
E_2 , °C	5.59	4.74	0.43
E_3 , %	32.71	27.75	2.54
CPU (sec)	114.5	127.0	93.3
Number of Iterations	19	19	14

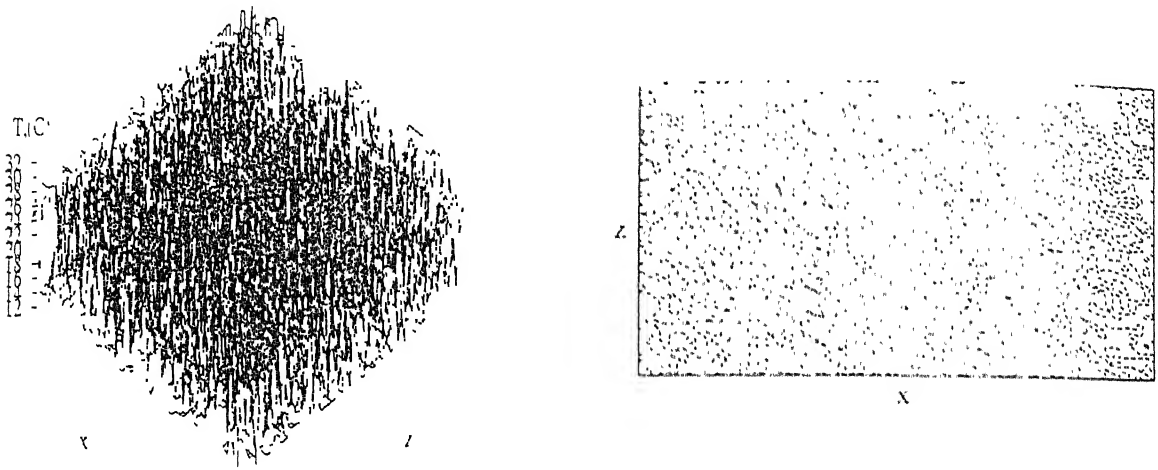


Figure B.10: Reconstructed Temperature Surface (Left) and Isotherms (Right) of the midplane of the Fluid Layer using AVMART1, Initial Guess (4), Two Dimensional Longitudinal Rolls

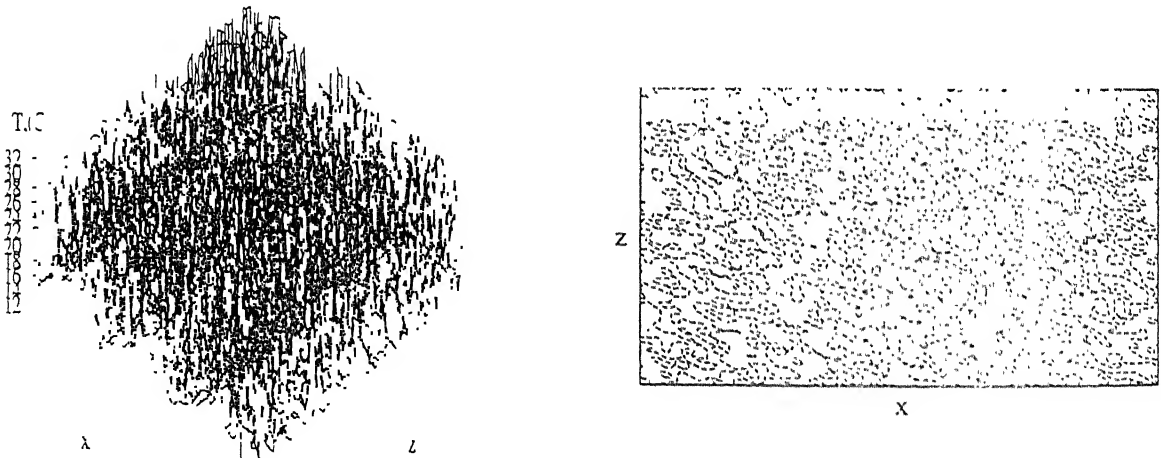


Figure B.11: Reconstructed Temperature Surface (Left) and Isotherms (Right) of the midplane of the Fluid Layer using AVMART2, Initial Guess (4), Two Dimensional Longitudinal Rolls

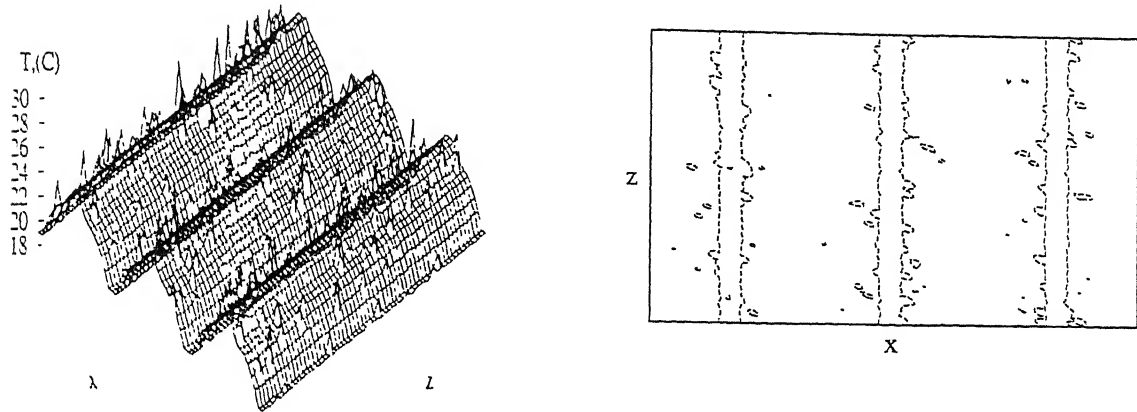


Figure B.12: Reconstructed Temperature Surface (Left) and Isotherms (Right) of the midplane of the Fluid Layer using AVMART3, Initial Guess (4), Two Dimensional Longitudinal Rolls

Table B.8: Fractional Distribution of the E_1 Error over the Fluid Domain, Initial Guess (4). Temperature Field in the Form of Longitudinal Rolls

Number of points (%) having error in the range	AVMART1	AVMART2	AVMART3
> 95 %	0.01	0.007	0.01
75-95 %	5.02	1.11	0.20
50-75 %	38.40	12.97	0.73

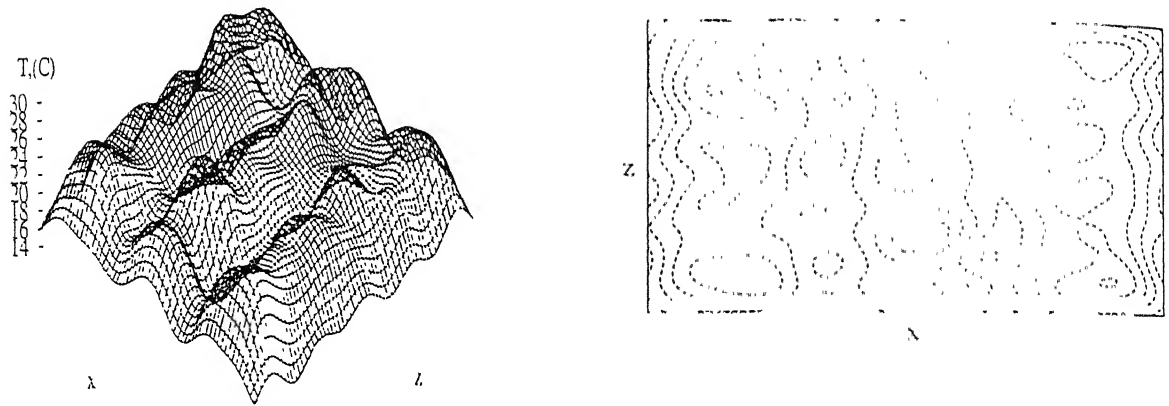


Figure B.13: Filtered Reconstructed Temperature Surface (Left) and Isotherms (Right) of the midplane of the Fluid Layer using AVMART1, Initial Guess (1), Two Dimensional Longitudinal Rolls

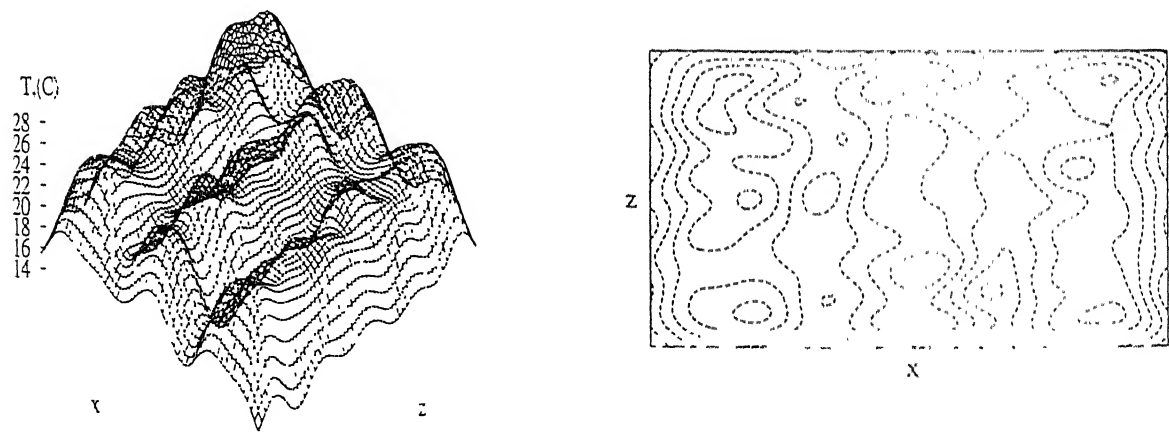


Figure B.14: Filtered Reconstructed Temperature Surface (Left) and Isotherms (Right) of the midplane of the Fluid Layer Using AVMART2, Initial Guess (4), Two Dimensional Longitudinal Rolls

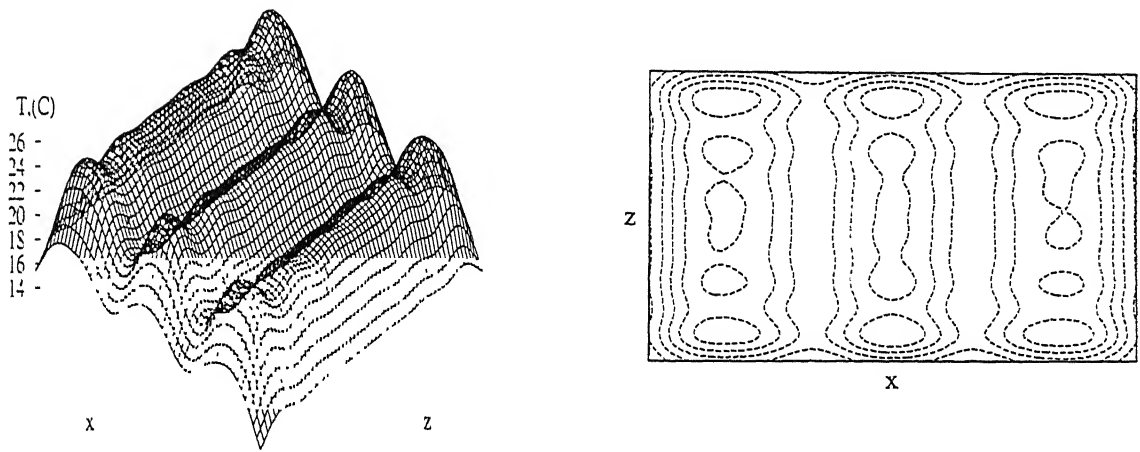


Figure B.15: Filtered Reconstructed Temperature Surface (Left) and Isotherms (Right) of the midplane of the Fluid Layer Using AVMART3, Initial Guess (4), Two Dimensional Longitudinal Rolls

B.2 Sensitivity Analysis for Initial Guess with a Three Dimensional Cubic Cell Pattern

The numerically generated temperature field comprising of a cubic cell pattern is considered next for the analysis of its sensitivity to initial guess. The temperature field in this case is completely three dimensional. Reconstruction is once again based on 2-view tomography using the 0° and 90° projection angles. Four different initial guesses used were :

1. Constant temperature field ($=1^\circ\text{C}$)
2. Constant temperature field ($=100^\circ\text{C}$)
3. Temperature distribution corresponding to two dimensional longitudinal rolls
4. Random field between 0 and 1°C (RMS = 0.5°C)

The initial guess of a constant temperature field at 1°C is considered first. Figure B.16-B.18 shows the reconstructed surface and the isotherms for the three AVMART algorithms. Qualitatively all the three algorithms are seen to predict the same temperature field. The errors are slightly higher compared to the earlier reconstruction of longitudinal rolls. Table B.9 shows the three different errors E_1 , E_2 and E_3 for the present calculations. Table B.10 shows the distribution of the errors in the fluid domain. The three algorithms are seen to produce essentially similar fields from error distribution point of view as well.

Table B.9: Comparison of the Three AVMART Algorithms: Initial Guess (1). Temperature Field in the Form of Cubic Cells

	AVMART1	AVMART2	AVMART3
$E_1, ^\circ\text{C}$	1.97	1.97	1.97
$E_2, ^\circ\text{C}$	0.49	0.48	0.49
$E_3, \%$	2.86	2.79	2.86
CPU (sec)	58.2	78.5	89.7
Number of Iterations	9	12	14

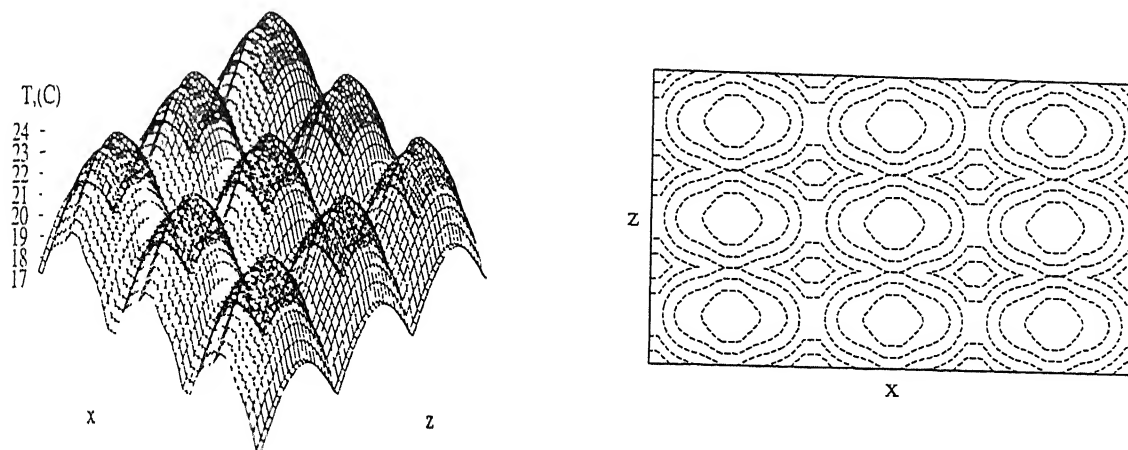


Figure B.16: Reconstructed Temperature Surface (Left) and Isotherms (Right) of the midplane of the Fluid Layer using AV MART1, Initial Guess (1), Cubic Cell Pattern

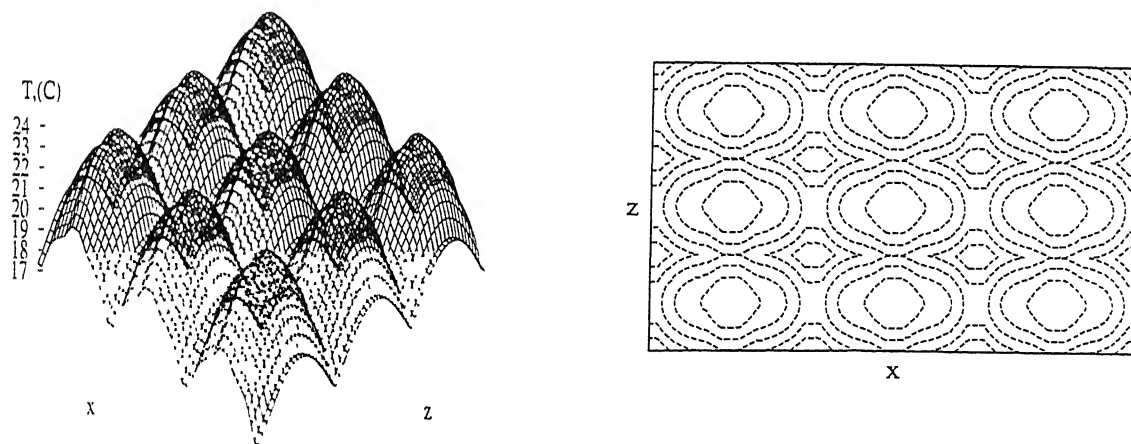


Figure B.17: Reconstructed Temperature Surface (Left) and Isotherms (Right) of the midplane of the Fluid Layer using AV MART2, Initial Guess (1), Cubic Cell Pattern

The results for the second initial guess corresponding to a constant temperature field of 100°C are considered next. These are found to be very close to the results obtained with an initial guess of 1°C . The reconstructed temperature surfaces and isotherms for

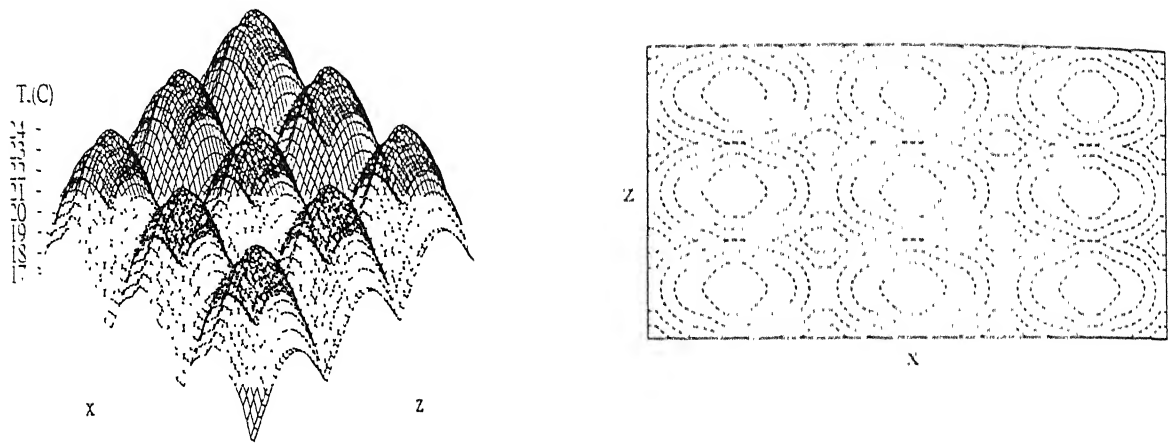


Figure B.18: Reconstructed Temperature Surface (Left) and Isotherms (Right) of the midplane of the Fluid Layer using AVMART3. Initial Guess (1), Cubic Cell Pattern

Table B.10: Fractional Distribution of the E_1 Error over the Fluid Domain, Initial Guess (1), Temperature Field in the Form of Cubic Cells

Number of points (%) having error in the range	AVMART1	AVMART2	AVMART3
> 95 %	0.17	0.17	0.17
75-95 %	0.57	0.48	0.57
50-75 %	5.76	5.15	5.73

the three algorithms are shown in Figure B.19-B.21. Table B.11 and Table B.12 present the errors as well as their fractional distribution over the entire fluid domain. As seen earlier, the maximum errors are localized and errors over most of the fluid layer is small and evenly distributed.

The third initial guess is the temperature field corresponding to the two dimensional longitudinal roll pattern. The reconstructed temperature surface and isotherms are presented for this initial guess in Figure B.22-B.24. The errors and the distribution of errors are presented in Table B.13- B.14. The errors are seen to have remained the same as in the case of an unbiased initial field. Qualitatively also, the reconstructed temperature surface

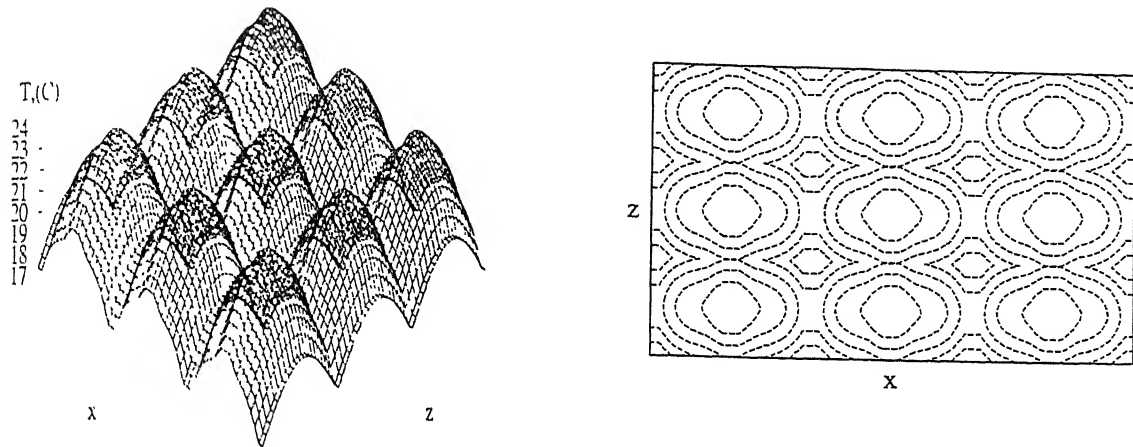


Figure B.19: Reconstructed Temperature Surface (Left) and Isotherms (Right) of the midplane of the Fluid Layer using AV MART1, Initial Guess (2). Cubic Cell Pattern

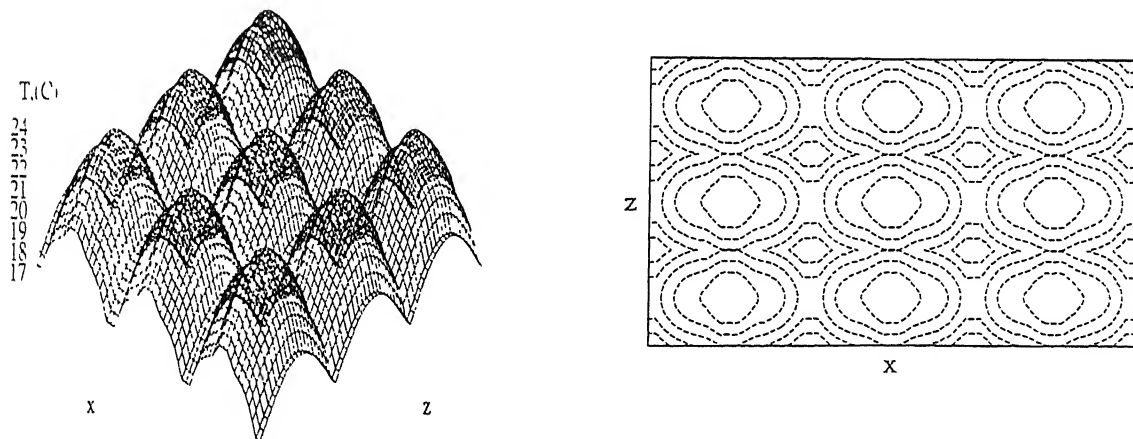


Figure B.20: Reconstructed Temperature Surface (Left) and Isotherms (Right) of the midplane of the Fluid Layer using AV MART2, Initial Guess (2). Cubic Cell Pattern

is close to that of the original. Thus an initial guess of two dimensional rolls is seen to be an unbiased initial guess for the cubic cell pattern. The discussion in Section B.1 showed that the reverse was not true. In contrast, the two dimensional roll is a constant along

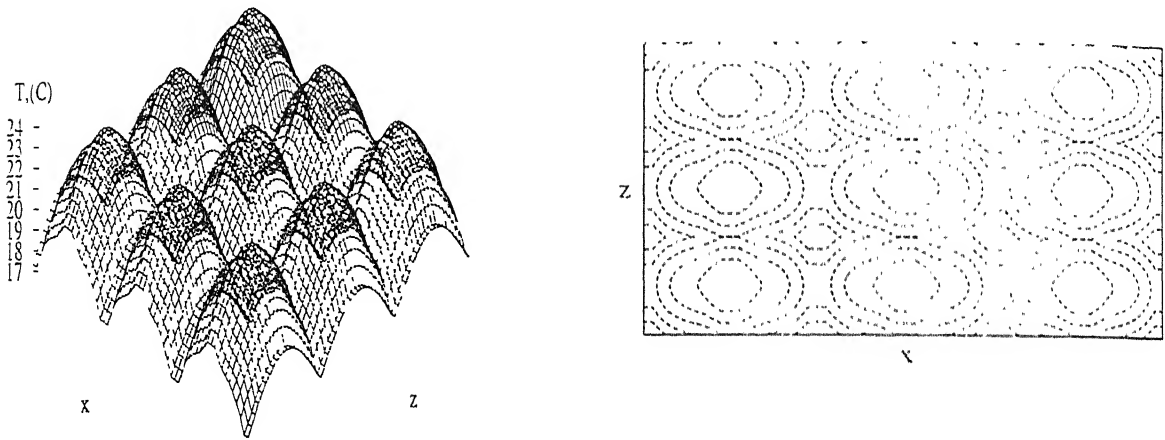


Figure B.21: Reconstructed Temperature Surface (Left) and Isotherms (Right) of the midplane of the Fluid Layer using AVMART3, Initial Guess (2), Cubic Cell Pattern

Table B.11: Comparison of the Three AVMART Algorithms: Initial Guess (2), Temperature Field in the Form of Cubic Cells

	AVMART1	AVMART2	AVMART3
$E_1, ^\circ\text{C}$	1.97	1.97	2.21
$E_2, ^\circ\text{C}$	0.48	0.48	0.50
$E_3, \%$	2.86	2.86	2.94
CPU (sec)	58.4	88.3	89.4
Number of Iterations	9	14	14

the roll axis and acts like a constant field in the initial guess. The distribution of errors are found to be identical for all the three algorithms.

The fourth initial guess taken up for analysis is a random field. The reconstructed field here qualitatively looks like a random field superimposed over the cubic cells (Figure B.25-B.27). The reconstructed field was filtered to remove the high wavenumber components. The hidden cubic cells structure stand out in the filtered field, but are distorted in shape. The filtered temperature surface and isotherms are shown in Figure B.28- B.30. The errors are larger in this case. The errors and distribution of errors over the fluid

Table B.12: Fractional Distribution of the E_1 Error over the Fluid Domain, Initial Guess (2), Temperature Field in the Form of Cubic Cells

Number of points (%) having error in the range	AVMART1	AVMART2	AVMART3
> 95 %	0.17	0.17	0.09
75-95 %	0.57	0.57	0.60
50-75 %	5.76	5.73	3.70

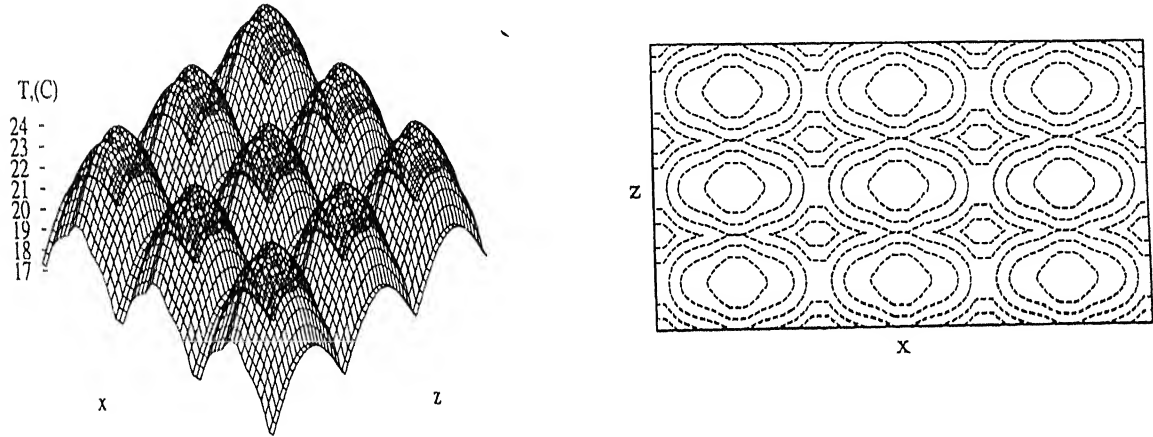


Figure B.22: Reconstructed Temperature Surface (Left) and Isotherms (Right) of the midplane of the Fluid Layer using AVMART1, Initial Guess (3), Cubic Cell Pattern

domain are given in Tables B.15-B.16. For a noisy initial guess, the AVMART3 is again found to be the best from the view point of computer time as well as errors.

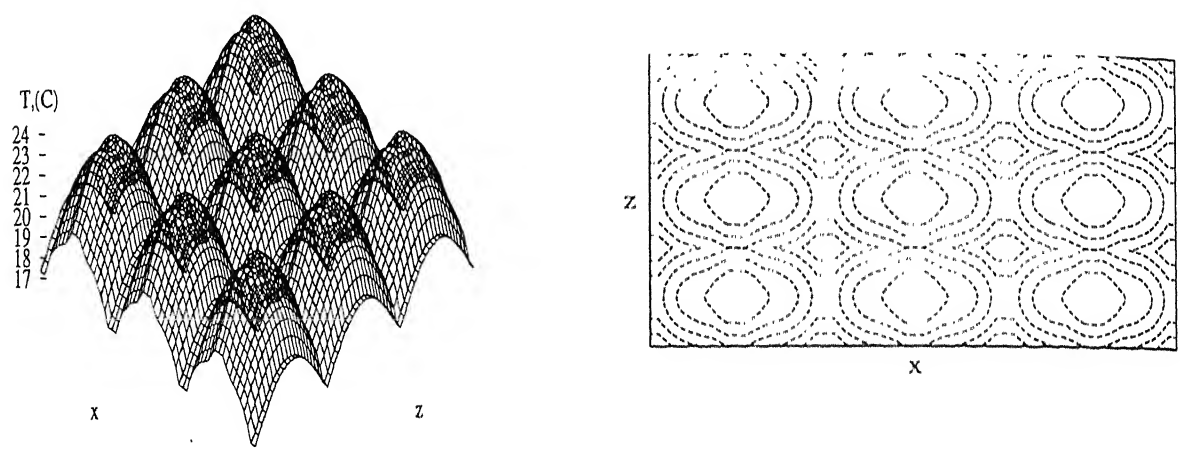


Figure B.23: Reconstructed Temperature Surface (Left) and Isotherms (Right) of the midplane of the Fluid Layer using AVMART2, Initial Guess (3), Cubic Cell Pattern

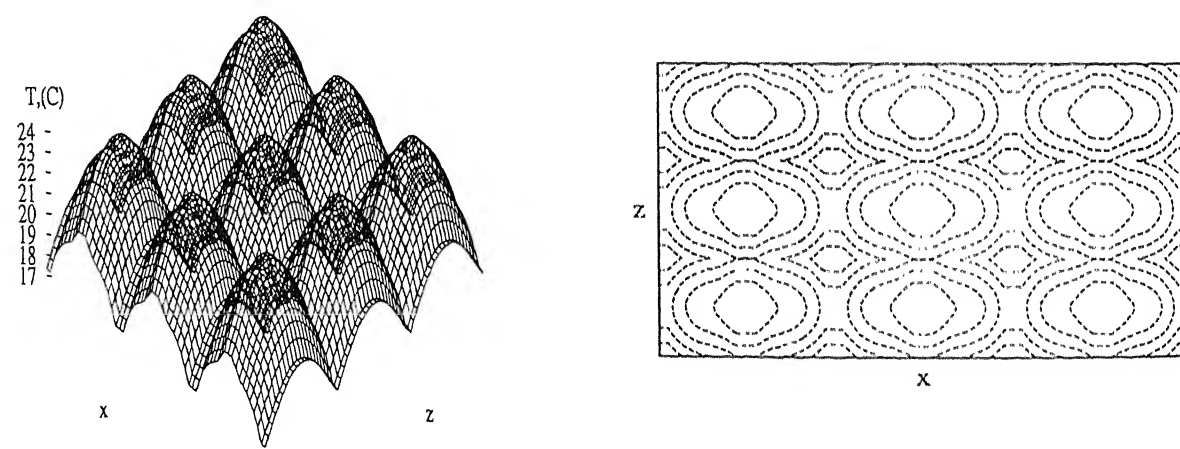


Figure B.24: Reconstructed Temperature Surface (Left) and Isotherms (Right) of the midplane of the Fluid Layer using AVMART3, Initial Guess (3), Cubic Cell Pattern

Table B.13: Comparison of the Three AVMART Algorithms: Initial Guess (3), Temperature Field in the Form of Cubic Cells

	AVMART1	AVMART2	AVMART3
$E_1, ^\circ\text{C}$	1.98	1.98	1.98
$E_2, ^\circ\text{C}$	0.49	0.49	0.49
$E_3, \%$	2.86	2.86	2.86
CPU (sec)	54.9	78.3	81.1
Number of Iterations	8	12	12

Table B.14: Fractional Distribution of the E_1 Error over the Fluid Domain, Initial Guess (3), Temperature Field in the Form of Cubic Cells

Number of points (%) having error in the range	AVMART1	AVMART2	AVMART3
> 95 %	0.17	0.17	0.17
75-95 %	0.60	0.62	0.62
50-75 %	5.68	5.58	5.58

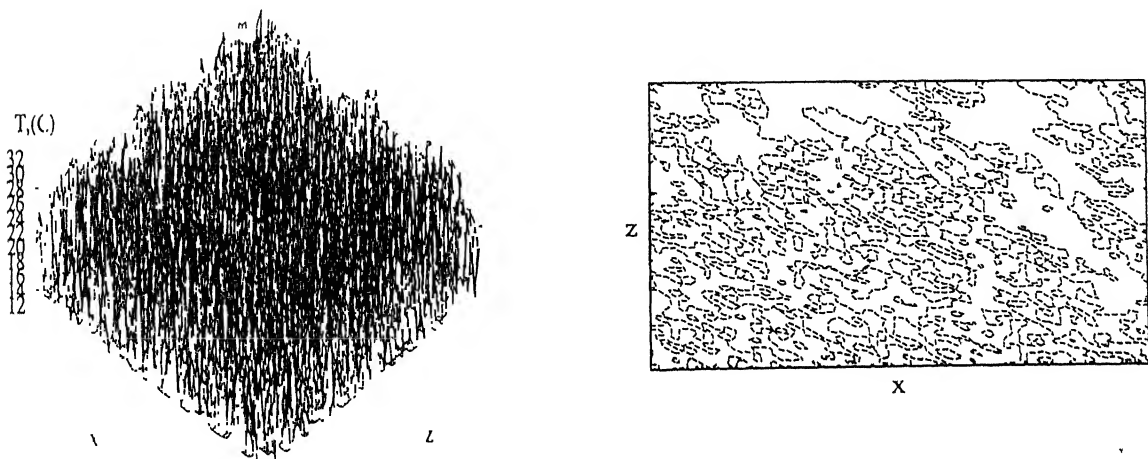


Figure B.25: Reconstructed Temperature Surface (Left) and Isotherms (Right) of the midplane of the Fluid Layer using AVMART1, Initial Guess (4), Cubic Cell Pattern

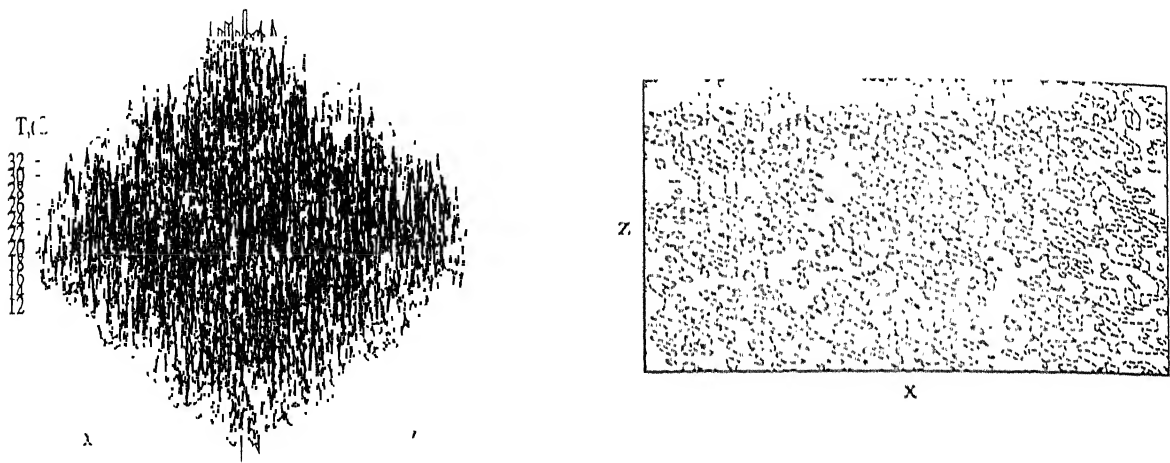


Figure B.26: Reconstructed Temperature Surface (Left) and Isotherms (Right) of the midplane of the Fluid Layer using AVMART2, Initial Guess (4), Cubic Cell Pattern

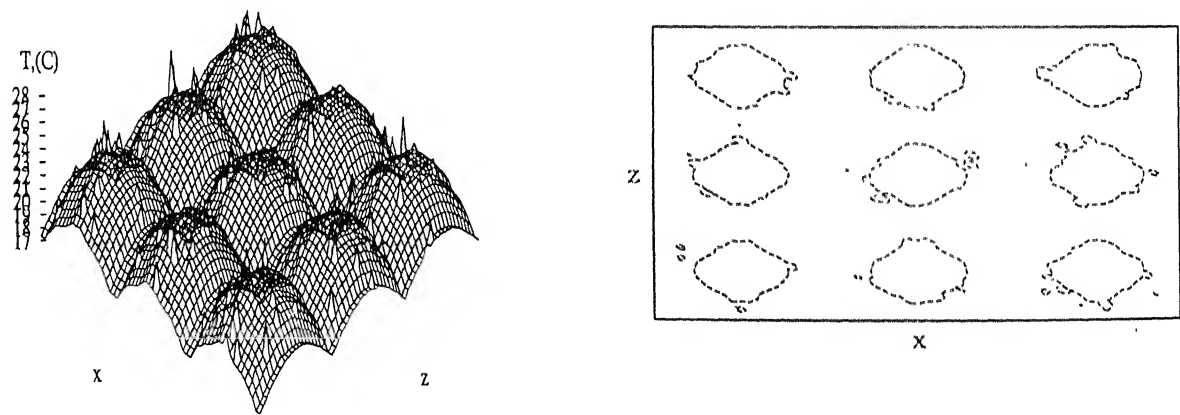


Figure B.27: Reconstructed Temperature Surface (Left) and Isotherms (Right) of the midplane of the Fluid Layer using AVMART3, Initial Guess (4), Cubic Cell Pattern

Table B.15: Comparison of the Three AVMART Algorithms: Initial Guess (4), Temperature Field in the Form of Cubic Cells

	AVMART1	AVMART2	AVMART3
E_1 , °C	12.15	13.42	6.20
E_2 , °C	5.59	4.74	0.60
E_3 , %	32.70	27.77	3.50
CPU (sec)	100.4	112.3	90.8
Number of Iterations	15	17	14

Table B.16: Fractional Distribution of the E_1 Error over the Fluid Domain, Initial Guess (4), Temperature Field in the Form of Cubic Cells

Number of points (%) having error in the range	AVMART1	AVMART2	AVMART3
> 95 %	0.02	0.01	0.002
75-95 %	5.79	2.00	0.02
50-75 %	34.46	11.92	0.30

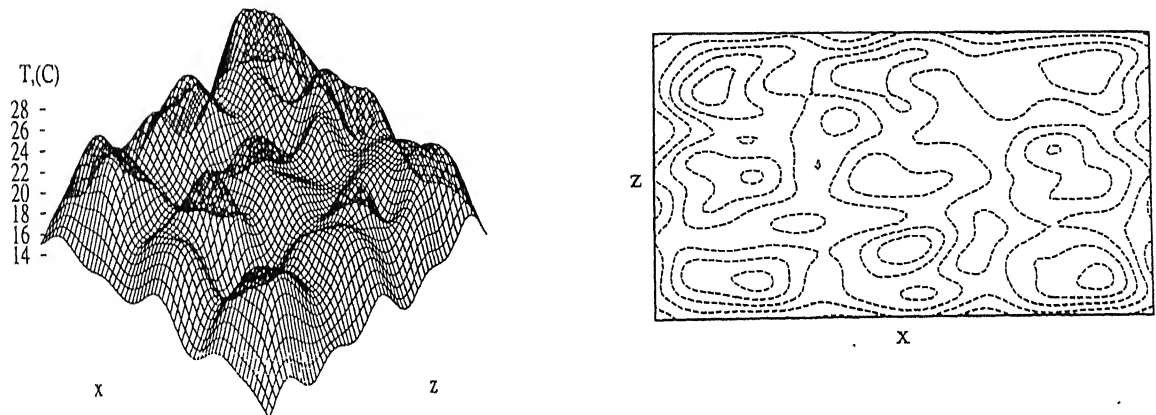


Figure B.28: Filtered Reconstructed Temperature Surface (Left) and Isotherms (Right) of the midplane of the Fluid Layer using AVMART1, Initial Guess (4), Cubic Cell Pattern

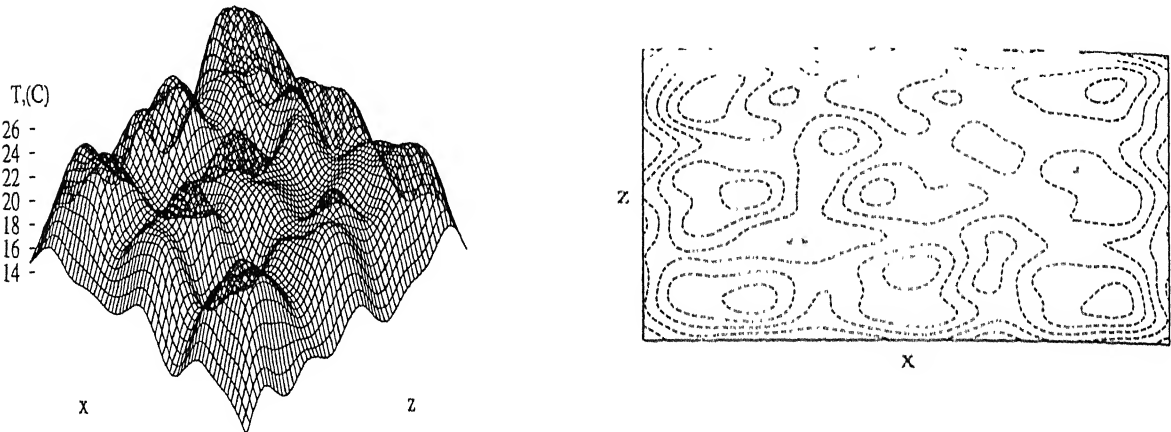


Figure B.29: Filtered Reconstructed Temperature Surface (Left) and Isotherms (Right) of the midplane of the Fluid Layer using AVMART2, Initial Guess (4), Cubic Cell Pattern

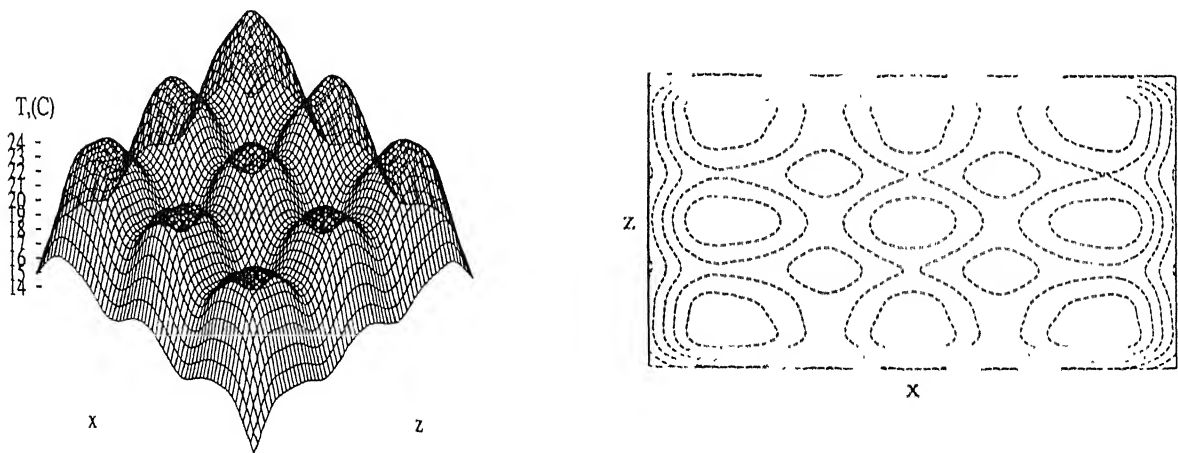


Figure B.30: Filtered Reconstructed Temperature Surface (Left) and Isotherms (Right) of the midplane of the Fluid Layer using AVMART3, Initial Guess (4), Cubic Cell Pattern

Major conclusion that can be drawn on the basis of the above results are the following:

1. An unbiased initial guess such as constant temperature field gives best results. It predicts the temperature field with reasonable accuracy.
2. A biased initial guess in the form of a flow structure is seen to lead to a biased result, the reconstructed field retaining some similarity with the initial pattern.
3. Initial guess in the form of random numbers predicts the overall shape of the temperature field but superimposed with random variations at high wavenumbers. These can be removed by using filters, but the shape of the filtered temperature surface is seen to be distorted.
4. Among the three versions of AVMART, all of them show similar properties but AVMART2 is seen to have marginally superior properties in terms of errors and convergence rates.

Appendix C

Sensitivity to Noise in Projection Data

In real experiments the projection data recorded generally has noise superimposed on it. The sources of noise in projection data are speckle, inaccuracies in processing operations and interpolation from fringes to a uniform grid. Including all sources a maximum of 5% noise in the projection data is expected in the present experiments. This number is drawn from the Nusselt number calculations. This gives confidence that noise in the projection data is reasonably low. Further a good energy balance is also seen in all the experiments. Hence the assumption of 5% noise level in the projection data can be taken as acceptable.

For numerical testing, 5% RMS noise has been added to the projections recorded from the numerical temperature field. Noise signal has been produced by generating random numbers. A 5% (RMS) noise corresponds to a maximum noise amplitude of about 10% in the projection data.

Figure C.1 shows the projection data for view angles of 0, 6, 90 and 150° corresponding to two dimensional longitudinal rolls in the fluid layer with the added 5% noise. Figure C.2 shows the projection data for the same view angles in the presence of 5% noise for cubic cells in the fluid layer.

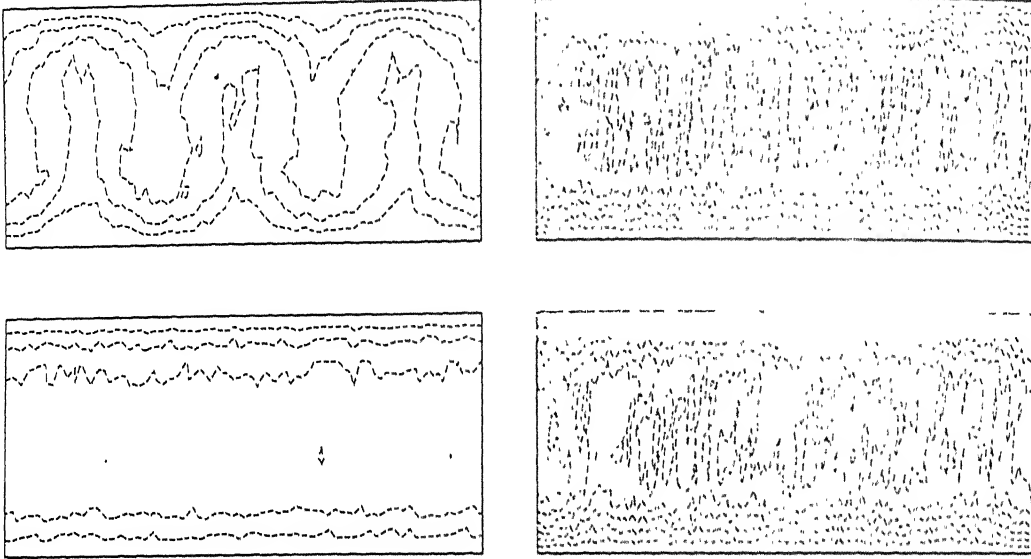


Figure C.1: Noisy Projection Data corresponding to Longitudinal Roll Formation in the Fluid Layer, Top left 0° , Top right 60° , Bottom left 90° and Bottom right 150°

C.1 Sensitivity of Longitudinal Rolls

To analyse the effect of noise, two view reconstruction is once again analysed. The projection angles considered for reconstruction are 0 and 90° . The initial guess in all the two-view calculations is a constant temperature field. Figures C.3-C.5 show the reconstructed temperature surface and isotherms using the three AVMART algorithms. Figures C.6-C.8 show the Fourier filtered temperature surface and the corresponding isotherms. The actual roll structure is now clearly visible.

In the presence of 5% noise, the reconstructed field is still realized in the form of rolls. The noise level in the reconstructed field is found to be of the same order as in the projection data. All the three algorithms were seen to converge unambiguously to similar solutions. Table C.1 shows the magnitude of three different errors in the reconstructed field. Table C.2 shows the distribution of the fractional error over the fluid domain. It can

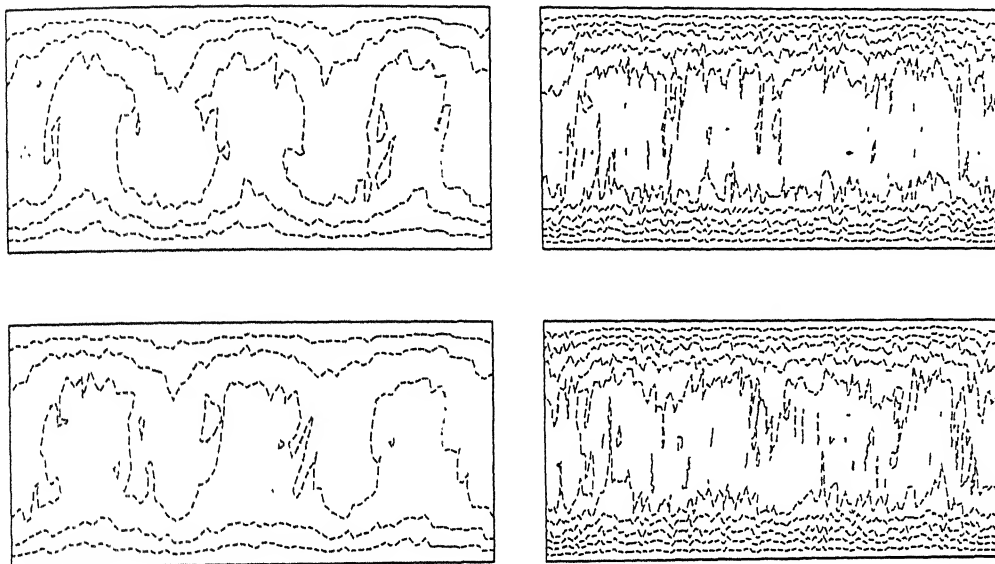


Figure C.2: Noisy Projection Data corresponding to Cubic Cell Formation in the Fluid Layer, Top left 0° , Top right 60° , Bottom left 90° and Bottom right 150°

be seen that the large errors are present only over a small fraction of the fluid domain and are localized. More than 50% of the fluid region has error less than 50% of E_1 reported in Table C.1. In comparison to the calculation with zero noise, one can see larger errors due to noise and some delay in convergence, that is an increase in CPU time.

The noisy projection data has been employed for 4-view reconstruction of the temperature field. The two view reconstruction using AVMART2 with noisy projection data has been used as an initial guess. Figures C.9-C.11 show the reconstructed temperature surface and isotherms from all the three AVMART algorithms. Figures C.12-C.14 show the Fourier filtered temperature surface and the isotherms. The main observation is that the error in the reconstructed field increases with the inclusion of additional noisy projections. Tables C.3 and C.4 show the error levels in the reconstructed data and the distribution of these errors inside the fluid layer. The AVMART2 and AVMART3 algorithms perform well in the presence of noise. AVMART2 requires less computer time

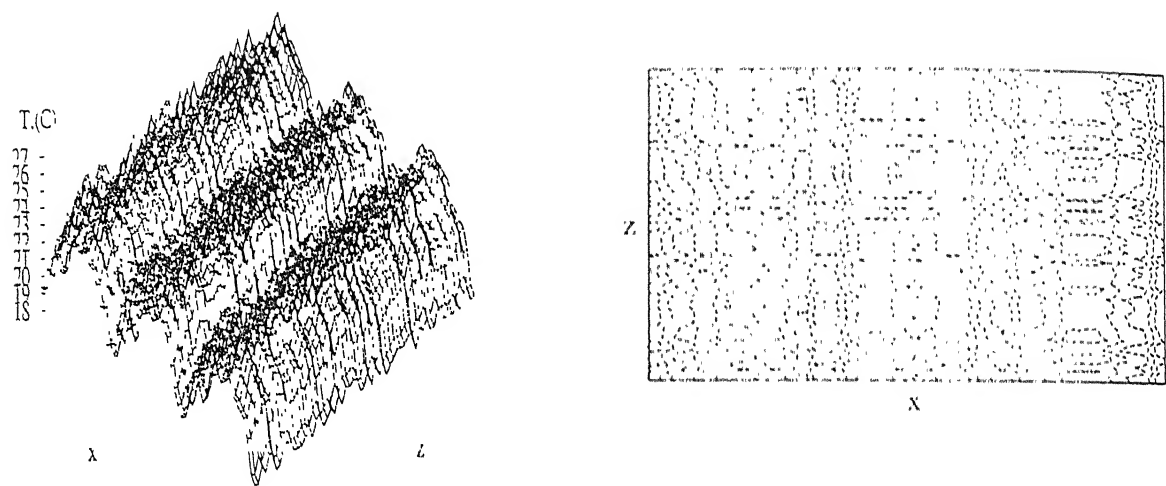


Figure C.3: Reconstructed Temperature Surface (Left) and Isotherms (Right) of the mid-plane of the Fluid Layer using AVMART1, Noisy Projection Data, 2-view Reconstruction, Two Dimensional Longitudinal Rolls

Table C.1: Comparison of the Three AVMART Algorithms: Temperature Field in the Form of Longitudinal Rolls, with 5% Added Noise in Projection Data, 2-view Reconstruction

	AVMART1	AVMART2	AVMART3
$E_1, \text{ }^\circ\text{C}$	2.80	2.80	2.80
$E_2, \text{ }^\circ\text{C}$	0.97	0.97	0.97
$E_3, \%$	5.69	5.69	5.69
CPU (sec)	58.8	91.8	93.1
Number of Iterations	9	14	14

compared to AVMART3.

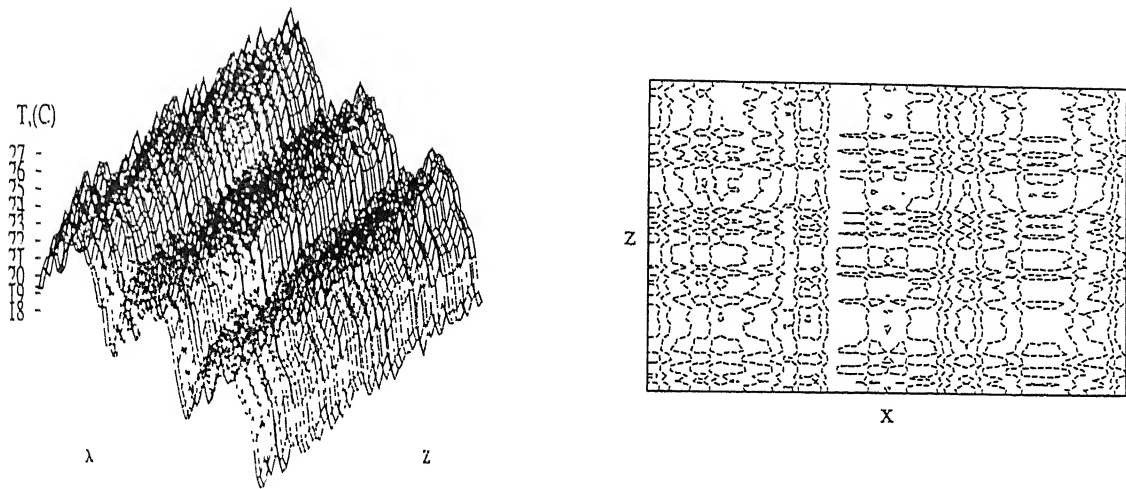


Figure C.4: Reconstructed Temperature Surface (Left) and Isotherms (Right) of the mid-plane of the Fluid Layer using AVMART2, Noisy Projection Data, 2-view Reconstruction, Two Dimensional Longitudinal Rolls

Table C.2: Fractional Distribution of the E_1 Error over the Fluid Domain, Temperature Field in the Form of Longitudinal Rolls, with 5% Added Noise in Projection Data, 2-view Reconstruction

Number of points (%) having error in the range	AVMART1	AVMART2	AVMART3
> 95 %	0.01	0.01	0.01
75-95 %	2.81	2.82	2.76
50-75 %	14.75	14.76	14.81

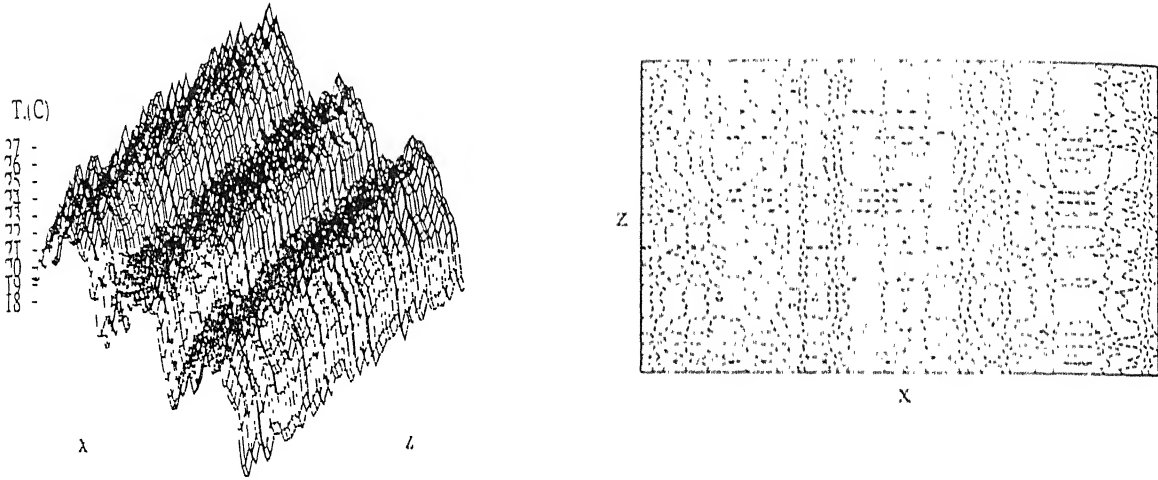


Figure C.5: Reconstructed Temperature Surface (Left) and Isotherms (Right) of the mid-plane of the Fluid Layer using AVMART3, Noisy Projection Data, 2-view Reconstruction, Two Dimensional Longitudinal Rolls

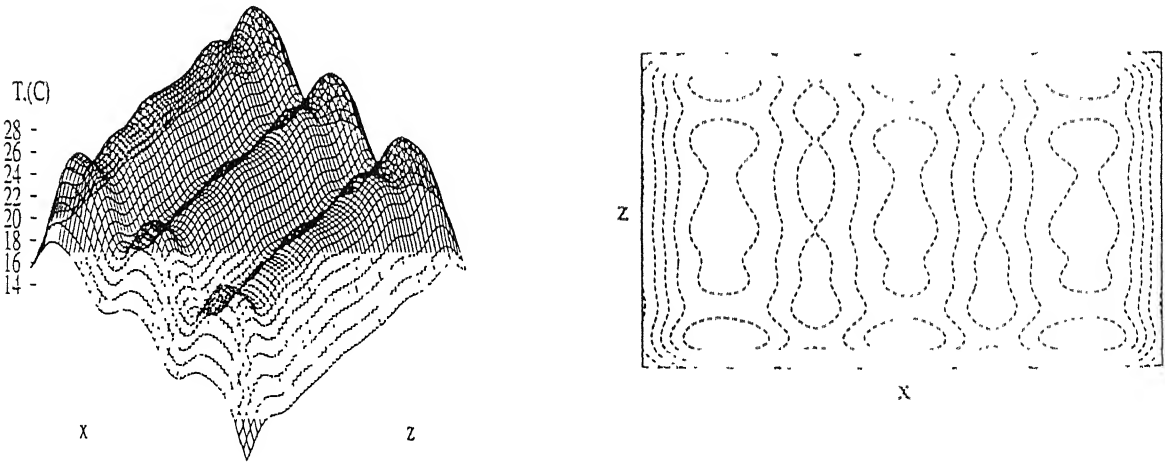


Figure C.6: Fourier Filtered Reconstructed Temperature Surface (Left) and Isotherms (Right) of the midplane of the Fluid Layer Using AVMART1, Noisy Projection Data, 2-view Reconstruction, Two Dimensional Longitudinal Rolls

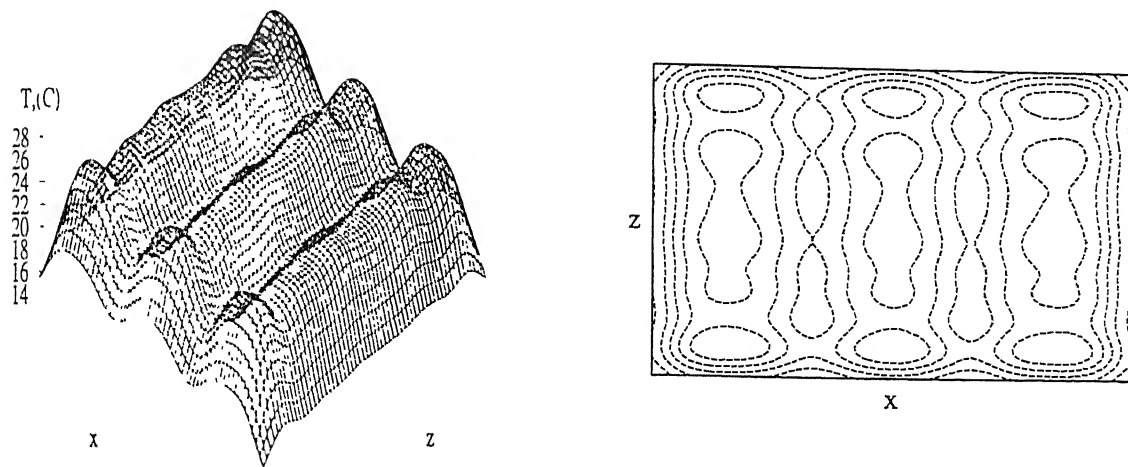


Figure C.7: Fourier Filtered Reconstructed Temperature Surface (Left) and Isotherms (Right) of the midplane of the Fluid Layer Using AVMART2, Noisy Projection Data, 2-view Reconstruction, Two Dimensional Longitudinal Rolls

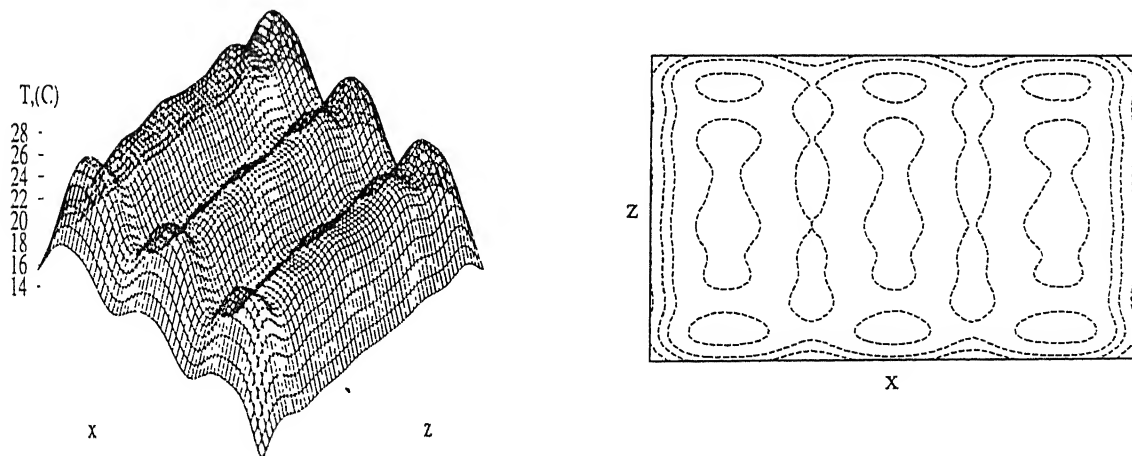


Figure C.8: Fourier Filtered Reconstructed Temperature Surface (Left) and Isotherms (Right) of the midplane of the Fluid Layer Using AVMART3, Noisy Projection Data, 2-view Reconstruction, Two Dimensional Longitudinal Rolls

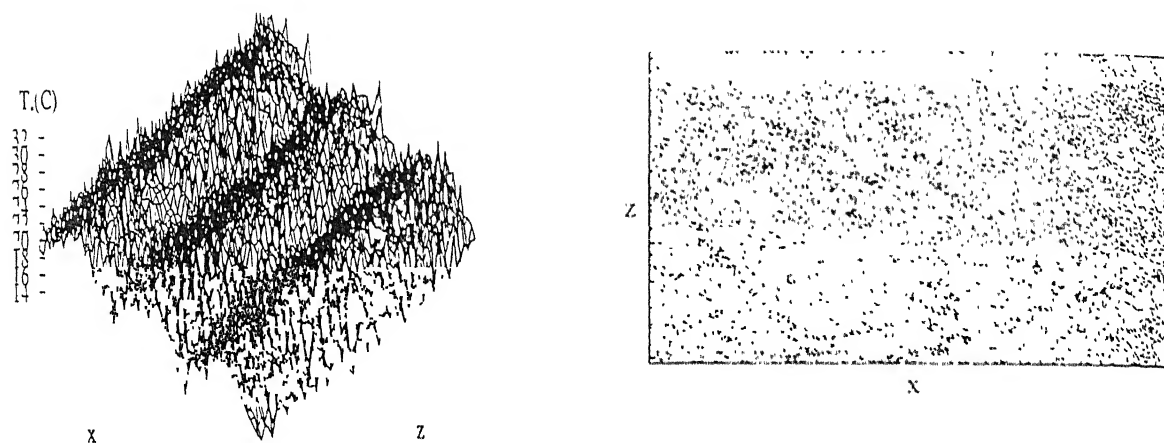


Figure C.9: Reconstructed Temperature Surface (Left) and Isotherms (Right) of the mid-plane of the Fluid Layer using AV MART1, Noisy Projection Data, 4-view Reconstruction, Two Dimensional Longitudinal Rolls

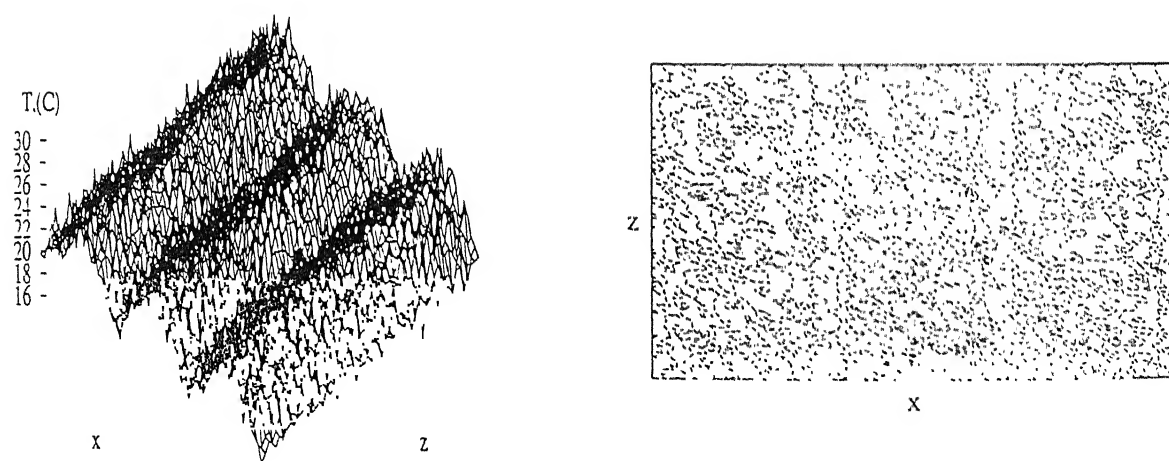


Figure C.10: Reconstructed Temperature Surface (Left) and Isotherms (Right) of the mid-plane of the Fluid Layer using AV MART2, Noisy Projection Data, 4-view Reconstruction, Two Dimensional Longitudinal Rolls

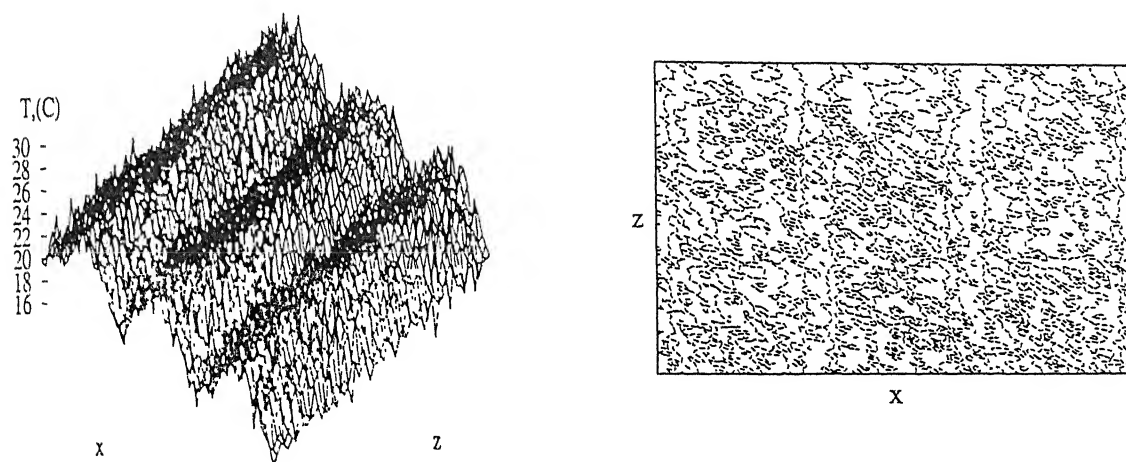


Figure C.11: Reconstructed Temperature Surface (Left) and Isotherms (Right) of the midplane of the Fluid Layer using AVMART3, Noisy Projection Data, 4-view Reconstruction, Two Dimensional Longitudinal Rolls

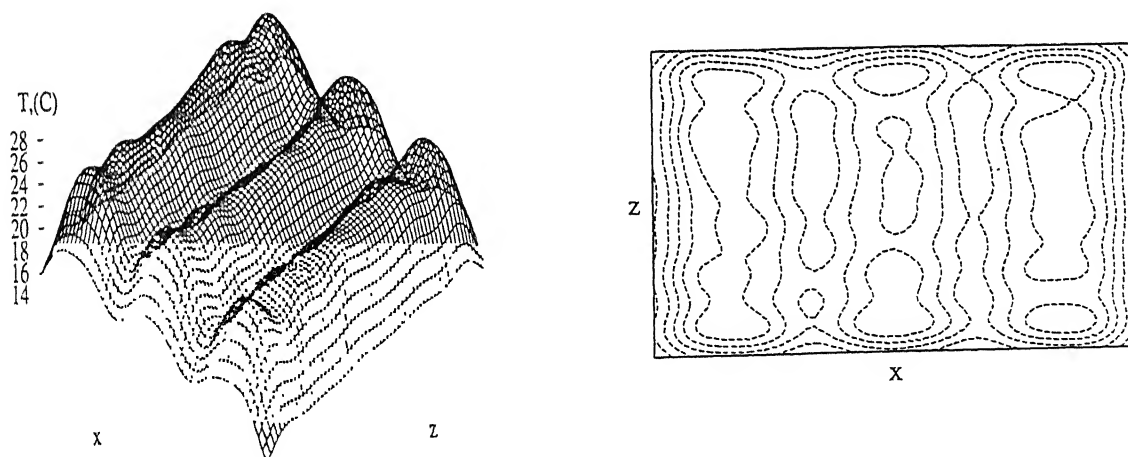


Figure C.12: Fourier-filtered Reconstructed Temperature Surface (Left) and Isotherms (Right) of the midplane of the Fluid Layer using AVMART1, Noisy Projection Data, 4-view Reconstruction, Two Dimensional Longitudinal Rolls

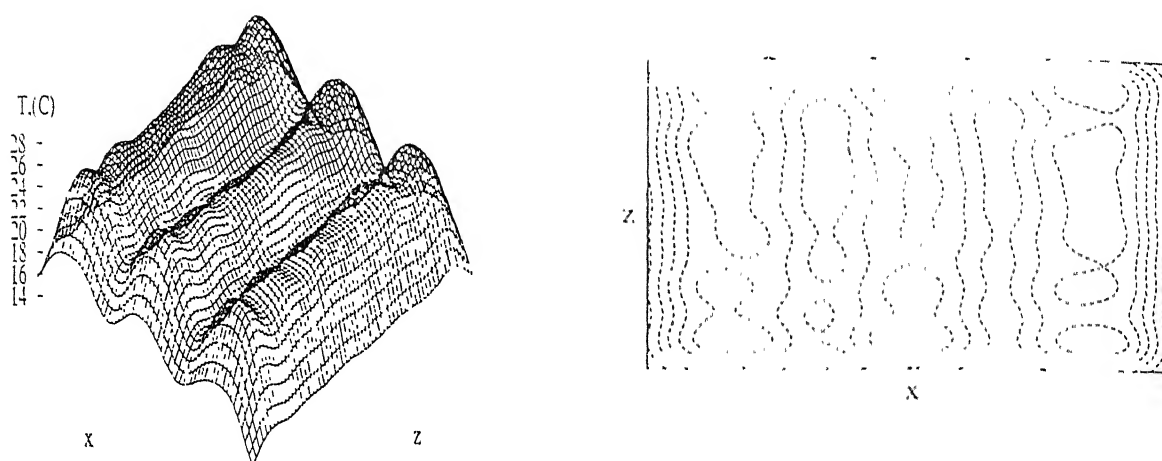


Figure C.13: Fourier-filtered Reconstructed Temperature Surface (Left) and Isotherms (Right) of the midplane of the Fluid Layer using AVMART2, Noisy Projection Data, 4-view Reconstruction. Two Dimensional Longitudinal Rolls

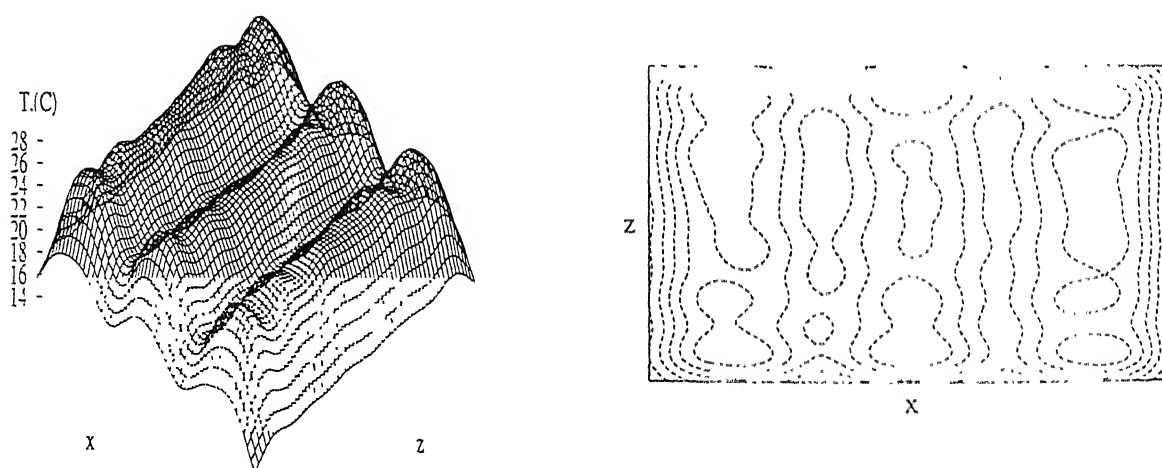


Figure C.14: Fourier-filtered Reconstructed Temperature Surface (Left) and Isotherms (Right) of the midplane of the Fluid Layer using AVMART3, Noisy Projection Data, 4-view Reconstruction. Two Dimensional Longitudinal Rolls

Table C.3: Comparison of the Three AVMART Algorithms: Temperature Field in the Form of Longitudinal Rolls, with 5% Added Noise in Projection Data, 4-view Reconstruction

	AVMART1	AVMART2	AVMART3
E_1 , °C	10.80	5.60	5.61
E_2 , °C	1.70	1.29	1.29
E_3 , %	9.97	7.55	7.55
CPU (sec)	3360.0	933.2	971.1
Number of Iterations	190	51	51

Table C.4: Fractional Distribution of the E_1 Error over the Fluid Domain, Temperature Field in the Form of Longitudinal Rolls, with 5% Added Noise in Projection Data, 4-view Reconstruction

Number of points (%) having error in the range	AVMART1	AVMART2	AVMART3
> 95 %	0.007	0.002	0.002
75-95 %	0.029	0.131	0.129
50-75 %	0.373	3.843	3.825

C.2 Sensitivity of Cubic Cells

The two view reconstruction for the cubic cell pattern is evaluated next in the presence of noisy projection data. Figures C.15-C.17 show the reconstructed temperature surface and isotherms using the three AVMART algorithms. The projection angles considered for reconstruction are again 0° and 90° . All the three algorithms converged to similar solution unambiguously. Figures C.18-C.20 show the Fourier-filtered temperature surface and isotherms of the reconstructed temperature field from the noisy projection data. The reconstructed field is recognisable in the form of cubic cells. The noise level in the reconstructed field is found to be slightly higher than the noise level in the projection data. Table C.5 shows the magnitude of the three different errors. Table C.6 shows the distribution of the fractional error over the fluid domain. All three algorithms are practically equal in terms of performance, though AVMART2 is seen to be slightly better.

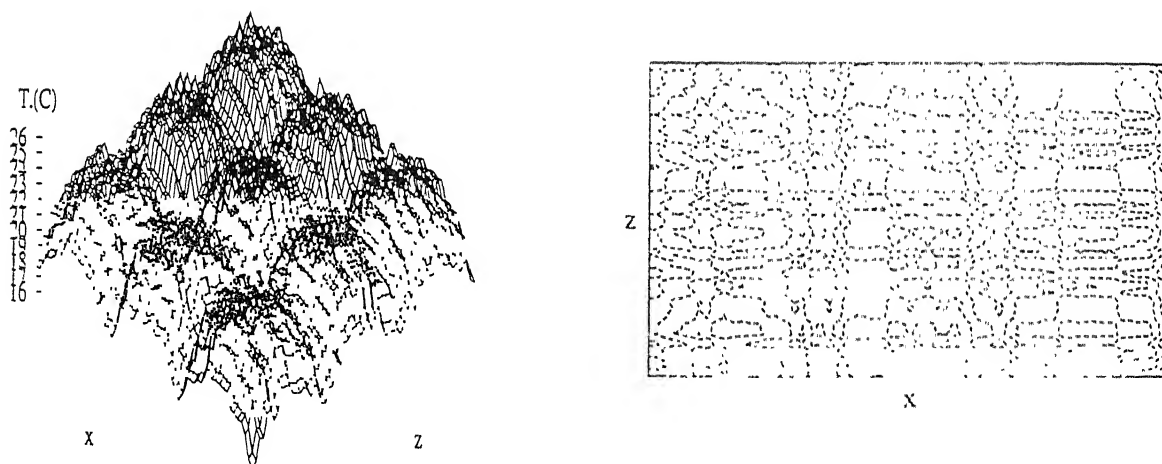


Figure C.15: Reconstructed Temperature Surface (Left) and Isotherms (Right) of the mid-plane of the Fluid Layer using AVMART1, Noisy Projection Data, 2-view Reconstruction, Cubic Cell Pattern

The noisy projection data has been employed for 4-view reconstruction of the temperature field. The two-view reconstruction using the noisy projection data obtained from the AVMART2 algorithm has been used as an initial guess. The error in the reconstruction is found to be greater than with 2-views alone. This shows the process of

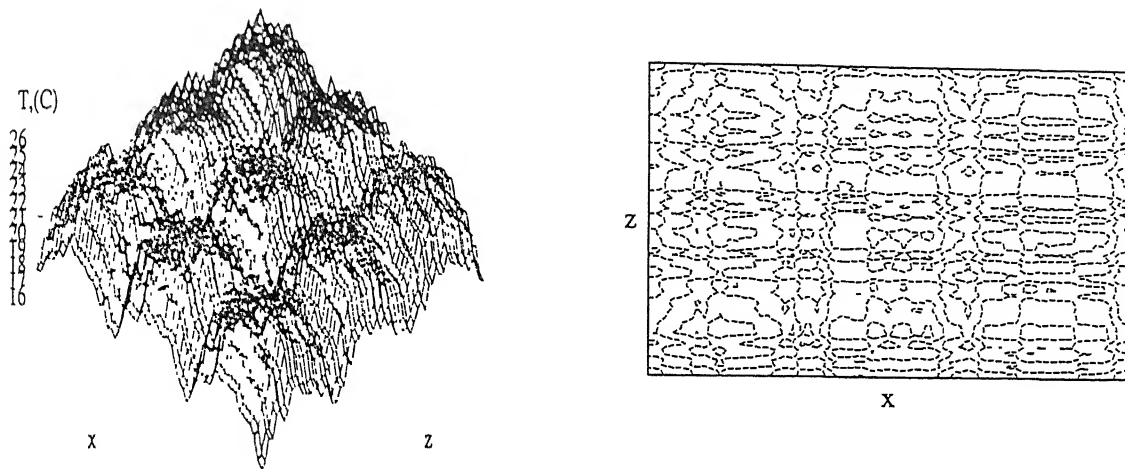


Figure C.16: Reconstructed Temperature Surface (Left) and Isotherms (Right) of the mid-plane of the Fluid Layer using AVMART2, Noisy Projection Data, 2-view Reconstruction, Cubic Cell Pattern

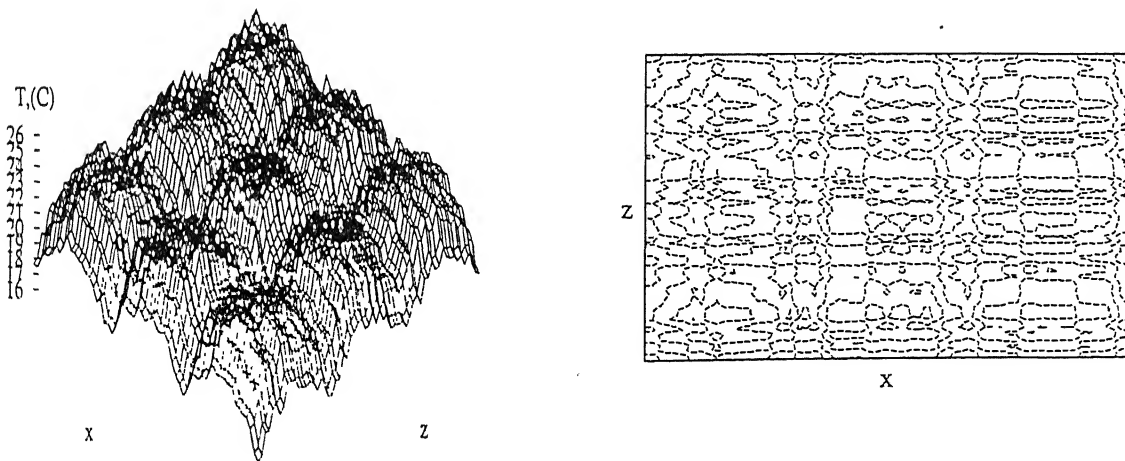


Figure C.17: Reconstructed Temperature Surface (Left) and Isotherms (Right) of the mid-plane of the Fluid Layer using AVMART3, Noisy Projection Data, 2-view Reconstruction, Cubic Cell Pattern

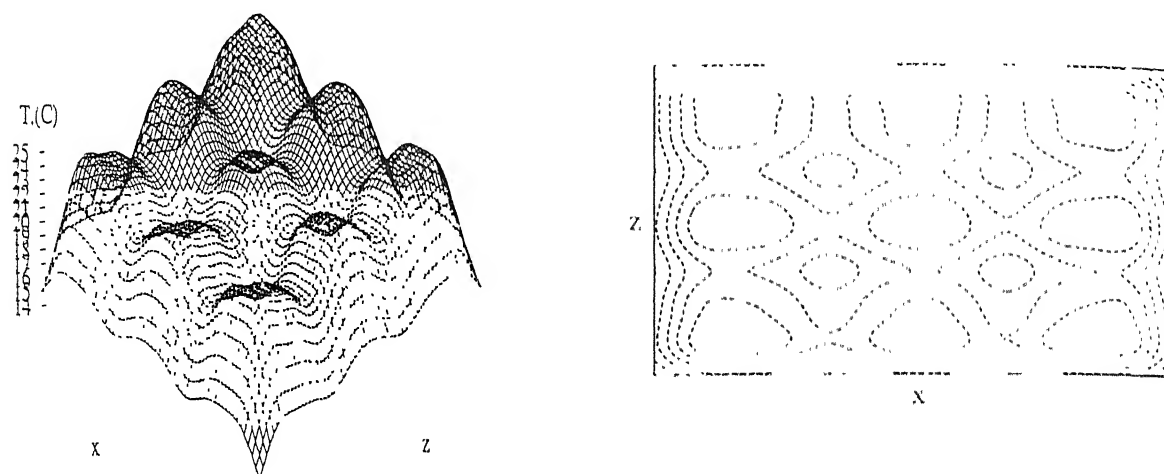


Figure C.18: Fourier-filtered Reconstructed Temperature Surface (Left) and Isotherms (Right) of the midplane of the Fluid Layer using AVMART1, Noisy Projection Data, 2-view Reconstruction, Cubic Cell Pattern

Table C.5: Comparison of the Three AVMART Algorithms: Temperature Field in the Form of Cubic Cells, with 5% Added Noise in Projection Data, 2-view Reconstruction

	AVMART1	AVMART2	AVMART3
$E_1, ^\circ\text{C}$	4.452	4.449	4.450
$E_2, ^\circ\text{C}$	1.08	1.08	1.08
$E_3, \%$	6.37	6.36	6.37
CPU (sec)	58.0	77.8	90.9
Number of Iterations	9	12	14

error amplification as more noisy projection data is included in the reconstruction process. Figures C.21-C.23 show the reconstructed temperature surface and isotherms from all the three AVMART algorithms. The corresponding Fourier-filtered temperature surfaces and isotherms are shown in Figures C.24-C.26.

Table C.7 and Table C.8 shows the error levels in the reconstructed data and the distribution of these errors inside the fluid layer. The AVMART2 and AVMART3 algo-

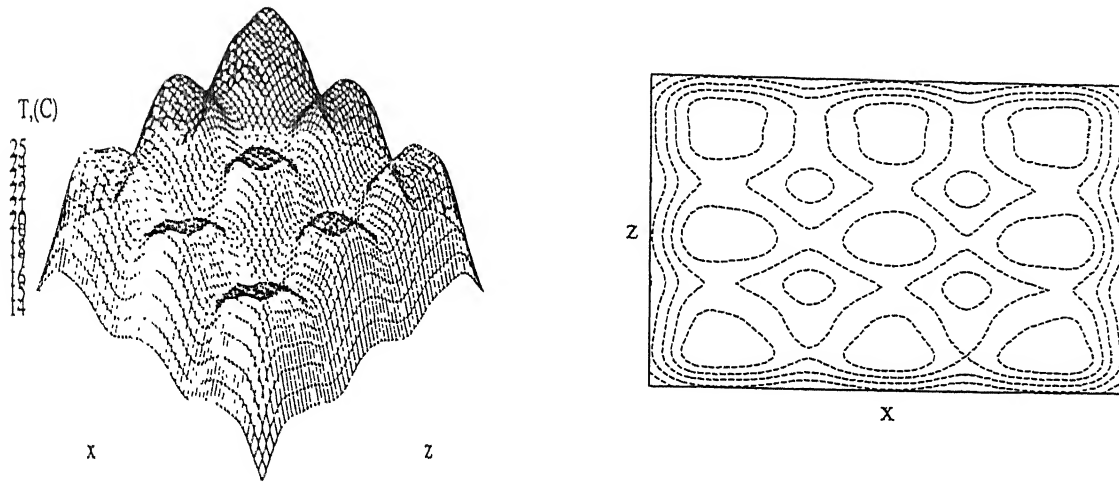


Figure C.19: Fourier-filtered Reconstructed Temperature Surface (Left) and Isotherms (Right) of the midplane of the Fluid Layer using AVMART2, Noisy Projection Data, 2-view Reconstruction, Cubic Cell Pattern

Table C.6: Fractional Distribution of the E_1 Error over the Fluid Domain, Temperature Field in the Form of Cubic Cells, with 5% Added Noise in Projection Data, 2-view Reconstruction

Number of points (%) having error in the range	AVMART1	AVMART2	AVMART3
> 95 %	0.004	0.004	0.004
75-95 %	0.222	0.200	0.222
50-75 %	4.400	4.387	4.400

rithms are seen to perform better than AVMART1 in the presence of noise and with more than two projections. AVMART2 is superior to AVMART3 since it takes a smaller CPU time.

Subbarao *et al* (1997) have concluded that MART3 is superior among the ART, MART and optimization family of algorithms. To test this result further, one set of reconstruction was carried out using 2-views of 0 and 90° for the problem with two dimensional longitudinal rolls. The projection data is superimposed with 5% noise and an

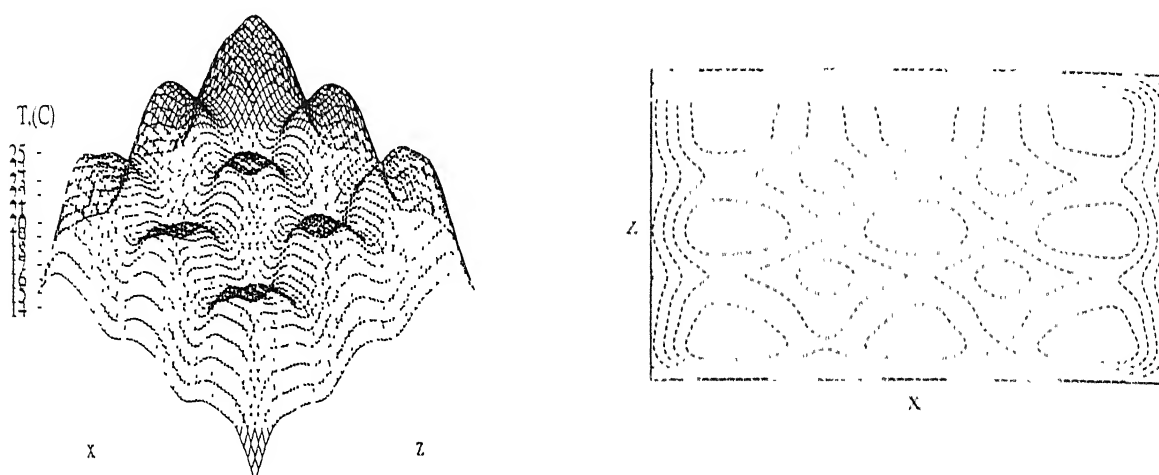


Figure C.20: Fourier-filtered Reconstructed Temperature Surface (Left) and Isotherms (Right) of the midplane of the Fluid Layer using AVMART3, Noisy Projection Data, 2-view Reconstruction, Cubic Cell Pattern

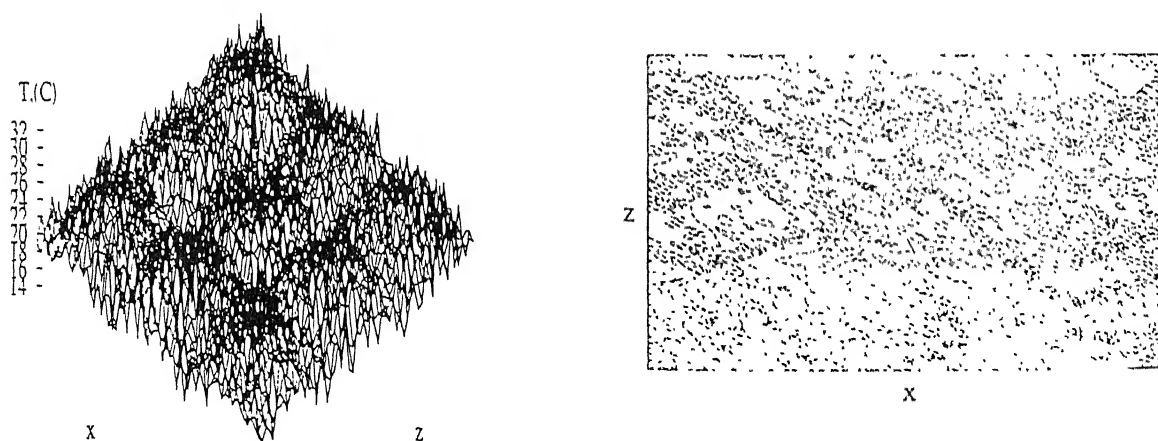


Figure C.21: Reconstructed Temperature Surface (Left) and Isotherms (Right) of the midplane of the Fluid Layer using AVMART1, Noisy Projection Data, 4-view Reconstruction, Cubic Cell Pattern

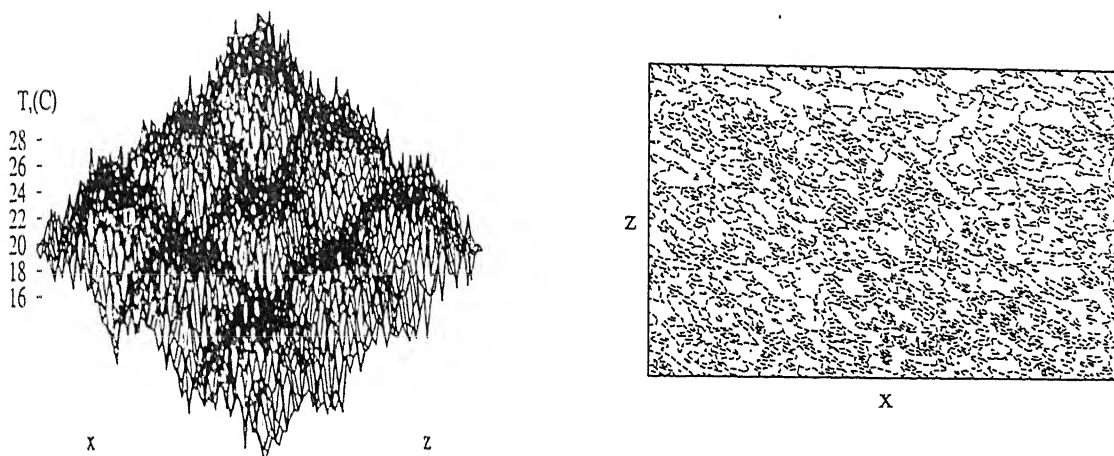


Figure C.22: Reconstructed Temperature Surface (Left) and Isotherms (Right) of the mid-plane of the Fluid Layer using AVMART2, Noisy Projection Data, 4-view Reconstruction, Cubic Cell Pattern

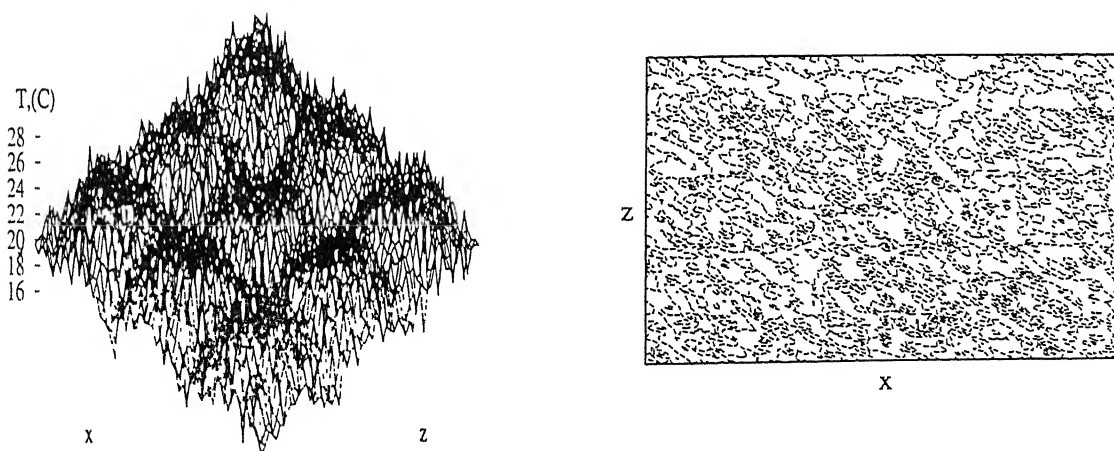


Figure C.23: Reconstructed Temperature Surface (Left) and Isotherms (Right) of the mid-plane of the Fluid Layer using AVMART3, Noisy Projection Data, 4-view Reconstruction, Cubic Cell Pattern

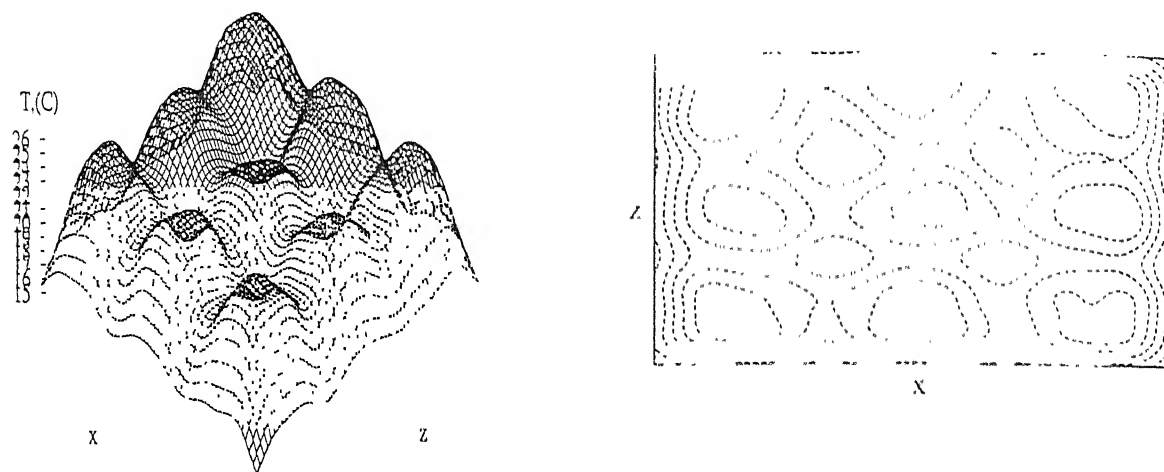


Figure C.24: Fourier-filtered Reconstructed Temperature Surface (Left) and Isotherms (Right) of the midplane of the Fluid Layer using AVMART1, Noisy Projection Data, 4-view Reconstruction, Cubic Cell Pattern

Table C.7: Comparison of the Three AVMART Algorithms: Temperature Field in the Form of Cubic Cells, with 5% Added Noise in Projection Data, 4-view Reconstruction

	AVMART1	AVMART2	AVMART3
$E_1, ^\circ\text{C}$	11.80	5.52	5.52
$E_2, ^\circ\text{C}$	1.78	1.36	1.36
$E_3, \%$	10.41	8.00	8.00
CPU (sec)	3558.7	954.3	989.6
Number of Iterations	190	53	53

initial guess of a constant temperature field was used. The MART3 algorithm was chosen for testing. Figure C.27 shows the reconstructed temperature surface and isotherms over the central horizontal plane of the fluid layer. Table C.9 shows the three different errors for the MART3 algorithm. Errors in this case are seen to be amplified by a factor of 4 compared to the initial noise level. The corresponding reconstruction using AVMART2 shows that the error level in the reconstructed field is the same as in the projection data. The computer time for MART3 is also higher by a factor of 4. Table C.10 shows the

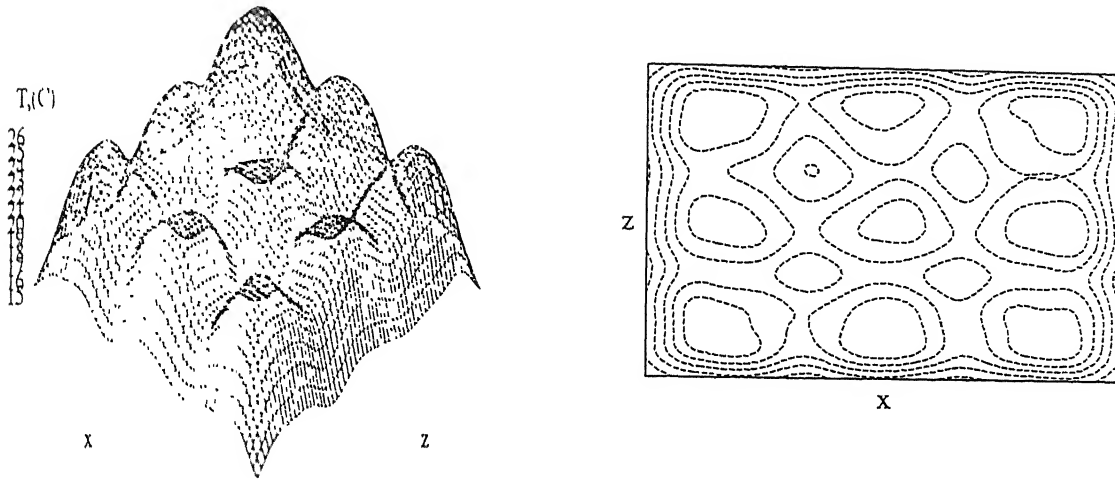


Figure C.25: Fourier-filtered Reconstructed Temperature Surface (Left) and Isotherms (Right) of the midplane of the Fluid Layer using AVMART2, Noisy Projection Data, 4-view Reconstruction, Cubic Cell Pattern

Table C.8: Fractional Distribution of the E_1 Error over the Fluid Domain, Temperature Field in the Form of Cubic Cells, with 5% Added Noise in Projection Data, 4-view Reconstruction

Number of points (%) having error in the range	AVMART1	AVMART2	AVMART3
> 95 %	0.004	0.007	0.007
75-95 %	0.029	0.349	0.346
50-75 %	0.276	5.186	5.177

fractional distribution of the E_1 error over the fluid layer. Error distribution for both the algorithms are seen to be fairly similar.

The major conclusions that can be drawn from the numerical results presented above are :

1. The three AVMART algorithms show similar performance in the presence of noise in the projection data. AVMART2 is however marginally superior in terms of errors

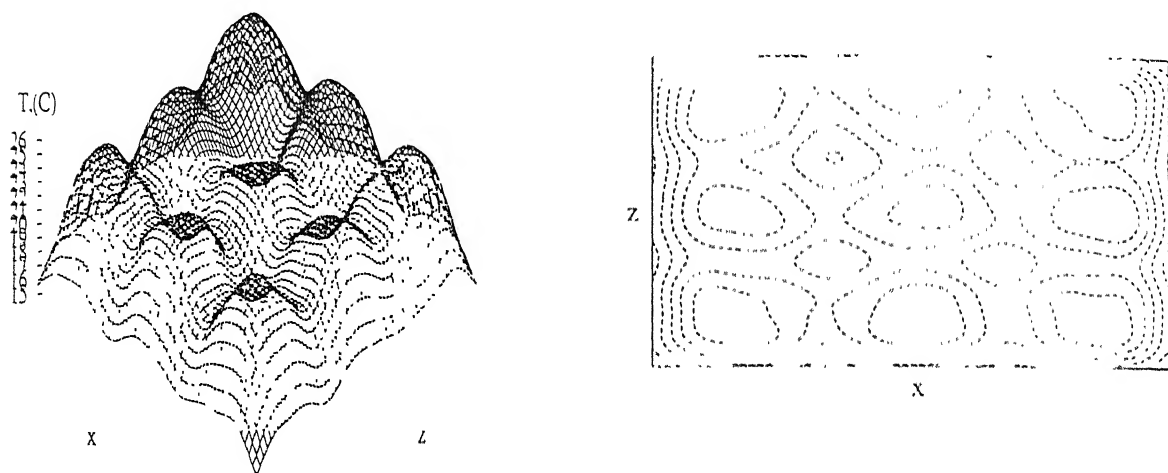


Figure C.26: Fourier-filtered Reconstructed Temperature Surface (Left) and Isotherms (Right) of the midplane of the Fluid Layer using AVMART3, Noisy Projection Data, 4-view Reconstruction, Cubic Cell Pattern

Table C.9: Comparison of the MART3 Algorithm with AVMART2 Algorithm: Temperature Field in the Form of Two Dimensional Longitudinal Rolls, with 5% Added Noise in Projection Data, 2-view Reconstruction

	MART3	AVMART2
$E_1, ^\circ\text{C}$	12.30	2.80
$E_2, ^\circ\text{C}$	3.76	0.97
$E_3, \%$	22.00	5.68
CPU (sec)	344.2	91.8
Number of Iterations	4	14

and CPU time.

2. The noise in the projection data persists after reconstruction, but the dominant trend can be identified after Fourier-filtering.
3. Increasing the number of noisy projections amplifies the error in reconstruction.
4. AVMART2 clearly shows superiority over MART3 for noisy projection data. Hence

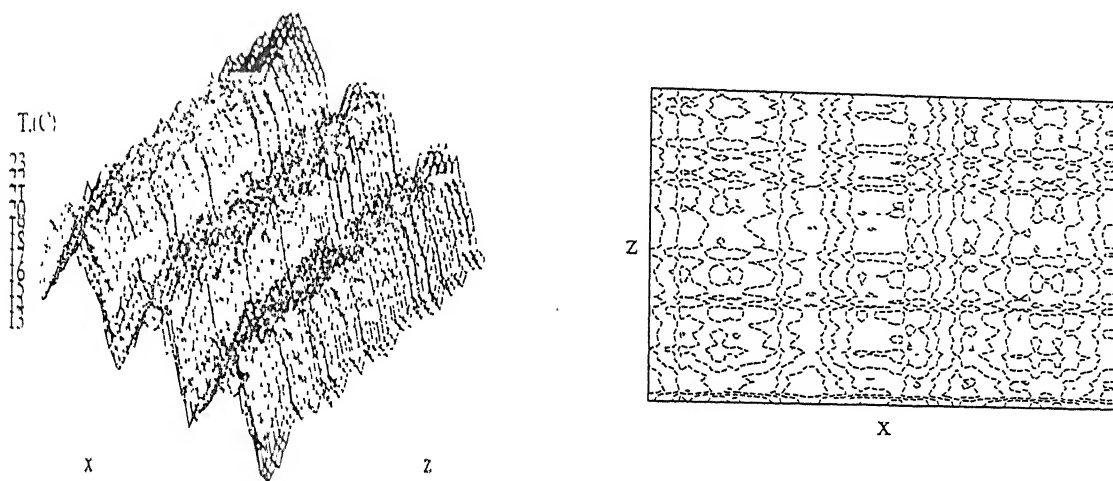


Figure C.27: Reconstructed Temperature Surface (Left) and Isotherms (Right) of the midplane of the Fluid Layer using MART3, Noisy Projection Data, 2-view Reconstruction, Two Dimensional Longitudinal Rolls

Table C.10: Fractional Distribution of the E_1 Error over the Fluid Domain: Comparison Between MART3 and AVMART2 Algorithms, Temperature Field in the Form of Two Dimensional Longitudinal Rolls, with 5% Added Noise in Projection Data, 2-view Reconstruction

Number of points (%) having error in the range	MART3	AVMART2
> 95 %	0.043	0.012
75-95 %	1.172	2.821
50-75 %	13.40	14.76

it supercedes MART3 as the favoured tomographic algorithm for interferometry.

Appendix D

Implementation of the Lagrange Multiplier Technique

D.1 Maximization of Entropy Through Lagrangian Multipliers

The projection data P_i are the line integrals of the field data f_j and so

$$\sum_{j=1}^{j=N} w_{ij} f_j = P_i \quad (\text{D.1})$$

where $i = 1, 2, \dots, M$ and $j = 1, 2, \dots, N$, M and N being respectively the total number of rays in the projection data and cells in the discretization. The entropy function is defined as:

$$\text{Entropy} = - \sum_{j=1}^{j=N} f_j \ln f_j \quad (\text{D.2})$$

The entropy maximization technique is to maximize the entropy function defined in Equation D.2 with the projection data as a constraint (Equation D.1). The maximization of a function under certain constraints can be achieved through the method of Lagrangian multipliers. In this method, we construct the composite function:

$$F(f_j) = - \sum_{j=1}^{j=N} f_j \ln f_j - \sum_{i=1}^{i=M} \lambda_i \left\{ \sum_{j=1}^{j=N} (w_{ij} f_j) - P_i \right\} \quad (\text{D.3})$$

where λ_i are the Lagrangian multipliers. Under the maximization condition we require $\frac{\partial F}{\partial f_j} = 0$, Hence from Equation D.3,

$$\frac{\partial F}{\partial f_j} = -(1 + \ln f_j) - \sum_{i=1}^{i=M} \lambda_i w_{ij} = 0 \quad (D.4)$$

Equation D.4 leads to

$$f_j = \exp(-1 - \sum_{i=1}^{i=M} \lambda_i w_{ij}) \quad (D.5)$$

Substituting Equation D.5 in Equation D.1 and simplifying results in

$$\sum_{j=1}^{j=N} w_{ij} \prod_{i=1}^{i=M} (\exp(-\lambda_i w_{ij}) = P_i \exp(1) \quad (D.6)$$

Replacing $\exp(-\lambda_i) = x_i$ Equation D.6 can be written as

$$\sum_{j=1}^{j=N} w_{ij} \prod_{i=1}^{i=M} (x_i)^{w_{ij}} = P_i \exp(1) \quad (D.7)$$

Assuming,

$$g_i(x_i) = \sum_{j=1}^{j=N} w_{ij} \prod_{i=1}^{i=M} (x_i)^{w_{ij}} \quad (D.8)$$

Equation D.7 reduces to

$$g_i(x_i) = P_i \exp(1) \quad (D.9)$$

Equation D.9 has to be solved iteratively. Let $x_i^{(1)}$ be the first guess for the solution set. Then $g_i(x_i)$ can be linearized by expanding it using Taylor series around $g_i(x_i^{(1)})$.

$$g_i(x_i) = g_i(x_i^{(1)}) + \left(\frac{\partial g_i}{\partial x_1}\right)_{x_i^{(1)}} \Delta x_1^{(1)} + \left(\frac{\partial g_i}{\partial x_2}\right)_{x_i^{(1)}} \Delta x_2^{(1)} + \dots + \left(\frac{\partial g_M}{\partial x_M}\right)_{x_i^{(1)}} \Delta x_M^{(1)} \quad (D.10)$$

Hence Equation D.9 can now be solved using the standard Gauss-Siedel procedure to obtain the value of x_i . Since x_i are directly related to the λ_i , these can be used with Equation D.5 to obtain the solution f_j .

9.2 Minimization of Energy Through Lagrangian Multipliers

The energy function is defined as:

$$\text{Energy} = - \sum_{j=1}^{j=N} f_j^2 \quad (\text{D.11})$$

The composite energy function can be constructed using Lagrange multipliers as

$$F(f_j) = - \sum_{j=1}^{j=N} f_j^2 - \sum_{i=1}^{i=M} \lambda_i \left[\sum_{j=1}^{j=N} w_{ij} f_j - P_i \right] \quad (\text{D.12})$$

Under the minimization condition

$$\frac{\partial F}{\partial f_j} = -2f_j - \sum_{i=1}^{i=M} \lambda_i w_{ij} = 0 \quad (\text{D.13})$$

Equation D.13 leads to

$$f_j = -\frac{1}{2} \sum_{i=1}^{i=M} \lambda_i w_{ij} \quad (\text{D.14})$$

Substituting Equation D.14 in Equation D.1 and simplifying

$$\sum_{i=1}^{i=M} \lambda_i \sum_{j=1}^{j=N} w_{ij} w_{kj} = -2P_k \quad (\text{D.15})$$

where $k = 1, 2 \dots N$.

Equation D.15 is a system of linear equations with the multipliers λ_i as the unknown. This set of equations can be solved through the Gauss-Seidel iterations to obtain the solution for λ_i . Equation D.14 gives the value of the field to be reconstructed, once the λ_i 's are known.

128770

Date Stamp **A128770**

This book is to be returned on the
date last stamped.

This image shows a blank sheet of white paper with horizontal blue ruling lines. A single vertical red margin line runs down the center of the page, creating two equal-width columns. The paper appears to be from a notebook or a standard composition book. There are no markings, text, or drawings on the page.

A 128770

TH

NET/1998/P

M687e